MAX-PLANCK-INSTITUT FÜR KOLLOID- UND GRENZFLÄCHENFORSCHUNG

Laser Patterned N-doped Carbon: Preparation, Functionalization and Selective Chemical Sensors

Dissertation

Zur Erlangung des akademischen Grades

Doktor der Naturwissenschaften („Doctor rerum naturalium“, Dr. rer. nat.)

in Fach Chemie

Spezialisierung: Anorganische und Allgemeine Chemie

Eingereicht an der Mathematisch-Naturwissenschaftlichen Fakultät - Institut für Chemie der Humboldt-Universität zu Berlin von

Huize Wang

Präsidentin der Humboldt-Universität zu Berlin
Prof. Dr. Julia von Blumenthal

Dekanin der Mathematisch-Naturwissenschaftlichen Fakultät

Prof. Dr. Caren Tischendorf

Gutachter/innen: 1. Prof. Dr. Nicola Pinna

2. Prof. Dr. Dr. h.c. Markus Antonietti

3. Prof. Dr. Yan Lu

Tag der mündlichen Prüfung: 30.05.2023

https://doi.org/10.18452/26753

Do the difficult things while they are easy and do the great things while they are small. A journey of a thousand miles must begin with a single step.

(Lao Tzu)

Abstract

The recent global COVID-19 pandemic clearly displayed that the high costs of medical care on top of an aging population bring great challenges to our health systems. As a result, the demand for personalized wearable devices to continuously monitor the health status of individuals by non-invasive detection of physiological signals, thereby providing sufficient information for health monitoring and even preliminary medical diagnosis, is growing. For the fabrication of such flexible electronic sensors, inexpensive materials for mass-scale production are required. In general, carbon-based materials with high electrical conductivity, high surface areas, and high mechanical and chemical stability have competitive potential. However, a lack of simple and suitable processing methods and poor reproducibility still bring challenges to the practical application of carbon-based devices. Laser-carbonization, as a new processing technology, is a green tool with low solvent use and energy cost to generate small-scale, flexible electronic materials.

This dissertation summarizes my research on laser-carbonization as a tool for the synthesis of functional materials for flexible gas sensors. The whole work is divided into four parts. Compared with commonly used polymers as precursors (e.g., polyimide and graphene oxide), the first part presents an integrated two-step approach starting from molecular precursor to prepare laser-patterned (nitrogen-doped) carbon (LP-NC). The second part shows the fabrication of a flexible LP-NC sensor architecture for room-temperature sensing of CO_2 via laser conversion of an adenine-based primary ink. By the unidirectional energy impact in conjunction with depth-dependent attenuation of the laser beam, a novel layered sensor heterostructure with a porous transducer and an active sensor layer is formed. This molecular precursor-based laser carbonization method enables the modification of printed carbon materials. It is demonstrated that the properties of LP-NC can be selectively tuned by adding porogens, additives, or reactants to the primary film. In the third part, it is shown that impregnation of LP-NC with MoC_{1-x} nanoparticle alters the charge carrier density, which, in turn, increases the sensitivity of LP-NC towards gaseous analytes. The last part explains that the electrical conductivity and surface properties of LP-NC can be modified by adding different concentrations of $Zn(NO_3)_2$ into the primary ink to add selectivity elements to the sensor materials. Based on these factors, the LP-NC-based sensor platforms prepared in this study exhibited high sensitivity and selectivity for different volatile organic compounds.

Zusammenfassung

Die kürzliche globale COVID-19-Pandemie hat deutlich gezeigt, dass hohe medizinische Kosten eine große Herausforderung für unser Gesundheitssystem darstellen. Daher besteht eine wachsende Nachfrage nach personalisierten tragbaren Geräten zur kontinuierlichen Überwachung des Gesundheitszustands von Menschen durch nicht-invasive Erfassung physiologischer Signale. Kohlenstoffbasierte Materialien mit hoher elektrischer Leitfähigkeit, großer Oberfläche und hoher mechanischer und chemischer Stabilität haben Wettbewerbspotenzial bei der Herstellung solcher flexiblen elektronischen Sensoren. Probleme wie das Fehlen einfacher und geeigneter Verarbeitungsmethoden und die schlechte Reproduzierbarkeit stellen jedoch immer noch Herausforderungen für die praktische Anwendung von kohlenstoffbasierten Geräten dar. Die Laserkarbonisierung ist ein neuartiges lösungsmittelarmes, energiearmes und umweltfreundliches Herstellungswerkzeug für kleine, flexible elektronische Materialien.

Diese Dissertation fasst die Forschung zur Laserkarbonisierung als Werkzeug für die Synthese flexibler Gassensoren zusammen und präsentiert die Arbeit in vier Teilen. Der erste Teil stellt ein integriertes zweistufiges Verfahren zur Herstellung von laserstrukturiertem (Stickstoff-dotiertem) Kohlenstoff (LP-NC) ausgehend von molekularen Vorstufen vor. Der zweite Teil demonstriert die Herstellung eines flexiblen Sensors für die CO_2 Erfassung basierend auf der Laserumwandlung einer Adenin-basierten Primärtinte. Die unidirektionale Energieeinwirkung kombiniert mit der tiefenabhängigen Abschwächung des Laserstrahls ergibt eine neuartige geschichtete Sensorheterostruktur mit porösen Transducer- und aktiven Sensorschichten. Dieser auf molekularen Vorläufern basierende Laserkarbonisierungsprozess ermöglicht eine selektive Modifikation der Eigenschaften von gedruckten Kohlenstoffmaterialien durch Hinzufügen von Porogenen, Additiven oder Reaktanten zu Primärfilmen. Im dritten Teil wird gezeigt, dass die Imprägnierung von LP-NC mit MoC_{1-x}-Nanopartikeln die Ladungsträgerdichte verändert, was wiederum die Empfindlichkeit von LP-NC gegenüber gasförmigen Analyten erhöht. Der letzte Teil erläutert, dass die Leitfähigkeit und die Oberflächeneigenschaften von LP-NC verändert werden können, indem der Originaltinte unterschiedliche Konzentrationen von $Zn(NO_3)_2$ zugesetzt werden, um die selektiven Elemente des Sensormaterials zu verändern. Basierend auf diesen Faktoren zeigte die hergestellte LP-NC-basierte Sensorplattform in dieser Studie eine hohe Empfindlichkeit und Selektivität für verschiedene flüchtige organische Verbindungen.

Acknowledgment

The writing of my doctoral dissertation has come to an end, and my doctoral study is coming to an end. I will leave the Max Planck Institute and embark on a new life journey. This period of doctoral study is undoubtedly an unforgettable landscape in my life. I will cherish this memory and commemorate it well. My heartfelt thanks go to the supervisors, family, and friends who have accompanied me all the way through the ups and downs. Your existence will be written into my life memory.

First of all, I would like to express my deepest appreciation to my great supervisor, Prof. Dr. Markus Antonietti, for providing me with the precious opportunity to support my doctoral work at Max Planck Institute of Colloids and Interfaces. Thanks to him for opening the door to science for me. I enjoy every discussion with him and really appreciate he always gives me countless inspirations for future scientific research directions.

I would like to acknowledge Prof. Dr. Nicola Pinna from Humboldt University of Berlin for the supervision of the thesis. Thanks to him for imparting me with a lot of experience in sensors and giving suggestions on the research topics.

I would like to express my deepest gratitude to my group leader Dr. Volker Strauss. He has been a great support to me for the past four years, and he has never refused to help me. He has always been experienced and visionary in every scientific discussion in the past. He also helped me solve many difficulties and encouraged me. He taught me a lot in the field of laser carbon synthesis and carbonaceous materials, and I grew up a lot under his teaching. Volker has been such a great supervisor and best friend to me.

My great thanks to the present and past members of new carbonization concepts: Dr. Simon Delacroix, Dr. Pablo Jiménez-Calvo, Sanghwa Moon, and Ines Below-Lutz. In particular, I would like to thank Ines for his great support in the purchase of chemical reagents and the use of instruments. I am also very grateful to all my colleagues and technicians for data collection. Many thanks and respect also to all the technicians in the department. Thank Heike Runge, Bolortuya Badamdorj, Antje Völkel and Jessica Brandt. I want to thank all my colleagues at MPI who have helped me. Although I might not know your name, your face will always be in my memory.

Last but not least, a special thanks to my family. Thanks for their unquestionable support and dedication. Special thanks to my wife Su. She is always by my side to support and encourage me whenever I fail or encounter difficulties.

Here, I would like to thank my committee members and reviewers for their valuable suggestions and time.

Table of Contents

1. Motivation

In recent years, with the rapid expansion of the population, the excessive development of the economy, and the excessive use of resources, the environment has been increasingly affected. Occurring disasters and diseases made people realize their unpreparedness for unexpected and undetected instances. In particular, during the global COVID-19 pandemic, the high cost of medical care and the aging population has brought great challenges to the health system. As a model case of the resulting demands, personalized wearable devices, which can continuously monitor the health status of individuals by non-invasive detection of physiological signals, thereby providing sufficient information for health monitoring and even preliminary medical diagnosis, are growing.

Such flexible electronic sensors that meet the needs of human beings with high performance being at the same time renewable, sustainable, and environment-friendly have attracted widespread attention among materials scientists. The current materials research for such devices should strictly focus on two aspects: 1) the use of sustainable resources instead of expensive and hazardous materials, 2) simple and low-energy cost manufacturing processes.

Carbon, as the fourth most abundant element in the universe, can provide solutions that balance economic interest and the environment. Carbon-based materials (e.g., porous carbons, graphenes, carbon nanotubes) with excellent electrical conductivity, high surface areas, and high mechanical and chemical stability have high competitive potential in advanced flexible electronics, such as supercapacitors, batteries, gas sensors, biosensors, etc. In addition, by bonding carbon atoms with other metal and non-metal atoms, the microporous structure, polarity and electronic charge distribution of carbon materials can be adjusted to the different application fields. However, a lack of simple and suitable processing methods and poor reproducibility still brings challenges.

A new processing technology, namely laser carbonization, stands out in this vision. Unlike traditional pyrolysis methods that can produce bulk carbon materials on a large scale, laser carbonization is local, additive, and good for the milligram scale. Due to the low solvent use or precursor product requirements, laser carbonization can be considered a green method to generate small-scale electronics.

As early as the 1980s and 90s, scientists experimentally proved the feasibility of laser carbonization. With the rapid development of flexible electronics and the promotion of sustainable use of biological resources over the past decade, laser carbonization has regained

the focus of materials scientists as it demonstrates a high-speed processing, low energy consumption and direct patterning process to achieve functional carbon films.

This thesis aims to provide an in-depth look at the fundamentals of laser carbonization by using molecular precursors and applying laser-carbonized carbon films to flexible gas sensors. Through the selection of versatile organic ink compositions, the interaction between sensor performance and the pore structure, atomic structure, and surface properties of laser-carbonized porous nitrogen-doped carbon materials was studied. For instance, nitrogen-doped carbons were proposed for selective CO_2 capture as they intrinsically provide selective binding sites for CO_2, and based on that, we used a nitrogen-rich molecular precursor on a flexible substrate to produce a nitrogen-containing carbon material by laser carbonization that can be used for selective CO_2 detection. In addition, by introducing metal salts into the primary organic ink, the nanoparticles generated *in situ* can modify the electric properties, surface active area, and surface polarity of the corresponding laser-patterned nitrogen-doped carbons, thereby improving the sensitivity and selectivity towards special analytes (e.g., VOCs)

2. Background and scope

2.1 The excellent properties of carbon

Carbon, the sixth element in the periodic table, is the chemical basis of all life on Earth.[1] It is one of the most abundant materials in the universe (4th most abundant element by mass), only outpassed by hydrogen, helium and oxygen. Carbon-carbon bonds are strong and stable, and can form longer chains. Thus, carbon can form an almost infinite number of different compounds. For instance, the simplest organic compounds are hydrocarbons. These compounds have a backbone of carbon chains with hydrogen atoms bonded, terminating their structure.[2] A smaller number of carbon-containing compounds are inorganic, which mainly fall into the following three categories: carbon oxides (such as carbon monoxide and carbon dioxide), carbonates, and cyanides.[3]

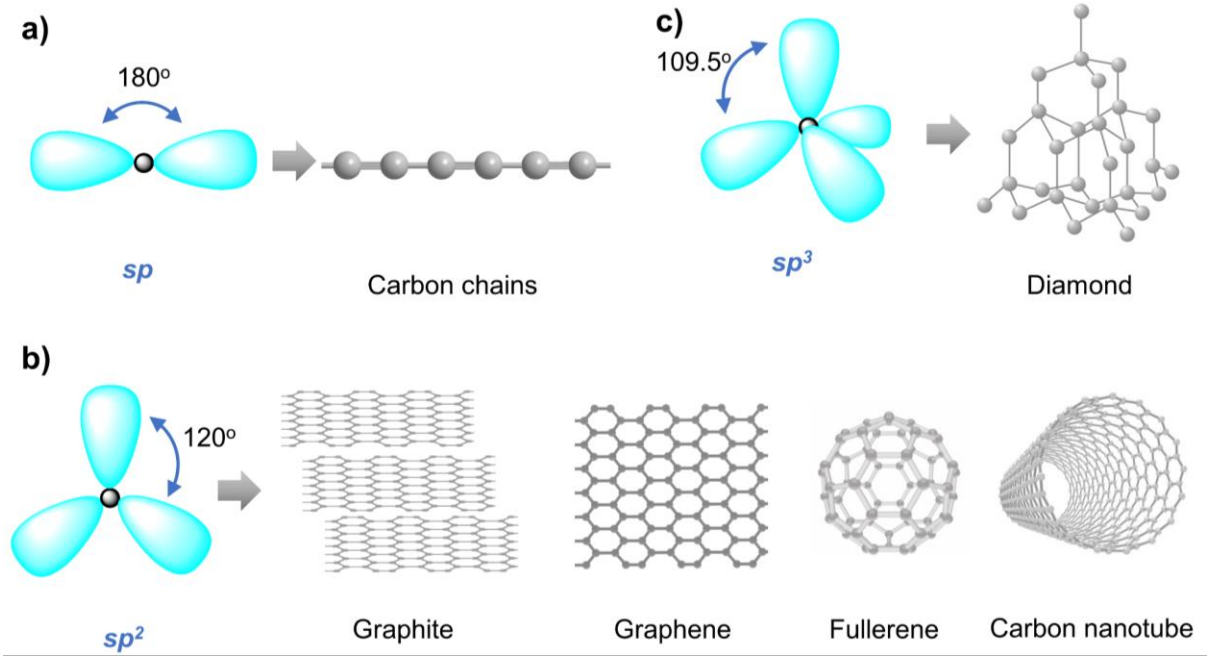

Figure 2. 1. *Schematic illustration of various carbon allotropes according to the three kinds of carbon hybridization: a) sp hybridization: carbon chains; b) sp^2 hybridization: graphite, graphene, fullerene, carbon nanotube; c) sp^3 hybridization: diamond.*[4–6]

Due to the instability of single carbon atoms, carbon generally exists stably in the form of a multi-atonic structure, and there are many allotropes in different arrangements. In general, these allotropes can be classified according to the character of carbon hybridization (**Figure 2. 1**): sp hybridization carbyne (such as cumulene, polyyne),[5,6] sp^2 hybridization (e.g., graphite, graphene, fullerenes, and carbon nanotubes), sp^3 hybridization (e.g., diamond), as well as several mixed sp^2-sp^3 forms (e.g., amorphous carbon)

There is one other common classification of carbon allotropes based on dimensionality[7]: zero-dimensional fullerenes, one-dimensional carbon nanotubes, two-dimensional graphene, three-dimensional diamond, amorphous carbon and graphite.

The hybridization of carbon atoms' electronic states produces varying electronic and mechanical properties. Carbon has the potential to form conductive bonds in sp, sp^2 hybridization and is a wide-gap semiconductor in sp^3 tetrahedral coordination. For instance, graphene has a characteristic semimetal electronic structure with a linear band dispersion and extraordinarily high electron mobility up to 200000 $cm^2 \cdot (Vs)^{-1}$ at lower temperatures, as well as a high electric conductivity of $1.46 \pm 0.82 \times 10^6$ $S \cdot m^{-1}$.[8,9] The intrinsic tensile strength of graphene is 130.5 GPa, and Young's modulus is 1 TPa.[10] In contrast, 3D diamond is a wide-band-gap (5.47 eV) semiconductor and the hardest natural existing material.[11,12] Each allotrope has a unique structure and physical and chemical properties. The fundamental study and technological application of all carbon allotropes and even the discovery of new carbon forms continue to attract intensive attention.

2.2 Synthesis methods for carbon materials

As mentioned above, each form of carbon has unique properties. sp^2 hybridization endows carbon materials with high electrical conductivity and chemical and thermal stability. sp^2 carbon and the hybrid sp^2-sp^3 materials are used in a wide range of applications, such as gas storage,[13] catalysts,[14] fuel cells,[15] batteries,[16] supercapacitors,[17] water/air purifications.[18,19] Moreover, carbon nanomaterials (such as graphene, CNTs, carbon black, and hybrid structured carbon materials) are most commonly used in flexible and wearable sensors.[20,21] Controlling the properties of reaction products by understanding the influence of precursors and reaction parameters is one of the great challenges for the further commercial application of carbon materials.

Pyrolysis, which is defined as the thermally induced chemical decomposition of organic materials in the absence of oxygen, is the most common process in carbon nanomaterial synthesis.[22] During pyrolysis, polymer or molecular precursors are heated to high temperatures in an inert environment, which leads to thermal decomposition of the precursor to produce volatile products and leave a carbon-rich solid residue.

At high temperatures, the breaking of covalent bonds and rearrangements of bonds are induced to form thermodynamically stable products. Pyrolysis of organic precursors leaves mostly carbon as the residue. Two centuries ago, people carbonized cellulose fibers extracted from

cotton and bamboo at high temperatures to make carbon filaments for incandescent lamps[23]. The modern developed chemical vapor deposition (CVD) technique for the synthesis of carbon materials is also based on the principle of pyrolysis, but allows the volatile reactive fragments to recondense.[24]

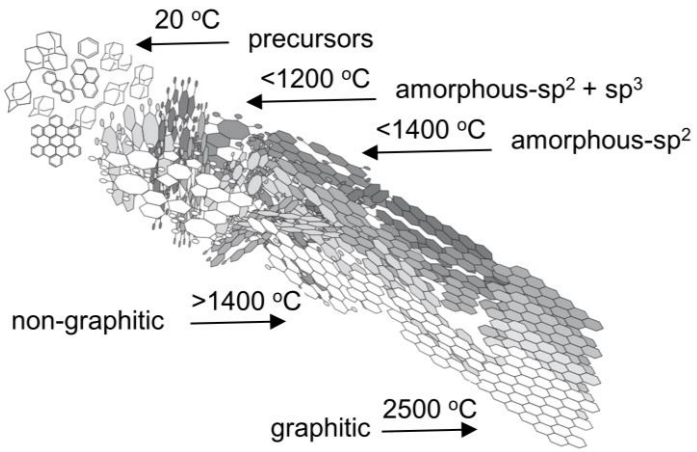

Figure 2. 2 *Illustration of the different stages of crystallinity during a carbonization process from molecular precursors to graphitic carbon.*[25]

During pyrolysis, the structure and composition of carbonized materials are strongly dependent on the reaction conditions, especially the temperature. Schuepfer et al. reported a generalized transformation scheme from organic precursors to graphitic carbon through different "carbon" stages, as shown in **Figure 2. 2**. Above 2500 °C, graphitic carbon is formed, which is composed of purely sp^2-hybridized carbon. Artificial synthetic graphite is produced by heating carbon-rich precursors such as petroleum coke and coal tar in the range of 2500-3000 °C. The transformation of non-graphitic carbon into graphitic carbon is referred to as graphitization.[26]

The degree of graphitization is controlled by the chemical structure of the starting materials and heating temperature. First, the carbonization precursors are distinguished as graphitizable or non-graphitizable carbons, which was first identified by Rosalind Franklin.[27] In brief, graphitizable carbons can be transformed into crystalline graphite by heating to 3000 °C, while non-graphitizable carbons cannot be transformed into graphite at any temperature but into non-crystalline, glass-like carbon with two-dimensional structural elements and a fullerene-related structure.[28,29] Second, the production of graphite from graphitizable carbons also depends on the carbonization temperature. At the relatively lower temperature range between 1400-2500 °C, so-called non-graphitic carbon is formed (**Figure 2. 2**).[30]

As mentioned above, diamond exhibits a purely sp^3-hybridized form of carbon. Synthetic diamonds were first produced in the 1950s. The extreme experiments condition (under a pressure of 5.7 GPa and a temperature of 1260 °C) and high-purity graphite powders as a precursor are used to produce diamonds.[31]

A mixture of sp^2 and sp^3-hybridized carbon without any appreciable long-range order is referred to as amorphous carbon.[32] Amorphous carbon is typically obtained at pyrolysis temperatures of below 1400 °C (**Figure 2. 2**) and contains a certain degree of disorder (non-crystallinity), in contrast to the crystalline structures of diamond and graphite. In some cases, graphitic layers are arranged almost parallel to one another but with a random orientation normal to the layers, are formed a structure which is called turbostratic graphite.[33]

2.3 The porosity properties of carbon

2.3.1 Overview of porous carbon

Carbonization process is a thermal decomposition of materials, creating gaseous leaving fragments. Every carbonization reaction is accompanied by a loss of material mass, resulting in porosity.

Porous materials are classified into three types according to the diameter of the pores, as defined by the International Union of Pure and Applied Chemistry-USA(IUPAC) [34]. As shown in **Figure 2. 3 a,** the pore dimeter of microporous materials is less than 2 nm. In Mesoporous materials, the pore dimeter is between 2 and 50 nm. Macroporous materials have fairly large pores with a diameter of more than 50 nm. Activated carbons are one representative example of porous carbon materials.[29] Due to their high degree of microporosity, specific surface areas of activated carbons may exceed 3,000 $m^2 \cdot g^{-1}$.[35] Importantly, porous carbons such as carbon aerogels and carbon foams have a typical hierarchical (fractal) porosity, spanning pore scales from macroscopic to mesoscopic to microporous (**Figure 2. 3 b)**. This structure enables the entire surface area of the porous material to be exposed to a potential liquid or gas environment.

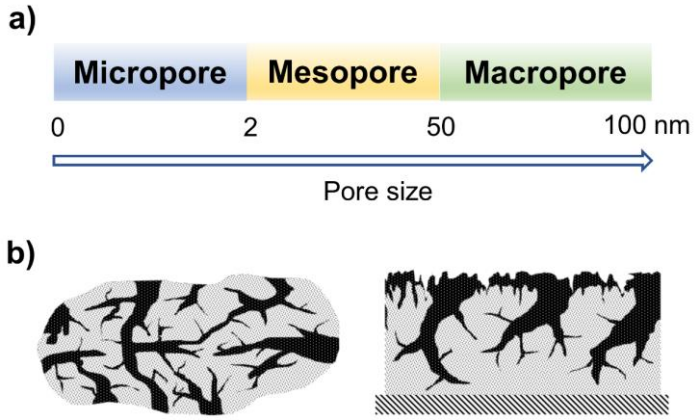

Figure 2. 3. *a) Classification of porosity based on pore diameter: microporous, mesoporous, and microporous materials; b) Illustration of the hierarchical porous structure of bulk porous carbons and substrate-supported porous carbons film.*[36,37]

As porosity brings a high surface area to the carbon materials, porous carbons are used in a wide range of applications, such as separation,[38] adsorption,[39] energy storage,[40] catalysis, and catalyst support, etc.[41] Different porosity properties are required for the different applications. Therefore, a comprehensive characterization of the pore characteristics of these porous materials, such as pore size, surface area, porosity, and pore size distribution, is required in order to select suitable applications or optimize the performance of hierarchically structure materials.[42] Furthermore, it is of great importance to study different synthetic methods of porous carbons with tuned porosity properties and understand the property-structure relationships.

2.3.2 Activation

There are a number of strategies to introduce and modify porosity. One of the common methods is activation, which is divided into physical and chemical activation.

The process of physical activation consists of two steps. First, carbonization at a medium-high temperature (300-800 °C), the precursor is pyrolyzed in an inert atmosphere with gases such as argon or nitrogen. During this first step, the volatile fraction of the precursor materials is released, and a carbonaceous residue, the char, is formed. Char has a rudimentary porous structure. In the second step, char is heated at a higher temperature (700-1000 °C) in the presence of an activating agent.[43]

CO_2 and steam are the most widespread activating agents.[43,44] The CO_2 activation is based on the well-known Boudouard equilibrium (**Equation 2.1**). During this reaction, carbon dioxide reacts with carbon to carbon monoxide at higher temperatures, which leads to carbon etching.

This process favors microporosity formation. In steam activation, water can etch carbon atoms by forming CO and hydrogen (**Equation 2.2**). The generated CO participates in the water gas shift reaction to generate CO_2 (**Equation 2.3**). Compared with carbon dioxide activation, steam-prepared activated carbons show larger mesopore and macropore volumes and a lower micropore volume.[45]

$$x\ CO_2\ (g) + C_y\ (s) \rightleftharpoons 2x\ CO\ (g) + C_{x-y}\ (s) \quad (2.1)$$

$$x\ H_2O\ (g) + C_y\ (s) \rightleftharpoons x\ CO\ (g) + x\ H_2\ (g) + C_{y-x}\ (s) \quad (2.2)$$

$$CO\ (g) + H_2O\ (g) \rightleftharpoons CO_2\ (g) + H_2\ (g) \quad (2.3)$$

In terms of chemical activation, the carbon precursor is impregnated with a chemical etching agent, such as H_3PO_4, KOH, and $ZnCl_2$, then heated to a temperature of 450-700 °C. Carbon atoms are partially removed through chemical reactions with the activation agent, creating porosity. The generated porous carbon materials are washed to remove the activation agent, which can often be recycled. Chemical activation can endow the final synthesized porous carbon material with a higher specific surface area and as a well-tailored microporosity, but lower carbon yield.[46]

2.3.3 Templating

Besides physical and chemical activation, another commonly used strategy is templating to introduce porosity in carbon materials, where a controllable pore structure and relatively narrow pore size distribution can be achieved by using various structure-directing agents (SDA).[47] Generally, three types of templates, classified as hard-templating, soft-templating and salt-templating, are applied.

The hard-templating process consists of three steps (**Figure 2. 4**): First, as-synthesized templates are infiltrated with carbon precursors by wet impregnation, melt-infiltration, chemical vapor deposition, or combinations thereof. Secondly, the mixture is pyrolyzed at high temperatures under a defined atmosphere to produce a template-carbon composite. Third, hard templates are removed by acid and alkali rinsing so that a pore appears in the place of hard templates.[48] Therefore, the selected template determines the size, structure and connectivity of the pores in the carbon materials. The commonly used hard templating agents include zeolites, mesoporous silicas, colloid crystals, aluminum oxide membranes, and nanostructured

inorganic materials (e.g., MgO, $CaCO_3$, ZnO, Fe_2O, KCl) for the synthesis of porous carbon materials.[48,49]

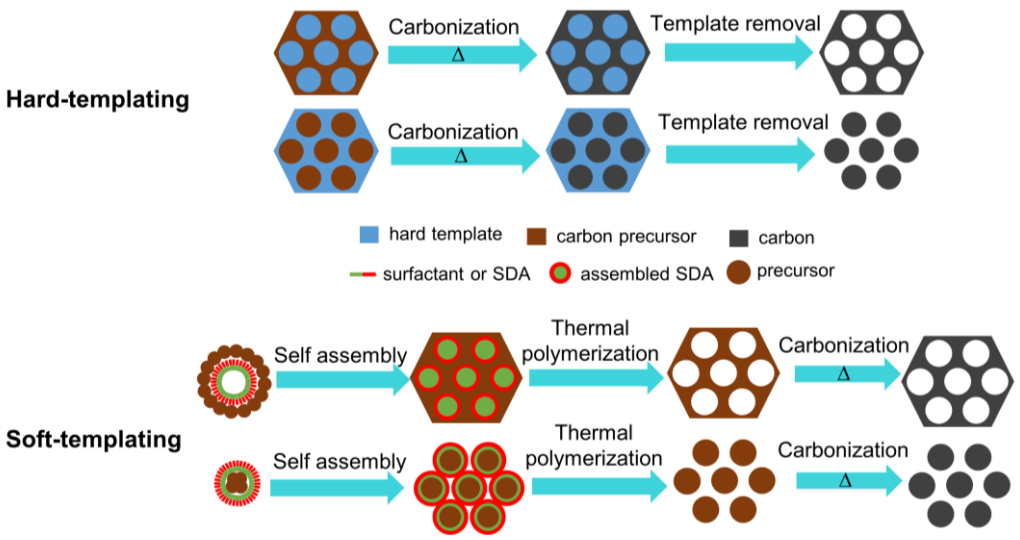

***Figure 2. 4**. Schematic illustration of the hard- and soft-templating approach.*[50]

Among these various hard templates, ZnO hard templates are regarded as a special option due to their unique physicochemical properties. During the pyrolysis process, the carbon precursor easily reacts with ZnO to generate carbon monoxide by a carbothermal reduction reaction (**Equation 2.4)**, in which the ZnO is reduced to Zn. This is a chemical activation. Importantly, when the reaction temperature is increased to 900 °C, the produced Zn evaporates, thus avoiding the process of removing the template by acid or alkali washing. ZnO thereby has the dual function of hard templating and chemical activation, resulting in a carbon material with a well-defined pore structure and narrow pore size distribution.

$$ZnO\,(s) + C\,(s) \rightarrow Zn\,(g) + CO\,(g) \qquad (2.4)$$

The soft-templating approach also includes three steps but involves a collaborative assembly process in the liquid phase (**Figure 2. 4**): First, self-assembly of carbon precursors with the structure-directing agent (SDA) (such as surfactants, copolymer) occurs, driven by van-der-Waals and Coulomb interaction forces.[51] Second, carbon precursors undergo a cross-linking process to receive thermal stability. Finally, the soft templates are removed during carbonization.[52] For instance, Dai and co-workers first reported the preparation of highly ordered and well-oriented mesoporous carbon by using resorcinol-formaldehyde resin as carbon precursor and self-assembled block copolymer poly(styrene)-block-poly(4-vinylpyridine) as templating agents.[53] Oriented cylindrical pores perpendicular to the substrate

with a size of about 35 nm were obtained after carbonization. Moreover, the use of triblock copolymer as SDA (e.g., Pluronic F127,[54,55] PEO-PPO-PEO[56]) enables ordered pore structures.

Salt-templating is another inexpensive and effective method for the modulation of the pore structure base on the reaction of carbon precursors in molten salt media. When heating the mixture to the melting point of the salt, the salt is mixed with the carbon precursor, or the carbon precursor is dissolved into the molten salt phase. After carbonization, the porosity of carbon materials is achieved by removing the salt phase with H_2O. Alkali metal halides are commonly used due to a relatively lower melting point range between 470 and 800 °C. The melting point can be further lowered by using eutectic mixtures. Some typical eutectic mixture samples are $LiCl/ZnCl_2$ (294 °C), $NaCl/ZnCl_2$ (270 °C), and $KCl/ZnCl_2$ (230 °C), as reported by Fechler et al..[57] In this study, using these three different mixtures resulted in the generation of porous carbon materials with different pore structures.[57] Therefore, the melting points of metal halide or eutectic mixture, the size of salt ions, and the miscibility between salt and precursor are the critical parameters for the synthesized pore properties of the final carbons.

2.4 Surface engineering of carbon materials

2.4.1 Heteroatom-doping carbons

In addition to the architecture of the pore structure of carbon materials, another important characteristic is their chemical surface properties. For interface applications such as gas capture or gas sensors, the surface functionality of the carbons plays an important role in the performance. The common strategies to modulate surface functionality include heteroatom-doping and metal deposition.

In general, heteroatom doping involves the replacement of some carbon atoms in the carbon skeleton with other heteroatoms (e.g., boron, nitrogen, phosphorus, sulfur, oxygen), where the heteroatoms and carbon atoms are covalently bonded. When heteroatoms of different sizes and electronegativity than carbon are introduced into the carbon host, bond polarization occurs between the heteroatoms and carbon atoms, resulting in charge redistribution, and the electronic and chemical properties of the carbon material change.[58–63] For instance, doping electron donors (n-type doping) and electron acceptors (p-type doping) intentionally adjust the Fermi level position of graphene films and improve the carrier concentration towards desired applications.[64,65] Another effect is that the doping of oxygen atoms changes the surface polarity of carbon materials. Changes in surface polarity can also affect the adsorption behavior of analytes or reactants on the surface of adsorbents (carbon materials). F. Rodriguez-Reinoso et

al. studied that different numbers of oxygen surface groups on microporous activated carbons exhibit specific adsorption trends for different polar molecules (N_2, SO_2, H_2O, and CH_3OH).[66]

2.4.2 Nitrogen-containing carbons

N-containing carbons are most studied as heteroatoms-doped carbons, and N-doping gives the materials n-type electronic behavior and redistributes charge in the carbon framework.[67] Moreover, nitrogen can introduce Brønsted basicity to the carbon surface, which in extreme leads to Frustrated Lewis pairs (FLPs) between nitrogens and electron-poor carbon atoms.[67,68] Nitrogen in carbon can be in the form of internal doping (pyrrolic N, pyridinic N, graphitic N, N-oxides), [59] surface functional groups (amine, amide, nitro, cyano and nitrogen oxide),[69] but also can occur regularly in stable compounds like carbon nitrides(e.g. g-C_3N_4, C_2N_3, or C_3N_5)[70–72] as illustrated in **Figure 2. 5**.

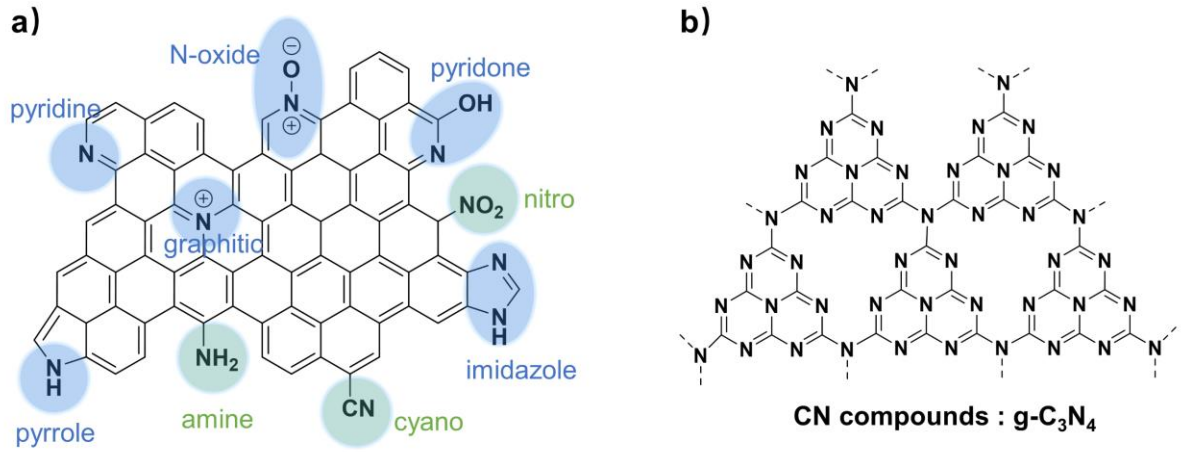

***Figure 2. 5**. a) Schematic representation of nitrogen functionalities in carbons and b) one representation of CN compounds: g-C_3N_4*

One common route to synthesize nitrogen-containing materials is condensing nitrogen-rich molecular precursors such as urea, melamine, or nucleobases at temperatures lower than 1000 °C.[59,73] Another common route is co-pyrolyzing pre-synthetic carbon materials with reactive small nitrogen-containing molecules (NH_3, CH_3CN, CH_2N_2).

In general, the nitrogen content of the final nitrogen-doped carbon material depends on the nitrogen-containing precursor and carbonization temperature. A decrease in the nitrogen content and an increase in the carbon content are observed with increasing temperatures.[74] As Gehring et al. reported,[75] poly-acrylonitrile as precursor condenses between 300 and 650 °C and loses nitrogen, then the nitrogen remains stable at 21 wt% upon heating above 650 to 1000 °C. After that, the nitrogen content drops to 11 wt%. At temperatures above 1400 °C, only 2.5 wt% nitrogen remains in carbon material, complemented by a carbon content close to

97.5%. Another interesting trend is the evolution of nitrogen functional groups: nitrogen present in six-membered rings such as pyridinic N or graphitic N exhibits high thermal stability.[74] At high temperatures, pyrrolic N and pyridinic N, convert to graphitic N.[75]

Nitrogen-doped carbon materials have a very wide range of applications based on their unique properties. For example, the doping of nitrogen can modulate the electrochemical potential, making carbon more chemically stable against oxidation (so-called noble carbon) (**Figure 2. 6 a**). This "noble carbon" has an excellent performance in many applications such as chemical catalysts, ORR electrocatalysts, supercapacitors, electrodes for metal-air batteries, etc.[76] Nitrogen-containing materials are also often used for CO_2 capture, where the basicity and polarizability of the adsorbent can be further enhanced by various nitrogen functionalization on the carbon pore surface, thus enhancing the adsorption capacity of CO_2.[68,77] Moreover, carbon materials with high nitrogen content (N-doped carbon or porous carbon nitride) have a higher heat of adsorption for CO_2 (**Figure 2. 6 b**), which is beneficial for CO_2 capture at lower concentrations.[78–80]

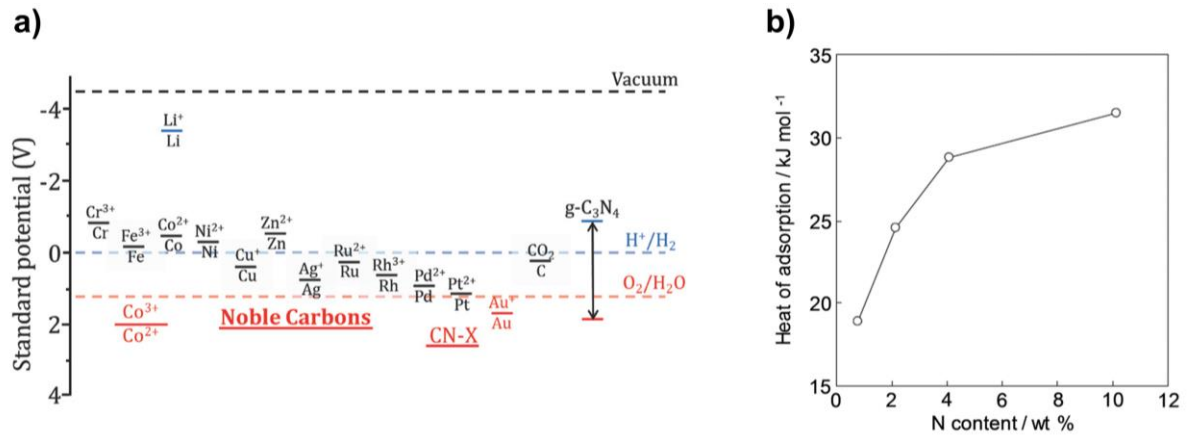

Figure 2. 6. *a) Electrochemical potentials or HOMO/LUMO levels (for semiconductors) for some known metals and (nitrogen-containing) carbon materials;* [76] *b) change in the isosteric enthalpy of CO_2 adsorption with nitrogen content for nitrogen-doped polypyrrole-based porous carbons at a surface coverage of ~ 0.6 mmol g^{-1}.*

2.4.3 Functionalization of (N-doped) carbons by metal nanoparticles

Porous carbon or N-doped carbon can be functionalized by introducing ions, metal atoms, or metal-based nanoparticles on the surface. The introduced metal nanoparticles combined with (nitrogen-doped) carbon materials as support undergo orbital overlap or electronic connection to a "diode" structure in extended semiconductor-metal connections known as the Mott-Schottky effect. In general, the Mott-Schottky effect describes the transfer of electrons until the Fermi levels are the same on both sides of the interface between metal and carbon material,

which effectively creates a charged interface with electrons or negative space charge on the nobler side, while the less noble side is positively charged and depleted of electrons due to oxidation.[67]

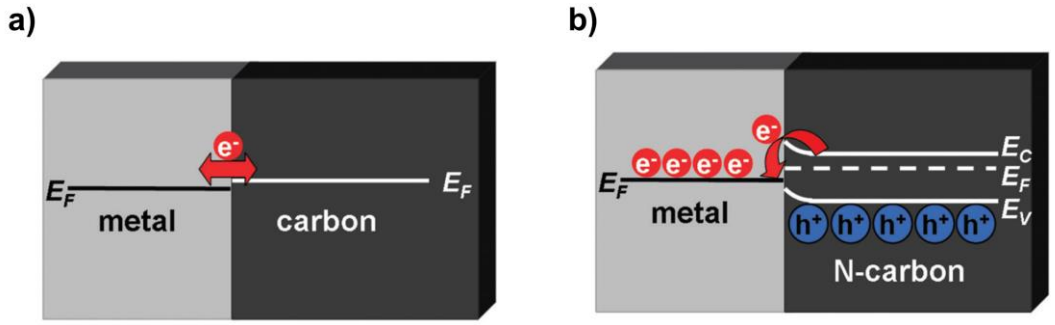

***Figure 2.** 7. a) Schematic view of the typical metal-carbon contact and b) metal-N-carbon contact.*[67]

As shown in **Figure 2. 7 a**, graphitic carbon is regarded as a neutral support because the work functions of metal and graphitic carbon are comparable. When the metal and carbon are in contact, electrons can flow quite freely between the metal and carbon. [81,82] On the other hand, when nitrogen (as an electron donor) is inserted into carbon frameworks, the position of the valence or conduction band changes, resulting in a change in the work function and sometimes a slight opening of the bandgap.[67] Once the bandgap of N-carbon is opened, electron transfer may lead to the formation of a space charge layer between the metal and N-carbon (**Figure 2. 7 b)**, thereby enhancing the catalytic activity or adsorption activity of nitrogen-doped carbon.[83,84]

2.5 Laser carbonization

2.5.1 Overview

The previous sections describe the fundamentals and complexities of carbonization and introduce some of the essential tuning strategies for selectively modifying the properties of carbonized materials. However, these conventional synthetic methods and modification strategies are usually accompanied by certain disadvantages, such as low productivity, harsh preparation conditions, high energy consumption, and large chemical waste in the preparation of graphene or carbon nanotubes[85]. Therefore, low-cost and scalable alternative technology for producing high-performance carbon materials is urgently needed.

In particular, in thin-film or flexible electronics, their application is often hampered by processing limitations due to their pervasive insolubility and fragile surface chemistry. Direct laser patterning technology has recently become an enabler of flexible electronics in many

fields, from industry to medicine. Focused laser beams induce photothermal or photochemical reactions with high precision locally, which is difficult to achieve using conventional thermal treatment. As a fabrication technique, laser patterning does not require masks, photolithography, or toxic etch chemicals, thereby increasing the design flexibility, productivity, and eco-friendliness of the fabrication process.[85] This selective synthesis and patterning strategy minimizes using raw materials, solvents, and reagents, avoids tedious post-processing procedures and reduces environmental impact. Compared with conventional synthesis methods of carbon-based materials, laser patterning technology has the advantages of high spatial resolution, non-contact processing, simple scalability, high productivity, low energy consumption, environmental protection, cost-effectiveness, and 3D compatibility. As a result, as shown in ***Figure 2. 8***, the number of scientific articles related to laser-carbonization in various fields of science has grown tremendously in the past decade, which means that more and more scientists are focusing on this direct laser patterning technology.

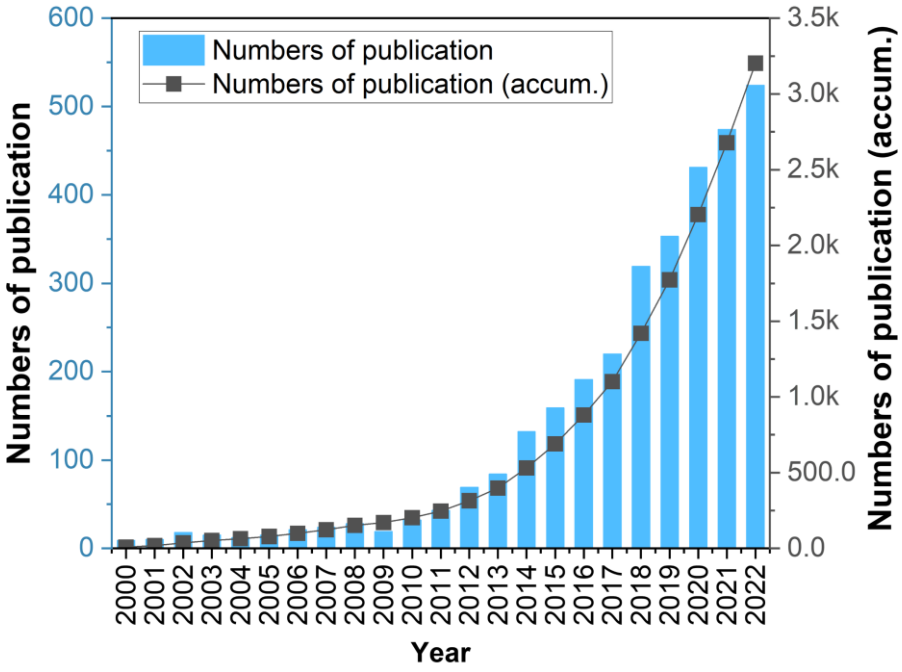

Figure 2. 8*. The number of articles related to laser carbon published in journals each year and the curves of the accumulative (accum.) number of articles (The data comes from Web of Science, the search keywords are: laser-carbonization and laser-induced graphene).*

The first reports on the laser-induced structural modification of organic materials (polyimide) appeared in the 1980s.[86,87] After nearly 30 years, in 2010, Youglai Zhang et al. developed a novel method to fabricate micrometer-sized graphene circuits on graphene oxide films through the femtosecond laser reduction process (***Figure 2. 9*** **a**).[88] Research in this laser-reduced

graphene oxide received a great deal of attention following this first report. Then graphene oxide can be reduced by CO_2 laser or LightScribe laser to generate 3D graphene, which is applied to the flexible supercapacitors.[89,90] A few years later, in 2014 (***Figure 2. 9*** **b**), Tour et al.[91] reported the conversion of a commercial polyimide (PI) film into 3D porous laser-induced graphene (LIG) under ambient conditions using a CO_2 laser. This so-called laser-induced graphene exhibits a good electrical conductivity of 25 S cm^{-1}, high porosity of 340 m^2 g^{-1}, as well as high thermal stability up to 900 °C.[91] Since then, research on laser carbonization has increased rapidly (***Figure 2. 8***). In 2016, Denis Go et al. presented the generation of carbon nanofiber nonwovens from polyacrylonitrile (PAN) by laser-carbonization (**Figure 2. 9 c**). [92]

These discoveries lead to numerous research activities in which highly graphitic carbon materials were successfully produced after laser-carbonization using other commercial polymers (such as polysulfone,[93] polyfluorene,[94] and poly-dimeethylsiloxane[95,96]) and natural polymerized materials (such as starch,[97] lignin,[98] paper,[99] wood,[100] Kevlar textile[101]).

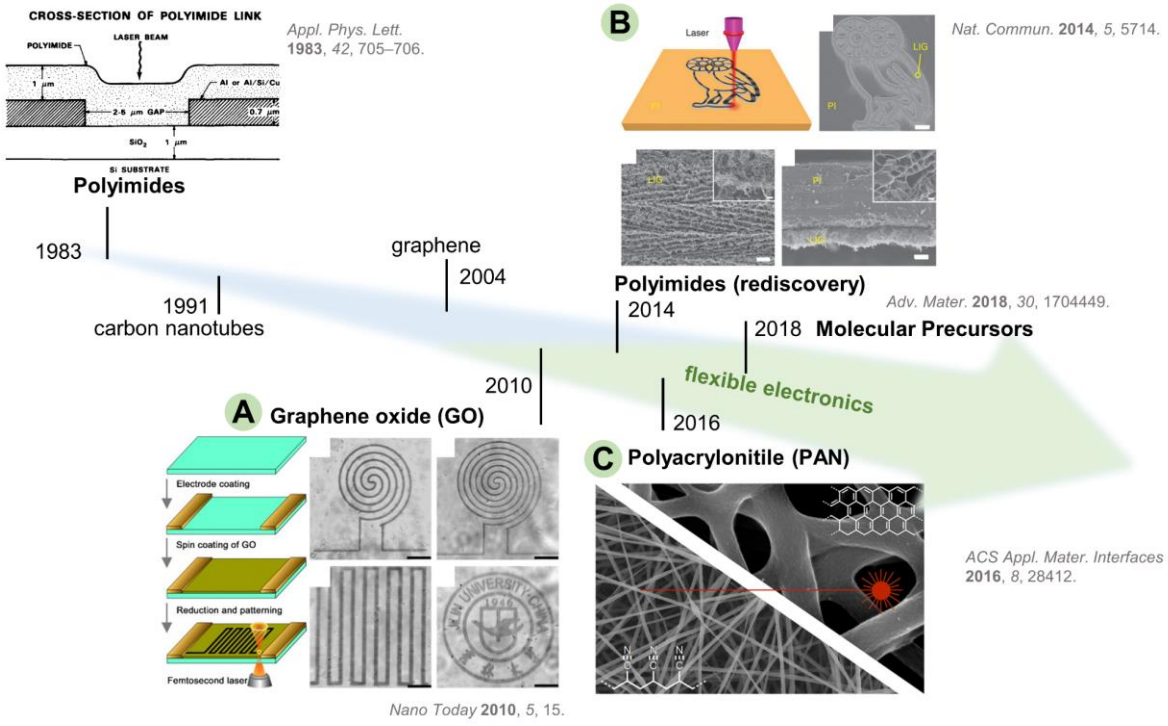

Figure 2. 9*. Timeline of some studies on the topic of laser-carbonization.[50] a) "Writing" conductive patterns of graphene into graphene oxide primary films with a 790 nm femtosecond laser in 2010;[102] b) "Writing" conductive patterns of LC-PI into commercial PI primary films with a 10.6 μm CO_2-laser in 2014; [91] c) Laser-induced carbonization of carbon nano-fabrics based on PAN.[103]*

In recent years, the research on laser-carbonization of carbon materials mainly focuses on the laser-induced carbonization process of polymers, while the direct carbonization of molecular starting materials is less covered. The reason is that the high-energy impact of the laser beam

causes the evaporation of volatile molecular species and prevents the effective formation of the carbon network. In 2018, Strauss et al. developed the thermal conversion of molecular precursors into so-called carbon nanodots (CND), which is considered to be a pre-carbonized or a pre-condensed intermediate, was reported.[104] After pre-carbonization (300 °C), organic materials are less volatile, and the procedurally complicated dehydration reactions are completed. Laser-treatment of such pre-carbonized products leads to conductive porous carbon films similar to laser-induced graphene. This discovery sparked our interest in studying the process and mechanism of laser-carbonization to improve material properties for thin-film electronic devices.

2.5.2 Process parameters

Regardless of the starting polymer or pre-carbonized materials used, the laser-induced localized reactions strongly depend on the laser processing parameters and material properties. These factors will ultimately affect the morphology, crystallinity, surface area, and conductivity of laser carbon materials**.** Especially the laser parameters like wavelength (λ), incident power (P), scanning speed (υ), fluence (E), pulse duration (τ), pulse frequency or repetition rate (f), spot size (d), and beam shape were in the center of several studies. Other reaction parameters like reaction atmosphere and pressure are also critical. Moreover, the properties of the precursor materials, like extinction coefficients, composition, heat conductivity and heat capacity, as well as the reactivity of the precursor films, are important to consider. In this chapter, only a few prominent influencing factors will be discussed.

First, a complete understanding of the basic principles of the laser induction process is essential for adjusting parameters during the experiment. A common description of laser beam-materials interaction is given in **Figure 2. 10**.[105] The keyhole is formed by a laser beam delivering enough energy to vaporize the material. Around the small hole, the material may melt to form a molten pool. At the same time, the impact of laser energy causes plastic deformation of the surrounding material. Inside the keyhole, the laser beam is reflected several times and finally absorbed. Above the keyhole, there is a plasma plume of ejected matter and gas.

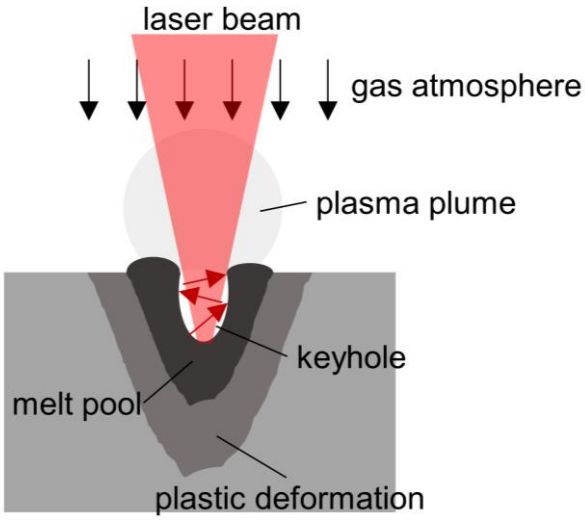

***Figure 2. 10**. Illustration of some common beam-material interactions.*[106]

In the previous description, the pyrolysis temperature will affect the morphology, degree of graphitization and crystallinity of carbon materials. In the laser-carbonization process, the output energy of the laser and the absorption of photons by the material, and the energy conversion efficiency play the critical role in the properties of final laser carbon materials.

For instance, the power density and the wavelength are the main criteria for laser processing. According to Planck's equation (**Equation 2.5**), the wavelength determines the energy of each photon.

$$E = h\nu \tag{2.5}$$

The power density depends on the beam diameter (spot size) in the focus of the laser according to **Equation 2.6**,

$$I = \frac{p}{\pi r^2} \tag{2.6}$$

where p is the effective power in W, and r is the focus radius of the laser lens. For example, a 1 W laser that is focused to a spot size of 0.2 mm results in a power density of 3200 $W \cdot cm^{-2}$. If a pulsed mode with a certain frequency is used for the experiment, the resulting photon density per area and each pulse is given by **Equation 2.7**,

$$f = \frac{p}{\omega e \pi r^2} \tag{2.7}$$

where p is effective power in *W*, ω is the laser frequency, *e* is the photon energy, and *r* is the focus diameter of the laser lens.

Another parameter is fluence, the energy delivered per unit area, which is a direct result of the laser power and the spot size (the focus). Fluence is generally divided into two types: linear fluence F_L in J·cm^{-1} and area fluence F_A in J·cm^{-2}. The values of fluence are given by **Equations 2.8 and 2.9**,

$$F_L = \frac{p}{v} \tag{2.8}$$

$$F_A = \frac{p}{vd} \tag{2.9}$$

where v is the scanning speed, and d is the focus diameter of the laser lens.

Fluence, incident power, and scanning speed

In most studies, the physical or chemical properties of materials are optimized by adjusting the laser power P, laser speed v, and fluence F_A. For instance, Faisal Mahmood et al. reported the formation of porous graphene from kraft lignin via laser patterning. [98] They studied the effect of laser power on the degree of graphitization of the material characterized by Raman spectroscopy. Obviously, high power, that is, high energy density (according to **Equation 2.8**), is more conducive to the formation of smaller structure-sized carbon materials with fewer defects and higher graphitization degree (**Figure 2. 11**). The study from Wan et al., where they used a 780 nm laser operating at 50 MHz (70 fs) with a power range between 3 and 13 mW, also show a clear dependence of the degree of carbonization on the laser power characterized by X-ray Photoelectron Spectroscopy.[107] Therefore, the influence of the threshold fluence (laser energy density) on laser-carbonization degree indicates a photo-thermal rather than a photo-chemical mechanism during laser-carbonization process. Furthermore, the laser scanning speed is a specific parameter related to the reaction kinetics during laser-carbonization.

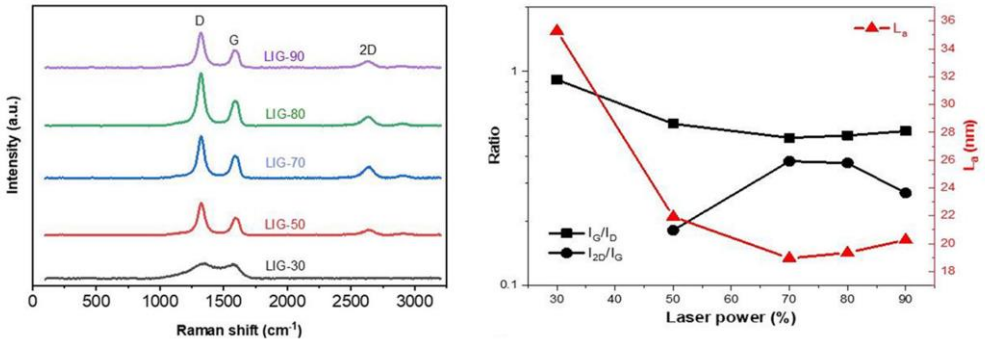

***Figure 2. 11**. left: Raman spectra and right: ratios of I_G/I_D and I_{2D}/I_G as well as average crystalline size (La) of laser carbon materials at different powers by using kraft lignin as precursor.*[98]

The electrical conductivity pair is an extremely important factor in evaluating the performance of flexible electronics. In the study from Jesper Edberg et at.,[108] it is important to note that the electrical conductivity depends not only deeply on the laser parameters used but also is related to the composition of starting materials. Moreover, the surface morphology and porosity of carbon materials show an excellent correlation with power and ink composition (**Figure 2. 12**). This will undoubtedly provide a valuable way to optimize material properties and application performance.[108]

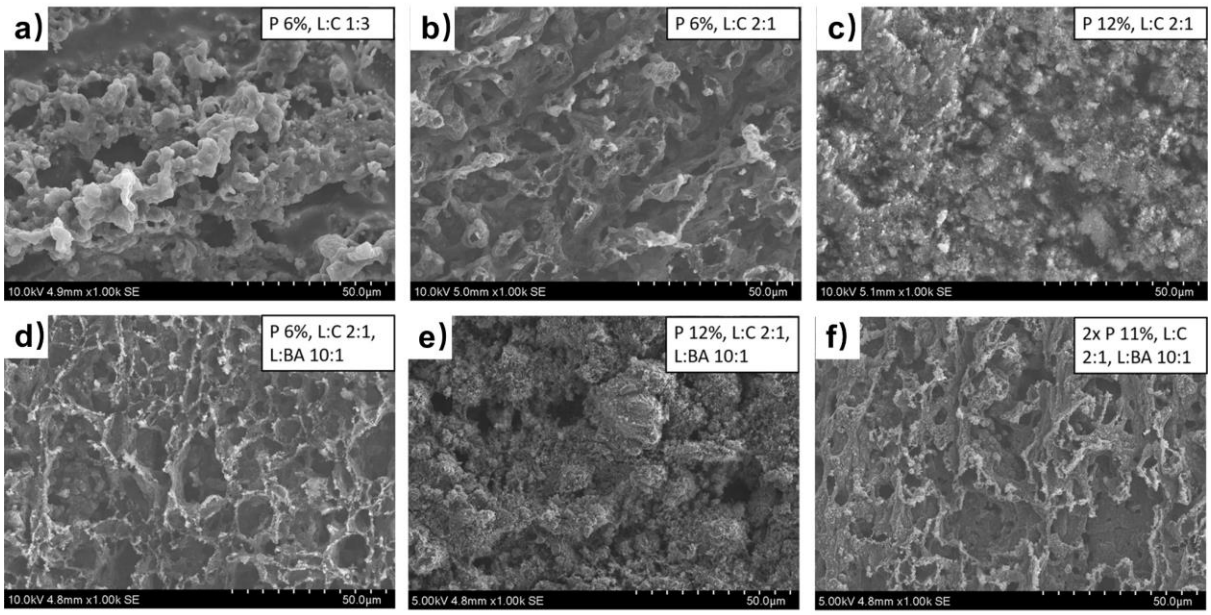

***Figure 2. 12**. SEM images of laser carbons produced from different ink compositions and laser parameters.*[108]

In addition, the laser scanning speed is a special parameter that affects the kinetics of laser-carbonization reaction, which is reflected in the elemental composition of the final product.[109,110]

Extinction coefficients

As mentioned above, even small changes in the composition of the ink under the same conditions of laser-carbonization can cause a particularly large difference in the property of the final product, especially on the surface properties. In addition to the parameters of the laser, another critical factor, namely the primary film's absorption of incident photons beam with a specific wavelength, also determines the final degree of laser-carbonization. An exemplary study in 2019 focused on the laser-carbonization of PI and proposed a photothermal carbonization mechanism based on plume formation.[111] The specific vibration absorption efficiency of the initial material in the mid-IR laser wavelength is closely related to the formation of the plume. According to this study, the extinction of the laser beam in PI films

follows the Beer-Lambert law. Therefore, the extinction coefficient should be an essential parameter for laser-carbonization efficiency in the following studies. The extinction coefficient is usually determined by Fourier-transform infrared spectroscopy (FT-IR) under a particular wavelength of CO_2 laser (10.6 μm),[111] which is the resonant energy range of C-H and C-H_2 vibrations. In addition, plasma absorption of particles or polymer precursors also exists in this wavelength range.

Reaction atmosphere

Regardless of traditional pyrolysis or laser-carbonization, the reaction gas atmosphere has a significant influence on the surface properties of the carbonized film. In 2017, Tour et al. demonstrated the surface modification of carbon materials, specifically turning of hydrophobicity and hydrophilicity, by controlling the gas atmosphere (air, O_2, Ar, H_2, 3%H_2/Ar during the laser-carbonization process.[112] **Figure 2. 13** shows a significant change in the water contact angle on the laser carbon surfaces from 0° (super hydrophilic) when using O_2 or air, to >150° (superhydrophobic) when using Ar or H_2.[112] This indicates that the surface polarity is much greater in an oxygen-containing atmosphere for materials made by the laser-carbonization process.[112,113]

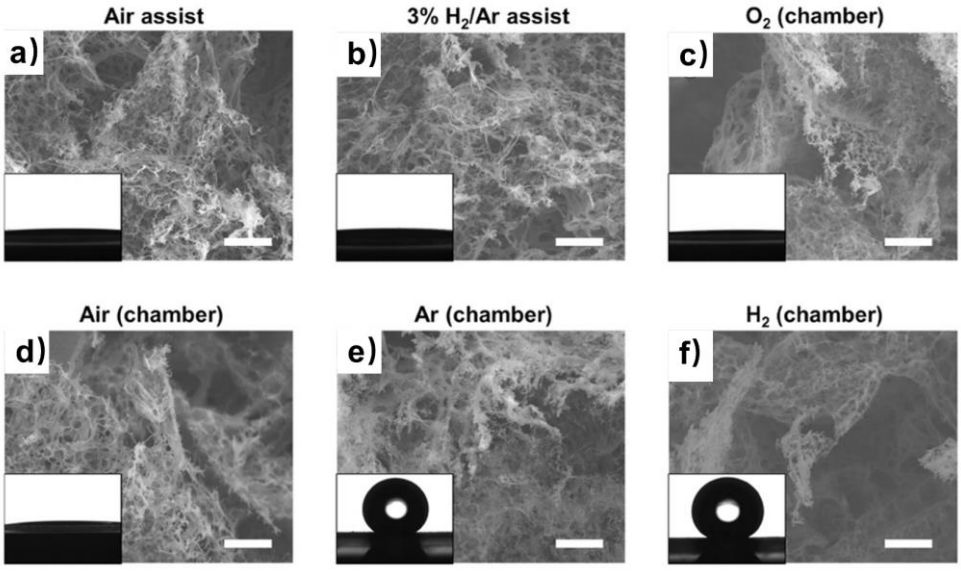

Figure 2. 13*. Top view SEM images of laser carbonized samples prepared under different gas atmospheres: Gas assist: air, 3% H_2/Ar. Controlled atmosphere chamber: O_2, air, Ar, H_2. Scale bars: 2 μm. Inset pictures are the water droplet appearance on the surface.*[112]

The wavelength of the laser used should also be considered. Currently, the most commonly used laser source for laser-carbonization of PI is the CO_2 laser (λ = 10.6 μm), although short UV lasers (248, 308, and 351 nm) were used in earlier studies of the mechanism of PI laser-

carbonization. Research on the effect of different laser types on carbonized materials is very rare. However, it is important to note that the more intuitive impression of the change in laser wavelength is that the energy of each individual laser photon changes according to Planck's equation (**Equation 2.5**). Moreover, the extinction coefficient of different precursors is the same at a certain wavelength, which also directly affects the degree of laser-carbonization of materials.

2.6 Application of laser-patterned carbon in sensors

The electrically conductive carbon materials obtained from laser-carbonization are generally useful for application in film-based flexible electronics such as sensors,[113–122] supercapacitors,[123–125] heaters,[126,127] catalysts.[128,129] All these applications rely on large interface materials and the interaction of gaseous or liquid media with the electronic surface or specific active sites on the surface of the materials. The laser-patterned carbon (LP-C) exhibits intrinsic porosity, excellent mechanical properties, and good electrical conductivity with a high graphitized carbon structure, which makes it suitable for applications as a sensor. LP-C is most commonly used in mechanical sensors and chemical sensors (**Figure 2. 14**).

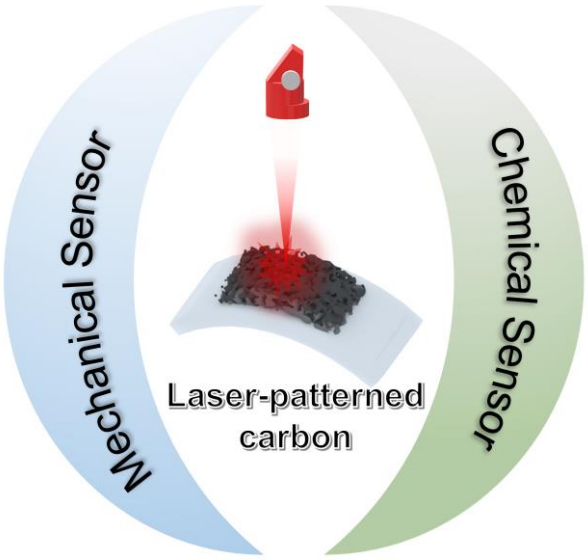

***Figure 2. 14**. Overview of sensor applications for laser-carbonized materials: chemical and mechanical sensors.*

2.6.1 LP-C-based mechanic sensors

Sensors operating in different environments require different mechanical properties. For mechanic sensors, mechanical flexibility and stretchability are properties that should be considered. LP-C based on a flexible substrate (such as PI) shows good mechanical flexibility.[114,130,131] For instance, Peng et al.[130] analyzed boron-doped LP-C fabricated on a PI

substrate. Thanks to the mechanical strength endowed by the flexible substrate PI to LP-C, the capacitance retention of boron-doped LP-C capacitors is still kept at nearly 100% at a bending radius of 17 mm.[130]

Mechanic sensors are widely used in subtle human motion detection, sign language translation, and soft robotic gripper.[132] Duan et al. reported a resistive e-skin model based on laser-carbonized materials used for the remote control of robots.[133] As shown in **Figure 2. 15 a**, first converting the current analog signal to an analog voltage signal, followed by analog-to-digital signal conversion. The resistive electronic skin can generate real-time voltage signals under six motion states (**Figure 2. 15 b)**. Based on this, after installing five strain sensors on the finger joints of the hand, the relative voltage change of the electronic skin for a specific gesture can be observed (**Figure 2. 15 c)**.[134]

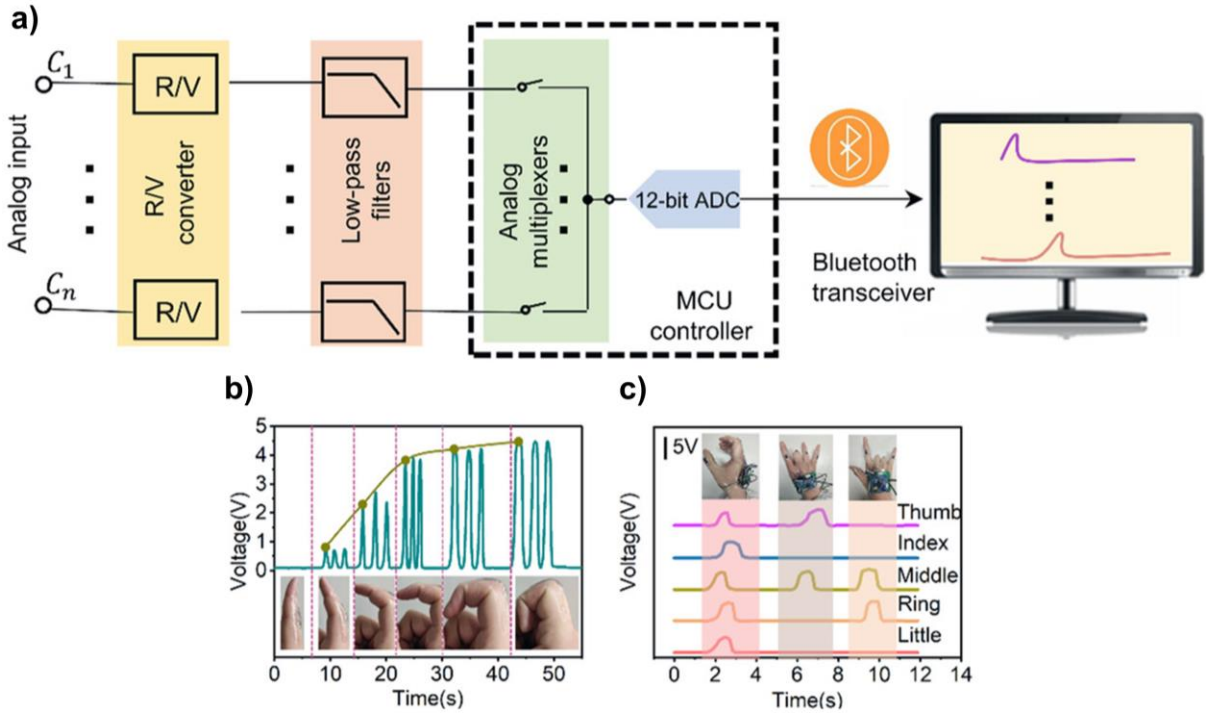

***Figure 2. 15**. a) The circuit diagram showing the signal flow in the real-time robot remote control system, from acquired analog signals of resistance to digital signals of voltage. b) The dependence of the acquired voltage signals on index finger movement. The insets show the photograph of the six bending states. c) Using the generated signals from the resistive sensors to express the letter c, number 8, and phase "I love you".*[134]

Furthermore, in 2018, Wang et al. proposed that laser carbon materials can be used as strain sensors to capture human finger and soft robot motion by improving the homogeneity and integrity of laser carbonized materials.[134] Chhetry et al. fabricated a MoS_2/LP-C strain sensor for the detection of voice, eye-blinking, and pulse wave.[135]

2.6.2 LP-C-based chemical sensors

Chemical sensors are devices for the specific detection of chemical species and can be used in the examination of pollutants in drinking water, food safety, toxic gas and greenhouse gases emissions around industries, and indoor air quality. In addition, a chemical sensor can also be used in the quantitative detection of biomarkers in body fluid analysis to provide preliminary evidence for medical diagnosis.[136]

The basic working principle of a chemical sensor is that the device converts chemical information into an electrically detectable output. In other words, a chemical sensor converts the concentration of a specific sample component or the overall component analysis into an analytically valuable signal. As shown in **Figure 2. 16**, a chemical sensor generally consists of two parts: the active sensing materials as the sensing layer and the transducer layer. The sensing layer is responsible for interacting with the target analyte, and the result of this binding interaction is a change in material properties, such as mass and conductivity. Sensors then convert this change into readable electrical signals.[137]

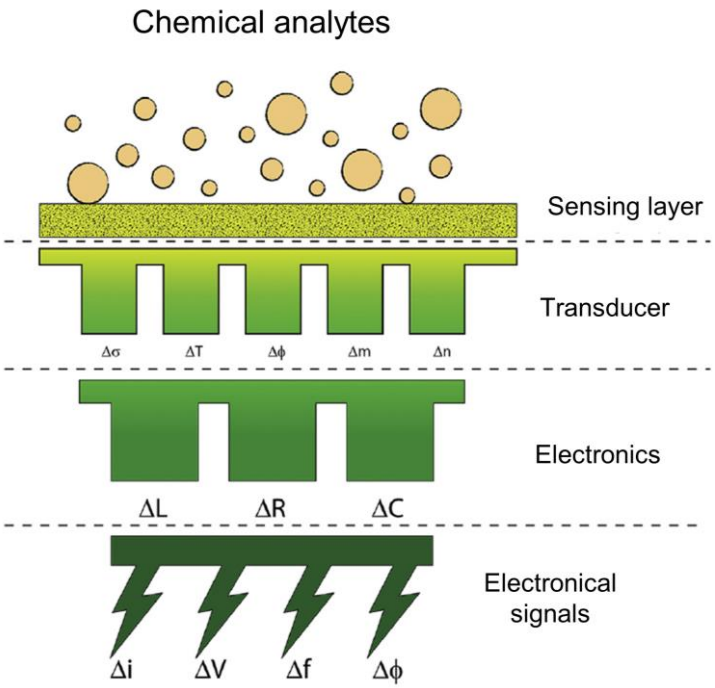

Figure 2. 16*. Schematic structure of a chemical sensor. Upon interaction with analytes (chemical stimulus), the sensing layer undergoes the change of some physical properties (Δs: conductivity, ΔT: temperature, ΔF: work function, Δm: mass, Δn: refractive index), which are converted by the transducer into the variation of the corresponding electric parameter, then originating the final sensor signal.*[138]

Common commercial materials for detecting chemicals are mainly based on metal semiconductors, especially metal oxides. Operating temperatures of 200-400 °C make these

materials highly sensitive indeed, but the stability of the materials and the expensive manufacturing equipment do not allow them to operate under ordinary conditions. Alternative materials such as graphene, carbon nanotubes, and nanoparticle-functionalized composites are promising for room-temperature detection of volatile analytes. However, these materials are often accompanied by high production costs. For practical applications and everyday use, ideal sensor materials are small, flexible, non-toxic, inexpensive, simple to produce, biodegradable, and operable at room temperature.[139]

Laser-patterning of materials may provide a solution for the ideal sensing materials for advanced sensor on-chip applications. For instance, Stanford et al. fabricated a flexible gas sensor base on LP-C from PI, which shows the high surface area and thermal conductivity.[114] When different types of gases were put in, different degrees of resistivity response occurred due to the difference in thermal conductivity (**Figure 2. 17**).

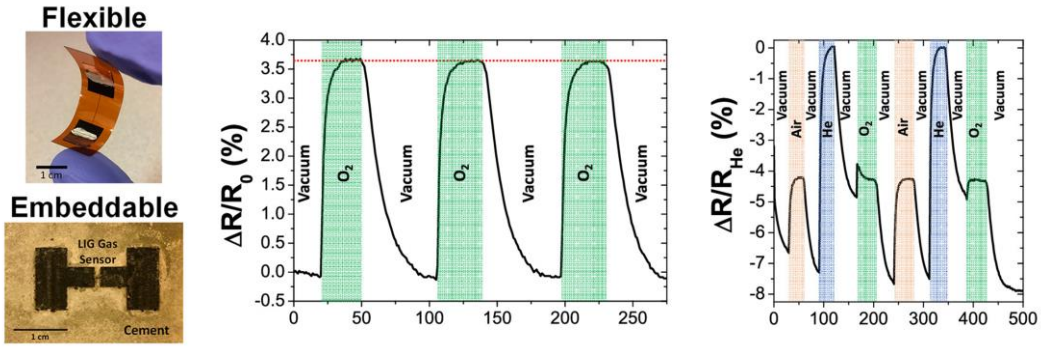

Figure 2. 17. *Laser-patterned carbon from PI as a gas sensor: shaded regions indicate when the sensor was exposed to the various gases.*[114]

Furthermore, Wu et al. designed a simple resistive device architecture based on LP-C from PI to detect gaseous ammonia quantitatively. In this study, the sensitivity is 0.087% ppm^{-1} for sensing 75 ppm ammonia at room temperature achieved, and the response and recovery times of the sensor are 214 and 222 s, respectively.[140] On the other hand, the sensor still exhibited better performance at high temperatures.

Yu el at. proposed a flexible sensor array electronic tongue system that is fabricated on PI substrate by the laser patterning process. The sensor platforms were post-functionalized with either rGO, PANI or Au nanoparticle and used to detect components of different analytes (i.e. salt (NaCl), sugar (sucrose) or vinegar by acquiring a signal of impedance change).[141]

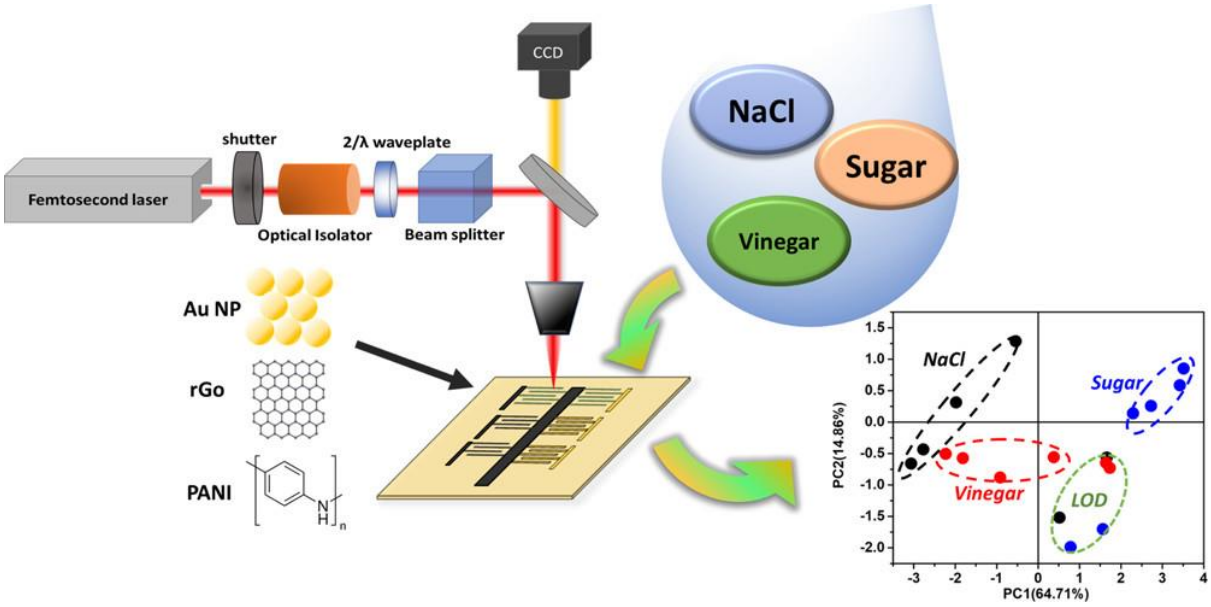

***Figure 2. 18**. Laser carbonized materials from PI with different surface tuning by rGO, PANI and Au nanoparticle as flexible sensor array for multi flavors detection.*[142]

2.6.3. Challenges

In general, before a certain sensor can be successfully commercialized, one of the biggest challenges is to design a specific active site in the sensor material and exhibit a near-absolute selective sensing behavior and fast sensing for a specific analyte. In the few examples mentioned above, it can be seen that they are still far away from real industrial applications, and there are still some challenges—for example, lower selectivity sensing and lower sensing performance in the general environment.

A possible solution is that the tuning of the surface chemical properties or physical property of laser-patterned carbon results in the modification of adsorption characteristics based on the working mechanism (**Figure 2. 18**). Therefore, it is of great importance to identify new precursor materials for the selective integration of functional groups. Furthermore, it is necessary to establish a fundamental understanding of sensor detection principles (i.e., analyte-material interaction and electron transduction) and apply it to the optimization of sensor materials. A well-established sensor is a product of combining mechanistic studies with the systematic tuning of the chemical composition and surface chemistry of laser-carbonized materials.

2.7 Scope of this work

Based on the above-described motivation, the background of the research literature, and the challenges faced in carbon material synthesis and application, the aim of this work is to identify general synthetic strategies to modify laser-patterned carbon for application in flexible chemical gas sensors.

As mentioned in the background section, conventional carbonization methods are beneficial for the mass production of carbon materials. However, there are still disadvantages of complex preparation processes and high energy consumption for film-based flexible electronic applications. As a part of the field of on-chip electronics, it provides a way to design eco-friendly and potentially biodegradable electronic materials. We know that molecular precursors are difficult to carbonize directly with laser beams. The porous carbon materials produced by laser-carbonization of polymer precursor materials (mainly PI and GO) show competitive physical and chemical properties and provide a fundamental concept base for our research.

Therefore, based on the laser-carbonization mechanism of the abovementioned polymers, we developed an integrated two-step approach starting from molecular precursor to prepare laser-patterned (nitrogen-doped) carbon, which will be presented in **Chapter 3**. In brief, Molecular starting materials are processed through a pre-carbonization step at low temperature (300-400 °C) to form carbon network formers (CNFAs), which are then laser patterned on flexible substrate. A set of three precursor systems (namely, glucose, citric acid and urea, cytosine) was identified, and an in-depth morphological and compositional study of the laser carbonized material was carried out. Furthermore, the resulting laser-patterned carbon (LP-C) or N-doped carbon (LP-NC) was morphologically compared to its conventional pyrolytic reference product. Distinctive features of a general porous structure and a carbonization gradient induced by the top-to-bottom energy input are observed. The microstructure, elemental composition, and resulting electronic properties are also different, as analyzed by X-ray photoelectron spectroscopy (XPS) and wide-angle X-ray scattering (WAXS).

Nitrogen-doped carbon materials are a class of sustainable materials for selective CO_2 adsorption. In **Chapter 3**, the presented concepts are successfully implemented. Based on this, **Chapter 4** demonstrates the fabrication of a flexible LP-NC sensor architecture for room-temperature sensing of CO_2 via single-laser conversion of an adenine-based primary ink. By the unidirectional energy impact in conjunction with depth-dependent attenuation of the laser beam, a novel layered sensor heterostructure with a porous transducer and an active sensor

layer is formed. Comprehensive microscopic and spectroscopic cross-sectional analyses confirm the preservation of the high content of imidazole nitrogen in the sensor. The performance was optimized in terms of material morphology, chemical composition, and surface chemistry to achieve a linear relative resistive response of up to $\Delta R/R_0$ = -14.3% (10% of CO_2). The sensor is operable even in humid environments and shows good performance upon strong mechanical deformation.

As mentioned above, based on the Mott-Schottky effect, the functionalization of metal nanoparticles on nitrogen-doped carbon can tune the electronic properties of the material to enhance the adsorption capacity for small molecules. Compared with the use of polymers as precursors, the concept based on molecular precursors can more easily insert metal nanoparticles into carbon frameworks. Therefore, **Chapter 5** demonstrates the selective modification of the structural and electronic properties of LP-NC to enhance their sensitivity in the resistive gas sensor. In this work, sodium iodide as porogen was used to increase the specific surface area of LP-NC. Furthermore, the impregnation of LP-NC with MoC_{1-x} (< 10 nm) nanoparticles was achieved by the addition of ammonium heptamolybdate into the precursor film. The resulting doping-sensitive nano-grain boundaries between p-type carbon and metallic MoC_{1-x} lead to an improvement of the VOC sensing response of $\Delta R/R_0$ = -3.7% or -0.8% for 1250 ppm acetone or 900 ppm toluene at room temperature, respectively, which is competitive with other carbon-based sensor materials.

In **Chapter 5**, it will be shown that the modified LP-NC exhibits an excellent sensing performance. However, in the face of the challenges of practical commercial applications, the selectivity towards VOCs with different polarities needs to improve. **In Chapter 6,** the electrical conductivity and surfaces property of LP-NC were modified by adding different concentrations of $Zn(NO_3)_2$ into the primary ink. Upon adding a certain amount of $Zn(NO_3)_2$, a noticeable 43-fold increase in the sensor response ($\Delta R/R_0$ = −21.5% toward 2.5% acetone) was achieved. This effect is explained by a significant increase in the measurable surface area up to ∼700 $m^2 \cdot g^{-1}$ due to the carbothermic reduction supported by nitrate oxidation and the subsequent in-situ formation of ZnO nanoparticles. Varying Zn concentrations or the addition of as-prepared ZnO nanorods lead to different surface properties as the surface area, porosity, and polarity of LP-C. A predominant effect of the surface polarity on the selectivity toward different analytes of the sensors during physisorption, e.g., acetone vs. toluene, were identified and tested.

3. Laser-patterned (N-doped) carbon (LP-NC)

3.1 Introduction

As discussed in **Chapter 2.5**, laser-carbonization provides an opportunity to open the field of film-based electronics for carbonized materials. In general, laser-induced or assisted synthesis, not only limited to carbon, has attracted a great deal of attention among materials scientists.[143] A major advantage of laser synthesis is the possibility to fine-pattern films according to the requirements of the application and tunability with regard to laser wavelengths and energy input. The precursors are directly carbonized on the substrate, and their properties are adjusted by careful selection of the laser parameters.[103]

As the introduction above demonstrates, the polymer polyimide is by far the most commonly used precursor.[85] However, the oversimplified precursor selectivity limits the practical application of the final product. The molecular precursor is undoubtedly an excellent solution. In fact, the molecular precursor is easy to vaporize under the high-energy laser beam, so the effective and precise utilization of the molecular precursor for laser carbonization is very challenging.

This chapter presents a method involving the essential step of pre-carbonization of molecular precursor to obtain laser-carbonized materials. After annealing the molecular precursors at 300 °C, the carbon content increases, and small graphitic domains form. These pre-carbonized intermediates are then processed into inks, which are applied on different substrates and finally carbonized in the laser beam.

By comparing the characteristics of laser-carbonized products with traditional carbonized samples, some prerequisites for selecting laser-carbonized molecular precursors were obtained. This work demonstrates three precursor systems: citric acid/urea, cytosine, and glucose. The details of the work will be shown below.

Term of use: This chapter is adapted with permission from my own original work:

H. Wang, S. Delacroix, O. Osswald, M. Anderson, T. Heil, E. Lepre, N. Lopez-Salas, R. B. Kaner, B. Smarsly, V. Strauss, Laser-carbonization: Peering into the formation of micro-thermally produced (N-doped)carbons. *Carbon* **176**, 500–510 (2021)

3.2 Preparation of LP-NC

Laser-carbonized materials from the molecular precursor are obtained in two processes (***Figure 3. 1***): pre-carbonization and laser-carbonization. First, the molecular precursor (citric acid/urea, glucose, and cytosine) was pre-carbonized at 300 °C in a muffle furnace under N_2 gas to obtain the carbon network-forming agents (CNFAs). The reason for the pre-carbonization is to avoid the evaporation of molecule precursors, and the pre-carbonized products are referred to as CA/U (300), glucose (300), and Cytosine (300). Second, the CNFAs are processed into inks by using ethylene glycol as a dispersant. The inks are then cast on the flexible PET substrate and dry to obtain uniform films with a thickness of around 35 µm. The films are then irradiated with a CO_2 laser (with a wavelength of 10.6 µm) with the desired pattern at ambient conditions, and finally, the unexposed material is rinsed off with water. The materials obtained are referred to as glucose (300)-ls, CA/U (300)-ls, or cytosine (300)-ls, indicating the laser treatment of the CNFAs.

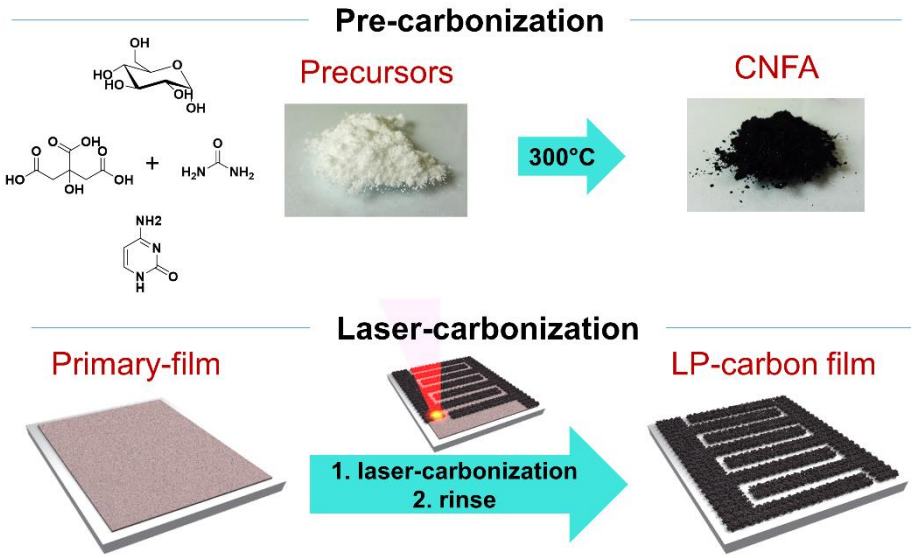

Figure 3. 1. *Scheme of carbon laser-patterning process: 1. Pre-carbonization of the molecular precursor at 300 °C; 2. Laser-carbonization of primary films to LP-carbon films.*

3.3 Characterization results of LP-NC

The primary films before laser-carbonization show a granular appearance with a grain size of around 100 µm. After laser-carbonization, all films on the PET show a highly disordered and porous morphology (**Figure 3. 2**).

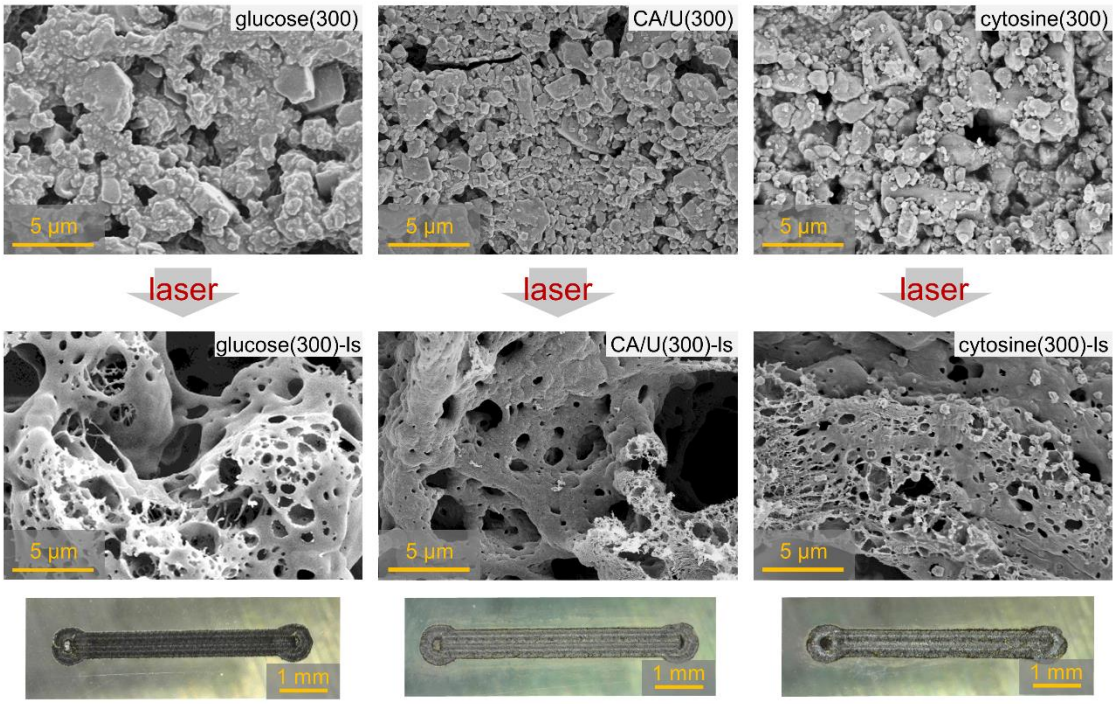

Figure 3. 2. *Scanning electron micrographs of the primary films of glucose (300), CA/U (300), and cytosine (300) before (upper) and after laser treatment (lower). Bottom: photographs of the laser-carbonized films on PET substrates.*

The laser parameters, such as incident power in W and scanning speed in ms mm^{-1}, play an essential role in the electrical properties of LP-carbon films. The laser parameters are related to the energy fluence in J m^{-1} quantified in the 2D plot shown in **Figure 3. 3 b**. Generally, the slower the speed, the higher the power, resulting in higher fluence.

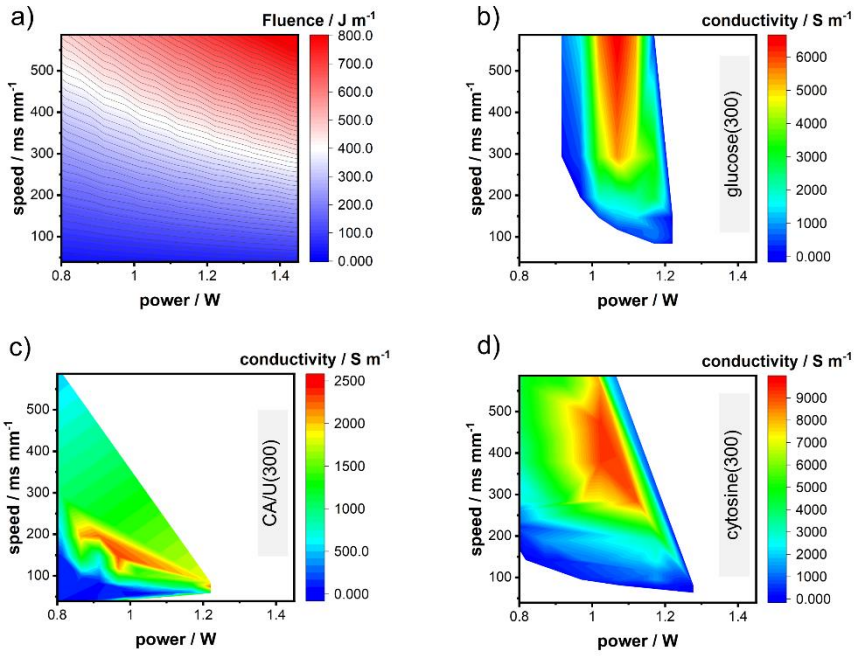

Figure 3. 3. *a). The radiant fluence of the laser energy versus scanning speed and laser power; b-d)2D plot of electrical conductivity of glucose (300)-ls, CA/U (300)-ls, and cytosine (300)-ls in dependence of laser power and laser scanning speed.*

We tested these settings for the three selected laser-carbonized films. Each film shows a specific response pattern strongly dependent on scanning speed. Glucose (300)-ls shows the best response at a scanning speed of ~ 600 ms mm^{-1}, while CA/U (300)-ls and cytosine (300)-ls show the best response at faster speeds of ~ 146 and ~ 378 ms mm^{-1}, respectively. The power used is very low, between 0.8-1.5W. In the end, the maximum conductivities of glucose (300)-ls, CA/U (300)-ls, and cytosine (300)-ls exhibit 6500, 2300, and 9500 S m^{-1}, respectively. Laser settings outside the range of the colored areas shown are either too strong or too weak. Too low fluence fails to complete the carbonization, and too high fluence leads to the complete evaporation of the film. We assume that the carbonization yield improves when higher conductivities are achieved.

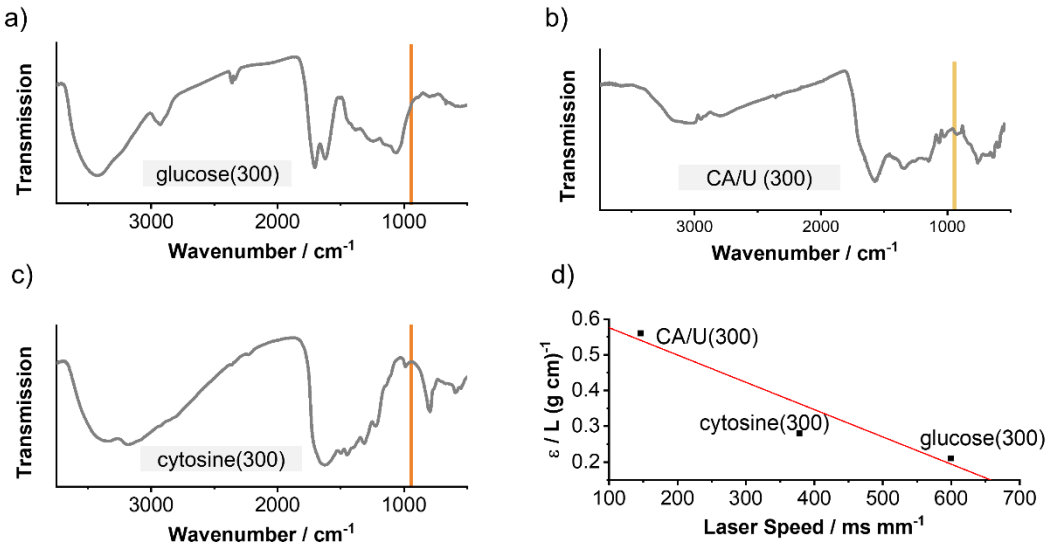

Figure 3. 4 *a-c) FT-IR spectra of glucose (300), CA/U (300), and cytosine (300) with the excitation energy of the laser indicated as an orange line; d) Correlation plot of extinction coefficient at the excitation wavelength versus laser speed used for the best electrical conductivity.*

To explain this observation, we examined the lasing-material interaction by infrared spectroscopic analysis (**Figure 3. 4**). The excitation wavelength of the laser is 10.6 µm, corresponding to an energy of 943 cm^{-1}, located in the typical fingerprint region of C=C and C-H resonance bending vibrations. All three CNFAs show weak adsorption in this region. We determined their extinction coefficients at the laser wavelength and the correlation with the laser scanning speed used for the best electrical conductivity. The CA/U (300) has a higher extinction coefficient $\varepsilon = 0.56$ L $(g\ cm)^{-1}$ and needs a higher laser scanning speed to achieve the highest electrical conductivity, while cytosine (300) and glucose (300) have lower extinction coefficients $\varepsilon = 0.28$ and 0.21 L $(g\ cm)^{-1}$, respectively that need a slower laser scanning speed. Therefore, the pre-carbonization results in cross-linking molecular precursors to prevent vaporization. The resonance absorption of specific molecular bonds under this CO_2 laser energy region results in the dissociation of bonds and instant high temperature, which causes carbonization of pre-carbonized materials (CNFAs).

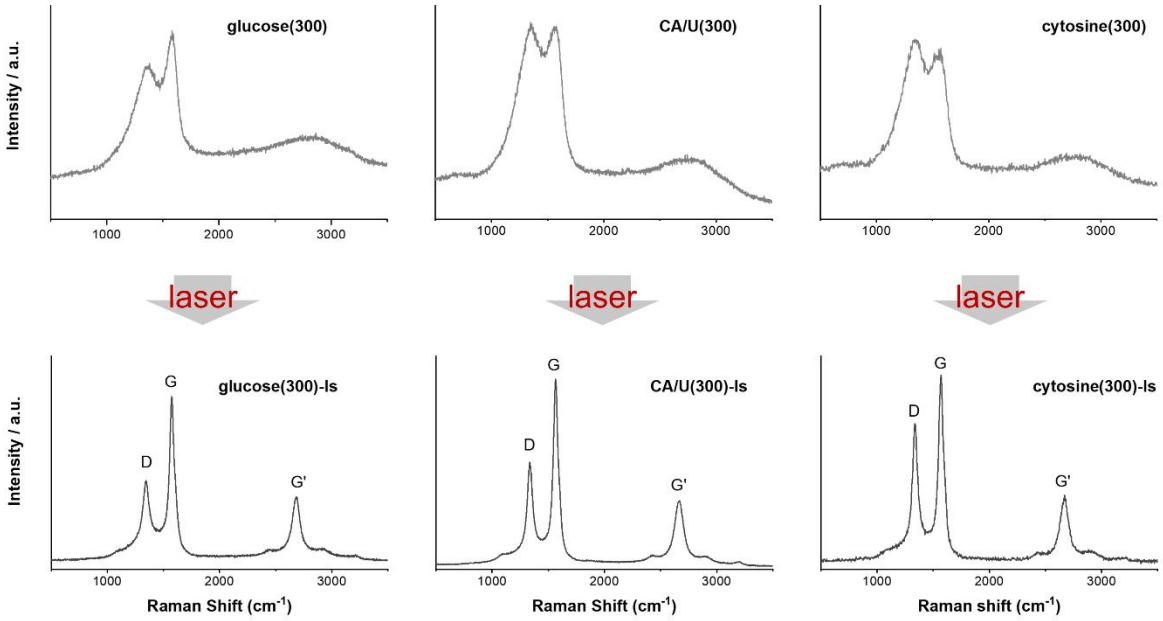

Figure 3. 5 *Raman spectroscopy of the primary films of glucose (300), CA/U (300), and cytosine (300) before (upper) and after laser treatment (lower).*

Figure 3. 5 shows the change of Raman signals of films after the laser-patterning process. The Raman spectra of all laser-carbonized films show sharp D-, G-, and G'- that indicate a high degree of carbonization on top of films. Furthermore, a relatively low D-band is remarkably strong in the Raman spectra that show a well-defined and extended graphene is formed on top of the laser-carbonized film, which usually can be observed in the carbon materials synthesized by conventional pyrolysis at temperatures above 1800 °C.[25] An overall characterization of the bulk film by Raman spectroscopy is challenging due to the coverage of the porous surface structure.

The porous morphology of laser-carbonized films indicates a high surface area. The methylene blue (MB) adsorption method (Experimental Section)[104,144] is used to determine the active surface areas of laser-carbonized products. A set of six measurements per sample were conducted to give average values of 135 ± 29, 165 ± 17, and 68 ± 19 m^2 g^{-1} for glucose (300)-ls, CA/U (300)-ls, and cytosine (300)-ls, respectively.

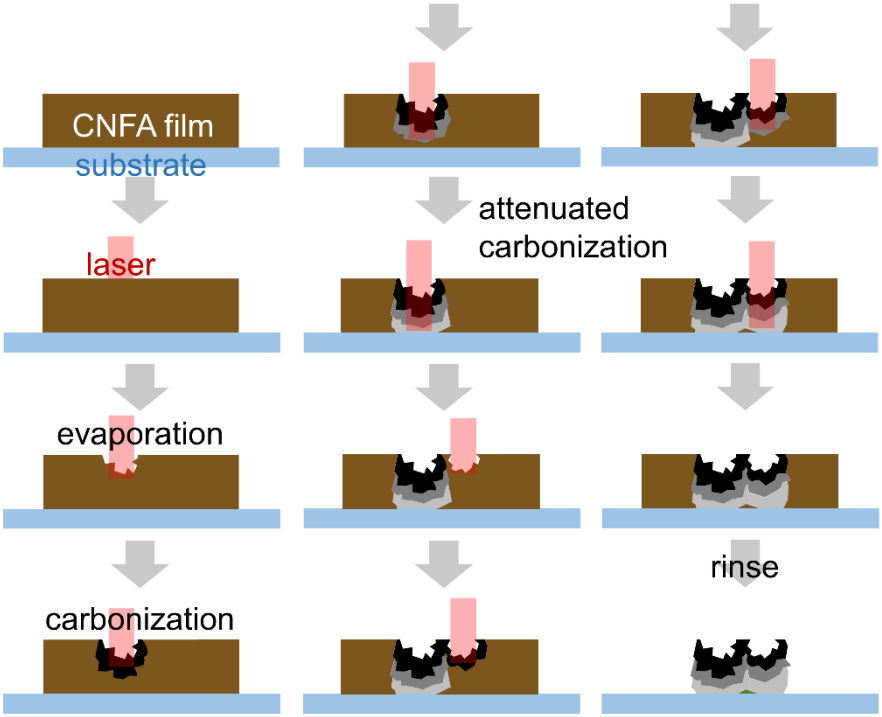

Figure 3. 6 *Scheme illustration of laser-carbonization process on a substrate: Laser impact causes evaporation, induces carbonization of the upper layer and lower degree carbonization of the lower layers due to attenuation of the laser energy; after finishing the laser-patterning, the unexposed films are removed by rinsing with water.*

Based on these observations, we propose a mechanism for laser-carbonization, as shown in **Figure 3. 6**. The penetration depth of approximately 35 µm of the laser is estimated by the Beer-Lambert law. The high energy impact of the laser causes the upper layer of the CNFA film to evaporate. Then, the carbonization/C-C bond formation occurs, which causes the upper layer of the material to be carbonized. The laser radiation is then attenuated by the carbonized layers, which dissipate the radiation in the form of heat across the film. After finishing the laser patterning, the unexposed films are removed by rinsing them with water—a carbonized film with a gradient of the degree of carbonization results. Our observation corroborates the suggested mechanism that thicker layers result in incompletely carbonized films resulting in delamination, while thinner films cause the substrate to become heated. PET, as a flexible substrate, melts. Therefore, precise control of the film thickness and the laser parameters is essential.

3.4 Comparison with conventional pyrolysis products

To gain a deeper understanding of the particularity of the microstructure of laser-carbonized materials. We compared the laser-carbonized materials and conventionally pyrolyzed carbon materials in the chamber oven at 950 °C.

First, we collected bulk powders of laser-carbonized materials (see Experiment Section) and pyrolyzed carbon to obtain insights into element composition. As shown in **Table 3. 1**,

Table 3. 1. *Elemental mass percentage of the CNFAs, LP-carbon, and references obtained from combustion elemental analysis and energy dispersive X-ray analysis.*

	Elemental analysis of the collected powders				***EDX of the as-prepared films***			
	C	**N**	**H**	**C/N**	**C**	**N**	**O**	**C/N**
glucose (theor.)	40	-	7	-	40	-	53	-
glucose(300)	63	-	5	-	76	-	24	-
glucose(300)-ls	75	-	2	-	97	-	3	-
glucose(950)	77	-	1	-	81	-	19	-
CA/U (theor.)*	29	23	5		29	23	43	
CA/U(300)	47	19	3	2.4	54	27	19	2.0
CA/U(300)-ls	68	13	1	5.2	92	-	8	-
CA/U(950)	86	13	0	6.6	81	16	3	5.1
cytosine (theor.)	43	38	5		43	38	14	
cytosine(300)	50	33	3	1.5	55	34	11	1.6
cytosine(300)-ls	50	27		1.9	83	7	9	-
cytosine(950)	80	15	0	5.3	81	18	1	4.5

**The composition of 1:3 citric acid/urea was assumed as used in the starting reagent reacting via HPPT as an intermediate product of the citric acid/urea reaction.*[145] *The grey highlighted numbers were obtained from the as-prepared films. All other numbers were obtained from the collected powders.*

Clearly, the conventional pyrolysis process (whether at 300 and 950 °C) results in decreases in nitrogen and an increase in carbon. According to EDX, the carbon content on top of the films in glucose (300)-ls, CA/U (300)-ls, and cytosine (300)-ls reaches 97 wt%, 92 wt%, and 83 wt%, respectively, which are much higher than the bulk powder with 75, 68 and 50 wt% detected by EA. This is consistent with the Raman spectra, demonstrating the gradual weakening of laser energy in the cross-section and a higher degree of carbonization at the top of the film compared to the average for the bulk film. Moreover, the carbon content of glucose (950), CA/U (950), and cytosine (950) obtained by EA analysis is higher than the laser-treated samples, which also shows a low degree of carbonization in the lower layer of films. This interpretation agrees well with the thermogravimetric analysis. As shown in **Figure 3. 7**, the spectra of the thermogravimetric analysis show a gradual mass loss of ~16 wt% starting at ~400 °C for CA/U (300)-ls and mass loss of ~17 wt% for CA/U (300)-ls(N_2). This mass loss is not observed with CA/U (950).

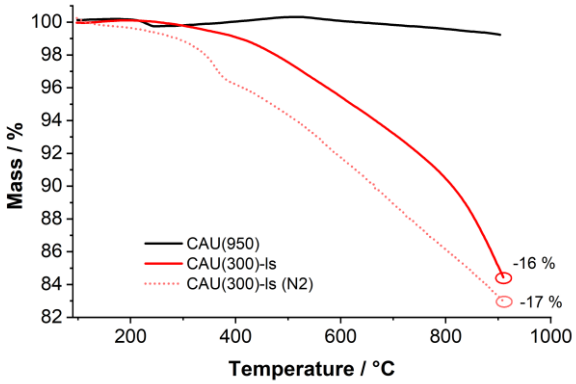

Figure 3. 7*. Comparative thermogravimetric analysis of CA/U (950) (black line) and CA/U (300)-is obtained by laser carbonization in the air (red line) and N_2 atmosphere (dotted line).*

Furthermore, the SEM of laser-carbonized bulk powder shows a higher degree of disorder and a more porous morphology compared with reference pyrolyzed samples (***Figure 3. 8***). Concerning the blowing effect of glucose during the heating process,[146,147] sheet-like structures appear in glucose (300)-ls and glucose (950), but the dimensions in glucose (300)-ls are much smaller.

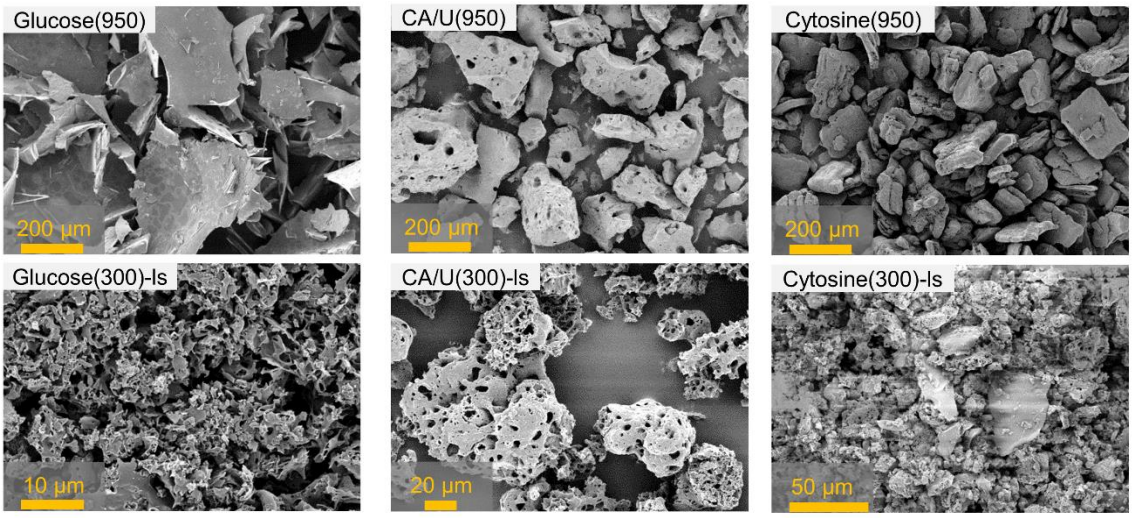

Figure 3. 8*. Scanning and transmission electron micrographs of the laser-carbonized samples and the references synthesized by conventional pyrolysis under 950 °C.*

More insights about the microstructures are obtained in the TEM analysis. All samples show predominantly amorphous character (**Figure S 1**). Small graphitic domains except for cytosine (300)-ls are observed in the HRTEM images (**Figure 3. 9**),

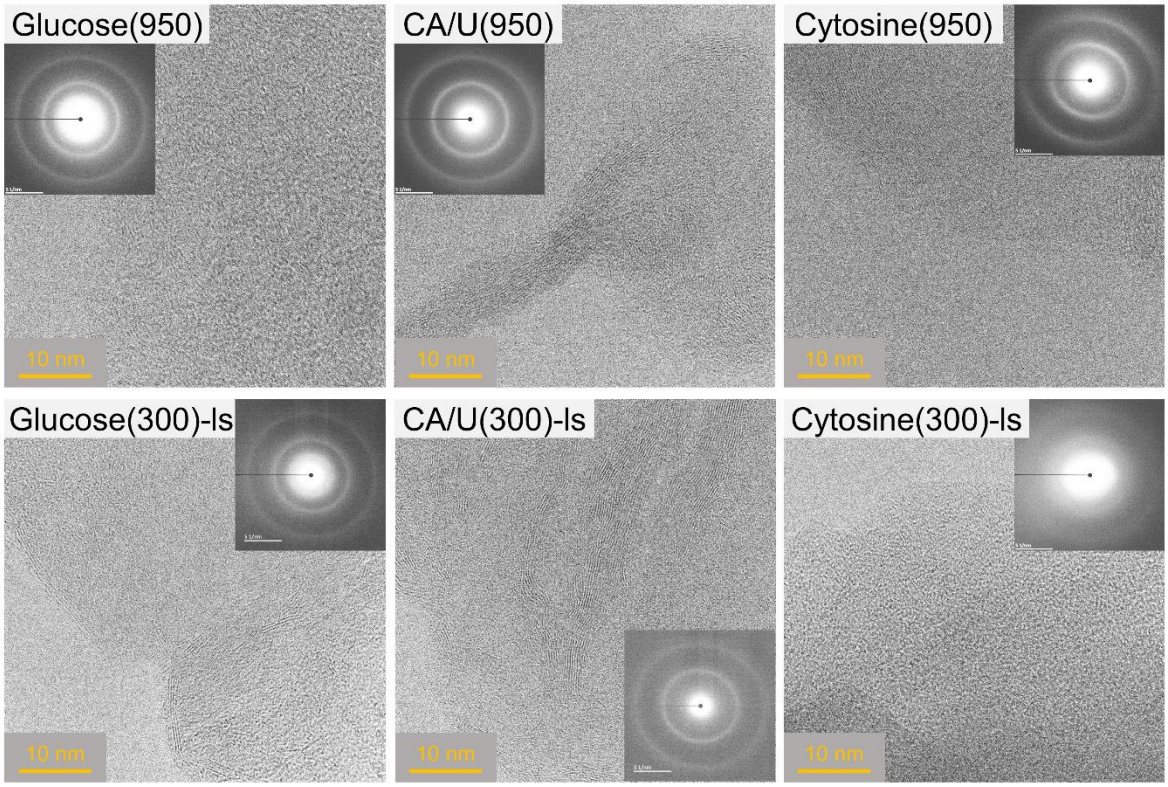

Figure 3. 9. *High-resolution transmission electron micrographs of fragments of glucose(950), glucose(300)-ls, CA/U(950), CA/U(300)-ls, and cytosine(950), and cytosine(300)-ls. The insets show the electron diffraction pattern of the selected areas.*

XPS analysis shows more information on the chemical composition of all samples (**Figure S 2-4**). In the C_{1s} area, there are four main signals at 284.4, 285.7, 286.6, and 288.1 eV assigned to sp^2 and sp^3 carbon, C-N/C-O, and C=N/C=O, respectively. The two main signals in the N_{1s} area at 398.8 and 400.3 eV originate from pyridinic and pyrrolic nitrogen, respectively. In the O_{1s} region, two peaks appear at 531.7 and 533.8 eV and are assigned to C-O and C=O, respectively. The areas of the fitted curves concerning the sum of all signals yield the mass percentage of the detected species. These were plotted in diagrams to compare different samples (**Figure 3. 10**).

In all glucose series samples, sp^2 carbon content is very high. Glucose (950) contains the highest carbonization yield, with a carbon content of 93%. However, the oxygen content of glucose (300)-ls is significantly higher than glucose (950) due to the high content of the C-O bond. In the CA/U series samples, sp^2 carbon content shows a different trend. Laser carbonized sample CA/U (300)-ls contains a higher sp^2 carbon content of 45% than CA/U (950). In the N_{1s} region, the pyridinic nitrogen content decreased after laser-carbonization and conventional pyrolysis, while pyrrolic nitrogen increased. The oxygen content of CA/U (300)-ls is

significantly higher than in the reference CA/U (950), which agrees with the element analysis results.

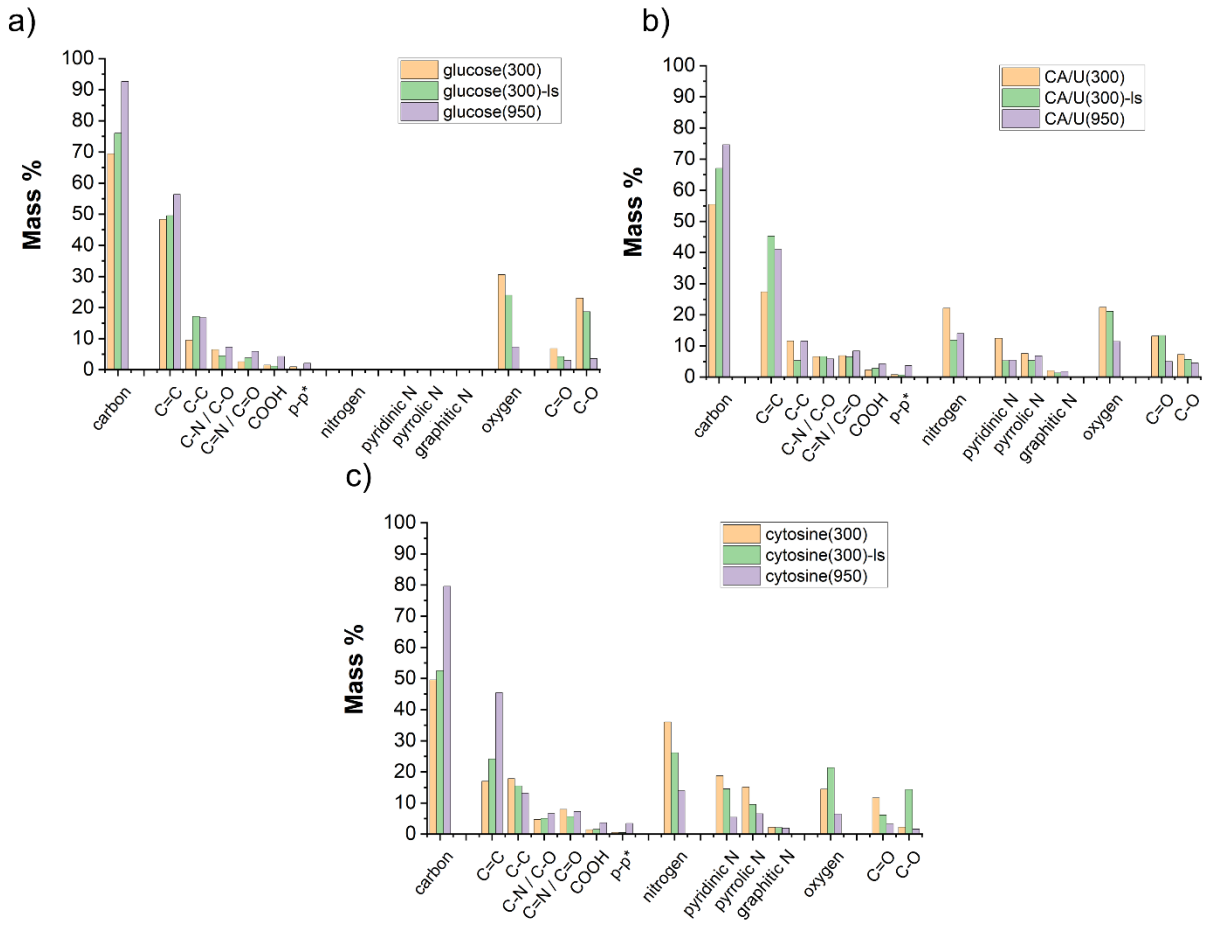

***Figure 3. 10**. a-c) elemental and chemical bond composition diagrams of the CNFAs, the laser-carbonized samples, and the references obtained by X-ray photoelectron spectroscopy.*

For cytosine (300), after laser treatment, sp^2 content increased, while sp^3 decreased. The oxygen content of cytosine (300)-ls is higher than the CNFA cytosine (300) and the reference cytosine (950), where the C-O species is the dominant peak in the O_{1s} spectrum. The reference cytosine (950) has the lowest nitrogen content.

The quantitative XPS analysis of the collected powder samples corroborates the proposed reaction mechanism. Laser carbonization generally results in increased surface oxygenation of carbon compared to pyrolysis. The reason is that the reactive side species are not removed fast enough in laser carbonization, which oxidizes the carbon surface, while there are steady evaporation and transport of reactive side products in conventional pyrolysis. The increase of sp^2 content after laser treatment probably is caused by interconnection/polymerization of the graphitic domains, which is the primary reaction occurring upon laser-carbonization.

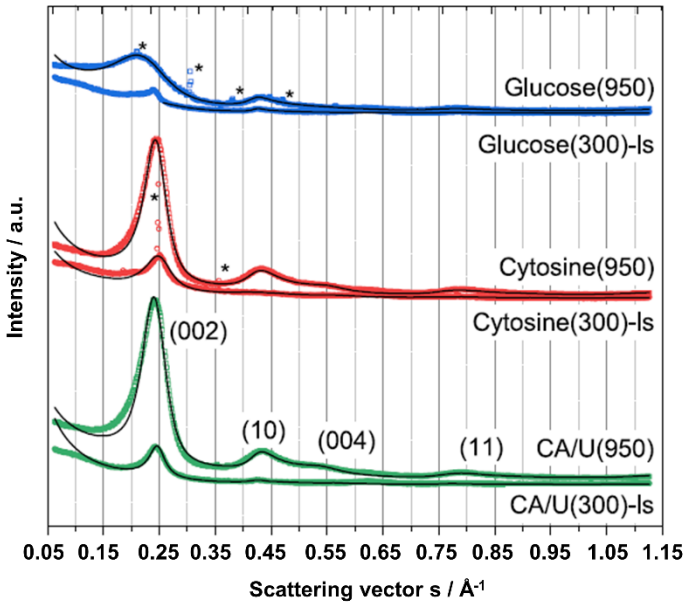

Figure 3. 11. *Measured (dots) and fitted (line) WAXS patterns of glucose (300)-ls, CA/U (300)-ls, and cytosine (300)-is, in comparison to the reference samples pyrolyzed at 950 °C: glucose (950), CA/U (950), and cytosine (950).*

To compare the graphitic domains and crystallinity of the lasered and pyrolyzed samples, we performed a comprehensive WAXS analysis. As shown in **Figure 3. 11**, the WAXS pattern exhibits the characteristics of non-graphitic carbons that generally show broad and asymmetric (hk) reflection peaks (**Figure S 5**). Layer size (L_a) and stack heights (L_c) give more detail for the microstructural parameters. Moreover, the average graphene layer distance (a_3) and the disorder, e.g., the deviation of the C-C bond length (σ_1) and the deviation in the layer distance (σ_3), also reflect the characteristic parameters of these non-graphitic carbons. Here, we used the theoretical function model of Ruland and Smarsly to fit the whole scattering vector range of the WAXS pattern. A description of the model is given in the Experimental Section.

All simulated parameters of samples are listed in **Figure S 7**. In general, CA/U (950) and cytosine (950) show a clear (002) and a small broad (004) reflection, while in the pattern of glucose (950), the (004) reflection is almost invisible. In condition, CA/U (950) and cytosine (950) have similar average layer distance a_3 and stacking heights L_c. However, the deviation of the layer distances σ_3 = 20% of CA/U (950) is higher than cytosine (950), which indicates that the stacking structure in CA/U (950) is more disordered than in cytosine (950). The higher oxygen content of CA/U (950) may be responsible for the disordered structure[148].

Comparing cytosine (300)-ls and cytosine (950), the stacking in cytosine (300)-ls suffers from a significantly higher disorder compared to the reference cytosine (950), which is represented

by the higher deviation from the graphitic layer distance (σ_3) of 0.50 Å for cytosine (300)-ls compared to 0.35 Å for cytosine (950). Furthermore, the average stack height (L_c) for cytosine (300)-ls was calculated to be slightly higher than for cytosine (950). The high amount of oxygen in cytosine (300)-ls also rationalize the absence of (10), (004), (11) reflections in the WAXS pattern, which indicates cytosine (300)-ls does not contain ordered sp^2 structures.

For the glucose (300)-ls and glucose (950), glucose (300)-ls consists of smaller graphene layers (L_a = 50 Å) and a significantly lower disorder (σ_3 = 0.1) than glucose (950). These parameters suffer from a large calculation error due to the very small and broad reflections in the WAXS pattern. Furthermore, comparing CA/U (950) and CA/U (300)-ls, CA/U (300)-ls consists of smaller graphene domains (L_a = 50 Å) than CA/U (950) (L_a = 31 Å), relatively lower disorder (σ_1 = 0.15), which indicate a more ordered sp^2 structure than conventional pyrolysis.

Therefore, the choice of precursor has a major influence on the microstructure of the resulting product. The laser-carbonized samples consist of a significantly disordered stacking structure, which is directly shown by the smaller and broader (002) and (004) reflections or their complete absence compared to the references. The disorder parameters for stacking (α_{3min}, α_3) are generally higher than for the reference samples. The amount of oxygen inside the products (CA/U, cytosine) and in the precursor (glucose) seems to significantly influence the formation of the microstructure in the effects. More precisely, oxygen prevents the condensation of perfect graphite-like stacking structures in glucose (300)-ls or even ordered sp^2 layers as in cytosine (300)-ls (high s1). For CA/U, on the other hand, laser-carbonization leads to significantly larger and higher-ordered sp^2 layers. In general, laser-carbonization leads to larger, non-graphitic carbon domains. In principle, producing large and ordered sp^2 layers but with highly disordered stacks is possible. Notably, the degree of disorder is expected to be a consequence of the gradient in the degree of carbonization.

3.5 Summary

In conclusion, unlike conventional pyrolysis, where the thermal process usually takes a few hours, laser-carbonization needs milliseconds. In addition, laser-carbonized samples generally show greater disorder, and a high degree of oxygenation on their surfaces throughout the film. Based on this comparative study with three precursors, we found that pre-carbonization of the molecular precursors is a prerequisite for laser-carbonization. New precursor systems can be explored, and their laser reaction conditions can be rationalized and potentially predicted based on their extinction coefficient. Laser-carbonization offers a wide range of possibilities for

synthesizing selective materials that can be applied in the field of flexible two-dimensional electronics.

4. A flexible resistive nitrogen-doped carbon sensor for the detection of CO_2

4.1 Introduction

Monitoring CO_2 is imperative to understand its origin and impact. Both the global climate crisis and the current COVID-19 pandemic have shifted attention and created awareness of the need for comprehensive CO_2 monitoring on local and global scales.[149,150] To fight global warming, a deeper awareness of the public for the impact of greenhouse gases like CO_2 may be required. In industrial and work environments, high concentrations of CO_2 (in)directly pose health risks due to acidosis or the enrichment of undesired species like viruses or may cause performance loss even during office work.[151] Capable smart mobile devices and flexible wearables to collect exhaled breath may support decentralized healthcare as well as professional and amateur sport.[152]

Handheld or stationary infrared absorption sensors represent state-of-the-art device technology but exhibit limitations regarding versatility, compactness, and integrability.[153] Integrated micro-sensors, with a superior property portfolio including small size, flexibility, and low cost, would facilitate comprehensive spatial and temporal analyses of CO_2 in a wide range of applications.[136]

Metal oxide-based resistive gas sensors are state-of-the-art devices owing to their high sensitivity, low cost, and simplicity.[153] However, for practical application, metal oxide gas sensors generally have the disadvantages of high working temperatures and low intrinsic flexibility.[154–157] A promising alternative is carbon nanomaterials (CNMs) that are selectively sensitive to CO_2 at room temperature. Carbon nanotubes or graphene have been favored candidates due to their high surface areas, high charge carrier mobilities, excellent mechanical properties, and low thermal noise.[158,159] A common solution to achieve selectivity in CNMs is synthetic functionalization or hybridization (with metals or metal oxides) on their surface to provide specific active sites or tune the electronic properties, respectively.[158,160] However, the relatively high costs associated with sophisticated fabrication processes and expensive manufacturing setups are still a challenge for commercial applications.[161–164]

As discussed in **Chapter 2.4**, another promising cost-effective alternative is nitrogen-doped carbons (NCs) as they intrinsically provide selective binding sites for CO_2. N-doped carbons obtained from direct pyrolysis are a class of materials that have been widely studied for

selective CO_2 capture or conversion.[79,165–170] In particular, polypyrrole or imidazole-based carbons have demonstrated a remarkable CO_2 sorption capacity due to their specific chemical interactions.[78,171,172]

Based on the successful implementation of the concepts in **Chapter 3,** after undergoing an integrated two-step approach, the nitrogen-containing precursors can be transformed into a nitrogen-doped carbon material. In this work, adenine was used as a precursor for the preparation of a carbon network-forming agent (CNFA) due to its rich nitrogen functionalities. The process parameters were optimized in terms of precursor preparation, laser parameters, reaction atmosphere, porosity, and film thickness. In order to enhance the response to CO_2, glucose was added as a foaming agent. The mechanism is elucidated in a cross-sectional HR-(S)TEM analysis. The performance of the flexible polyethylene terephthalate (PET)-supported LP-NCs to sensing CO_2 at different atmospheric contents was tested in dry and humid environments. The newly fabricated LP-NC sensor strips exhibit high sensitivity to CO_2 at room temperature, excellent mechanical flexibility, good cycling stability, and a degree of selectivity towards CO_2 in humid environments.

Term of use: This chapter is adapted with permission from my own original work:

H. Wang, C. O. Ogolla, G. Panchal, M. Hepp, S. Delacroix, D. Cruz, D. Kojda, J. Ciston, C. Ophus, A. Knop-Gericke, K. Habicht, B. Butz, V. Strauss, Flexible CO_2 Sensor Architecture with Selective Nitrogen Functionalities by One-Step Laser-Induced Conversion of Versatile Organic Ink. *Adv. Funct. Mater.*, 2207406 (2022)

4.2 Design of CO_2 gas sensor trips

Laser-patterned N-doped carbon (LP-NC) sensor strips were fabricated using a two-step approach, including precursor film preparation and laser-carbonization. As a nitrogen-rich molecular precursor, adenine ($C_5N_5H_5$) was chosen. The latter was pre-carbonized at temperatures between 300-400 °C for two h in a tube furnace under a flow of nitrogen **(Figure 4. 1 a)**. The thus obtained pre-carbonized powder, the so-called carbon network-forming agent (CNFA), was then processed to dry films on PET with a standard thickness of 75 µm (**Figure 4. 1 c**). In the second step, laser-carbonization (**Figure 4. 1 d**) was performed: the dry films were irradiated with a mid-infrared CO_2-laser under different atmospheres (air, N_2, or O_2) to create LP-NC sensor strips. Then, the unexposed precursor films were rinsed off the substrate with deionized water. In each batch, 36 gas sensor strips were produced in only 144 s on a PET sheet of 20 cm^2 (**Figure 4. 1 e-g**). Subsequently, the LP-NC strips were tested as resistive sensor platforms to detect CO_2 in a gas-flow cell with different concentrations at room temperature **(Figure 4. 1 h)**. In each measurement, a sensor strip was placed into a gas flow cell, and electrodes connected the two ends of the sensor platform to measure the impedance in a four-probe arrangement. Two parallel connected mass flow controllers controlled the gas composition inside the cell to ensure a constant gas flow with compositions of 0.5% - 10% CO_2 gas in N_2 or air as carrier gas.

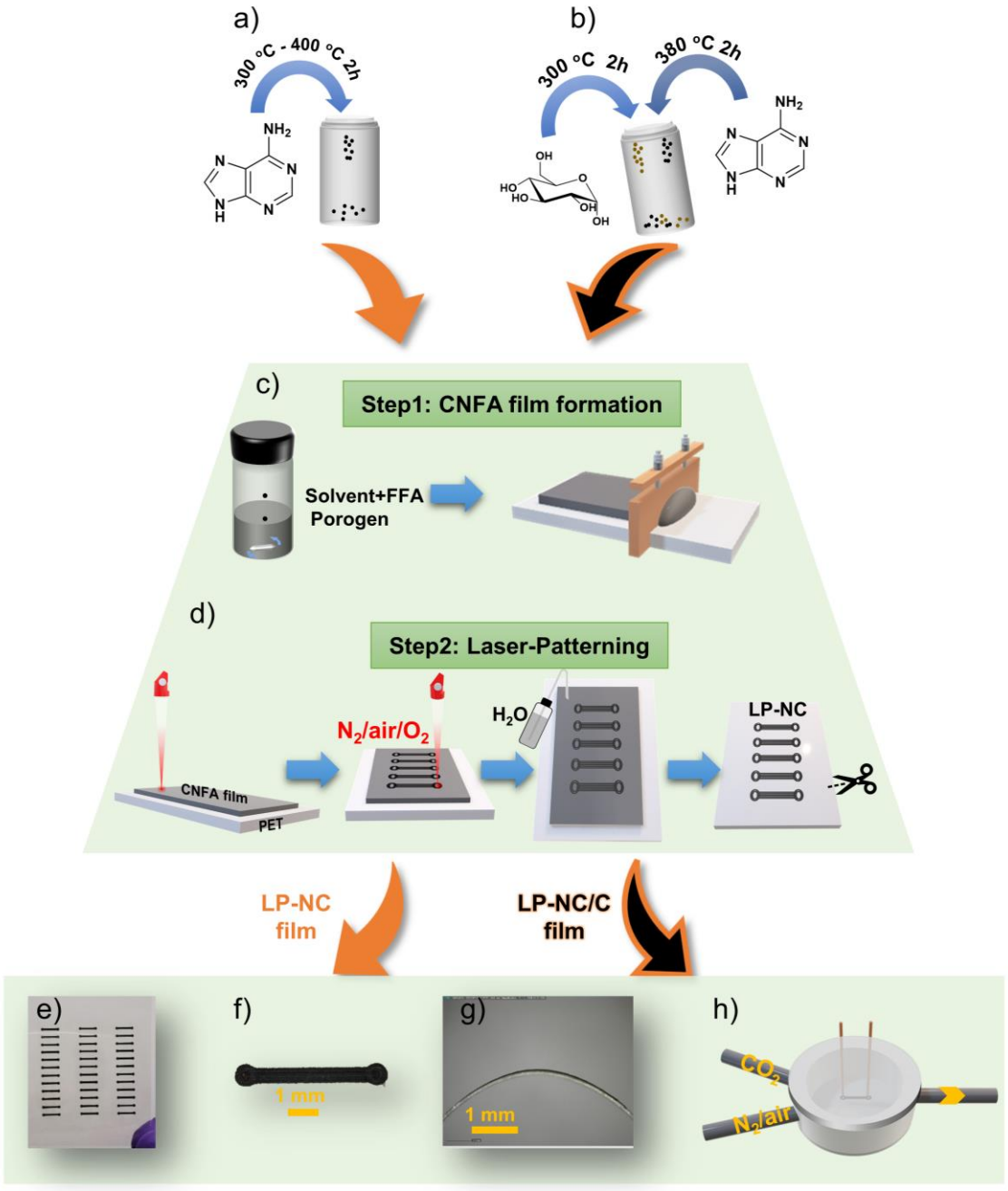

Figure 4. 1. *Scheme of the sensor strip fabrication process. a-b) Preparation of precursor inks; c) Application of homogeneous CNFA films on a PET substrate; d) Laser-patterning of CNFA films and subsequent rinsing with H_2O to obtain the LP-NC sensor strips; e) Photograph of a 20 cm^2 PET substrate with 36 LP-NC sensor strips; f) Optical micrograph showing the dimensions of a sensor-strip used for the resistive gas-sensing experiment; g) Photograph of a sensor strip on flexible PET bent in a positive direction; h) Illustration of the gas-sensing cell used to characterize the resistive response of the LP-NC sensor strips in different environments.*

4.3 Materials optimization

In order to improve the sensor response, the LP-NC films were sequentially optimized in terms of 1) pre-carbonization parameters, 2) laser parameters, 3) process atmosphere, 4) porosity, and 5) film thickness.

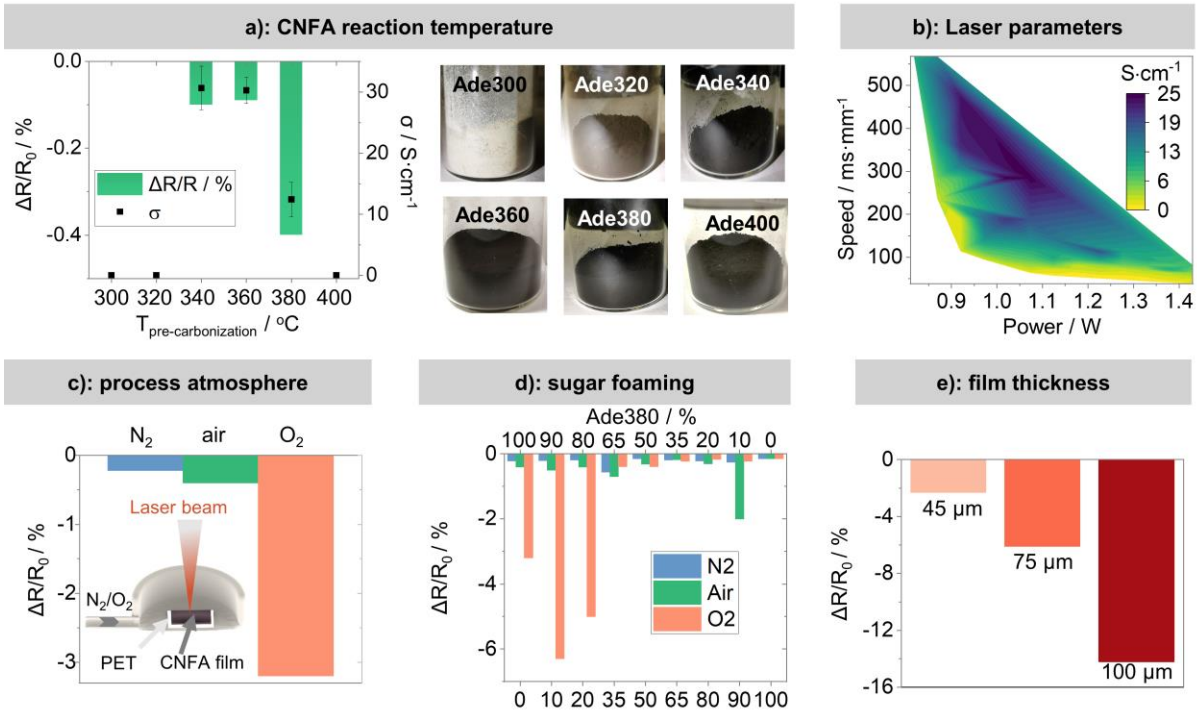

Figure 4. 2. Materials optimization. *a) Electric sheet conductivities (black dots) and resistive response (green column) of sensor strips LP_{air}_Ade300-400 upon exposure to 10% CO_2 with film thicknesses 75 µm; b) 2D plot of the electrical conductivities of LP_{air}_Ade380 in dependence of laser power and scanning speed; c) Resistive response of LP_Ade380 produced in different atmospheres (N_2/air/O_2) upon exposure to 10% CO_2; inset: side view illustration of the fabrication of LP-NC films inside an open-top atmospheric chamber; d) Resistive response (to 10% CO_2) of LPN_2_Ade380, LPair_Ade380, and LPO_2_Ade380 upon mixing with different mass proportions of Glu300; e) Resistive response of LP_{O2}-$Ade380_{90}$/$Glu300_{10}$ with different thickness of 45, 75, 100 µm using N_2 as carrier gas (grey: carrier gas, yellow: mixed gas with 10% CO_2).*

4.3.1 Screening CNFAs reaction temperature

In the previous chapter, we demonstrated that pre-carbonization of the molecular precursors is required for laser-carbonization, as it condenses the precursors and supports the formation of a conductive carbon film during subsequent laser-carbonization. Notably, the selection of the pyrolysis temperature during pre-carbonization is critical to the electronic properties of the final LP-NC. To identify the optimal pyrolysis temperature, adenine was pyrolyzed at temperatures between 300-400 °C, and their products were tested as CNFAs. The samples are

denoted concerning the annealing temperature; for example, Ade380 represents adenine annealed at 380 °C. Notably, as the pre-carbonization temperature increases, the color of the products becomes darker, from light brown over dark brown to black. (**Figure 4. 2**)

4.3.2 Laser parameters

Next, we optimized the laser processing parameters, i.e., the incident power and scanning speed, as they are critical for the carbonization process of the selected CNFA-Ade380. The plot in **Figure 3. 3 a** (**Chapter 3**) quantifies energy fluence based on the power and scanning speed relationship. In general, slower speed and higher power produce higher energy fluence. Each CNFA gives a characteristic response pattern in terms of resulting conductivity, as shown in the 3D plot in **Figure 4. 2 b**. Ade380 shows the highest conductivity of 24 $S \cdot cm^{-1}$ at a speed of 350 ms·mm-1 and a power of 1.05 W. The optimal speed of 186 $S \cdot cm^{-1}$ and the laser power of 1.1 W were optimized for sensing performance.

4.3.3. Process atmosphere

Another critical factor for the properties of the LP-NC films is the reaction atmosphere, as laser patterning involves high temperatures and combustion processes. Aiming to expand the range of properties of LP-NC, especially tuning the sorption capacity of the LP-NC surface, we employed an open-top atmospheric chamber (**Figure 4. 2 c**) to fabricate LP-NC under controlled reaction atmospheres. The resulting LP-NC films are denoted accordingly. For example, LP_{N2}- Ade(380) represents laser-patterned Ade380 under an N_2 atmosphere. In terms of surface porosity, the LP-NC films seem to be unaffected by the reaction atmosphere (Figure S4). However, when changing from N_2 or air to an O_2 atmosphere, the resistive response upon exposure to 10% CO_2 was increased by nearly one order of magnitude from -0.22% to -3.2%.

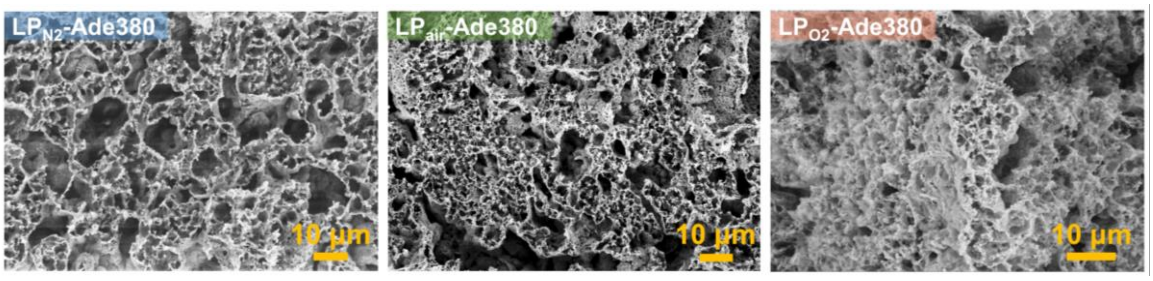

Figure 4. 3. *Top view SEM images of laser-carbonized films fabricated under N_2, air, and O_2 atmospheres.*

4.3.4. Pore tuning with sugar foaming

Increasing porosity leads to improving the accessibility of CO_2 to active sites in the film. Glucose is a well-known precursor for carbonized materials that generate high surfaces by foaming. The foaming, i.e., the formation of bubbles, is commonly observed in thermally treated carbohydrates.[147] Carbon foam is obtained when using pre-carbonized glucose (Glu300) as a CNFA in laser patterning. Bubbles in a size range between tens of nanometers up to several microns are observed throughout the $LP_{N2/air/O2}$-Glu300 films **(Figure 4. 4).**

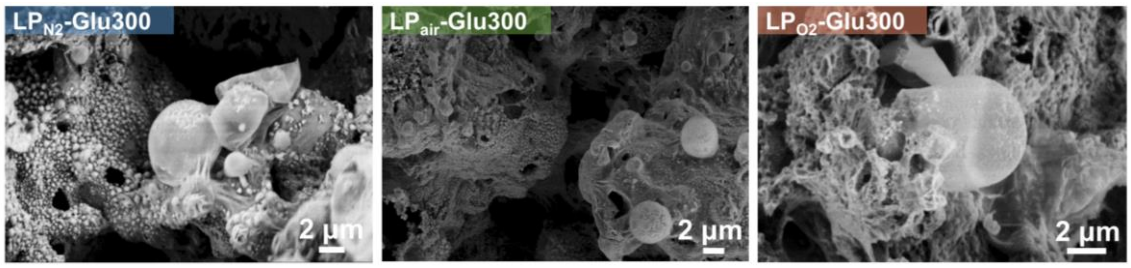

Figure 4. 4 *Top view SEM images of laser-carbonized obtained from Glu300 as a CNFA in different process atmospheres.*

Prior to laser treatment, the CNFA films of Glu300 and Ade380 show the granular starting morphology with micron-sized particles (**Figure 4. 5**), and the EDX elemental maps show several nitrogen-free domains in the film deriving from Glu300. The foaming of Glu300 during laser-carbonization is used to increase the porosity of the LP-NC. To test this hypothesis, nine compositions with different mixing ratios (Glu300 and Ade380) were tested for the response toward exposure to 10% CO_2 (Figure 2D). The best response is obtained for adding 10 wt% of Glu300 to the Ade380 precursor film (LP_{O2}-$Ade380_{90}$/$Glu300_{10}$) produced under O_2, reaching $\Delta R/R_0$ = -6.3 %. As a reference, the pure glucose-derived LP-Cs were tested, but all samples, regardless of the atmosphere ($LP_{N2/air/O2}$-Glu300), showed a low response of only $\Delta R/R_0 \approx$ -0.15 % to exposure of 10% CO_2.

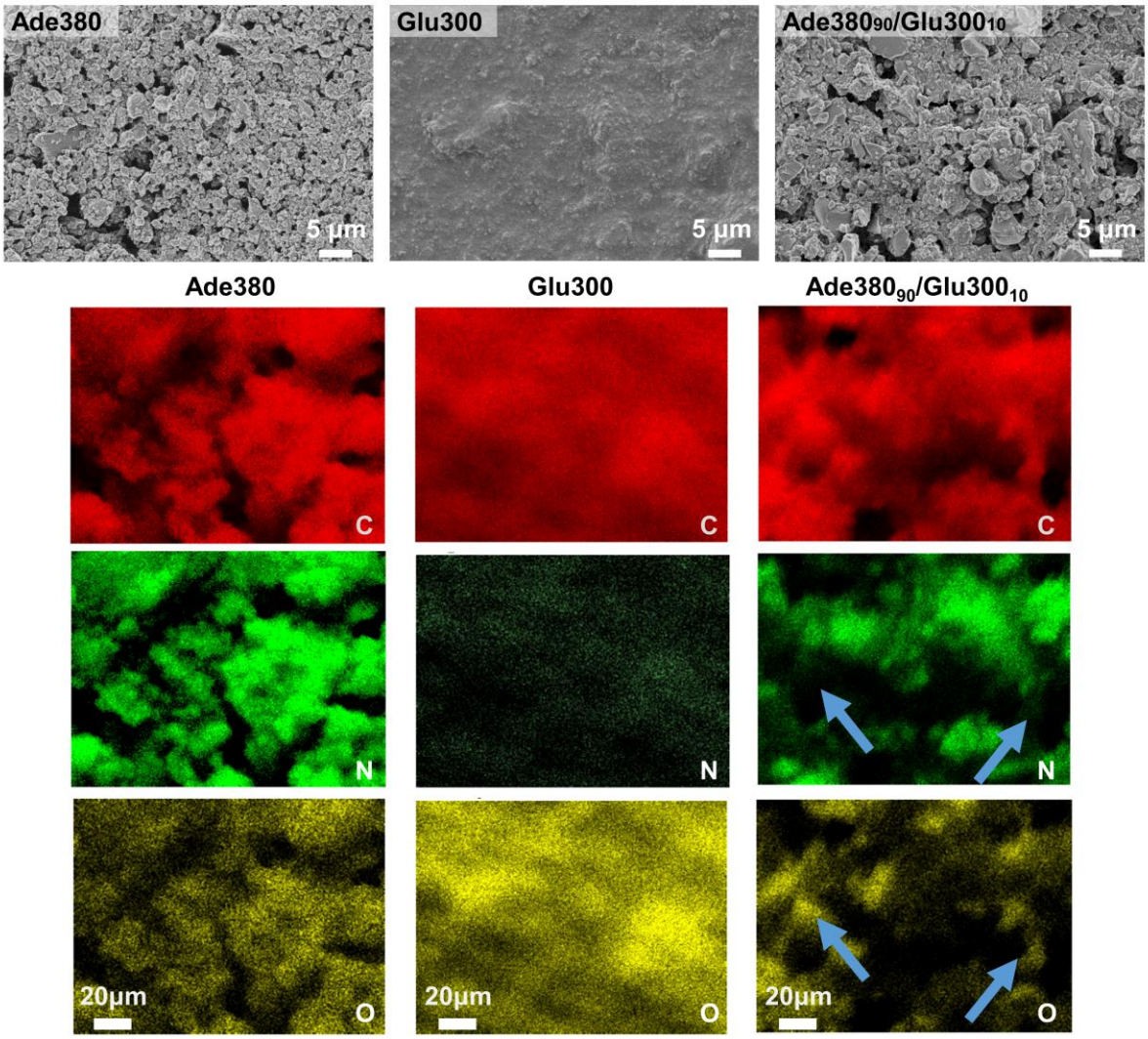

Figure 4. 5. *SEM images of the CNFA films Ade380, Glu300, and Ade38090/Glu30010 and their corresponding EDX mapping analysis. The nitrogen in the Glu300 is from PVP. The CNFA films show a granular appearance with grain sizes ranging between 5-100 microns.*

4.3.5 Film thickness

Finally, the thickness of the precursor film was optimized for high response to CO_2. Thus, we tested the effect of film thickness on detecting 10% CO_2 by recording the resistive response of LP_{O2}-Ade380$_{90}$/Glu300$_{10}$ (**Figure 4. 2 e**). Generally, thicker films give a higher response. In our experiments, the LP-NC film with a thickness of 100 µm shows the best response of $\Delta R/R_0$ = -14.3%. Thicker films delaminate upon rinsing.

4.4 Characterization and discussion

The optimized laser-carbonized films LP_{O2}-$Ade380_{90}/Glu300_{10}$ were morphologically and chemically investigated. Throughout the entire laser-irradiated area, the film shows the typical porous morphology obtained upon laser-treatment (**Figure 4. 6 a**). This morphology is obtained independent of the reaction atmosphere. However, under oxygen, a crumpled surface structure with feature sizes on the order of 100-300 nm on top of the film appears, which is attributed to the enhanced combustion process in the presence of O_2 (**Figure 4. 6 b**). This, in turn, leads to enhanced carbonization on the surface. For all reaction atmospheres, the Raman spectra taken on the top of the films show common features of a turbostratic graphitic material, i.e., the presence of sharp D-, G-, and D´-bands, indicating a high degree of carbonization on top of the films (**Figure 4. 6 c**). Notably, the film obtained in oxygen atmosphere, LP_{O2}-$Ade380_{90}/Glu300_{10}$, shows a significantly higher degree of carbonization as only negligible contributions of sp^3- and disorder-related D4 and D3 bands at 1200 and 1460 cm^{-1}, respectively, and a lower defect-attributed D-band compared to LP_{N2}-$Ade380_{90}/Glu300_{10}$ are observed.

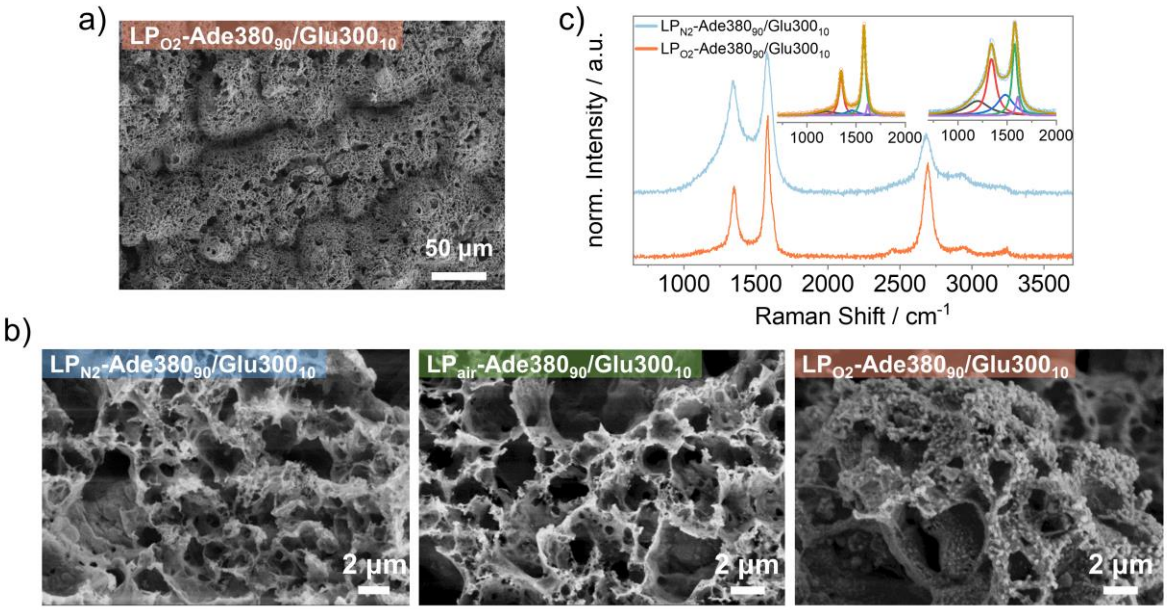

Figure 4. 6 *a) Top view SEM images with the lower magnification of LP_{O2}-$Ade380_{90}/Glu300_{10}$; b) Top view SEM images with higher magnification of LP_{N2}-$Ade380_{90}/Glu300_{10}$, LP_{air}-$Ade380_{90}/Glu300_{10}$, and LP_{O2}-$Ade380_{90}/Glu300_{10}$.*

Viewed from the optical micrographs and SEM micrographs of a cross-section of the final optimized film, the synergistic foaming effect results in a clearly open-pore morphology though the cross-section of the film (**Figure 4. 7 a,b**). The depth-dependent attenuation of the irradiation was successfully utilized in one-step laser treatment to create the lateral

heterostructure with transducer and sensor sub-layers (**Figure 4. 7**, **Figure 4. 8**). As shown in **Figure 4. 7**, the sodium is uniformly distributed in the lower layer, and the missing regions of sodium are derived from the embedding resin. In addition, compared with the non-uniform N distribution, some micron-sized with low-content N regions are attributed to the globular glucose-based CNFA.

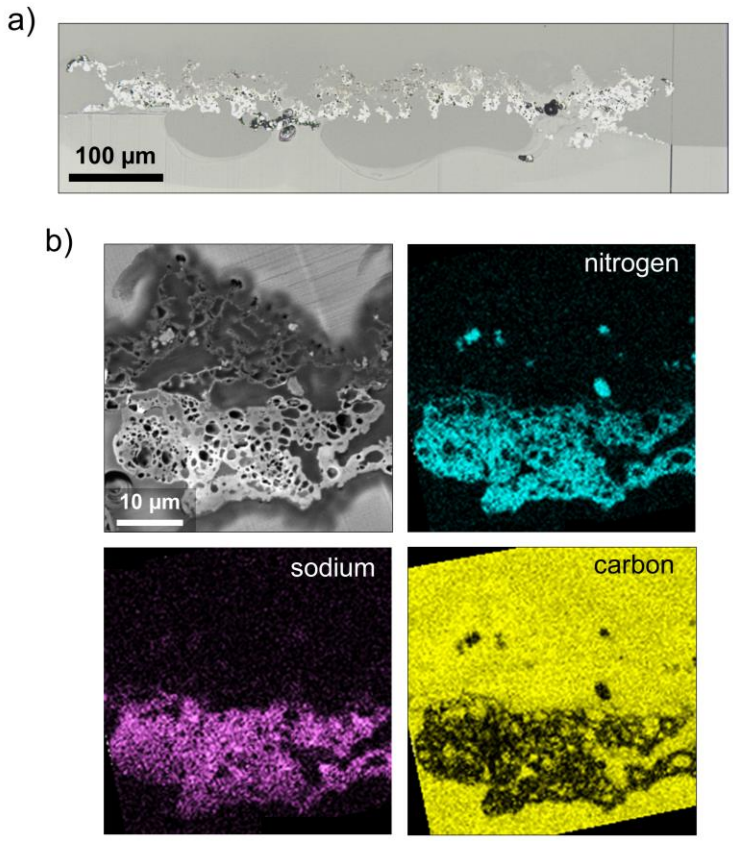

***Figure 4.** 7. a) Optical bright-field micrograph of embedded LP_{O2}-$Ade380_{90}$/$Glu300_{10}$ sensor (microtomy block surface in reflection; b) Cross-sectional backscatter SEM micrograph of LP_{O2}-$Ade380_{90}$/$Glu300_{10}$ with correlated EDXS element maps (composition in at% with the sum of C, N, O, Na being considered 100 at%)*

As shown in **Figure 4. 7 b** and **Figure 4. 8 a**, in the upper transducer layer, open, interconnected macropores are generated, where these regions are completely infiltrated by epoxy resin. That pore network ensures excellent accessibility to the active N-sites of the sensor layer by the analyte and carrier gas. Only a sparse network of graphitized carbon remains, which is laterally interconnected and ensures a sufficient charge transport capability. The sensor layer exhibits a generally lower degree of porosity, as expected from the reduced laser impact at larger depths. Only a minor volume fraction of enclosed meso-and macropores was observed. The foaming agent becomes pyrolyzed or partially transformed into graphitized carbon, whereas the porogen NaI (partially) evaporates, with NaI still being present in the sensor layer (**Figure 4. 7**). In **Figure 4. 8 a**, there is a narrow transition zone between the sensor and transducer layer.

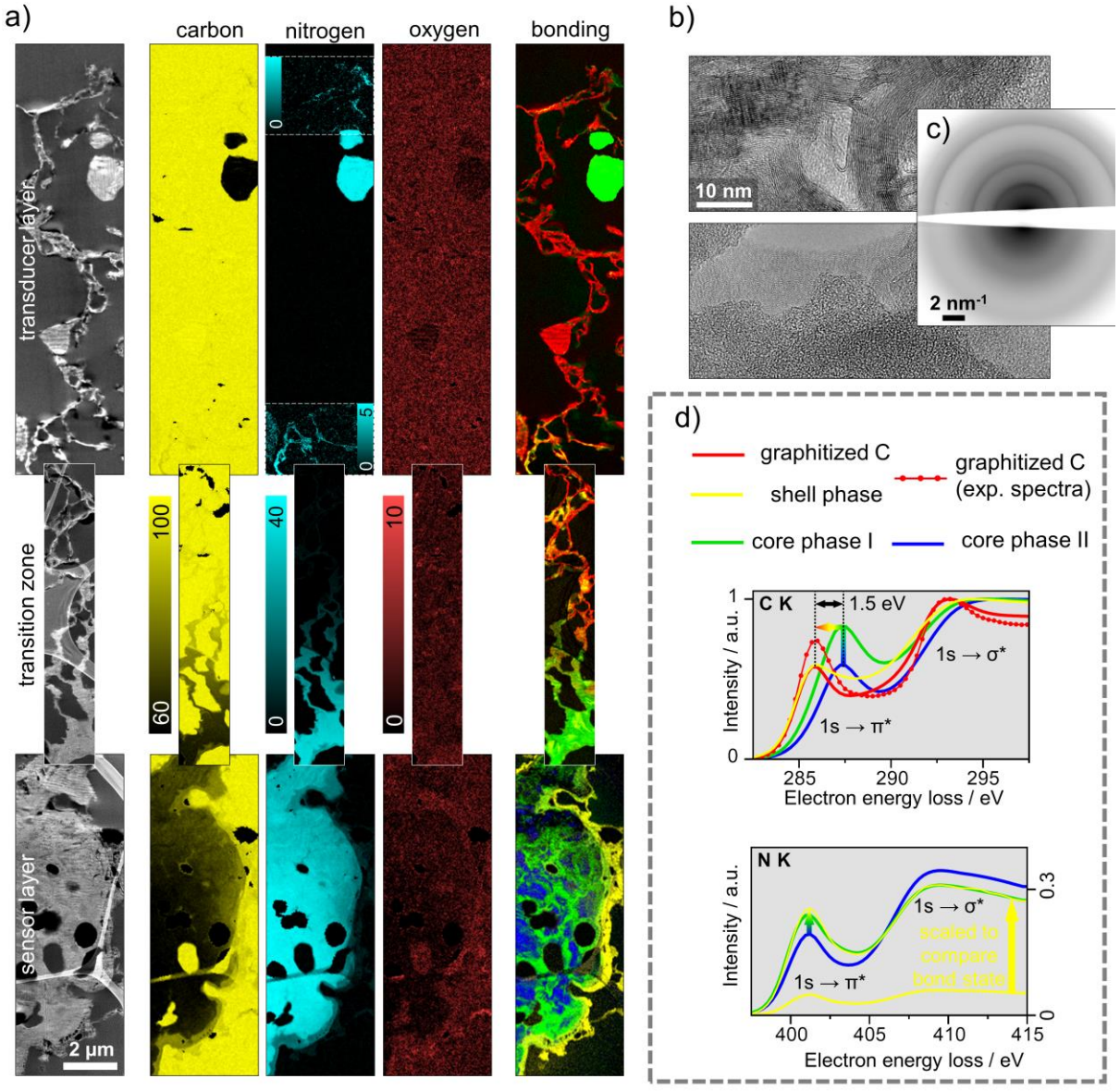

Figure 4. 8. *a) Cross-sectional TEM analyses (microtomic, epoxy-embedded cross-section) of representative regions (not necessarily adjacent) of the transducer and sensor layers as well as the transition zone: (left) HAADF-STEM micrographs with a few uninfiltrated pores (black), embedding epoxy resin (homogeneous dark gray), and superimposed lacey TEM support film (wavy horizontal contrast features in the STEM image of the sensor layer indicate slight thickness variations due to microtomic sectioning), (center) corresponding EELS element maps with color codes in at% (sum of C, N, O being considered 100 at%) with locally enhanced contrast in upper N map (0-5 at%) where nitrogen is present, (right) bond mapping showing distributions (weightings) of major phases identified by PCA (red: graphitized carbon, yellow: shell phase, green/blue: core phases I/II). b) Exemplary HRTEM images of the transducer layer and sensor layer; c) SAED patterns of graphitized carbon and shell regions; d) Respective PCA spectra of those phases with selected energy-loss ranges of C and N ionization edges (background corrected, C edge normalized, N relative to C.*

The cross-sectional TEM analyses show elemental composition and chemical bond gradients. Obviously, nitrogen-rich particles were found concentrated in lower layers (sensor layer), while

the graphitized carbon skeleton of the central transducer layer did not show any nitrogen signals. This also indicates the preferential loss of nitrogen in the carbonization process.

Therefore, we performed chemical bond analysis by principal component analysis (PCA)[173] of the EELS dataset (Methods section). Four major phases were clearly identified throughout the device cross-section (**Figure 4. 8**). Those are the graphitized carbon phase (red), the shell phase (yellow), and the two core phases I/II (green/blue) of the same composition but in significantly different bond states. The EELS PCA spectra of those phases and their spatial distributions are shown in **Figure 4. 8 a**, **d**. Those PCA components were validated by comparing them to 50 (summed and normalized) representative experimental spectra (marked by lines with symbols in **Figure S 8**).

Within the sensor layer, the shell region shows a decrease in local N content, while the N content in the core region is constant. The concentration ratio of N/C = 35:55 (at%) in the laser-treated core region is slightly lower than the composition of the adenine-CNFA. Substantial concentrations of oxygen of the order of 5 at% are present, both in the transducer layer as well as the shell of the sensor layer, due to the conversion in an oxygen environment

Furthermore, the sensor layer is amorphous (**Figure 4. 8 b**) and consists of three N-containing phases, which are a shell phase (yellow) and two less transformed core phases I/ II (green/blue) of the same composition but in different bond states.[174] As shown in the spectra of C K edges (**Figure 4. 8 d**), a high degree of sp^2 hybridization of both elements in all phases is confirmed with an increase in the early stage of the transformation from core phase II to I (**Figure 4. 8 a**, blue to green). From the spectroscopic data (**Figure 4. 8 d, Figure S 8**), it can be observed that the graphitized carbon is dominated by C=C bonds, whereas in the two core phases with high N content, it is dominated by C=N bonds. Partial electron transfer from C to N causes the spectral shift by 1.5 eV.[175] Dilution of N makes the shell phase a transition state between the two extremes (spectral superposition) between both C=C and C=N bonds exist.

In contrast, there is generally no shift of the N K ionization edge (cf. energy loss at $1s \rightarrow \pi^*$) because the bond partners of any nitrogen atom are most probably carbon atoms independent of the N content of the respective phase (**Figure 4. 8 d**). The same integral N K intensities of the two core phases I/II reflect the similar composition of the core regions, whereas the reduced N content of the rim phase is evident from the reduced N K signal (with respect to the corresponding C signals of the different phases). However, a systematic change of the shapes of the N as well as C ionization edges from the core phases II to I is observed, i.e., increasing

1s → π*:1s → σ* ratios, indicating the increase of sp^2-bound nitrogen as well as carbon in core phase I.[176] The shell phase exhibits a very similar shape of the N ionization edge and thus similar nitrogen bonding as core phase I.

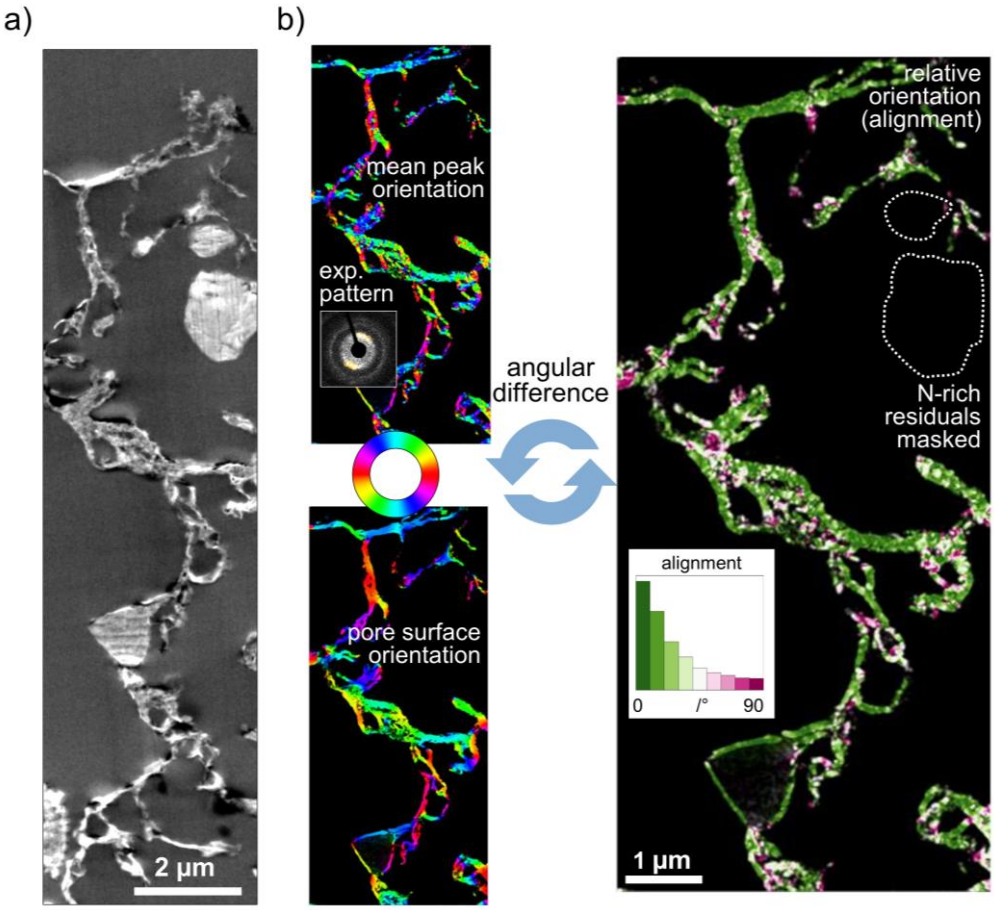

***Figure 4. 9**. a) STEM image of transducer layer; b) Determination of local basal-plane alignment[177] with respect to the respective pore surface (similar region as in a) by comparing the mean peak orientations of (001) Bragg peaks of graphitic carbon for all probed positions (2-fold rotational symmetry applied, exemplary microprobe diffraction pattern depicted) and local orientation of the pore surface calculated from two independent derivatives using a Gaussian kernel with a standard deviation of 8 probe positions (2-fold rotational symmetry applied). Details about the utilized flowline visualization are found in Ref.*[178]

Within the transducer layer, high graphitization of the upper layer due to the intense thermal influence of the laser-carbonization, according to the HRTEM (**Figure 4. 8 b**). In more detail, 4D-STEM revealed a strong interplay of local morphology and local crystal structure within the transducer layer. The systematic alignment of the surface-near graphite basal planes parallel to the local pore surfaces is indicated in individual HRTEM micrographs (**Figure S 9**). The representative region of the transducer layer yielded more than 50% of the graphitic material (with (001) excited for evaluation) within only ± 20° misalignment (**Figure 4. 9 b**).

In general, two major aspects have been described that facilitate the adsorption of CO_2 in porous carbon materials, which are CO_2-specific binding sites (nitrogen)[69,179,180] in conjunction with increased surface polarity by ionic groups (oxygen).[179] DFT calculations confirm a strong, energetic interaction between CO_2 and N-containing functional groups, in particular to multi-N-containing species like imidazole units.[181] Laser-treatment of the LP_{O2}-$Ade380_{90}$/$Glu300_{10}$ sensor under O_2 atmosphere enhances its surface polarity by introducing oxygen-containing groups such as C-O and C=O and consequently enhances the response. The specific binding of CO_2, on the other hand, is explained by the presence of pyrrolic N species.[167] For a correlation to the chemical bonding within the optimized sensor, surface X-ray photoelectron spectroscopy (XPS) and global IR spectroscopy.

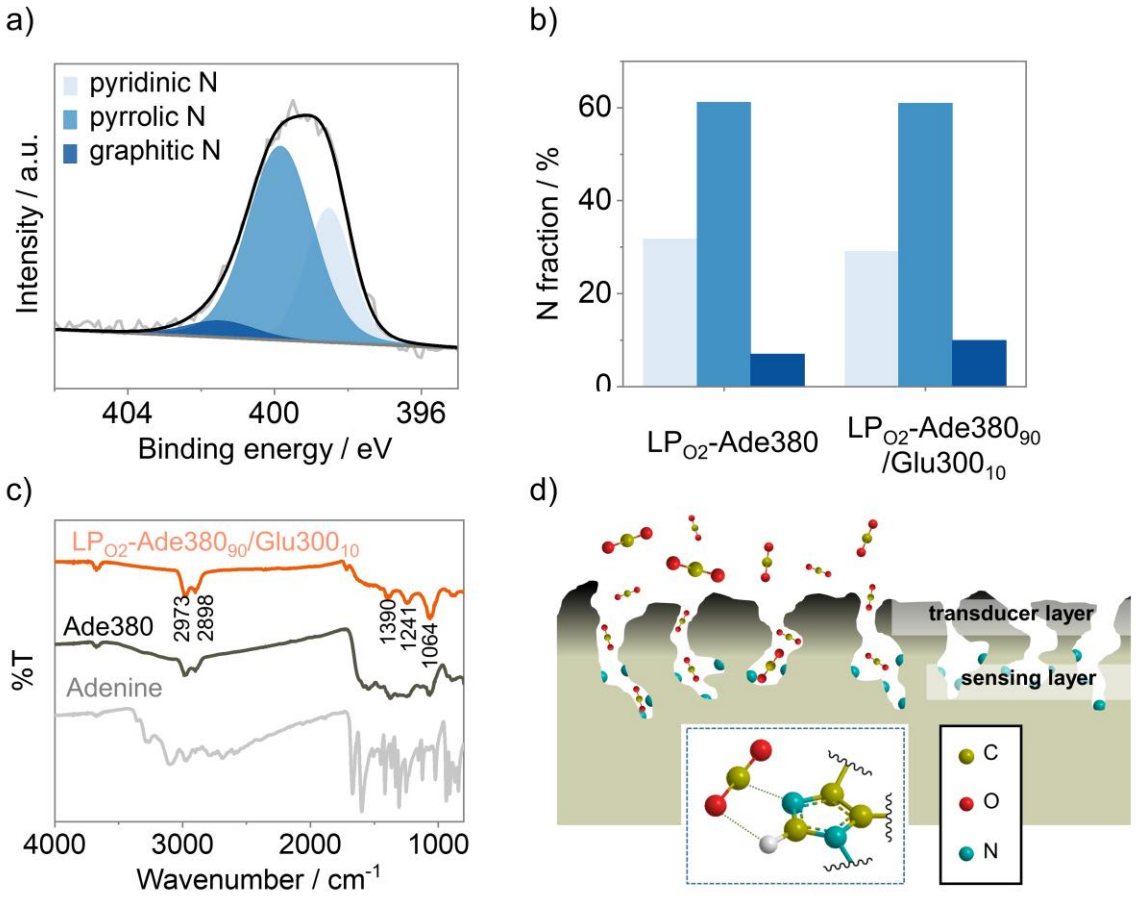

Figure 4. 10 *a) X-ray photoelectron spectrum with the emphasis on the N/1s region of LP_{O2}-$Ade380_{90}$/$Glu300_{10}$ sensor; b) Composition of nitrogen of LP_{O2}-$Ade380_{90}$/$Glu300_{10}$ in comparison to LP_{O2}-Ade380 obtained by XPS; c) Fourier-transform infrared spectrum of adenine, Ade380, and LP_{O2}-$Ade380_{90}$/$Glu300_{10}$; d) Schematic function of sensor.*

XPS confirms a high degree of carbonization and the presence of oxygen and nitrogen-containing functional groups by the prominent sp^2-carbon peak at 284.6 and in the C_{1s} region and signals at 285.4, 286.1, and 287.5 eV assigned to sp^3-carbon, C-N/C-O, and C=N/C=O,

respectively (**Figure S 10**, **Figure S 11**). Oxygen is bound in the form of C=O, C-O (aliphatic), and C-O (aromatic), as evidenced by a set of three peaks at 531.3, 532.4, and 533.6 eV.[182] Most importantly, the N1s area shows a prominent signal at 399.8 eV stemming from pyrrolic/imidazolic N and two minor peaks at 398.5 and 401.5 eV typical for pyridinic and graphitic N, respectively (***Figure 4. 10*** **a**).[183,184] Among the nitrogen functionalities, the pyrrolic/imidazolic species amount to 61%. This composition is independent of the addition of the foaming agent, as it is also observed for the pure LP_{O2}-Ade380 (**Figure 4. 10 b**). In accordance with the EELS bonding analysis, the XPS results support the interpretation of having imidazolic N groups as active sites but should not be interpreted as direct evidence.

Even after laser treatment of the pure adenine-CNFA as well as the optimized sensor, a variety of N functional groups is preserved in the N-containing phases of the lower layer of the LP-NC sensor. These functional groups are detected in the low energy region of the FT-IR spectrum at 1064, 1241, and 1390 cm^{-1} (***Figure 4. 10*** **c**). The latter two most likely originate from C-N stretching vibrations, either graphitic or pyrrolic N.[184,185] The XPS analysis shows a major content of pyrrolic/imidazolic N in the LP-NC films. It has been shown that pyrrolic N decomposes at temperatures >600-800 °C.[74] The cross-sectional analyses of the sensor indicate that the laser-induced reaction temperatures in the sensor layer are lower, and thus a major part of the pyrrolic N is preserved after laser treatment(***Figure 4. 10*** **d**). However, distinguishing different pyrrole/imidazole/graphitic nitrogen functional groups at the nanometer or even atomic scale is challenging because the overall signature of the spectrum has multiple contributions from different atomic configurations.

As a reference, an LP-NC film from cytosine without pyrrolic nitrogen was prepared, which did not show any sensing response (**Figure S 12**). Although laser-treatment of cytosine produces LP-NC films with a high nitrogen content and similar resistivity and morphology,[186] the inherent absence of pyrrolic N in the precursor only generates non-active N-sites. As an additional reference experiment, we prepared laser-carbonized polyimide (well-known as laser-induced graphene (LIG)). Again, no sensing response toward CO_2 was observed (**Figure S 13**). Noteworthy, the influence of the charge carrier properties of the LP-NC on the sensor performance, tested by Hall measurements, is negligible (**Figure S 14**). Only the charge carrier mobility is slightly increased in the sensors produced under oxygen. We assume that the combustion supported by O_2 increases the effective reaction temperature, which leads to a higher degree of graphitization and, thus, a higher charge carrier mobility.

4.5. Sensor performance

For the performance tests, we investigated LP_{O2}-$Ade380_{90}$/$Glu300_{10}$ with a thickness of 100 µm. The response of the LP-NC film ($\Delta R/R_0$) to different concentrations of CO_2 follows a linear trend (**Figure 4. 11 a**), indicating that no saturation is reached at the tested analyte concentrations. At low concentrations of 0.5% CO_2, a reasonable response of $\Delta R/R_0$ = -1.8% is measured. Fitting of the data in Figure 4 yields a sensitivity of S = -1.28×10^{-6} ppm^{-1} is obtained. The response is stable for a series of cycles and is identical in air or N_2 as carrier gas (**Figure 4. 11 b**). The response and recovery time during CO_2 cycling is the same in both environments with t_{res} = 25 s and t_{rec} = 60 s, respectively. This indicates that the presence of O_2 does not influence the detection mechanism. In addition, the optimized film LP_{O2}-$Ade380_{90}$/$Glu300_{10}$ shows a rather low sensing response to the volatile organic compounds (VOCs) acetone and ethanol as interference analytes (**Figure S15**).

The sensing performance of LP_{O2}-$Ade380_{90}$/$Glu300_{10}$ was further tested at different relative humidities (**Figure 4. 11 c**). Naturally, the polar LP-NC surface shows a high affinity to the adsorption of H_2O. Although LP_{O2}-$Ade380_{90}$/$Glu300_{10}$ shows a very strong and fast response to H_2O (up to 50% in RH=100%, **Figure S16**), it is noteworthy that an obvious and stable response to CO_2 at high relative humidities is still detectable (**Figure S17**). For example, in the range of RH = 40-80%, the response increases from $\Delta R/R_0$ = 0.25 to 0.53% (**Figure 4. 11 c)**. This shows that even in high relative humidity, the LP-NC shows a selective response to the adsorption of CO_2.

In order to understand the interaction between LP-NC and water or CO_2, respectively, the heat of adsorption $\Delta_{ads}H^0$ was determined using the van't Hoff equation (Methods section). All fitting parameters are given in **Figure S18-21** and **Table S 3-4**). LP_{O2}-$Ade380_{90}$/$Glu300_{10}$ shows very large $\Delta_{ads}H^0$ values of 34.1 $kJ \cdot mol^{-1}$ for CO_2. Similar values for $\Delta_{ads}H^0$ are commonly observed for the adsorption of CO_2 in porous N-doped carbons.[68] It is interesting to note that the $\Delta_{ads}H^0$ values for the reference LP_{O2}-Ade380 show lower values (namely 21.3 $kJ \cdot mol^{-1}$) (**Figure 4. 11 d**). Apparently, the foaming effect in LP_{O2}-$Ade380_{90}$/$Glu300_{10}$ results in a higher amount of exposed pyrrolic/imidazolic N and, thus, a favorable interaction with CO_2. Notably, the method is not suitable for the determination of $\Delta_{ads}H^0$ values for water.

The sensing properties of LP_{O2}-$Ade380_{90}$/$Glu300_{10}$ are largely retained upon mechanical deformation. First, the change in resistance (ΔR) upon quantitative bending was quantified using a movable electrode stage connected to a four-probe multimeter (**Figure S22**). The

change in resistance upon bending is reversible and is comparable to previously analyzed LP-Cs.[187] In order to simulate the bending of the sensor film on the finger (**Figure S23**), we placed a flexible hose with a diameter of ~6 mm under the sensor film resulting in a curvature of 0.25 mm^{-1} determined by translating the shapes from photographs into x-y data using the freeware Engauge Digitizer. Then the sensor performance in the bent state was analyzed in the gas-sensing cell (**Figure 4. 11 e-f**) (1000 s, 24 cycles). For comparison, the same sensor strip was analyzed in a flat state. Independent of the curvature, a stable response to 10% CO_2 is observed (**Figure 4. 11 f**). In the bent state, the initial resistance of the sensor is ~2240 Ω, which is significantly higher than in the flat state with ~1220 Ω. The response to CO_2 in the bent state is just half as low as in the flat state, averaging about $\Delta R/R_0$ = -2.9%. In addition, the response and recovery times, t_{res} and t_{rec}, remain unchanged. This indicates that the chemical binding sites to CO_2 in the LP-NC remain intact upon bending.

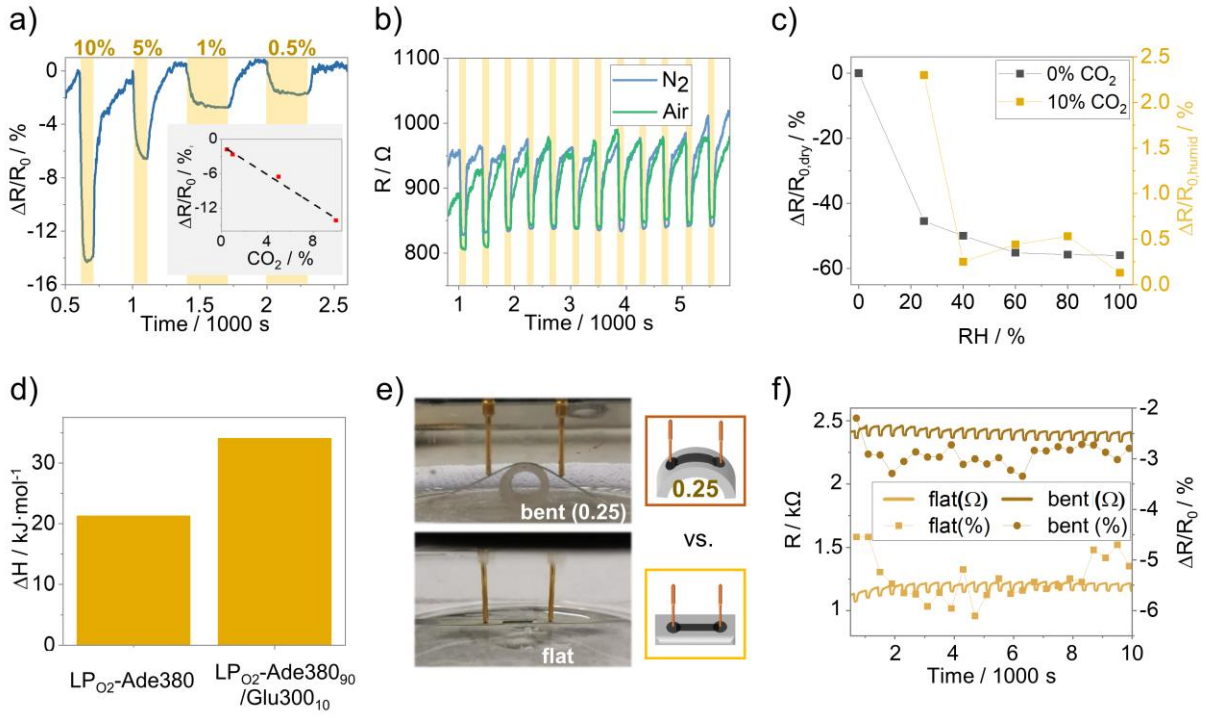

***Figure 4. 11**. Performance of LP_{O2}-$Ade380_{90}$/$Glu300_{10}$ sensor: a) Resistance response toward exposure to different CO_2 concentrations in N_2 as carrier gas; b) Resistance response toward 10% of CO_2 using N_2 (blue) or dry air (green) as carrier gas; C) Resistance response toward different relative humidities in the N_2 carrier gas (black) and to 10% CO_2 (90% N_2) at different humidities (orange); d) Values of $\Delta_{ads}H^0$ for CO_2 on the LP_{O2}-$Ade380_{90}$/$Glu300_{10}$ sensor in comparison to the reference LP_{O2}-Ade380; e) and f) Resistance response of a sensor with a thickness of 75 µm toward 10% of CO_2 upon bending (curvature: 0.25 mm^{-1}) (brown) compared to the flat state (orange) (N_2 carrier gas).*

To demonstrate the applicability in real environments, we used the LP_{O2}-$Ade380_{90}/Glu300_{10}$ sensor strip to measure the CO_2 level in exhaled breath. Portable CO_2 sensor devices are used as a low-cost and rapid assessment of the body's metabolism, providing a basis for early diagnosis of asthma, chronic obstructive pulmonary disease, and others.[188] In most studies, breath-monitoring sensors typically rely on anesthesia masks or special homemade masks to collect exhaled breath making these devices impractical for everyday use.[189,190] The herein-introduced flexible sensor is connected between two electrodes and placed directly in an open environment (**Figure S23**). In view of the rapid response and high sensitivity of LP_{O2}-$Ade380_{90}/Glu300_{10}$ at ambient conditions, it could potentially be used as real-time wearable breath detection sensor that can directly capture the CO_2 concentration.

4.6 Summary

The depth-dependent laser-induced conversion of organic precursor coatings has successfully been utilized to fabricate a complete flexible sensor architecture for selective CO_2 sensing at room temperature. The method exhibits decisive advantages for producing N-doped carbons from adenine as a precursor: the gradual carbonization induces the formation of a crystalline transducer layer but retains the active binding sites in the less impacted, buried sensor layer. By introducing glucose as an efficient foaming agent, the sensitivity is enhanced, as it systematically opens pore channels to access those active species. In turn, the active sites, i.e., imidazolic nitrogen, are preserved in the lower sensor layer. Systematic optimization of the sensor morphology and surface chemistry resulted in a drastic performance increase of almost two orders of magnitude.

The introduced fabrication route, based on mostly abundant organic precursors, is highly versatile as it facilitates the utilization of chemical functionalities of the primary ink by a simple one-step laser writing process. The well-defined morphology and chemical functionality of those sensor architectures may be tailored for other applications by changing/optimizing the vast process parameters, including the selected precursor materials with their specific functionalities, the ink composition, the primary coating thickness, the substrate, the laser-treatment parameters, and the conversion environment. This renders the proposed concept feasible for the application of sensor array technologies in wearable, easy-to-operate, and real-time sensing devices

5. In situ synthesis of molybdenum carbide nanoparticles incorporated into LP-NC

5.1. Introduction

According to the laser-patterning methods shown in the previous chapters, simple modifications with different types of functionalities or nanoparticles can be incorporated into the LP-NC network. As discussed in the background section, a common approach to increase the sensitivity of carbon materials is to integrate Schottky or heterojunctions,[191] for instance, combining carbon nanotubes with Au nanoparticles. These show a response of $\Delta R/R_0 = 4.6$ % to 800 ppm acetone.[192] Other examples are metal carbides and inorganic salts, which can modify the electronic and chemical properties of LP-NC networks to help improve sensitivity to certain analytes.[193]

Metal carbides are well known for their high electronic conductivity, thermal stability, and corrosion resistance.[194] These attributes raise interest in metal carbides as active materials in electronic and catalytic devices.[195–197] Due to their similar band structure to noble metals, metal carbides are often ascribed great potential to replace the former as catalysts.[198,199] Their catalytic activity also makes metal carbides interesting for sensing applications.[193,200–203] However, in pure form, metal carbides suffer from low specific surface areas, which is a drawback for sensing applications. Moreover, due to high hardness, their films tend to crack or delaminate from the substrates.[204]

In particular, molybdenum carbides (Mo_2C or MoC) have been widely studied and are commonly used as electrocatalysts for biomass degradation or water splitting.[198,205] Molybdenum carbides are usually synthesized during pyrolysis in the presence of a carbon source.[198] A great challenge is to increase their specific surface areas by nano-structuring. For example, nanoparticles with sizes between 10 and 30 nm were achieved via the urea glass route.[206] However, the formation of small, high surface-area molybdenum carbide nanoparticles is mostly achieved in conjunction with electronically active support materials, such as metallic or metal oxide supports but also conductive NCs or carbon nitrides.[207–209] In synergy, NCs, and nanocrystalline molybdenum carbides are expected to contribute their full performance towards improved interaction with adsorbates.[210]

In this chapter, MoC_{1-x} nanoparticles incorporated LP-NC synthesized by the laser-patterning process are used as chemiresistors for sensing volatile organic compounds (VOCs). The

specific surface areas of the LP-NC were increased by the addition of sodium iodide (NaI) as an IR-laser transparent porogen. The final LP-NC films were characterized by X-ray powder diffraction, high-resolution scanning, transmission electron microscopy, and energy-dispersive X-ray spectroscopy (EDXS), confirming the formation of the MoC_{1-x}-NC composite. Finally, defined resistive sensing platforms printed on polyethylenetherephthalate (PET) and their performance in sensing VOCs such as acetone, toluene, and hexane at different atmospheric contents were tested. Pure carbon materials usually have no or a rather low room temperature response to non-redox VOCs, such as acetone or alcohol. In composites, positive effects of carbons, such as graphene or carbon nanotubes, added in low percentages are increased conductivity and surface areas.[211–213] We show that carbon with only 13 wt% molybdenum is the active sensing material and outperforms other carbon materials in terms of resistive response.

Term of use: This chapter is adapted with permission from my own original work:

H. Wang, S. Delacroix, A. Zieleniewska, J. Hou, N. V. Tarakina, D. Cruz, I. Lauermann, A. J. Ferguson, J. L. Blackburn, V. Strauss, In Situ Synthesis of Molybdenum Carbide Nanoparticles Incorporated into Laser-Patterned Nitrogen-Doped Carbon for Room Temperature VOC Sensing. *Adv. Funct. Mater.*, 2104061 (2021)

5.2 VOCs sensor production

The process of laser-carbonization and sensor production has been described in chapters 4 and 5. In brief, mixtures of citric acid and urea were pyrolyzed in an oven at 300 °C for 2 hours under a nitrogen flow to obtain a black powder named carbon network forming agents (CNFAs). The CNFA was processed to highly viscous precursor inks (**Figure 5. 1 a**). The standard ink is composed of the CNFA, polyvinylpyrrolidone (PVP) as a film-forming agent (FFA), and ethylene glycol (EG) as a solvent. Additional components, such as porogens (NaI) and functional additives (ammonium heptamolybdate), were added to tune the properties of the final LP-NC. From these inks, films with thicknesses between 15-70 µm were prepared by doctor blading on a PET substrate and evaporating the solvent at 80 °C (**Figure 5. 1 b**). Then, carbonization was achieved by irradiating the films with a mid-infrared CO_2 laser with preset patterns (**Figure 5. 1 c**). After laser treatment, the unexposed precursor film was removed by rinsing with deionized water (**Figure 5. 1 c**). The resulting laser-carbonized structures are referred to as LP-NC films. Finally, the films were used as resistive sensor platforms to detect different VOCs in a gas flow cell (**Figure 5. 1 d**).

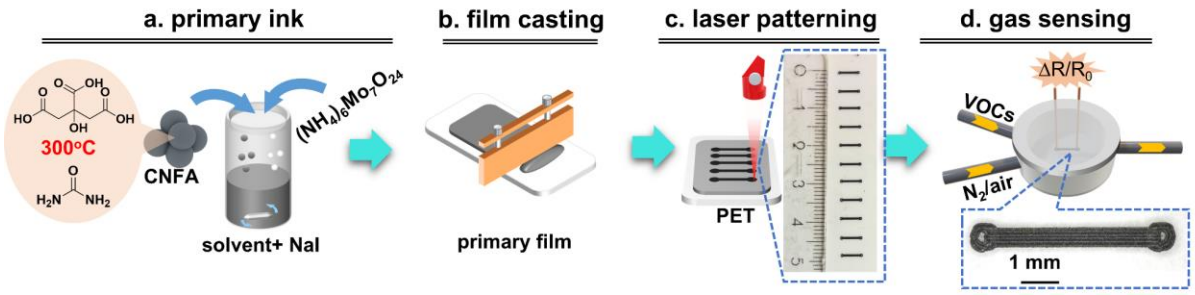

***Figure 5. 1**. Scheme of the sensor production and sensing process: a) primary ink preparation including CNFA, NaI as porogens and metal salt additives; b) film casting by doctor-blading; c) laser pattering process subsequent rinsing with H_2O to obtain the LP-NC sensor films (insert: the photograph of a set of sensor platforms on PET after rinsing with water); d) electro- chemical gas-sensing cell used to characterize the resistive response of the LP-NC sensor films in different environments (insert: optical micrograph showing the dimensions of the sensor-platform used for resistive gas-sensing experiments).*

5.3 LP-NC

The original elemental composition of the CNFA is 47 wt% carbon (C), 19% nitrogen (N), and 31% oxygen (O) as determined by elemental combustion analysis. Upon laser-treatment, the overall composition changes to 68% C, 13% N, and 27% O in the collected powders. (**Table 3. 1, chapter 3**)

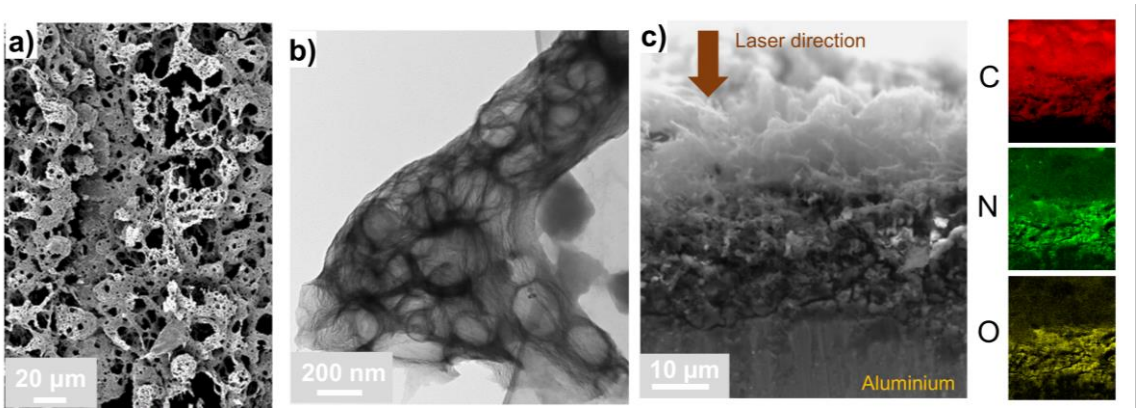

Figure 5. 2 *a) Top-view scanning electron micrograph of LP-NC film on the PET; b) Transmission electron micrograph of a fragment of LP-NC; c) Scanning electron micrograph of an LP-NC film on an aluminum sheet and corresponding EDX maps showing the qualitative carbon, nitrogen, and oxygen distribution across the film.*

The SEM image of LP-NC shows the typical foamy morphology composed of the conductive (nitrogen-doped) carbon network with macro and mesopores (**Figure 5. 2 a**). These pores evolve during the laser treatment upon the sudden release of gases, such as CO or CO_2. The presence of smaller mesopores is also observed by TEM (**Figure 5. 2 b**). Noteworthy, the degree of carbonization follows a gradient from the top to the bottom of the film, as demonstrated in EDX elemental analysis maps of cross-sections of the as-prepared LP-NC films (**Figure 5. 2 c**). Clearly, the top of the film is dominated by carbon, while large amounts of nitrogen and oxygen are detected towards the bottom of the film. On top of the film, the carbon content reaches 92 wt% C (8 wt% O).

For electronic sorption applications, such as sensors, the electrical conductivity and the specific surface areas (SSA) are pivotal factors. To tune the SSA and, thus, the sorption sensitivity of the sensor platforms, IR-transparent salts (alkali halides) were added as porogens. Among the typical IR-transparent salts, NaI shows the highest solubility in ethylene glycol, the solvent for the precursor ink. In this study, we focused on NaI only because the solubility of other salts in ethylene glycol, such as NaCl, KCl, NaBr, and KBr, is too low to reach porogenic activity. Its high solubility in water is also beneficial for the rinsing step after laser treatment. Different amounts of NaI (10-50 wt% with respect to the CNFA) were added to the precursor inks, and

their impact on the formation and properties of the LP-NC films were tested. The products are named LP-NC(NaI10-40) Larger amounts of NaI (> 40 wt%) result in the delamination of the films. Upon drying, a homogeneous precursor film is formed (**Figure 5. 3 a**). As demonstrated by the EDX maps in **Figure 5. 3 b**, the NaI is uniformly blended into the CNFA film and does not separate or form micro-crystallites. The distributed IR-transparent salt within the film transmits the laser energy and allows effective carbonization of the surrounding CNFA (**Figure 5. 3 c**). After laser treatment, the films show a uniform porous morphology similar to the reference LP-NC. The SEM analysis does not reveal major differences (**Figure 5. 3d**). A representative TEM image is in **Figure 5. 3 e** shows a strong resemblance to the reference LP-NC with bubble-like pores caused by the aforementioned laser-induced release of evaporating CNFA.

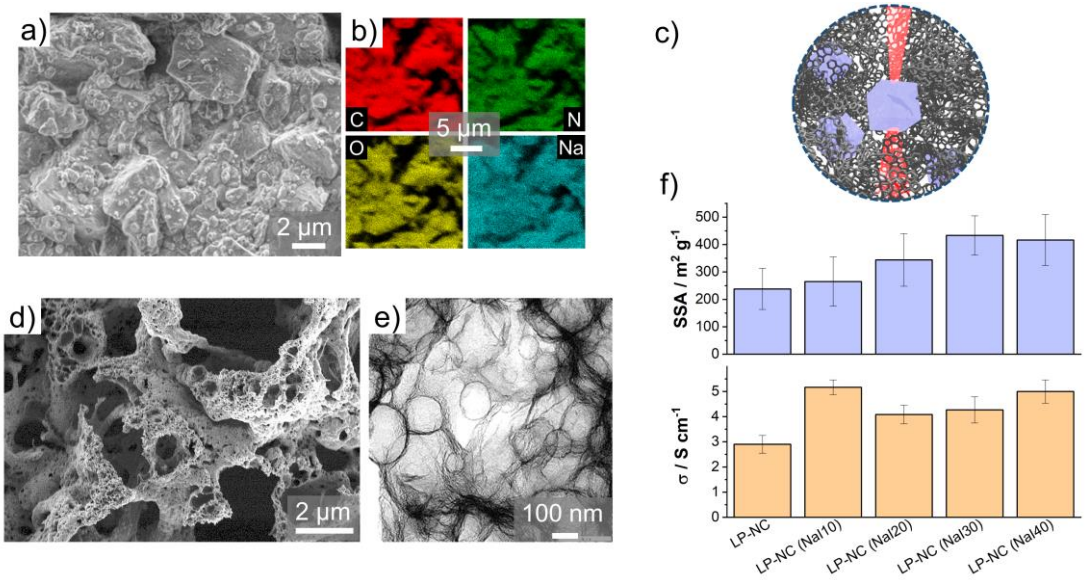

***Figure 5. 3**. a) Scanning electron micrograph of the CNFA film containing 40 wt% NaI and b) corresponding EDX maps; c) Illustration of the alkali halide salt embedded in the primary film consists of CNFA and transmittance for CO_2 laser radiation; d) Scanning electron micrograph of LP-NC(NaI40); e) Transmission electron micrograph of LP-NC(NaI40); f) upper: dependence of specific surface area on the amount of NaI added to the CNFA film; lower: dependence of sheet conductivity on the amount of NaI added to the CNFA film.*

In order to determine the SSAs of the LP-NC(NaI) films quantitatively, the methylene blue (MB) adsorption method was chosen, which is suitable for small quantities (< 1 mg) of carbonaceous samples. Noteworthy, the MB adsorption method typically gives lower SSA values for nitrogen-doped carbons, meaning that the absolute values can be treated as a lower limit for the true SSA. For comparison, a list with other carbon and nitrogen-doped carbon materials is given in **Table S 5**. The SSAs of the LP-NC were increased from ~238 to ~433 $m^2 \cdot g^{-1}$ upon adding 30-40 wt% NaI to the precursor ink (**Figure 5. 3 f**). This range is

similar to the range found for laser-induced graphene from polyimides (~340 m^2 g^{-1}).[91] The increased SSA by a factor of two and the largely unchanged morphological features of the LP-NC upon the addition of NaI into the precursor ink confirms its hypothesized role as a porogen. After laser treatment, the remaining NaI is removed by thorough rinsing of the film with H_2O, which is confirmed by EDX analysis of the final films (**Figure S 24**).

An electronic statistical analysis of 50 samples of the resulting LP-NC(NaI) films shows that the conductivity is generally higher when NaI is added (**Figure 5. 3 f**). Addition of 10 wt% NaI results in an increase from 2.8 to 5.2 S cm^{-1}. While higher amounts (20-40 wt%) cause a drop in conductivity, the conductivity remains above the reference sample without NaI. The addition of salt to the ink supports a better dispersion of the negatively charged CNFA particles due to the Debye-Hückel arrangement in a concentrated electrolyte solution. The Debye length is shortened, resulting in an improved dispersion. At concentrations > 20 wt%, the effect of NaI as a porogen from NaI crystallites sets in. LP-NC(NaI40) exhibits a positive Hall coefficient of RH = +0.19 cm^3 C^{-1} indicating an intrinsic p-type semiconducting behavior that is commonly observed for carbonaceous samples carrying oxygen functionalities on their surface.[214,215] Notably, as shown in **Table S 6**, the charge carrier mobility obtained from the Hall measurements of 0.23 cm^2 $(V\ s)^{-1}$ for LP-NC(NaI40) is higher than the reference LP-NC (0.12 cm^2 $(V\ s)^{-1}$), which is in line with the increased SSA and thus a larger conjugated surface.

Therefore, the presence of an IR-laser transparent salt in the precursor films supports the penetration of the laser energy into deeper layers of the precursor film (**Figure 5. 3 c**). Subsequently, larger amounts of material are carbonized and contribute to the overall conductivity. The higher value for only 10% NaI may be attributed to a lower porogenic activity at such low concentrations and a better percolation of the carbon network. 40 wt% of NaI appears to be the best compromise to maximize the porosity, the electronic conductivity and to conserve a good mechanical stability, i.e., avoiding delamination or cracking.

5.4 LP-MoC_{1-x}@NC

In order to increase the sensitivity towards different volatile organic compounds (VOCs), the LP-NC was impregnated with MoC_{1-x} nanoparticles. To this end, a molecular molybdenum precursor was added to the ink in addition to the CNFA, the FFA, and the porogen NaI. A negatively charged complex, ammonium heptamolybdate (AHM), was chosen to avoid flocculation in the precursor ink since the CNFA, CA/U(300), has a negative ζ-potential of -53 mV.[216] Rapid heating in the laser spot initiates the AHM decomposition and the nucleation of molybdenum carbide (MoC_{1-x}) nanoparticles.

First, we tested the influence of the AHM content on the electronic properties of the final laser-patterned films, denoted as LP-MoC_{1-x}(wt%)@NC (**Figure 5. 4 a**). The addition of 1 wt% AHM with respect to the mass of CNFA results in a drop in conductivity from 2.9 to 1.0 S cm^{-1}. Higher amounts of AHM, 5 or 10 wt%, cause the conductivity to increase again to 2.2 or 3.2 S cm^{-1}. The films containing 20 wt% appear brittle and crack easily, resulting in low conductivity and very high errors. The SSA remains largely unchanged (**Figure 5. 4 b**).

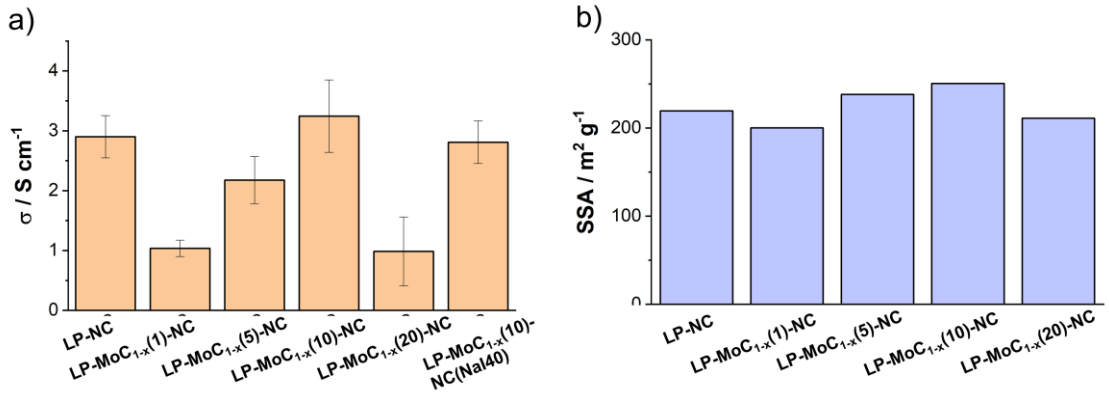

***Figure 5. 4**. a) Electrical sheet conductivity of LP-MoC_{1-x}@NC with different amounts of AHM in the inks; b) Specific surface areas of LP-MoC_{1-x}@NCs obtained with different amounts of AHM in the inks.*

The MoC_{1-x} nanoparticle impregnated LP-NC produced with 10 wt% of AHM in the precursor ink, referred to as LP-MoC1-x(10)@NC, was intensively characterized, as 10% of AHM appears to be the optimum content to preserve the mechanical stability and maximize the electronic conductivity. To determine the molybdenum content, the sample was analyzed by inductively coupled plasma mass spectrometry (ICP-MS). After laser treatment, the overall Mo content is 12.9 wt% in LP-MoC_{1-x}(10)@NC. The higher Mo content in comparison to the precursor ink (4.28 wt%) shows that the CNFA evaporates more than the Mo precursor (AHM) during the laser-carbonization. The overall foamy morphology of the LP-MoC_{1-x}(10)@NC films is, in principle, the same as for LP-NC (**Figure 5. 5 a**). In addition, the macroscopic

features, such as thickness and appearance, are not altered. The size range of the MoC_{1-x} nanoparticles, as observed in the TEM images in **Figure 5. 5 c,** is between 2 and 20 nanometers (**Figure S 25**).

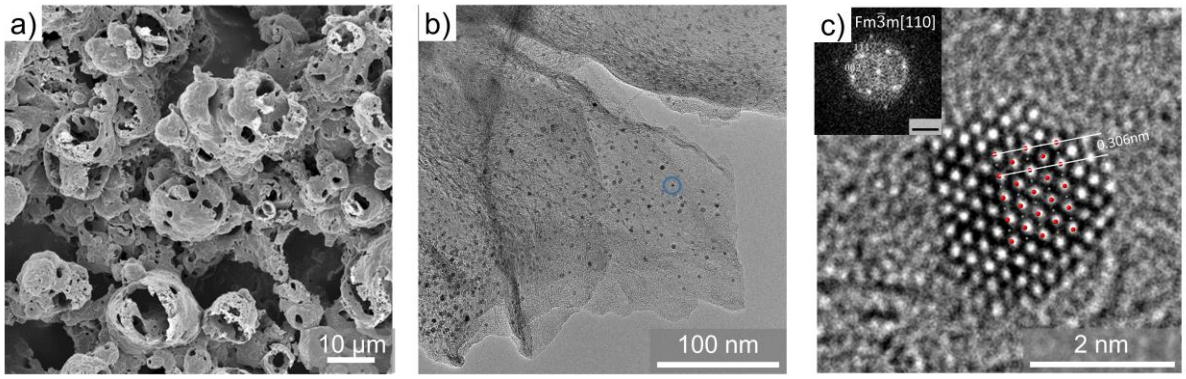

Figure 5. 5*. a) top-view SEM of LP-MoC_{1-x}(10)@NC; b) TEM of LP-MoC_{1-x}(10)@NC; c) HR-TEM of the particle indicated by the blue circle in (C). The inset in (D) shows the corresponding fast Fourier transform indexed in a cubic unit cell, sp.gr. $Fm\bar{3}m$. The scale bar is 5 nm^{-1}. The overlapping atoms demonstrate the locations of Mo (red) and C (grey) in the crystal.*

Fast Fourier transformed HRTEM images of the particles can be indexed in the cubic lattice with the unit cell parameter a = 4.15(4)Å, sp. gr. $Fm\bar{3}m$, and can be described with the NaCl-structure type typical for MoC_{1-x} solid solution (**Figure 5. 5 b, c**).[217] Furthermore, the EDX spectra and the STEM-EDXS maps (**Figure 5. 6**) of the LP-MoC_{1-x}(10)@NC sample show the presence of Mo, C, N, and O. However, signals of N and O are only visible on the spectra obtained from the carbon network, confirming the formation of molybdenum carbide particles.

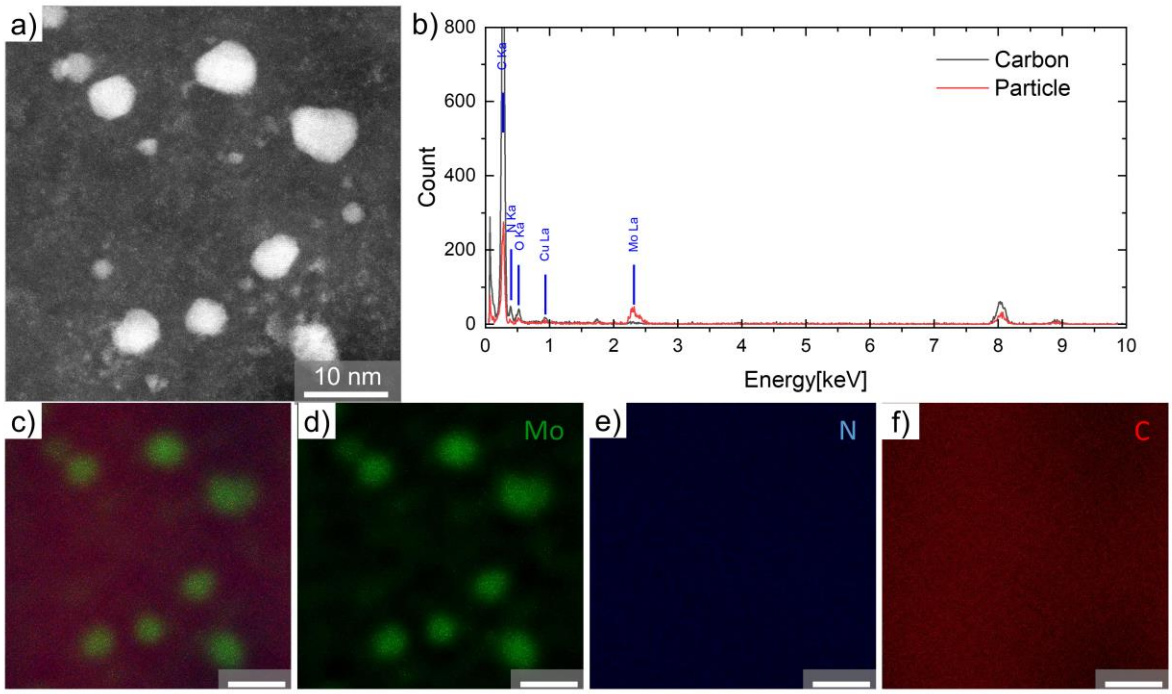

***Figure 5. 6**. a) ADF-STEM image of LP-MoC$_{1-x}$@NC(NaI40); b) EDX spectrum of the carbon substrate (grey) and the particle (red) regions in (a). c) The overlap of elemental mapping over the region (a). Elemental mapping of (d) Mo (green), (e) N (blue), and (f) C (red). The scale bar is 10 nm.*

As shown in **Figure 5. 7 a,** The XRD pattern of LP-MoC$_{1-x}$(10)@NC shows the presence of a graphitic peak at 27 °2θ, similar to that found for LP-NC, while all other peaks can be attributed to cubic MoC$_{1-x}$ with the unit cell parameter a = 4.253(5)Å.[218] Variations in the unit cell parameter obtained from FFT and the XRD data can be explained by both much lower accuracy of the lattice space determination of the HRTEM-FFT analysis and much lower statistics than in the case of XRD.

The Mo3d XPS core level spectrum is in **Figure 5. 7 b** shows the presence of Mo in the oxidation states Mo^0, Mo^{3+}, Mo^{4+}, and Mo^{6+}. The most prominent are Mo^0 at 228.1 (3d$_{5/2}$) and 231.3 eV (3d$_{3/2}$) and Mo^{6+} at 232.3 (3d$_{5/2}$) and 235.5 eV (3d$_{3/2}$). Minor signals at 228.8 (3d$_{5/2}$) and 232.4 eV(3d$_{3/2}$) and 229.7 (3d$_{5/2}$) and 233.4 eV (3d$_{3/2}$) are attributed to Mo^{3+} and Mo^{4+}, respectively. This oxidation pattern, especially the presence of Mo^0, is typical for MoC$_{1-x}$ or MoC.[219] The fitting data of the C1s, N1s, and O1s regions are presented in **Figure S 26**.

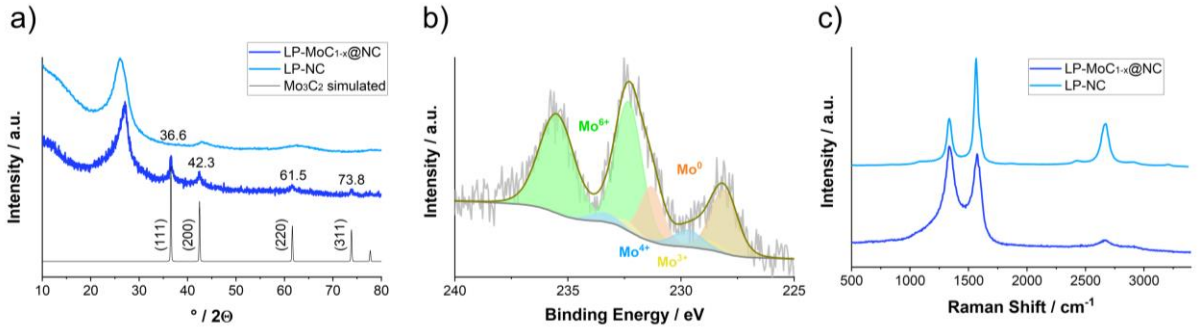

Figure 5. 7*. a) XRD patterns of LP-NC and LP-MoC$_{1-x}$(10)@NC, respectively, and the simulated pattern of Mo$_3$C$_2$; b) XPS spectra of the Mo$_{3d}$ core level of LP-MoC1−x(10)@NC; c) Raman spectra of LP-NC and LP-MoC$_{1-x}$(10)@NC.*

The Raman spectrum of LP-NC shows common features of a turbostratic graphitic material showing D, G, and G' vibration bands localized at 1335, 1573, and 2664 cm^{-1}, respectively. The pronounced D band indicates the presence of significant amounts of graphitic defects, such as sp^3-carbon, heteroatoms, or vacancies. The D-band of LP-MoC$_{1-x}$(10)@NC is much broader than LP-NC, which indicates the sp^2-defects in LP-MoC$_{1-x}$(10)@NC are significantly increased. The low density of the 2D band of LP-MoC$_{1-x}$(10)@NC shows the low degree of stacking of graphitized domains and carbon in the amorphous state.[25] Therefore, we infer a lower degree of stacking due to the presence of MoC$_{1-x}$ nanoparticles and a higher number of defects. From these observations, we deduce that the MoC$_{1-x}$ nanoparticles are not only grown on the surface but also incorporated into the LP-NC network. The size distribution of the MoC$_{1-x}$ nanoparticles is not affected by the presence of NaI during the laser-induced reaction (**Figure S 27**). As shown in the cross-sectional EDX maps of 70 µm thick LP-MoC$_{1-x}$(10)@NC(NaI40) films, the MoC$_{1-x}$ nanoparticles are uniformly distributed across the film (**Figure S 28**).

The formation of MoC$_{1-x}$ nanoparticles occurs *in situ* during laser-induced carbonization. A commonly accepted mechanism is the reduction of transient molybdenum clusters to molybdenum carbides by carbothermal reduction.[220] High carbon content and high temperatures (>1500 °C) in the laser spot facilitate the formation of MoC$_{1-x}$.[221] The presence of nanometer-sized graphitic domains surrounding the MoC$_{1-x}$ nanoparticles is confirmed by high-resolution STEM images shown in **Figure S 29**. The meso/macroscopic morphology of the LP-MoC$_{1-x}$(10)@NC is not significantly affected by the presence of AHM in the precursor ink. However, the electronic properties (i.e., electrical conductivity) are impaired, with the decreased conductivity upon adding small amounts of AHM (<10 wt%) consistent with perturbation due to the increased number of defects in the LP-NC network. Larger amounts of AHM support the nucleation of metallic MoC$_{1-x}$ nanoparticles, which contribute positively to

the overall conductivity. Hall measurements yielded a positive coefficient also for LP-MoC_{1-x}(10)@NC of R_H = +0.32 $cm^3 \cdot C^{-1}$. The charge carrier density is slightly lower with 1.96 × 10^{19} cm^{-3} than the LP-NC sample, while the charge carrier mobility is higher with 1.42 $cm^2 \cdot (V \cdot s)^{-1}$ (**Table S 6**). These electronic properties are affected by the addition of NaI. The Hall coefficient, R_H = +2.67 $cm^3 \cdot C^{-1}$, is significantly higher than LP-MoC_{1-x}@NC due to a three-fold increase in charge carrier mobility to 4.35 $cm^2 \cdot (V \cdot s)^{-1}$ and lower charge carrier density of 2.34 × 10^{18} cm^{-3}.

5.5 VOCs sensing

Finally, we tested films of the optimized materials, LP-NC(NaI40), LP-MoC_{1-x}(10)@NC, and LP-MoC_{1-x}(10)@NC(Na40)**,** as sensor platforms for resistive sensing of VOCs. A standard sensor pattern is made of five parallel laser lines of 5 mm in length distributed across a width of ca. 0.5 mm (**Figure 5. 1 d**). This simple geometry allows for the direct comparison of the properties of materials, while geometric effects are neglected. For each measurement, a sensor platform was placed into a gas-flow-cell and the two ends of the sensor platform were connected by electrodes to measure the impedance in a four-probe arrangement. The gas composition in the cell is controlled by two mass flow controllers connected in parallel, one for the analyte gas and the other for the carrier gas (N_2 or air) atmosphere (**Figure 5. 1 d**). Here, acetone was chosen as the primary target gas.

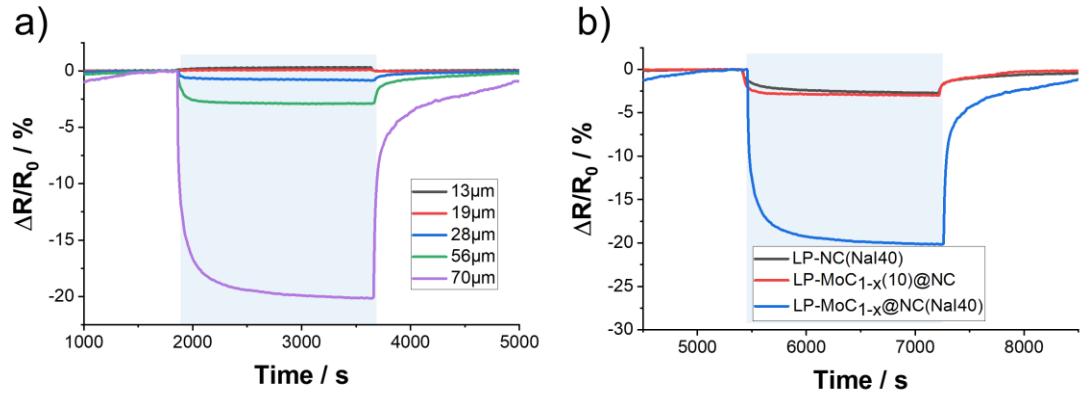

***Figure 5. 8**. a) Resistive response of LP-MoC_{1-x}@NC(NaI40) films of different thicknesses ranging between 13 and 70 µm upon exposure to 2.5% acetone; b) Response of the sensor materials LP-NC(NaI40), LP-MoC_{1-x}(10)@NC, and LP-MoC_{1-x}(10)@NC(NaI40) upon exposure to 2.5% acetone.*

First, we tested the effect of film thickness on acetone sensitivity, using the LP-MoC_{1-x}(10)@NC sensor as a representative platform (**Figure 5. 8 a**). The best results for this sensor were achieved with a thickness of 70 µm, so we utilized this thickness range for additional tests. Thicker films tend to delaminate during the rinsing step. Notably, for films thinner than

19 µm, a weakly positive response, i.e., an increase of resistivity upon exposure to acetone, is detected, which is attributed to a lower degree of graphitization and higher defect density in the laser-patterned carbon.

The resistivity response of LP-NC(NaI40) upon exposure to 2.5% acetone is $\Delta R/R_0$ = 2.7%, and a similar value of $\Delta R/R_0$ = 3.0% is detected for the non-porogen-containing LP-MoC_{1-x}(10)@NC. In LP-MoC_{1-x}(10)@NC(NaI40), the response is drastically increased by more than a factor of six giving $\Delta R/R_0$ = 20.2% for 2.5% acetone (**Figure 5. 8 b**). The response depends on the analyte concentration, as shown in **Figure 5. 9 a,** and a reasonable response of $\Delta R/R_0$ = 3.7% at relatively low analyte concentrations of 1250 ppm acetone is detected.

As shown in the previous study (**Chapter 3**), the surface of LP-NC by using citric acid and urea as molecular precursors, is largely oxygenated. Such oxygen-containing functional groups cause the surface to be preferentially susceptible to polar analytes, which is supported by the data shown in **Figure 5. 9 b**. The response towards polar acetone is significantly higher than to non-polar analytes such as hexane or toluene. The higher response to toluene in contrast to hexane is likely due to their attractive π-π interactions with π-conjugated domains on the surface of LP-MoC_{1-x}@NC(NaI40)**.**

The typical sensing mechanism for acetone with semiconductor materials like metal oxides or graphene composites is proposed to stem from the interaction with ionosorbed oxygen.[222] Before any sensor experiments, in the initial state, oxygen from the atmosphere is adsorbed and reduced to oxygen anions like O_2^-, O^-, or O^{2-} on the semiconductor surface, resulting in a decrease of the electron density in the composite material. In the presence of acetone, these oxygen anions react to form CO_2 resulting in an increase in the electronic density of the semiconductor.[223–225] However, this mechanism requires the supply of oxygen during operation and high operating temperatures. In our experiments, we used either nitrogen or dry air as carrier gases (**Figure 5. 9 c**). The response in terms of resistivity change in both media is the same. Moreover, the response time and the recovery time during acetone cycling are similar in both carrier gases. This indicates that the presence of O_2 does not influence the sensing behavior, as the effect on the electronic properties during acetone exposure is negligible. Therefore, we conclude that the change in resistance is dominated by electronic sensitization effects rather than chemical, i.e. physisorption of gaseous acetone onto the surface of the LP-MoC_{1-x}(10)@NC(NaI40) and the subsequent modulation of the depletion regions.[226]

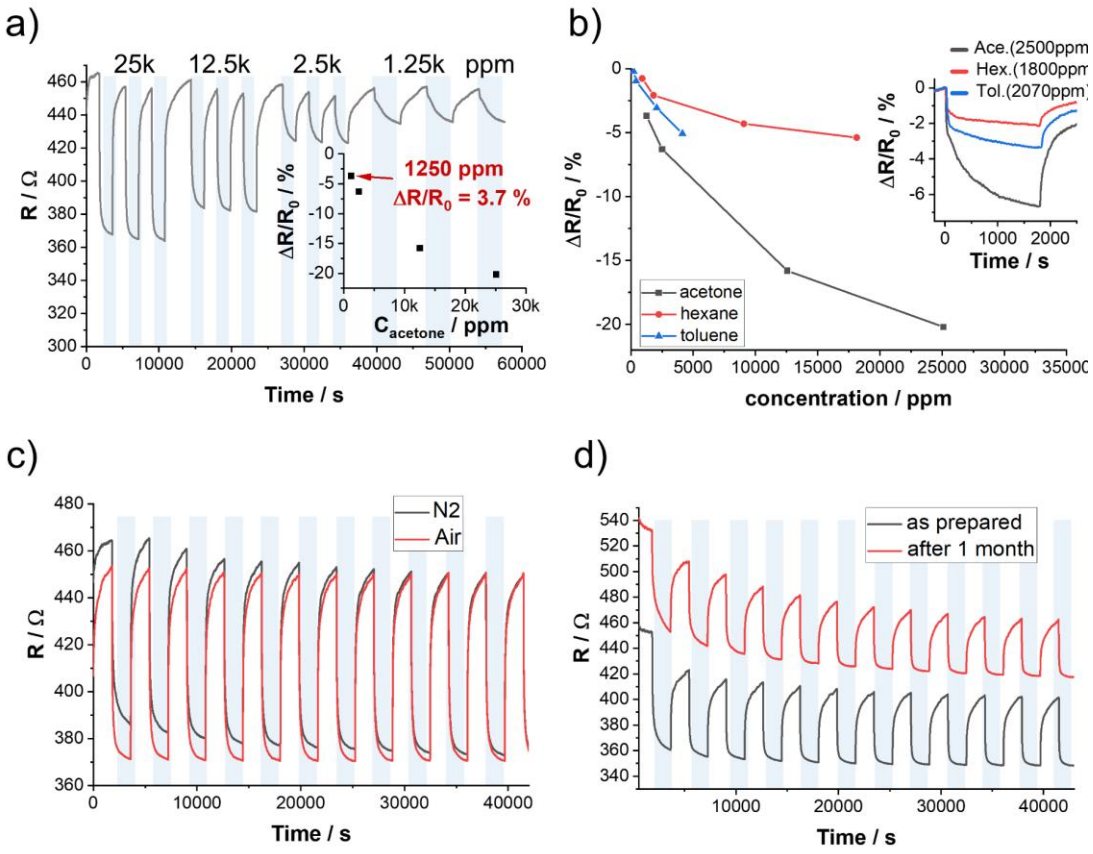

Figure 5. 9. *a) Resistive response of LP-MoC$_{1-x}$(10)@NC(NaI40) towards exposure to different concentrations of acetone; b) Comparison of the resistive response of LP-MoC$_{1-x}$(10)@NC(NaI40) towards different concentrations of acetone (black), hexane (red), and toluene (blue); c) Resistive response of LP-MoC$_{1-x}$(10)@NC(NaI40) after 1 month in comparison to a freshly prepared sensor platform; d) Resistive response of LP- LP-MoC$_{1-x}$(10)@NC(NaI40) towards 2.5% of acetone using N_2 (black) or dry air (red) as carrier gas.*

In the end, we tested the long-term stability of the sensor platforms. To this end, the sensor platform was stored under ambient conditions for one month and tested under the same conditions for sensing acetone (2.5%). With respect to the freshly prepared sample, the aged sample shows a slightly lower response of $\Delta R/R_0 = 15.8\%$ (**Figure 5. 9 d**). The reduced overall conductivity is attributed to a partial oxidation/degradation of the surface groups on the LP-MoC$_{1-x}$@NC(NaI40).

Considering these observations, our laser-patterned composite material shows intriguing performance in room temperature sensing of VOCs. Reliable room temperature sensing of VOCs using simple resistive architectures based on carbon is a challenge due to difficulties in processing and stability. Although many conventional sensing materials like metal oxides show a higher sensitivity at room temperature, their production and processing are rather tedious, requiring deposition on interdigitated gold electrodes.[227,228] In comparison to other carbon and

graphene-based materials, the performance of LP-MoC_{1-x}(10)@NC(NaI40) is competitive.[229–231] For example, multi-walled carbon nanotubes as p-type semiconductors show a response of ~0.4 % to 15 ppm acetone at room temperature.[211] Reduced graphene oxide (rGO) is often used as a conductive sensing platform showing $\Delta R/R_0$ values of ~1 % in response upon exposure to ~500-1000 ppm of different alcohols at room temperature.[212,213]

5.6 Sensing mechanisms

Generally, in carbonaceous materials, the active sites involved in the sensing mechanisms are presumed to be defects in the graphitic structure, such as vacancies or oxygen functional groups.[232] According to elemental analysis, Raman, and XRD, the conductive carbonized part of the LP-NC is composed of highly defective, porous, oxygenated turbostratic carbon. Its defective nature makes the surface rather polar with a high intrinsic binding affinity to polar analytes. In contrast to graphene with a largely unperturbed π-surface, the surface of LP-NC is not expected to be more sensitive with chemisorbed oxygen.

Taking these aspects into consideration the LP-NC sensor material differs from graphene. Due to its intrinsically oxygenated surface, LP-NC acts as a p-type semiconductor,[233] which is confirmed by positive Hall coefficients mentioned above. Upon interaction of the surface defects or functional groups with the analytes the charge carrier density within the LP-NC increases which is reflected in an increase in conductivity.[223]

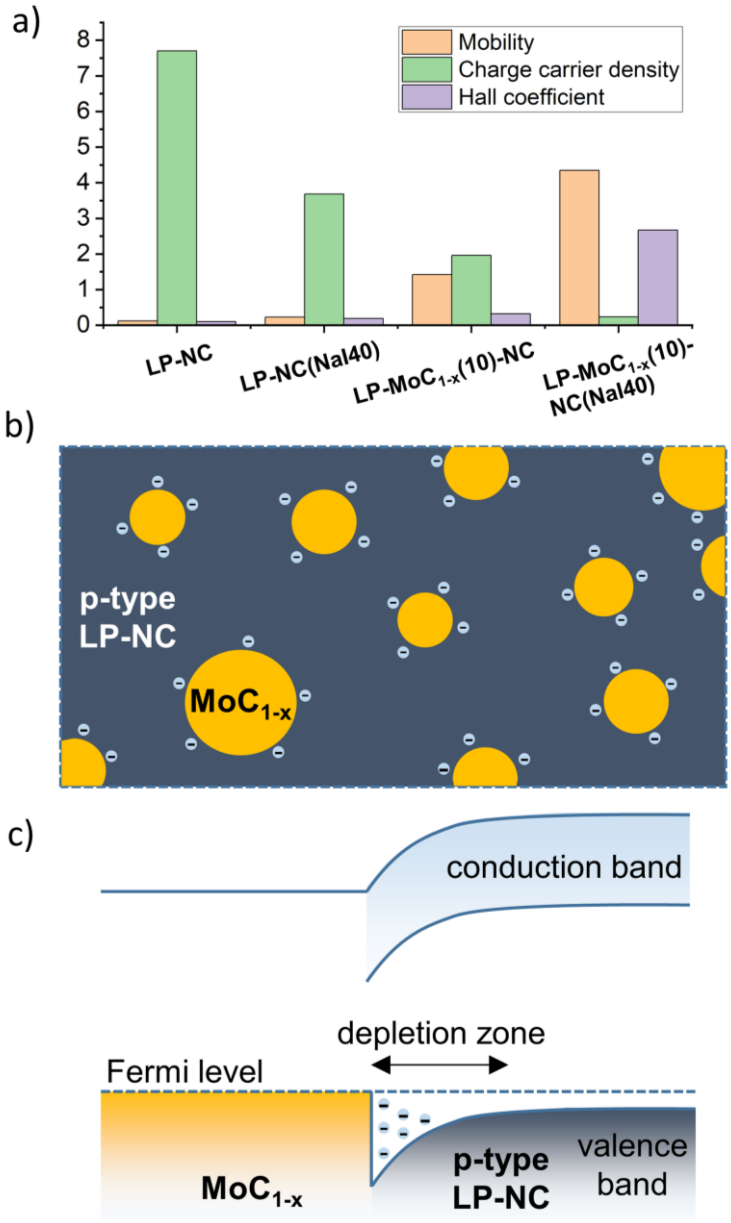

***Figure 5. 10**. a) Comparison of the charge carrier mobilities and densities and Hall coefficients of the four tested samples obtained by Hall measurements; b) Illustration of the charge accumulation by MoC_{1-x} nanoparticles embedded into a conductive p-type LP-NC network; C) Corresponding band-diagram illustrating the depletion zones created around the MoC_{1-x} nanoparticles.*

Here we introduced MoC_{1-x} nanoparticles into the LP-NC, and nanoscale grain boundaries are created between the metallic MoC_{1-x} and the semiconducting LP-NC. These cause the formation of Schottky junctions and thus depletion zones around the nanoparticles **(Figure 5. 10)**. According to the Mott theory, p-type semiconductors form rectifying contacts to metals of work function lower than that of the semiconductor, i.e. $\Phi_M < \Phi_S$ and ohmic contacts for $\Phi_M > \Phi_S$. The work function of MoC_{1-x} solid solution is difficult to determine experimentally. The work functions of metal carbides are highly dependent on the phase, the crystal facet, and

the type of termination. For example, the theoretically determined work functions of MoC or Mo_2C range between 3.4 and 7.5 eV.[234–236] Given the polydisperse nature of MoC_{1-x} incorporated into LP-NC, different facets, and compositions are exposed to the surrounding carbon. LP-NC is best compared with amorphous or poly-crystalline carbons, such as MWCNTs or carbon black. Their work functions are typically ~4.5 ± 0.3 eV.[237–239]

In the present case, the MoC_{1-x} nanoparticles accumulate charge carriers and create doping-sensitive zones. Acetone, as a closed shell molecule, is expected to interact with the LP-NC surface by the formation or enhancement of dipoles on the surface, which induce a charge modulation within the doping-sensitive grain boundaries.[240,241] Therefore, the higher sensing response in LP-MoC_{1-x}(10)@NC(NaI40) is explained by the lower charge carrier density in the overall material and the increased SSA.

This is the first example of a molecule-based laser-patterned resistive carbon sensor based on direct interactions with the target gas and the in-situ incorporation of metal nanoparticles. Synthetically and environmentally, this method displays an advantage over laser-induced graphenes (LIG) from polyimides, which have shown great promise as sensing platforms after post-functionalization with nanoparticles.[120,242–245] Conceptually, they are different in terms of morphology and detection mechanisms. For example, LIGs have shown a high response to different gases versus vacuum as a response to the different thermal conductivities of the respective gases.[114] In other concepts, laser-patterned resistive carbons are used as transducer platforms for functionalization with selective bio-receptors.[132] In our laser-patterned carbons and their nano-composites, we observe several effects simultaneously. On the one hand, we have a highly defective carbon, which allows an intrinsic room-temperature sensitivity towards different target gases. On the other hand, the uniform impregnation of MoC_{1-x} nanoparticles forms overlapping doping-sensitive Schottky junctions. Indeed, it has been shown, for example, that the particle size of certain materials and the subsequent generation of converging Schottky barriers lead to drastic increases in sensitivity.[246–248] Their exact synergetic effects are yet to be explored in future studies on the detailed sensing mechanism.

5.7 Summary

In this study, we demonstrated the applicability of laser patterning for resistive sensing of VOCs. The specific surface area of LP-NCs was increased by adding an infrared laser-transparent alkali metal halide salt (sodium iodide) to the precursor ink. In addition, the laser-induced Schottky junction created at the nanoscale grain boundary between the in situ

generated $MoC_{1-x,}$ and the conductive carbon network further reduces the carrier density, thereby significantly enhancing the sensitivity of the LP-NC film to acetone. Furthermore, the final optimized sensor LP-MoC_{1-x}(10)@NC(NaI40) is stable and reproducible and shows remarkable long-term stability.

Detecting analyte concentrations on the order of parts per billion remains very challenging for our materials. However, using molecular starting materials enables wide possibilities for tuning the compositional and electronic properties of the obtained films: e.g., tuning the graphitization degree, surface area, and pore size. The laser-patterning method, in principle, allows for the simple incorporation of different kinds of nanoparticles to promote sensitivity and selectivity toward different analytes.

6. Tuning the surface properties of porous laser-patterned carbon with ZnO hard-templates

6.1 Introduction

Volatile organic compounds (VOCs) are human-made contaminants in indoor environments as well as indicators for diseases.[249] Instruments for precise VOCs concentration monitoring are in high demand, first for identification and second for preventing diseases.[250,251] Among the conventional methods for gastrointestinal disease diagnosis are colonoscopies, tissue biopsies, or antimicrobial swab cultures.[252] All these techniques present the same drawbacks of being (semi-)invasive, time-consuming, expensive, not scalable, and requiring sophisticated chemical analysis instruments. On the other hand, indoor air quality control (hospitals) is an important analysis, typically conducted by certified large-scale chamber testing facilities (EN 16516).

With the rapid development of artificial intelligence (AI) and machine learning algorithms, small-scale sensor array technologies have again moved into the focus of attention as a tool for the realization of electronic noses.[253,254] Therefore, the mobile non-invasive chemical detection method of VOCs is expected to replace the traditional bulky physical instrument method. It is clear that neither oxide chemical sensors requiring high-temperature operation nor high-cost, high-performance carbon materials are good candidates. In **Chapter 5**, LP-C with tunable electronic properties exhibits very high and fast sensing performance to VOCs. However, the relatively low sensing selectivity is not sufficient for so-called electronic nose applications.

Therefore, in order to increase the selectivity of the LP-C sensor, a specific surface chemical modification is required based on the **Chapter 2** mentioned sensing mechanism of a chemical sensor (**Figure 2. 16**). In particular, the possibility to tune carbon properties by simple modification of the primary ink formulation has been demonstrated in **Chapter 5.**

The work in this chapter will demonstrate a facile method of introducing selective elements into LP-Cs to tune the surface polarity and active surface area of LP-C sensing materials, thereby realizing the selective detection of VOCs. Upon addition of minor amounts of zinc nitrate ($Zn(NO_3)_2$) as a precursor, small ZnO nanoparticles are formed *in situ* during the laser-carbonization. The role of zinc oxide (ZnO) as an intermediary porogen and graphitization agent has already been reported and successfully proven to increase the active surface area of porous carbon.[255–257] The high process temperatures in the upper layers support the direct

evaporation of the Zn formed during the Zn^{2+}→ZnO→Zn driven by the carbothermic reduction. In addition, we observe a variation in the surface relative to the Zn-concentration. The concentration dependent distribution of these graphitized domains and the increased surface area support the selectivity towards different VOCs by differentiating between their polarities. Moreover, direct addition of readily prepared ZnO nanorods as a precursor leads to the formation of larger graphitic domains, supported by Raman spectroscopy, facilitating the preferential detection of non-polar VOCs due to extended π-surfaces.

Term of use: This chapter is adapted with permission from my own original work:

H. Wang, P. Jiménez-Calvo, M. Hepp, M. A. Isaacs, C. Otieno Ogolla, I. Below-Lutz, B. Butz, V. Strauss, Laser-Patterned Porous Carbon/ZnO Nanostructure Composites for Selective Room-Temperature Sensing of Volatile Organic Compounds. *ACS Appl. Nano Mater.* (2023)

6.2. VOCs sensor preparation

Carbon laser patterning was performed according to a previously described protocol with several modifications. Here, the inks were prepared by two different routes, as illustrated in **Figure 6. 1**. In the first route, a citric acid/urea-based carbon network-forming agent (CNFA) was thoroughly mixed with a film-forming agent (FFA) containing solvent (ethylene glycol) and different amounts of $Zn(NO_3)_2$ were added (**Figure 6. 1 a).** The resulting viscous inks were doctor-bladed on PET substrates and dried to obtain films with a mean thickness of *ca.* 40 µm (**Figure 6. 1 b**). The films containing different amounts of $Zn(NO_3)_2$ are referred to as LP-C/Zn(1-8), with the number indicating the mass percentage of Zn with respect to the mass of CNFA (**Table 6. 1**). In the second route, for the composition of primary ink, pre-synthesized ZnO nanorods were added instead of $Zn(NO_3)$. The final laser carbonized sensor films are named LP-C/ZnO(x), with x indicating the mass percentage of Zn in the primary inks.

Resistive patterns in the dimensions of 5 × 0.5 mm were imprinted into the films with a high-precision CO_2 laser engraver. The laser parameters, i.e., scanning speed and power, were optimized to achieve a high degree of carbonization and high reproducibility in terms of conductivity. After laser-patterning, the unexposed precursor film was rinsed off with H_2O. Subsequently, the sensor strips LP-C/Zn(x), and LP-C/ZnO (x) were tested as resistive sensor platforms to detect different VOCs at room temperature in a gas-flow cell (**Figure 6. 1 d**).

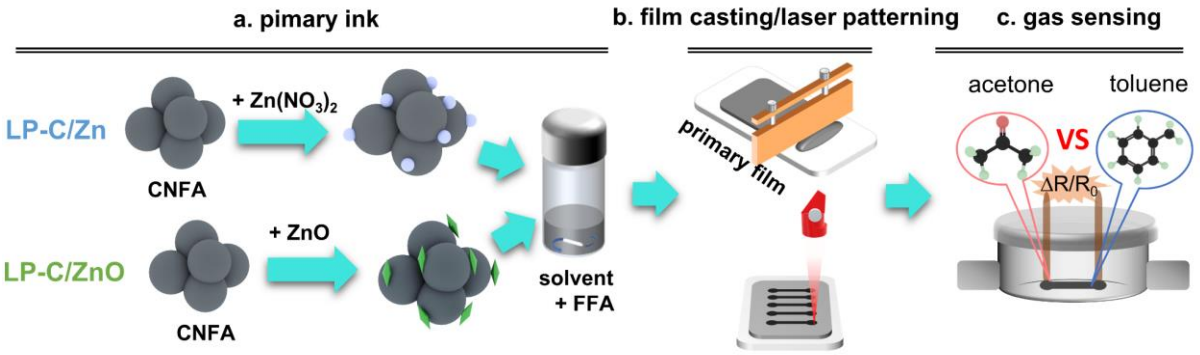

Figure 6. 1*. Illustration of the preparation process of the LP-C/Zn and LP-C/ZnO films and their characterization in a resistive gas sensing setup: a. preparation of primary ink; b. film casting on the flexible PET substrate and carbon laser-patterning of primary film; c. electrochemical gas-sensing cell used to characterize the resistive response of the LP-C sensor platforms in different gases inside the chamber.*

***Table 6. 1**. Composition of the investigated samples.*

sample	CA/U(300)	$Zn(NO_3)_2 \cdot 6\ H_2O$	ZnO nanorods	effective m_{Zn}
	mg	mg	mg	wt%
LP-C/Zn(0)	200	0		0%
LP-C/Zn(1)	200	10		1%
LP-C/Zn(2)	200	20		2%
LP-C/Zn(4)	200	40		4%
LP-C/Zn(5)	200	60		5%
LP-C/Zn(6)	200	80		6%
LP-C/Zn(7)	200	100		7%
LP-C/Zn(8)	200	120		8%
LP-C/ZnO(2)	200		5	2%
LP-C/ZnO(7)	200		20	7%

6.3. LP-C/Zn

The energy dispersive x-ray analysis of the top-view primary films of LP-C/Zn shows a homogeneous distribution of the zinc salt (**Figure S 30**). The topographical scanning electron microscopy (SEM) analyses of the LP-C/Zn films show a spore-like morphology for all zinc-containing samples (**Figure 6. 2**). In contrast, the reference LP-C/Zn(0) is characterized by an open hierarchical porous morphology (**Figure 6. 2**). Notably, the spore-like character of the LP-C/Zn films is more pronounced for higher Zn concentrations.

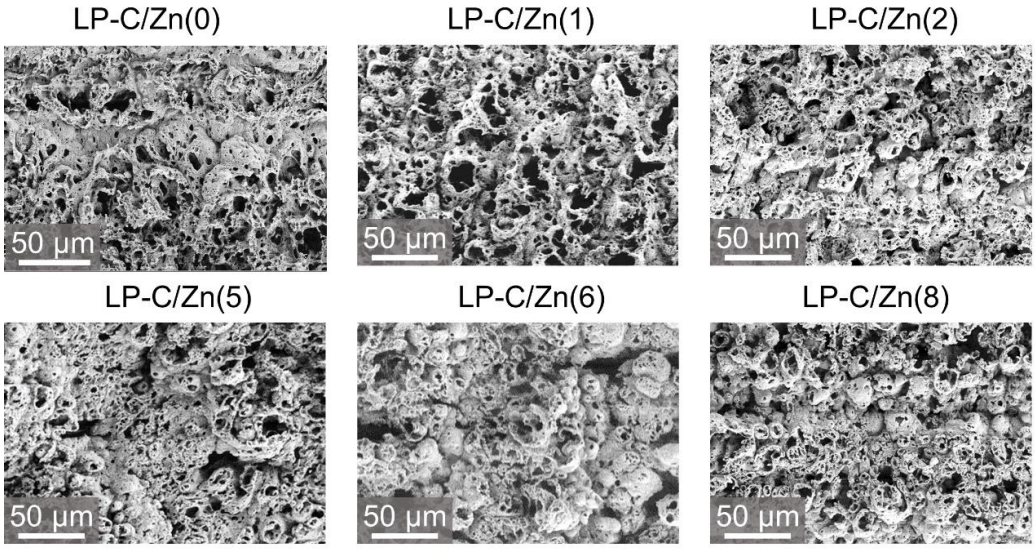

***Figure 6. 2**. Top-view scanning electron micrographs of LP-C/Zn (0), (1), (2), (5), (6), and (8).*

A crucial property of resistive sensors is their conductivity. First, we tested the impact of the addition of the zinc salt on the conductivity of the LP-C/Zn films by measuring the resistances of 30 sensor films of each as-prepared composite. A mean thickness of 40 µm was assumed for

the determination of the sheet conductivity.[187] As shown in **Figure 6. 3 a**, the conductivity drops from 4.6 in reference to 2.5 $S \cdot cm^{-1}$ at 1 wt% Zn (LP-C/Zn(1)). Up to a concentration of 6 wt% Zn (LP-C/Zn(6)), the conductivity is on the same order, while another drop in conductivity to 1.4 $S \cdot cm^{-1}$ is observed at concentrations >7 wt% of Zn. Notably, at concentrations >8 wt%, the films tend to crack upon drying and eventually delaminate during the laser process. Such quasi-linear conductivity trend may be explained by the different factors that influence porous carbon materials: grain boundaries, particle sizes, atomic arrangement, and wettability, among others.[258]

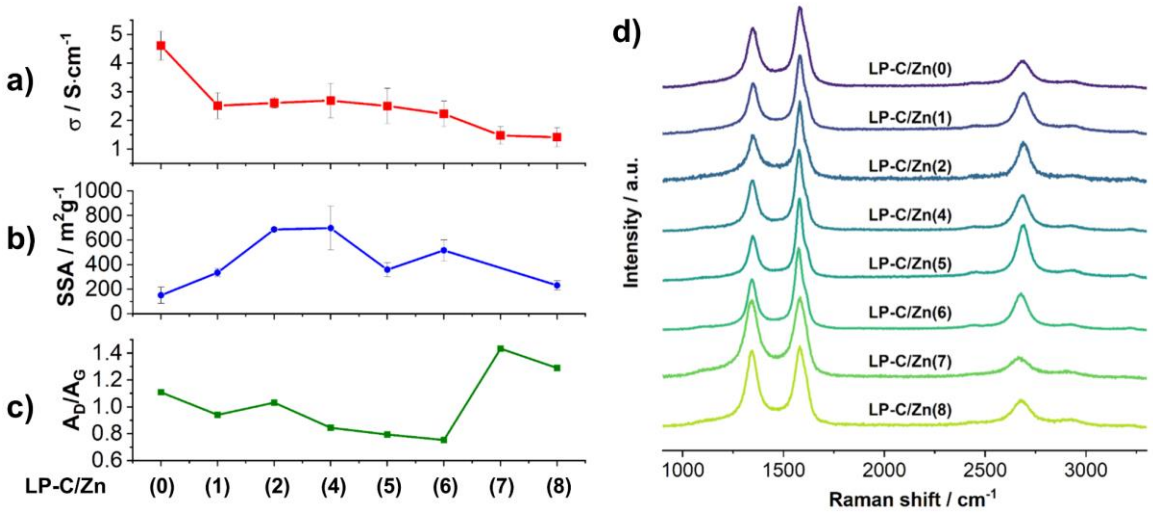

Figure 6. 3. *a) Plot of sheet conductivity and b) specific surface areas determined by the methylene blue adsorption method of the LP-C/Zn films; c) the A_D/A_G (area of the peak) ratio of LP-C/Zn films in the Raman spectra; d) Top-view Raman spectra of the LP-C/Zn films obtained with an excitation wavelength of 532 nm.*

The zinc salt is added with the intention of increasing the specific surface area (SSA) of the LP-C by exploiting the carbothermic reduction of *in situ*-generated ZnO nanoparticles.[259] Due to the low mass density of the films, a characterization of the SSA using quantitative gas sorption techniques is intricate. Therefore, we utilized the methylene blue (MB) adsorption method to obtain insights into the evolution of the SSAs. Noteworthy, the MB adsorption method is a liquid-based method and gives only indications about trends as it typically gives lower SSA values for nitrogen-containing carbons. Moreover, potentially existing micropores are not accessible with this measurement method. However, the trend shows unambiguously higher SSAs upon the addition of zinc salt to the precursor films. The highest value is reached for a concentration of 4 wt% of Zn (LP-C/Zn(4)) with ~700 $m^2 \cdot g^{-1}$ (**Figure 6. 3 b**). For higher zinc concentrations, the SSAs decrease steadily.

Raman spectra of the LP-C/Zn series (**Figure 6. 3 c-d and Figure S 31**) exhibited an interesting top-layer analysis, complementing structural observations and correlated trends. All samples show features of a highly carbonized material with pronounced D- and G-bands at 1348 and 1578 cm^{-1}, respectively. Minor contributions from disordered and amorphous carbon at 1200 and 1470 cm^{-1}, designated as D4 and D3, were also observed and considered in the fittings.[260,261] A clear trend towards high graphitization with lower defect density is observed as the A_D/A_G ratio reduces from 1.1 to 0.75 between LP-C/Zn(0) and LP-C/Zn(6) **(Figure 6. 3 c)**. This is concomitant with a decrease in the peak width of the 2D band at 2670 cm^{-1}, which indicates a higher stacking order of the graphite planes.[25] On the other hand, Raman spectroscopy is a surface-sensitive technique. Due to the porous surface structure of laser-carbonized samples, the overall Raman spectroscopy characterization of PET film samples is challenging.

Based on the structural and chemical gradients observed in the laser carbonized material in Chapter 4, a cross-sectional transmission electron microscopy (TEM) analysis was performed for the best performing sensor film, LP-C/Zn(5). To this end, the porous LP-C/Zn(5) sensor films were infiltrated and embedded in an epoxy resin and cut with a microtome into thin slices of ~50 nm thickness.[187] An optical micrograph of the block face is presented in **Figure 6. 4 a**. Across the entire section, the films show a distinct porosity with visible pore sizes on the order of 5-10 µm, represented in the scanning electron micrograph in **Figure 6. 4 b**.

The area in **Figure 6. 4 b** was further analyzed by energy dispersive X-ray (EDX) analysis to obtain an overview of the chemical composition across the film. As demonstrated in previous studies, due to the direct exposure to the laser beam, the upper layer consists of porous turbostratic graphite with a highly crystalline structure (**Figure 6. 4 c, d, e**), and it is free of Zn.[187] In the lower layers, significant amounts of Zn were detected (**Figure 6. 4 b**). Scanning transmission electron microscopy- electron energy loss spectroscopy (STEM-EELS) further confirmed the clear chemical and structural delineation between the highly graphitized top layer and the Zn/N-containing bottom layer (**Figure 6. 4 c, right**).

As shown in the high-resolution TEM (HRTEM) image and the corresponding selected area electron-detailed diffraction (SAED) pattern, The highly ordered graphitic structure in the upper layer of the sensor and the presence of ZnO in the lower part of the sensor result from the depth-dependent effect of laser pyrolysis (**Figure 6. 4 d, e, f**).

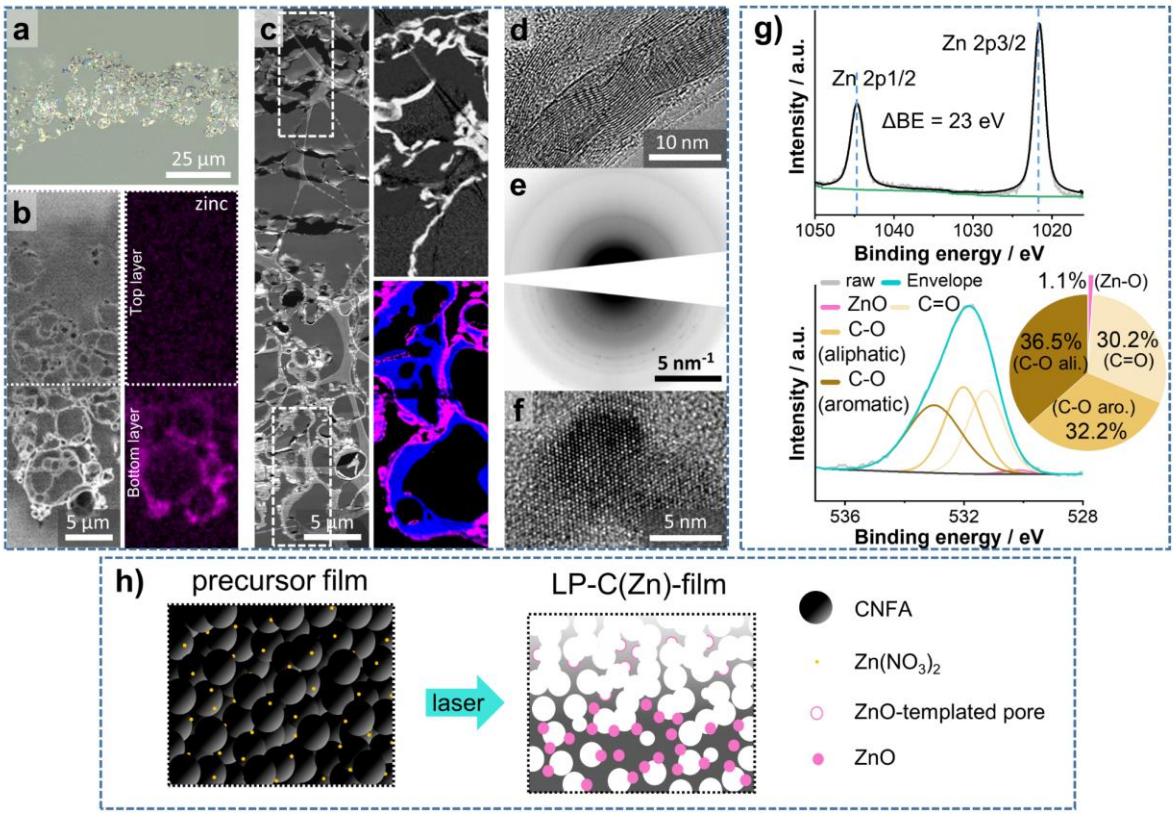

Figure 6. 4 *a) Cross-sectional optical micrograph of* ***LP-C/Zn(5)****; b) Cross-sectional backscatter SEM micrograph with correlated qualitative EDX element map of zinc (net intensities displayed); c) Cross-sectional TEM analyses of the sensor film: (left) representative high-angle annular dark- field (HAADF)-STEM micrograph with uninfiltrated regions (black), epoxy resin (dark grey), and lacey TEM support film (light grey), (top right) Graphitized carbon component in upper layer identified by principle component analysis (PCA), (bottom right) N (blue) and Zn (purple) distribution in bottom layer of sensor; d) Exemplary HRTEM image of graphitized carbon in upper region; e) Combined SAED pattern of graphitic domains in top layer and ZnO in bottom layer (logarithmic display); f) Exemplary HRTEM image of ZnO nanoparticle in lower layer; g) XPS analysis of the LP-C/Zn(5) film surface: XPS Zn 2p region (upper panel) and O 1s region with percentual peak distribution (lower panel); h) Proposed formation mechanism of the LP-C/Zn composite structure. $Zn(NO_3)_2$ is distributed among the CNFA particles in the precursor films. After laser-carbonization, the in situ generated ZnO nanoparticles catalyze the pore formation in the upper layer and remain in the lower layer.*

These observations were corroborated by X-ray photoelectron spectroscopy (XPS) (**Figure S 32, Figure S 33**). In the C_{1s} energy region, the main peak at 284.4 eV is attributed to sp^2-carbon, the other minor peaks at 285.2, 286.0, 287.5, and 289.1 eV correspond to sp^3-carbon, C-N/C-O, C=N/C=O, and COOH, respectively. The N_{1s} region of the laser-carbonized films (LP-C/Zn(x)) was deconvoluted into three individual peaks maximizing at 399.0, 400.0, and 401.4 eV corresponding to pyridinic, pyrrolic, and graphitic nitrogen, respectively. For the primary films C/Zn(x), two additional peaks at 402.8 and 406.4 eV originate from NO_3^- and

NO_2^-,[262]which are attributed to the addition of $Zn(NO_3)_2$ into the primary inks. The vanishing of these peaks confirms the decomposition of $Zn(NO_3)_2$ after laser-patterning.

In the Zn_{2p} region (**Figure 6. 4 g**), the two intense peaks centered at binding energies of 1021.5 and 1044.5 eV are attributed to Zn $2p_{3/2}$ and Zn $2p_{1/2}$. The Zn 2p spectra of Zn oxide suffers from an overlap of Zn metal peaks, which makes it difficult to determine the chemical state of Zn unambiguously.[263,264] Nonetheless, the different binding energy of oxygen in metal oxides compared to organic compounds are reflected in the O_{1s} region[264] and can be used to identify the variety of ZnO surfaces.[265] The O_{1s} signal is deconvoluted into four peaks (**Figure 6. 4 g)**: three major peaks centered at 531.2, 532.1, and 533.0 eV assigned to C=O. C-O(aliphatic) and C-O(aromatic),[182] respectively; along with a 0.8% peak contribution at 530.2 eV assigned to Zn-O.[265]

These results demonstrate the function of nano-sized ZnO as a pore templating agent in the upper layers of the film during laser-carbonization. The ZnO hard-templating effect based on the carbothermic reduction at different temperature stages occurs *in situ* within the time-frame of milliseconds in a one-step process. As **Figure 6. 4 h** shows, the homogeneously distributed zinc salt ($Zn(NO_3)_2$) in the primary films form ZnO nanoparticles upon elevating the reaction temperature during laser-carbonization. When the laser-induced temperature reaches ~ 670 °C the ZnO is reduced to Zn according to the carbothermic reduction mechanism, during which the carbon is oxidized to gaseous monoxide carbon ($CO_{(g)}$).[255] The remaining carbon is rearranged and recrystallized and thus forms highly graphitized domains (**Figure 6. 4 c, d, e**). At temperatures above the boiling point of zinc (907 °C), the liquid zinc evaporates. The high degree of graphitization and the absence of ZnO nanoparticles in the upper layers of the LP-C/Zn film indicate that the reaction temperatures are significantly higher than 907 °C. On the other hand, the presence of considerable amounts of ZnO nanoparticles and the rather amorphous character of the carbon in the lower layers indicates lower reaction temperatures below 670 °C. Due to continuous evaporation of the carbonaceous matrix in the lower layer under those conditions, surface enrichment as well as the ripening of the ZnO, occurs (**Figure 6. 4 c**).

6.4 LP-C/ZnO

For the LP-C/ZnO sensor films prepared with pre-synthesized ZnO nanorods as a precursor (**Figure 6. 1 a**), The rhombus-like ZnO nanorods with the average size of ~2 μm were randomly

distributed in the primary film and undergo the same *in situ* carbothermic reduction process during laser patterning (**Figure 6. 5 a, b**).

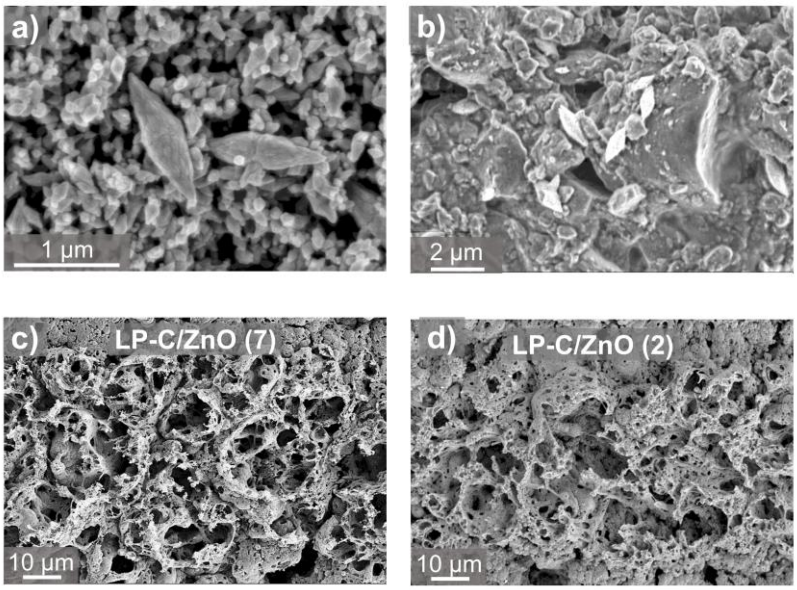

Figure 6. 5. *a) SEM of ZnO nanorods and b) top-view SEM of primary film of LP-C/ZnO(2); c) top-view SEM of LP-C/ZnO(7) and d) LP-C/ZnO(2) films.*

Due to their significantly larger size, the ZnO nanorods are expected to support the formation of larger graphitic domains in the upper layers of the LP-C films. Indeed, the SEM images show an open porous but non-sporulated morphology (**Figure 6. 5 c, d**).

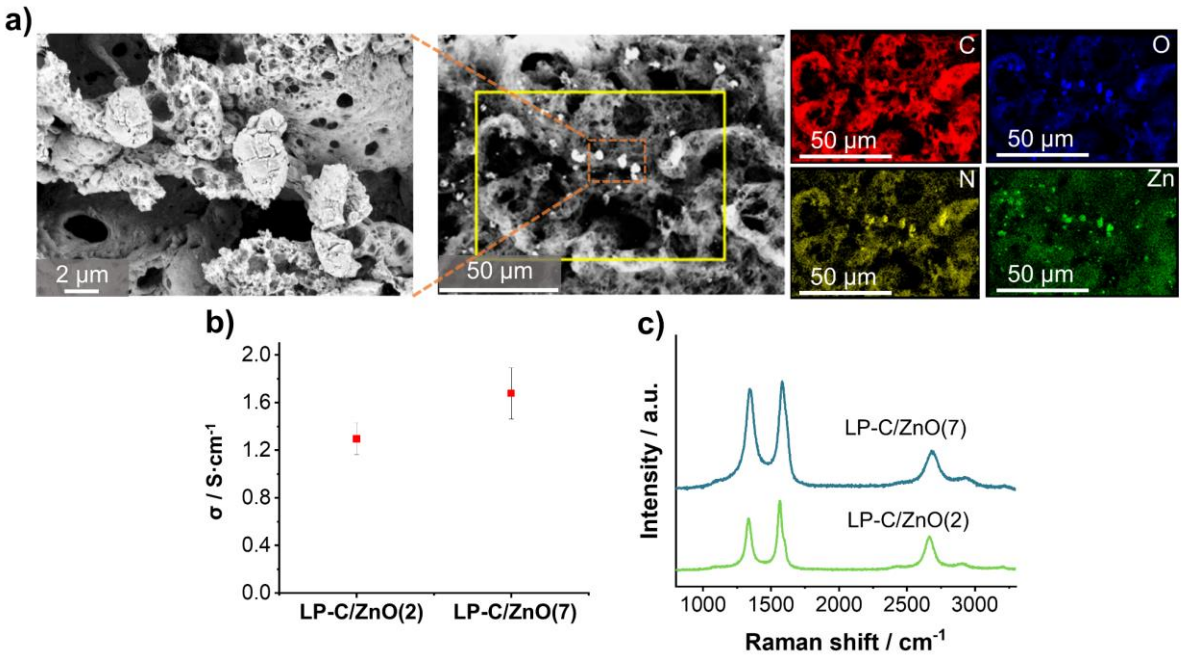

Figure 6. 6*.a) Exemplary top-view EDX map of sensor film LP-C/ZnO(2); b) Electrical conductivity of sensor films LP-C/ZnO(2) and LP-C/ZnO(7);c) Top-view Raman spectra of sensor films LP-C/ZnO(2) and LP-C/ZnO(7).*

After the laser-patterning process, it can be seen from the EDX mapping analysis (**Figure 6. 6 a**) that some of the ZnO nanorods or their debris are still distributed on the surface of the sensor films, but their shapes are enlarged or even broken due to the expansion effect. Regarding the characteristics in terms of electrical conductivity (**Figure 6. 6 b**) and graphitization (**Figure 6. 6 c**), the two representative samples, LP-C/ZnO(2) and LP-C/ZnO(7) show the addition of more ZnO resulted in an increase in conductivity and low degree of stacking of graphitized domains.

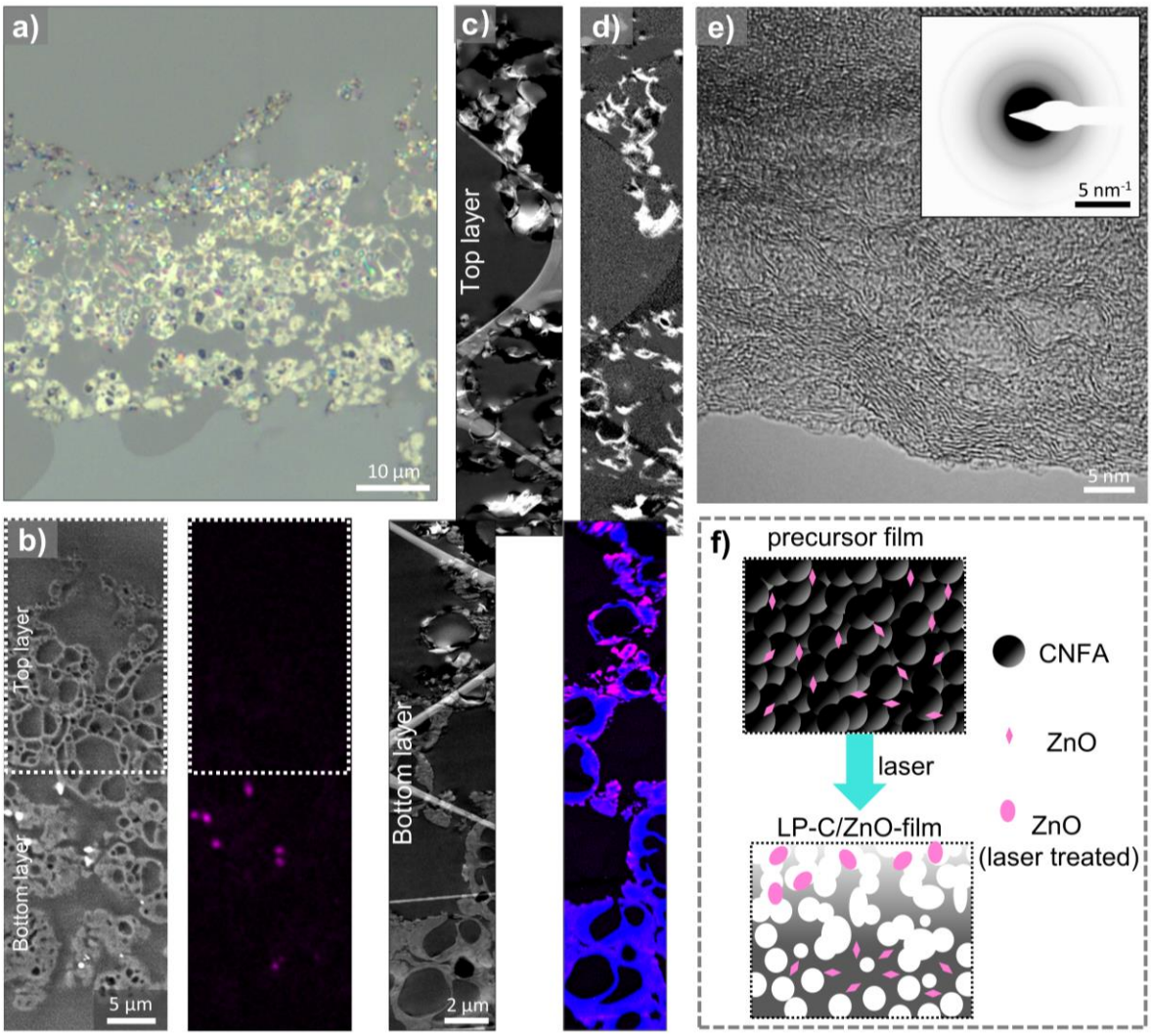

Figure 6. 7. *a) Cross-sectional optical micrograph of the sensor film; b) Cross-sectional backscatter SEM micrograph with correlated qualitative EDX element map of zinc (net intensities displayed); Cross-sectional TEM analyses of the sensor film: c) Representative high-angle annular dark- field (HAADF)-STEM micrograph with not infiltrated regions (black), epoxy resin (dark grey), and lacey TEM support film (light grey) d) (top) Graphitized carbon component in upper layer identified by PCA, (bottom) N (blue) and Zn (purple) distribution in the bottom layer of the sensor; e) HRTEM image of graphitized C of the top layer with corresponding SAED pattern (inset); g) Proposed formation mechanism of the LP-C/ZnO composite structure.*

In general, for the samples prepared with pre-synthesized ZnO nanorods, upon laser-patterning, the ZnO nanorods in the upper layer are partially reduced to Zn to catalyze the graphitization of surrounding carbon and then evaporate. Parts of the ZnO nanorods accumulate in the intermediate region of the bottom and top layer, whereas particle ripening is hindered in the lowest region due to pre-oxidation and lower temperatures (**Figure 6. 7**).

6.5 VOCs sensing

The increased SSA and the potential occurrence of ZnO-templated micropores is a great advantages for the sensitivity toward the detection of gaseous analytes. We tested the resistive response of each composite sensor film towards the exposure of representative polar and non-polar VOCs, namely acetone and toluene.[266] **Figure 6. 8** shows the response of each sensor film with different Zn content towards the test analytes. All samples, except for the reference without Zn, show a clear negative response upon exposure to acetone. The response to acetone rises with the Zn content and reaches a peak for the sample with 5 wt% of Zn (LP-C/Zn(5), e.g., $\Delta R/R_0$ = -21.5% at 2.5% acetone). In comparison to the samples with slightly less or more Zn, LP-C/Zn(4), and LP-C/Zn(6), the response is drastically lower by one order of magnitude. Also, the response towards the non-polar analyte, toluene, is enhanced in the zinc-containing films, although the trends are not as clear in this case. In fact, the reference film free of zinc shows no response towards toluene whatsoever. The highest response of $\Delta R/R_0$ = -0.9% to exposure of 0.4% toluene is observed for LP-C/Zn(2). Samples LP-C/Zn(4) and (5) give lower specific responses for toluene, and again LP-C/Zn(6) gives a decent response. The drastic increase in response at LP-C/Zn(5) is likely due to the formation of high amounts of micropores in this concentration regime.

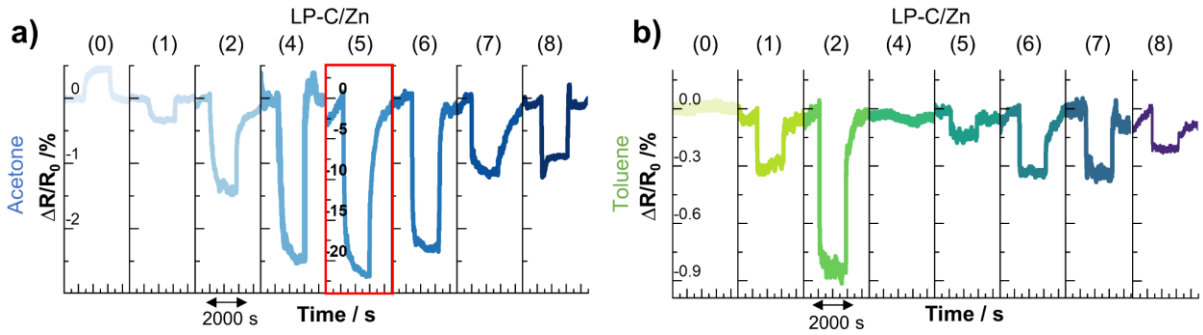

Figure 6. 8*. a) Sensing response of the LP-C/Zn films towards 2.5% acetone and b) 0.4% toluene.*

The response depends on the analyte concentration, as shown in **Figure 6. 9 *a,*** and a reasonable response of $\Delta R/R_0$ = -1.9% at relatively low analyte concentrations of 0.125% (1250 ppm) acetone is detected. With regard to selectivity, the sample **LP-C/Zn(5)** shows the highest

affinity and selectivity to polar VOCs at a lower concentration, e.g., ΔR/R = -4.7% at 0.4% acetone, ΔR/R = -3.0% at 0.4% ethanol (**Figure 6. 9 b),** while it shows little response to non-polar toluene and hexane at the same concentration. (**Figure 6. 9 b**). This response pattern indicates physisorption based on different binding mechanisms of polar and non-polar analytes. In addition, instability testing up to 24 hours, we observed that the sensitivity remained nearly constant over time (**Figure S 34**).

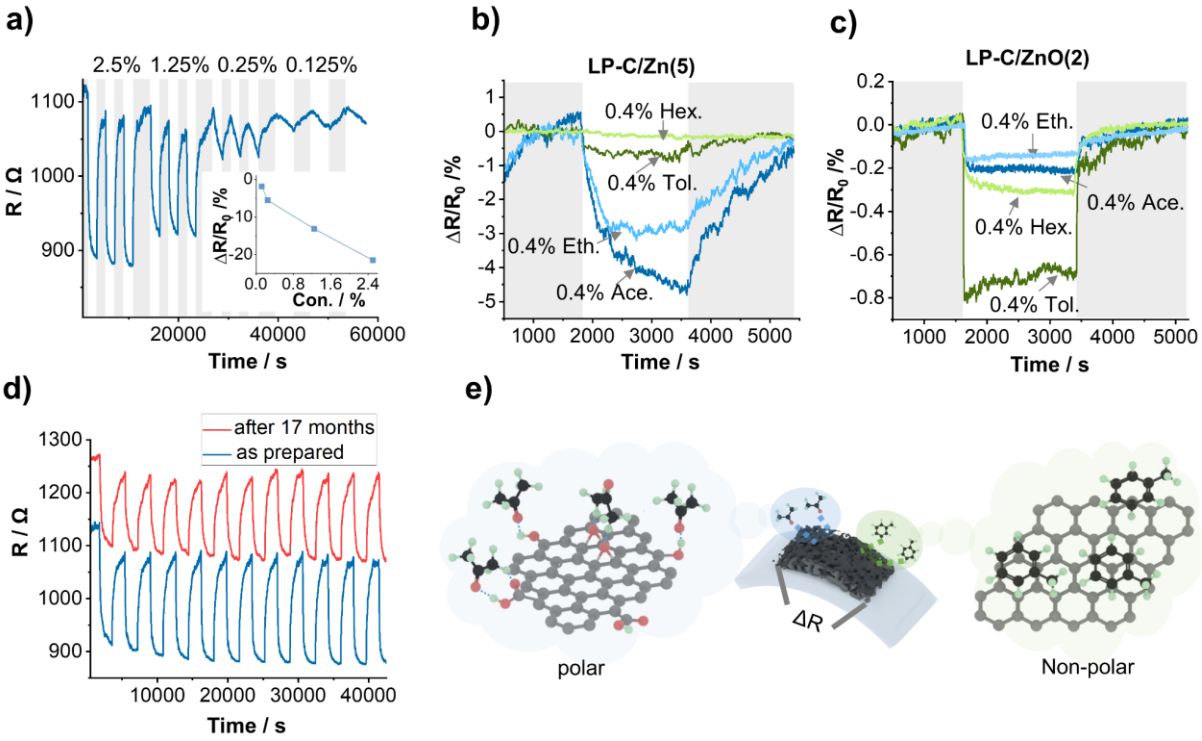

Figure 6. 9*. a) Resistive response of the LP-C/Zn(5) film towards 2.5%, 1.25%, 0.25%, and 0.125% acetone (inserted is a plot of sensitivity response ΔR/R₀ versus CO_2 concentration. The gray area: 100% nitrogen sparged, the non-gray area: contains different concentrations of analytes). b) Sensing response of the LP-C/Zn(5) film toward 0.4% acetone, 0.4% ethanol, 0.4% toluene, and 0.4% hexane. c) Sensing response of the LP-C/ZnO(2) film toward 0.4% acetone, 0.4% ethanol, 0.4% toluene, and 0.4% hexane. d) resistive response of LP-C/Zn(5) after 17 months towards 2.5% acetone in comparison to a freshly prepared sensor platform. e) Illustration of the adsorption mechanism of polar (acetone) and non-polar (toluene) analytes to polar (oxygenated) or non-polar (π-conjugated) surface.*

For the films of LP-C/ZnO (x) prepared with pre-synthesized ZnO nanorods, the sample containing 2 wt% Zn, i.e., LP-C/ZnO(2), shows a significantly higher selectivity towards non-polar 0.4% toluene and hexane with a response $\Delta R/R_0$ = -0.8 % and 0.3%, respectively, than to polar acetone ($\Delta R/R_0$ = -0.2 % at 0.4% acetone) and ethanal ($\Delta R/R_0$ = -0.13 at 0.4% ethanol) (**Figure 6. 9 c**). Furthermore, as shown in **Figure S 35**, LP-C/ZnO(2) shows good stability over

time test. A reasonable response of $\Delta R/R_0 = 0.14\%$ at a relatively low analyte concentration of 0.4% (400ppm) toluene is detected.

At last, we tested the long-term stability of the sensor platforms. We stored the sensor film LP-C/Zn(5) under ambient conditions for 17 months and tested it under the same 2.5 % acetone. Comparing the freshly prepared sample, the aged sample shows a slightly lower response of $\Delta R/R_0 = -12.7\%$ (**Figure 6. 9 d**). The reduced sensitivity is contributed by the increased initial resistance, which may be due to a partial oxidation/degradation of the surface groups on the sensor films.[34] Moreover, We tested the sensor films at different ambient temperatures (**Figure S 36**), and the room temperature of 25 °C shows the highest resistance response. On the other hand, a stable and fast response, even at an ambient temperature of 60 °C, is observed, which can be potentially applied to extreme heat environments.

In previous works, we demonstrated the polar character of the LP-C surface due to an abundance of oxygen functional groups.[267] For polar analytes such as acetone, two physisorption scenarios with polar sites on the surface need to be considered: hydrogen bonding and van der Waals interactions. Considering that the latter consists of contributions from the dipole, induction, and dispersion forces, the adsorption of acetone to the LP-C surface is mostly attributed to dipole-dipole interactions.[268–270] For toluene, on the other hand, dispersion forces or π-π stacking are implicit.[271,272] Taking these fundamental molecular interactions into consideration, the sorption selectivity in the different samples is attributed to the surface properties of the LP-C. Generally, the surface of the LP-C is polar and, therefore, sensitive to polar analytes. On the one hand, the hard-templating effect of ZnO nanoparticles promotes the formation of small pores and, eventually, micropores, which enhances the response toward acetone. On the other hand, the graphitization-catalyzing effect of ZnO during carbothermic reduction promotes the formation of an extended π-surface, which enhances the sensitivity towards toluene. (**Figure 6. 9 e)**.

6.6 Summary

The carbothermic reduction initiated by the presence of ZnO nanoparticles during laser-carbonization was studied. ZnO nanoparticles were generated *in situ* from $Zn(NO_3)_2$ that was added to the primary films. A comprehensive investigation of the chemical composition and microscopic morphology by XPS and cross-sectional HRTEM reveals a heterogeneous gradient profile due to the induced temperature gradient during laser-carbonization. Two positive effects were observed: 1) a significant increase of the active surface area due to the

hard-templating effect of the ZnO and 2) the catalysis of the graphitization around the ZnO nanoparticles. By careful selection of the initial $Zn(NO_3)_2$ concentration, the surface structure of the LP-C can be tuned in terms of porosity and surface polarity. Thereby, a drastically enhanced response towards VOCs and a differentiation by their polarity were achieved in resistive sensing experiments. At a concentration of 5 wt% Zn, the response towards acetone was increased by 43-fold with respect to the reference ($\Delta R/R_0$ = -21.5% at 2.5% acetone), which is attributed to a significantly higher porosity. As a proof of concept, the surface polarity was drastically reduced in additional experiments, in which pre-synthesized ZnO-nanorods were used as additives. Thereby, a response with a high selectivity towards toluene ($\Delta R/R_0$ = -0.8 % at 0.4% toluene), a representative non-polar analyte, was achieved. The herein-presented advancements in laser-carbonization may inspire the development of smart sensor arrays based on a simple materials processing technology. Yet, the increase of the sensitivity to the low ppm level and the decrease in the response times still remain a challenge.

7. Conclusions and perspectives

This dissertation summarizes and combines my research on laser-carbonization as a tool for the synthesis of functional materials for flexible gas sensors. Comprehensive approaches to laser-carbonization of molecular precursors are discussed in **Chapter 3**. Regarding molecular precursors, this work elucidates the fundamental importance of pre-carbonization and a mechanism for the formation of laser-carbonized films facilitated by fast photothermal reactions on the millisecond (kinetic) time scale. In **Chapter 4**, through the optimization of the process parameters (laser power, laser scanning speed, reaction atmosphere, molecular precursors, film thickness), a CO_2 sensor platform with high sensitivity and high selectivity was obtained. Moreover, to understand the adsorption mechanism of this sensor, a detailed and in-depth cross-sectional TEM characterization of the laser carbonized film shows that unidirectional energy shocks combined with deep attenuation of laser beams lead to layered sensor heterostructures with porous transducers layers (upper layers) and active sensor layers (lower layers). Laser-patterned nitrogen-doped carbon films on flexible substrates also exhibit good mechanical flexibility.

Chapters 5 and 6 show that this molecular precursor-based laser-carbonization method makes the modification of carbon materials much simpler. The properties of the laser-patterned carbon can be selectively tuned by adding porogens, additives, or reactants to the primary film. Thus, properties such as porosity, surface polarity, charge carrier density, or chemical composition are altered. Based on these factors, the VOCs sensor prepared in this study exhibited high sensitivity and selectivity for chemical analytes.

However, there are still some deficiencies in these works. For instance, characterizing the microstructure (porosity) of such a small amount of material and analyzing the correlation of porosity with chemical and electronic properties are very challenging. Even though the methylene blue method can give the specific surface area of the carbon material, there are still limitations compared to the physical gas adsorption method (BET method). **Chapter 3** only studies the relationship between laser wavelength and extinction coefficient for the precursor, but this is only a simple start for the precursor screening of laser-carbonization. Other factors, such as thermal conductivity, should also be taken into consideration.

So far, the sensors cannot detect lower gas analyte concentrations, such as parts-per-billion (ppb), and the practical application of the current laser-patterned nitrogen-doped carbon gas sensors is still limited. This requires further optimization of sensing devices and sensor

performance. The effect of water on CO_2 sensors based on carbon materials is still far from optimum. Current laser-patterned nitrogen-doped carbon sensor platforms exhibit strong adsorption properties to water. In follow-up studies, further modification of the material is needed to weaken the adsorption of water and enhance the selectivity of carbon dioxide.

Regardless, this laser-carbonized material demonstrates superior electrical conductivity, mechanical flexibility, high specific surface area, and high porosity. This molecular precursor-based laser-carbonization method is easy to operate, low in energy consumption, and easy to modify the material. Based on these advantages, laser-patterned carbon cannot only be applied to flexible sensors but also has great application potential in the fields of electrocatalysis, electrochemical capacitors, batteries, fuel cells, etc.

8. References

1. Greenwood, Norman Neill, A. E. *Chemistry of the Elements*. (Elsevier, 2012).
2. Andrew Burrows, John Holman, Andrew Parsons, Gwen Pilling, G. P. *Chemistry3 Introducing Inorganic, Organic and Physical Chemistry*. (Oxford University Press, 2017).
3. Spencer L. Seager, M. R. S. *Chemistry for today : general, organic, and biochemistry*. (Thomson-Brooks/Cole, 2005).
4. Kharisov, B. I. & Kharissova, O. V. General Data on Carbon Allotropes. in *Carbon Allotropes: Metal-Complex Chemistry, Properties and Applications* 1–8 (Springer International Publishing, 2019). doi:10.1007/978-3-030-03505-1_1.
5. Pan, B. *et al.* Carbyne with finite length: The one-dimensional sp carbon. *Sci. Adv.* **1**, (2015).
6. Casari, C. S., Tommasini, M., Tykwinski, R. R. & Milani, A. Carbon-atom wires: 1-D systems with tunable properties. *Nanoscale* **8**, 4414–4435 (2016).
7. Al-Jumaili, A., Alancherry, S., Bazaka, K. & Jacob, M. Review on the Antimicrobial Properties of Carbon Nanostructures. *Materials (Basel).* **10**, 1066 (2017).
8. Du, X., Skachko, I., Barker, A. & Andrei, E. Y. Approaching ballistic transport in suspended graphene. *Nat. Nanotechnol.* **3**, 491–495 (2008).
9. Lim, S., Park, H., Yamamoto, G., Lee, C. & Suk, J. W. Measurements of the Electrical Conductivity of Monolayer Graphene Flakes Using Conductive Atomic Force Microscopy. *Nanomaterials* **11**, 2575 (2021).
10. Lee, C., Wei, X., Kysar, J. W. & Hone, J. Measurement of the Elastic Properties and Intrinsic Strength of Monolayer Graphene. *Science (80-.).* **321**, 385–388 (2008).
11. Burchfield, L. A., Fahim, M. Al, Wittman, R. S., Delodovici, F. & Manini, N. Novamene: A new class of carbon allotropes. *Heliyon* **3**, e00242 (2017).
12. Wort, C. J. H. & Balmer, R. S. Diamond as an electronic material. *Mater. Today* **11**, 22–28 (2008).
13. Wang, H., Gao, Q. & Hu, J. High Hydrogen Storage Capacity of Porous Carbons Prepared by Using Activated Carbon. *J. Am. Chem. Soc.* **131**, 7016–7022 (2009).

14. Philippe Serp, J. L. F. *Carbon Materials for Catalysis*. (John Wiley & Sons, 2009).

15. Dicks, A. L. The role of carbon in fuel cells. *J. Power Sources* **156**, 128–141 (2006).

16. Togonon, J. J. H., Chiang, P.-C., Lin, H.-J., Tsai, W.-C. & Yen, H.-J. Pure carbon-based electrodes for metal-ion batteries. *Carbon Trends* **3**, 100035 (2021).

17. Wang, Y. *et al.* Recent progress in carbon-based materials for supercapacitor electrodes: a review. *J. Mater. Sci.* **56**, 173–200 (2021).

18. Gupta, S. Sen, Sreeprasad, T. S., Maliyekkal, S. M., Das, S. K. & Pradeep, T. Graphene from Sugar and its Application in Water Purification. *ACS Appl. Mater. Interfaces* **4**, 4156–4163 (2012).

19. Samantara, A. K., Ratha, S. & Raj, S. Functionalized Graphene Nanocomposites in Air Filtration Applications. in *Functionalized Graphene Nanocomposites and their Derivatives* 65–89 (Elsevier, 2019). doi:10.1016/B978-0-12-814548-7.00004-0.

20. Jian, M. *et al.* Advanced carbon materials for flexible and wearable sensors. *Sci. China Mater.* **60**, 1026–1062 (2017).

21. Li, S. *et al.* Recent Advances of Carbon-Based Flexible Strain Sensors in Physiological Signal Monitoring. *ACS Appl. Electron. Mater.* **2**, 2282–2300 (2020).

22. Devi, M., Rawat, S. & Sharma, S. A comprehensive review of the pyrolysis process: from carbon nanomaterial synthesis to waste treatment. *Oxford Open Mater. Sci.* **1**, 1–30 (2020).

23. Kingsland, L. C. Manufacture of carbon filaments. *Law and Contemporary Problems* vol. 13 354 (1948).

24. Manawi, Y., Ihsanullah, Samara, A., Al-Ansari, T. & Atieh, M. A Review of Carbon Nanomaterials' Synthesis via the Chemical Vapor Deposition (CVD) Method. *Materials (Basel).* **11**, 822 (2018).

25. Schuepfer, D. B. *et al.* Assessing the structural properties of graphitic and non-graphitic carbons by Raman spectroscopy. *Carbon N. Y.* **161**, 359–372 (2020).

26. graphitization. in *The IUPAC Compendium of Chemical Terminology* (International Union of Pure and Applied Chemistry (IUPAC), 2012). doi:10.1351/goldbook.G02691.

27. Crystallite growth in graphitizing and non-graphitizing carbons. *Proc. R. Soc. London. Ser. A. Math. Phys. Sci.* **209**, 196–218 (1951).

28. Harris †, P. J. F. Fullerene-related structure of commercial glassy carbons. *Philos. Mag.* **84**, 3159–3167 (2004).

29. *The IUPAC Compendium of Chemical Terminology*. (International Union of Pure and Applied Chemistry (IUPAC), 2019). doi:10.1351/goldbook.

30. Fitzer, E., Kochling, K.-H., Boehm, H. P. & Marsh, H. Recommended terminology for the description of carbon as a solid (IUPAC Recommendations 1995). *Pure Appl. Chem.* **67**, 473–506 (1995).

31. Li, Y. *et al.* Significant improvement of multi-seed method of diamond synthesis by adjusting the lateral cooling water temperature. *CrystEngComm* **19**, 6681–6685 (2017).

32. Robertson, J. Diamond-like amorphous carbon. *Mater. Sci. Eng. R Reports* **37**, 129–281 (2002).

33. Dasgupta, K. & Sathiyamoorthy, D. Disordered carbon–its preparation, structure, and characterisation. *Mater. Sci. Technol.* **19**, 995–1002 (2003).

34. Sing, K. S. W. Reporting physisorption data for gas/solid systems with special reference to the determination of surface area and porosity (Recommendations 1984). *Pure Appl. Chem.* **57**, 603–619 (1985).

35. Dillon, E. C., Wilton, J. H., Barlow, J. C. & Watson, W. A. Large surface area activated charcoal and the inhibition of aspirin absorption. *Ann. Emerg. Med.* **18**, 547–552 (1989).

36. *Porous Carbon Materials from Sustainable Precursors*. (Royal Society of Chemistry, 2015). doi:10.1039/9781782622277.

37. Liang, D. *et al.* Mechanism of the evolution of pore structure during the preparation of activated carbon from Zhundong high-alkali coal based on gas–solid diffusion and activation reactions. *RSC Adv.* **10**, 33566–33575 (2020).

38. Ma, X. *et al.* Activated Porous Carbon with an Ultrahigh Surface Area Derived from Waste Biomass for Acetone Adsorption, CO 2 Capture, and Light Hydrocarbon Separation. *ACS Sustain. Chem. Eng.* **8**, 11721–11728 (2020).

39. Sai Bhargava Reddy, M., Ponnamma, D., Sadasivuni, K. K., Kumar, B. & Abdullah, A. M. Carbon dioxide adsorption based on porous materials. *RSC Adv.* **11**, 12658–12681 (2021).

40. Vix-Guterl, C. *et al.* Electrochemical energy storage in ordered porous carbon materials.

Carbon N. Y. **43**, 1293–1302 (2005).

41. Matos, I., Bernardo, M. & Fonseca, I. Porous carbon: A versatile material for catalysis. *Catal. Today* **285**, 194–203 (2017).

42. Thommes, M. Physical Adsorption Characterization of Nanoporous Materials. *Chemie Ing. Tech.* **82**, 1059–1073 (2010).

43. Pallarés, J., González-Cencerrado, A. & Arauzo, I. Production and characterization of activated carbon from barley straw by physical activation with carbon dioxide and steam. *Biomass and Bioenergy* **115**, 64–73 (2018).

44. Linares-Solano, A., Salinas-Martínez de Lecea, C., Cazorla-Amorós, D. & Martín-Gullón, I. Porosity Development during CO 2 and Steam Activation in a Fluidized Bed Reactor. *Energy & Fuels* **14**, 142–149 (2000).

45. Molina-Sabio, M., Gonzalez, M. T., Rodriguez-Reinoso, F. & Sepúlveda-Escribano, A. Effect of steam and carbon dioxide activation in the micropore size distribution of activated carbon. *Carbon N. Y.* **34**, 505–509 (1996).

46. Sevilla, M. & Mokaya, R. Energy storage applications of activated carbons: supercapacitors and hydrogen storage. *Energy Environ. Sci.* **7**, 1250–1280 (2014).

47. Fuertes, A. B. Template synthesis of mesoporous carbons with a controlled particle size. *J. Mater. Chem.* **13**, 3085 (2003).

48. Zhang, W. *et al.* A review of porous carbons produced by template methods for supercapacitor applications. *New Carbon Mater.* **36**, 69–81 (2021).

49. Xia, Y., Yang, Z. & Mokaya, R. Templated nanoscale porous carbons. *Nanoscale* **2**, 639 (2010).

50. Devi, M., Wang, H., Moon, S., Sharma, S. & Strauss, V. Laser-Carbonization – A powerful tool for micro-fabrication of patterned electronic carbons. *Adv. Mater.* 2211054 (2023) doi:10.1002/adma.202211054.

51. Gu, D. & Schüth, F. Synthesis of non-siliceous mesoporous oxides. *Chem. Soc. Rev.* **43**, 313–344 (2014).

52. Chuenchom, L., Kraehnert, R. & Smarsly, B. M. Recent progress in soft-templating of porous carbon materials. *Soft Matter* **8**, 10801 (2012).

53. Liang, C., Hong, K., Guiochon, G. A., Mays, J. W. & Dai, S. Synthesis of a Large-Scale

Highly Ordered Porous Carbon Film by Self-Assembly of Block Copolymers. *Angew. Chemie Int. Ed.* **43**, 5785–5789 (2004).

54. Liang, C. & Dai, S. Synthesis of Mesoporous Carbon Materials via Enhanced Hydrogen-Bonding Interaction. *J. Am. Chem. Soc.* **128**, 5316–5317 (2006).

55. Tanaka, S., Nishiyama, N., Egashira, Y. & Ueyama, K. Synthesis of ordered mesoporous carbons with channel structure from an organic–organic nanocomposite. *Chem. Commun.* 2125–2127 (2005) doi:10.1039/B501259G.

56. Meng, Y. *et al.* A Family of Highly Ordered Mesoporous Polymer Resin and Carbon Structures from Organic−Organic Self-Assembly. *Chem. Mater.* **18**, 4447–4464 (2006).

57. Fechler, N., Fellinger, T.-P. & Antonietti, M. "Salt Templating": A Simple and Sustainable Pathway toward Highly Porous Functional Carbons from Ionic Liquids. *Adv. Mater.* **25**, 75–79 (2013).

58. Zhang, J. & Dai, L. Heteroatom-Doped Graphitic Carbon Catalysts for Efficient Electrocatalysis of Oxygen Reduction Reaction. *ACS Catal.* **5**, 7244–7253 (2015).

59. Inagaki, M., Toyoda, M., Soneda, Y. & Morishita, T. Nitrogen-doped carbon materials. *Carbon N. Y.* **132**, 104–140 (2018).

60. Hu, C. & Dai, L. Doping of Carbon Materials for Metal-Free Electrocatalysis. *Adv. Mater.* **31**, 1804672 (2019).

61. Cermignani, W., Paulson, T. E., Onneby, C. & Pantano, C. G. Synthesis and characterization of boron-doped carbons. *Carbon N. Y.* **33**, 367–374 (1995).

62. Kiciński, W., Szala, M. & Bystrzejewski, M. Sulfur-doped porous carbons: Synthesis and applications. *Carbon N. Y.* **68**, 1–32 (2014).

63. Xie, L. *et al.* Understanding the activity origin of oxygen-doped carbon materials in catalyzing the two-electron oxygen reduction reaction towards hydrogen peroxide generation. *J. Colloid Interface Sci.* **610**, 934–943 (2022).

64. Hu, Z. *et al.* Doping of Graphene Films: Open the way to Applications in Electronics and Optoelectronics. *Adv. Funct. Mater.* **32**, 2203179 (2022).

65. Hu, T. & Gerber, I. C. Theoretical Study of the Interaction of Electron Donor and Acceptor Molecules with Graphene. *J. Phys. Chem. C* **117**, 2411–2420 (2013).

66. Rodriguez-Reinoso, F., Molina-Sabio, M. & Munecas, M. A. Effect of microporosity

and oxygen surface groups of activated carbon in the adsorption of molecules of different polarity. *J. Phys. Chem.* **96**, 2707–2713 (1992).

67. Li, X. H. & Antonietti, M. Metal nanoparticles at mesoporous N-doped carbons and carbon nitrides: Functional mott–schottky heterojunctions for catalysis. *Chem. Soc. Rev.* **42**, 6593–6604 (2013).

68. Oschatz, M. & Antonietti, M. A search for selectivity to enable CO 2 capture with porous adsorbents. *Energy Environ. Sci.* **11**, 57–70 (2018).

69. Zhao, Y., Liu, X. & Han, Y. Microporous carbonaceous adsorbents for CO 2 separation via selective adsorption. *RSC Adv.* **5**, 30310–30330 (2015).

70. Inagaki, M., Tsumura, T., Kinumoto, T. & Toyoda, M. Graphitic carbon nitrides (g-C3N4) with comparative discussion to carbon materials. *Carbon N. Y.* **141**, 580–607 (2019).

71. Tang, D., Shao, C., Jiang, S., Sun, C. & Song, S. Graphitic C 2 N 3 : An Allotrope of g -C 3 N 4 Containing Active Azide Pentagons as Metal-Free Photocatalyst for Abundant H 2 Bubble Evolution. *ACS Nano* **15**, 7208–7215 (2021).

72. Kumar, P. *et al.* C 3 N 5 : A Low Bandgap Semiconductor Containing an Azo-Linked Carbon Nitride Framework for Photocatalytic, Photovoltaic and Adsorbent Applications. *J. Am. Chem. Soc.* **141**, 5415–5436 (2019).

73. Kossmann, J. *et al.* Guanine condensates as covalent materials and the concept of cryptopores. *Carbon N. Y.* **172**, 497–505 (2021).

74. Pels, J. R., Kapteijn, F., Moulijn, J. A., Zhu, Q. & Thomas, K. M. Evolution of nitrogen functionalities in carbonaceous materials during pyrolysis. *Carbon N. Y.* **33**, 1641–1653 (1995).

75. Gehring, M. *et al.* Carbonisation temperature dependence of electrochemical activity of nitrogen-doped carbon fibres from electrospinning as air-cathodes for aqueous-alkaline metal–air batteries. *RSC Adv.* **9**, 27231–27241 (2019).

76. Antonietti, M. & Oschatz, M. The Concept of “Noble, Heteroatom-Doped Carbons,” Their Directed Synthesis by Electronic Band Control of Carbonization, and Applications in Catalysis and Energy Materials. *Adv. Mater.* **30**, 1706836 (2018).

77. Ashourirad, B., Sekizkardes, A. K., Altarawneh, S. & El-Kaderi, H. M. Exceptional Gas

Adsorption Properties by Nitrogen-Doped Porous Carbons Derived from Benzimidazole-Linked Polymers. *Chem. Mater.* **27**, 1349–1358 (2015).

78. Sevilla, M., Valle-Vigón, P. & Fuertes, A. B. N-Doped Polypyrrole-Based Porous Carbons for CO 2 Capture. *Adv. Funct. Mater.* **21**, 2781–2787 (2011).

79. Naidu Talapaneni, S. *et al.* Chemical Blowing Approach for Ultramicroporous Carbon Nitride Frameworks and Their Applications in Gas and Energy Storage. (2016) doi:10.1002/adfm.201604658.

80. Ren, X. *et al.* N-doped porous carbons with exceptionally high CO2 selectivity for CO2 capture. *Carbon N. Y.* **114**, 473–481 (2017).

81. Di, Y., Wang, X., Thomas, A. & Antonietti, M. Making Metal□Carbon Nitride Heterojunctions for Improved Photocatalytic Hydrogen Evolution with Visible Light. *ChemCatChem* **2**, 834–838 (2010).

82. Wang, Y., Yao, J., Li, H., Su, D. & Antonietti, M. Highly Selective Hydrogenation of Phenol and Derivatives over a Pd@Carbon Nitride Catalyst in Aqueous Media. *J. Am. Chem. Soc.* **133**, 2362–2365 (2011).

83. Zhou, Y. *et al.* Enhancement of Pt and Pt-alloy fuel cell catalyst activity and durability via nitrogen-modified carbon supports. *Energy Environ. Sci.* **3**, 1437 (2010).

84. Lei, Z. *et al.* Highly dispersed platinum supported on nitrogen-containing ordered mesoporous carbon for methanol electrochemical oxidation. *Microporous Mesoporous Mater.* **119**, 30–38 (2009).

85. Le, T. D. *et al.* Recent Advances in Laser-Induced Graphene: Mechanism, Fabrication, Properties, and Applications in Flexible Electronics. *Adv. Funct. Mater.* **32**, 2205158 (2022).

86. Raffel, J. I., Freidin, J. F. & Chapman, G. H. Laser-formed connections using polyimide. *Appl. Phys. Lett.* **42**, 705–706 (1983).

87. Brannon, J. H., Lankard, J. R., Baise, A. I., Burns, F. & Kaufman, J. Excimer laser etching of polyimide. *J. Appl. Phys.* **58**, 2036–2043 (1985).

88. Zhang, Y. *et al.* Direct imprinting of microcircuits on graphene oxides film by femtosecond laser reduction. *Nano Today* **5**, 15–20 (2010).

89. El-Kady, M. F., Strong, V., Dubin, S. & Kaner, R. B. Laser Scribing of High-

Performance and Flexible Graphene-Based Electrochemical Capacitors. *Science (80-.).* **335**, 1326–1330 (2012).

90. Gao, W. *et al.* Direct laser writing of micro-supercapacitors on hydrated graphite oxide films. *Nat. Nanotechnol.* **6**, 496–500 (2011).

91. Lin, J. *et al.* Laser-induced porous graphene films from commercial polymers. *Nat. Commun.* **5**, 5–12 (2014).

92. Go, D. *et al.* Laser Carbonization of PAN-Nanofiber Mats with Enhanced Surface Area and Porosity. *ACS Appl. Mater. Interfaces* **8**, 28412–28417 (2016).

93. Singh, S. P., Li, Y., Zhang, J., Tour, J. M. & Arnusch, C. J. Sulfur-Doped Laser-Induced Porous Graphene Derived from Polysulfone-Class Polymers and Membranes. *ACS Nano* **12**, 289–297 (2018).

94. Morita, N. *et al.* Direct micro-carbonization inside polymer using focused femtosecond laser pulses. *Appl. Phys. Lett.* **105**, 201104 (2014).

95. Stankova, N. E. *et al.* fs- and ns-laser processing of polydimethylsiloxane (PDMS) elastomer: Comparative study. *Appl. Surf. Sci.* **336**, 321–328 (2015).

96. Atanasov, P. A. *et al.* Fs-laser processing of medical grade polydimethylsiloxane (PDMS). *Appl. Surf. Sci.* **374**, 229–234 (2016).

97. Chyan, Y. *et al.* Laser-Induced Graphene by Multiple Lasing: Toward Electronics on Cloth, Paper, and Food. *ACS Nano* **12**, 2176–2183 (2018).

98. Mahmood, F., Mahmood, F., Zhang, H., Lin, J. & Wan, C. Laser-Induced Graphene Derived from Kraft Lignin for Flexible Supercapacitors. *ACS Omega* **5**, 14611–14618 (2020).

99. Kulyk, B. *et al.* Laser-Induced Graphene from Paper for Mechanical Sensing. *ACS Appl. Mater. Interfaces* **13**, 10210–10221 (2021).

100. Ye, R. *et al.* Laser-Induced Graphene Formation on Wood. *Adv. Mater.* **29**, 1–7 (2017).

101. Wang, H. *et al.* Laser Writing of Janus Graphene/Kevlar Textile for Intelligent Protective Clothing. *ACS Nano* **14**, 3219–3226 (2020).

102. Zhang, Y. *et al.* Direct imprinting of microcircuits on graphene oxides film by femtosecond laser reduction. *Nano Today* **5**, 15–20 (2010).

103. Go, D. *et al.* Laser Carbonization of PAN-Nanofiber Mats with Enhanced Surface Area and Porosity. *ACS Appl. Mater. Interfaces* **8**, 28412–28417 (2016).

104. Strauss, V., Marsh, K., Kowal, M. D., El-Kady, M. & Kaner, R. B. A Simple Route to Porous Graphene from Carbon Nanodots for Supercapacitor Applications. *Adv. Mater.* **30**, 1–10 (2018).

105. Steen, W. M. & Mazumder, J. *Laser Material Processing*. (Springer London, 2010). doi:10.1007/978-1-84996-062-5.

106. Steen, W. M. & Mazumder, J. *Laser Material Processing*. (Springer London, 2010). doi:10.1007/978-1-84996-062-5.

107. Wan, Z. *et al.* Tuning the sub-processes in laser reduction of graphene oxide by adjusting the power and scanning speed of laser. *Carbon N. Y.* **141**, 83–91 (2019).

108. Edberg, J. *et al.* Laser-induced graphitization of a forest-based ink for use in flexible and printed electronics. *npj Flex. Electron.* **4**, (2020).

109. Nam, K.-H. *et al.* Laser direct write of heteroatom-doped graphene on molecularly controlled polyimides for electrochemical biosensors with nanomolar sensitivity. *Carbon N. Y.* **188**, 209–219 (2022).

110. Tran, T. X. *et al.* Laser-Induced Reduction of Graphene Oxide by Intensity-Modulated Line Beam for Supercapacitor Applications. *ACS Appl. Mater. Interfaces* **10**, 39777–39784 (2018).

111. Mamleyev, E. R. *et al.* Laser-induced hierarchical carbon patterns on polyimide substrates for flexible urea sensors. *npj Flex. Electron.* **3**, 2 (2019).

112. Li, Y. *et al.* Laser-Induced Graphene in Controlled Atmospheres: From Superhydrophilic to Superhydrophobic Surfaces. *Adv. Mater.* **29**, 1–8 (2017).

113. Mamleyev, E. R. *et al.* Laser-induced hierarchical carbon patterns on polyimide substrates for flexible urea sensors. *npj Flex. Electron.* **3**, 2 (2019).

114. Stanford, M. G., Yang, K., Chyan, Y., Kittrell, C. & Tour, J. M. Laser-Induced Graphene for Flexible and Embeddable Gas Sensors. *ACS Nano* **13**, 3474–3482 (2019).

115. Cardoso, A. R. *et al.* Molecularly-imprinted chloramphenicol sensor with laser-induced graphene electrodes. *Biosens. Bioelectron.* **124–125**, 167–175 (2019).

116. Xuan, X. *et al.* A highly stretchable and conductive 3D porous graphene metal

nanocomposite based electrochemical-physiological hybrid biosensor. *Biosens. Bioelectron.* **120**, 160–167 (2018).

117. Vanegas, D. *et al.* Laser Scribed Graphene Biosensor for Detection of Biogenic Amines in Food Samples Using Locally Sourced Materials. *Biosensors* **8**, 42 (2018).

118. Yang, Y. *et al.* A laser-engraved wearable sensor for sensitive detection of uric acid and tyrosine in sweat. *Nat. Biotechnol.* **38**, 217–224 (2020).

119. Zhang, Y. *et al.* Laser-induced Graphene-based Non-enzymatic Sensor for Detection of Hydrogen Peroxide. *Electroanalysis* **31**, 1334–1341 (2019).

120. Zhu, J. *et al.* Biomimetic Turbinate-like Artificial Nose for Hydrogen Detection Based on 3D Porous Laser-Induced Graphene. *ACS Appl. Mater. Interfaces* **11**, 24386–24394 (2019).

121. Alahi, M. E. E., Nag, A., Mukhopadhyay, S. C. & Burkitt, L. A temperature-compensated graphene sensor for nitrate monitoring in real-time application. *Sensors Actuators A Phys.* **269**, 79–90 (2018).

122. Yang, W. *et al.* Fabrication of Smart Components by 3D Printing and Laser-Scribing Technologies. *ACS Appl. Mater. Interfaces* **12**, 3928–3935 (2020).

123. Cao, L. *et al.* Stable and durable laser-induced graphene patterns embedded in polymer substrates. *Carbon N. Y.* **163**, 85–94 (2020).

124. Shi, X. *et al.* One-Step Scalable Fabrication of Graphene-Integrated Micro-Supercapacitors with Remarkable Flexibility and Exceptional Performance Uniformity. *Adv. Funct. Mater.* **29**, 1902860 (2019).

125. Zhang, W. *et al.* 3D Laser Scribed Graphene Derived from Carbon Nanospheres: An Ultrahigh-Power Electrode for Supercapacitors. *Small Methods* **3**, 1900005 (2019).

126. Chen, J., Wang, Y., Liu, F. & Luo, S. Laser-Induced Graphene Paper Heaters with Multimodally Patternable Electrothermal Performance for Low-Energy Manufacturing of Composites. *ACS Appl. Mater. Interfaces* **12**, 23284–23297 (2020).

127. Huang, L. *et al.* Highly Efficient and Rapid Inactivation of Coronavirus on Non-Metal Hydrophobic Laser-Induced Graphene in Mild Conditions. *Adv. Funct. Mater.* **31**, 2101195 (2021).

128. Ren, M., Zhang, J., Fan, M., Ajayan, P. M. & Tour, J. M. Li-Breathing Air Batteries

Catalyzed by MnNiFe/Laser-Induced Graphene Catalysts. *Adv. Mater. Interfaces* **6**, 1901035 (2019).

129. Han, X. *et al.* Laser-Induced Graphene from Wood Impregnated with Metal Salts and Use in Electrocatalysis. *ACS Appl. Nano Mater.* **1**, 5053–5061 (2018).

130. Peng, Z. *et al.* Flexible Boron-Doped Laser-Induced Graphene Microsupercapacitors. *ACS Nano* **9**, 5868–5875 (2015).

131. Tehrani, F. *et al.* Laser-Induced Graphene Composites for Printed, Stretchable, and Wearable Electronics. *Adv. Mater. Technol.* **4**, 1900162 (2019).

132. Huang, L., Su, J., Song, Y. & Ye, R. Laser-Induced Graphene: En Route to Smart Sensing. *Nano-Micro Lett.* **12**, 1–17 (2020).

133. Duan, S. *et al.* Waterproof Mechanically Robust Multifunctional Conformal Sensors for Underwater Interactive Human–Machine Interfaces. *Adv. Intell. Syst.* **3**, 2100056 (2021).

134. Duan, S. *et al.* Waterproof Mechanically Robust Multifunctional Conformal Sensors for Underwater Interactive Human–Machine Interfaces. *Adv. Intell. Syst.* **3**, 2100056 (2021).

135. Chhetry, A. *et al.* MoS 2 -Decorated Laser-Induced Graphene for a Highly Sensitive, Hysteresis-free, and Reliable Piezoresistive Strain Sensor. *ACS Appl. Mater. Interfaces* **11**, 22531–22542 (2019).

136. Swager, T. M. & Mirica, K. A. Introduction: Chemical Sensors. *Chem. Rev.* **119**, 1–2 (2019).

137. Mandoj, F., Nardis, S., Di Natale, C. & Paolesse, R. Porphyrinoid Thin Films for Chemical Sensing. in *Encyclopedia of Interfacial Chemistry* 422–443 (Elsevier, 2018). doi:10.1016/B978-0-12-409547-2.11677-4.

138. Mandoj, F., Nardis, S., Di Natale, C. & Paolesse, R. Porphyrinoid Thin Films for Chemical Sensing. in *Encyclopedia of Interfacial Chemistry* 422–443 (Elsevier, 2018). doi:10.1016/B978-0-12-409547-2.11677-4.

139. Wongkaew, N., Simsek, M., Griesche, C. & Baeumner, A. J. Functional Nanomaterials and Nanostructures Enhancing Electrochemical Biosensors and Lab-on-a-Chip Performances: Recent Progress, Applications, and Future Perspective. *Chem. Rev.* **119**, 120–194 (2019).

140. Wu, D. *et al.* A Simple Graphene NH3 Gas Sensor via Laser Direct Writing. *Sensors* **18**,

4405 (2018).

141. Yu, Y., Joshi, P. C., Wu, J. & Hu, A. Laser-Induced Carbon-Based Smart Flexible Sensor Array for Multiflavors Detection. *ACS Appl. Mater. Interfaces* **10**, 34005–34012 (2018).

142. Yu, Y., Joshi, P. C., Wu, J. & Hu, A. Laser-Induced Carbon-Based Smart Flexible Sensor Array for Multiflavors Detection. *ACS Appl. Mater. Interfaces* **10**, 34005–34012 (2018).

143. *Laser-Assisted Fabrication of Materials*. vol. 161 (Springer Berlin Heidelberg, 2013).

144. Maher F. El-Kady, Veronica Strong, Sergey Dubin, R. B. K. Laser Scribing of High-Performance and Flexible Graphene-Based Electrochemical Capacitors. *Science (80-.).* **335**, 1326–1330 (2012).

145. Strauss, V., Wang, H., Delacroix, S., Ledendecker, M. & Wessig, P. Carbon nanodots revised: The thermal citric acid/urea reaction. *Chem. Sci.* **11**, 8256–8266 (2020).

146. He, C., Jiang, Y., Zhang, X., Cui, X. & Yang, Y. A Simple Glucose-Blowing Approach to Graphene-Like Foam/NiO Composites for Asymmetric Supercapacitors. *Energy Technol.* **8**, 1900923 (2020).

147. Wang, X. *et al.* Three-dimensional strutted graphene grown by substrate-free sugar blowing for high-power-density supercapacitors. *Nat. Commun.* **4**, 2905 (2013).

148. Badaczewski, F. *et al.* Peering into the structural evolution of glass-like carbons derived from phenolic resin by combining small-angle neutron scattering with an advanced evaluation method for wide-angle X-ray scattering. *Carbon N. Y.* **141**, 169–181 (2019).

149. Oreskes, N. E SSAY on Climate Change. *Science (80-.).* **306**, 2004–2005 (2005).

150. Ripple, W. *et al.* World Scientists ' Warning of a Climate Emergency To cite this version : World Scientists ' Warning of a Climate Emergency. *Bioscience* (2019).

151. Permentier, K., Vercammen, S., Soetaert, S. & Schellemans, C. Carbon dioxide poisoning: a literature review of an often forgotten cause of intoxication in the emergency department. *Int. J. Emerg. Med.* **10**, 17–20 (2017).

152. Manzanedo, R. D. & Manning, P. COVID-19: Lessons for the climate change emergency. *Sci. Total Environ.* **742**, 140563 (2020).

153. Mulmi, S. & Thangadurai, V. Editors' Choice—Review—Solid-State Electrochemical

Carbon Dioxide Sensors: Fundamentals, Materials and Applications. *J. Electrochem. Soc.* **167**, 037567 (2020).

154. Wang, D. *et al.* CO2-sensing properties and mechanism of nano-SnO2 thick-film sensor. *Sensors Actuators, B Chem.* **227**, 73–84 (2016).

155. Hunge, Y. M., Yadav, A. A., Kulkarni, S. B. & Mathe, V. L. A multifunctional ZnO thin film based devises for photoelectrocatalytic degradation of terephthalic acid and CO2 gas sensing applications. *Sensors Actuators, B Chem.* **274**, 1–9 (2018).

156. Wang, X. *et al.* CO2 sensing of La0.875Ca0.125FeO3 in wet vapor: A comparison of experimental results and first-principles calculations. *Phys. Chem. Chem. Phys.* **17**, 13733–13742 (2015).

157. Yadav, A. A., Lokhande, A. C., Kim, J. H. & Lokhande, C. D. Highly sensitive CO2 sensor based on microrods-like La2O3 thin film electrode. *RSC Adv.* **6**, 106074–106080 (2016).

158. Llobet, E. Gas sensors using carbon nanomaterials: A review. *Sensors Actuators, B Chem.* **179**, 32–45 (2013).

159. Ratinac, K. R., Yang, W., Ringer, S. P. & Braet, F. Toward ubiquitous environmental gas sensors - Capitalizing on the promise of graphene. *Environ. Sci. Technol.* **44**, 1167–1176 (2010).

160. Leghrib, R. & Llobet, E. Quantitative trace analysis of benzene using an array of plasma-treated metal-decorated carbon nanotubes and fuzzy adaptive resonant theory techniques. *Anal. Chim. Acta* **708**, 19–27 (2011).

161. Wang, C. *et al.* Advanced Carbon for Flexible and Wearable Electronics. *Adv. Mater.* **31**, 1–37 (2019).

162. Keum, H., Mccormick, M., Liu, P., Zhang, Y. & Omenetto, F. G. RESEARCH ARTICLES Epidermal Electronics. **333**, (2011).

163. Dong, K. *et al.* A Stretchable Yarn Embedded Triboelectric Nanogenerator as Electronic Skin for Biomechanical Energy Harvesting and Multifunctional Pressure Sensing. *Adv. Mater.* **30**, 1–12 (2018).

164. Cai, L. *et al.* Super-stretchable, transparent carbon nanotube-based capacitive strain sensors for human motion detection. *Sci. Rep.* **3**, 1–9 (2013).

165. Yu, D. *et al.* Nitrogen-Doped Coal Tar Pitch Based Microporous Carbons with Superior CO 2 Capture Performance. (2018) doi:10.1021/acs.energyfuels.8b00125.

166. Wu, D., Li, Z., Zhong, M., Kowalewski, T. & Matyjaszewski, K. Templated Synthesis of Nitrogen-Enriched Nanoporous Carbon Materials from Porogenic Organic Precursors Prepared by ATRP**. doi:10.1002/anie.201309836.

167. To, J. W. F. *et al.* Hierarchical N-Doped Carbon as CO 2 Adsorbent with High CO 2 Selectivity from Rationally Designed Polypyrrole Precursor. (2015) doi:10.1021/jacs.5b11955.

168. Wei, J. *et al.* A Controllable Synthesis of Rich Nitrogen-Doped Ordered Mesoporous Carbon for CO 2 Capture and Supercapacitors. (2013) doi:10.1002/adfm.201202764.

169. Gong, J., Antonietti, M. & Yuan, J. Poly(Ionic Liquid)-Derived Carbon with Site-Specific N-Doping and Biphasic Heterojunction for Enhanced CO 2 Capture and Sensing. *Angew. Chemie* **129**, 7665–7671 (2017).

170. Ju, W. *et al.* Understanding activity and selectivity of metal-nitrogen-doped carbon catalysts for electrochemical reduction of CO2. *Nat. Commun.* **8**, 944 (2017).

171. Chandra, V. *et al.* Highly selective CO2 capture on N-doped carbon produced by chemical activation of polypyrrole functionalized graphene sheets. *Chem. Commun.* **48**, 735–737 (2012).

172. Venna, S. R. & Carreon, M. A. Highly Permeable Zeolite Imidazolate Framework-8 Membranes for CO 2 /CH 4 Separation. *J. Am. Chem. Soc.* **132**, 76–78 (2010).

173. Lucas, G., Burdet, P., Cantoni, M. & Hébert, C. Multivariate statistical analysis as a tool for the segmentation of 3D spectral data. *Micron* **52**–**53**, 49–56 (2013).

174. Jaleel, A. *et al.* Structural effect of Nitrogen/Carbon on the stability of anchored Ru catalysts for CO2 hydrogenation to formate. *Chem. Eng. J.* **433**, 133571 (2022).

175. Fernández, A. *et al.* Characterization of carbon nitride thin films prepared by dual ion beam sputtering. *Appl. Phys. Lett.* **69**, 764–766 (1996).

176. Wan, L. & Egerton, R. F. Preparation and characterization of carbon nitride thin films. *Thin Solid Films* **279**, 34–42 (1996).

177. Ophus, C. *et al.* Automated Crystal Orientation Mapping in py4DSTEM using Sparse Correlation Matching. *Microsc. Microanal.* **28**, 390–403 (2022).

178. Panova, O. *et al.* Diffraction imaging of nanocrystalline structures in organic semiconductor molecular thin films. *Nat. Mater.* **18**, 860–865 (2019).

179. Oschatz, M. & Antonietti, M. A search for selectivity to enable CO 2 capture with porous adsorbents. *Energy Environ. Sci.* **11**, 57–70 (2018).

180. Zhao, Y., Liu, X., Yao, K. X., Zhao, L. & Han, Y. Superior Capture of CO 2 Achieved by Introducing Extra-framework Cations into N-doped Microporous Carbon. *Chem. Mater.* **24**, 4725–4734 (2012).

181. Lee, H. M., Youn, I. S., Saleh, M., Lee, J. W. & Kim, K. S. Interactions of CO 2 with various functional molecules. *Phys. Chem. Chem. Phys.* **17**, 10925–10933 (2015).

182. Smith, M., Scudiero, L., Espinal, J., McEwen, J. S. & Garcia-Perez, M. Improving the deconvolution and interpretation of XPS spectra from chars by ab initio calculations. *Carbon N. Y.* **110**, 155–171 (2016).

183. Dante, R. C. *et al.* Nitrogen-carbon graphite-like semiconductor synthesized from uric acid. *Carbon N. Y.* **121**, 368–379 (2017).

184. Lazar, P., Mach, R. & Otyepka, M. Spectroscopic Fingerprints of Graphitic, Pyrrolic, Pyridinic, and Chemisorbed Nitrogen in N-Doped Graphene. *J. Phys. Chem. C* **123**, 10695–10702 (2019).

185. Misra, A., Tyagi, P. K., Singh, M. K. & Misra, D. S. FTIR studies of nitrogen doped carbon nanotubes. *Diam. Relat. Mater.* **15**, 385–388 (2006).

186. Wang, H. *et al.* Laser-carbonization: Peering into the formation of micro-thermally produced (N-doped)carbons. *Carbon N. Y.* **176**, 500–510 (2021).

187. Hepp, M. *et al.* Trained laser-patterned carbon as high-performance mechanical sensors. *npj Flex. Electron.* **6**, 3 (2022).

188. Donald, M. J. & Paterson, B. End tidal carbon dioxide monitoring in prehospital and retrieval medicine: A review. *Emerg. Med. J.* **23**, 728–730 (2006).

189. Güder, F. *et al.* Paper-Based Electrical Respiration Sensor. *Angew. Chemie* **128**, 5821–5826 (2016).

190. Maier, D. *et al.* Toward Continuous Monitoring of Breath Biochemistry: A Paper-Based Wearable Sensor for Real-Time Hydrogen Peroxide Measurement in Simulated Breath. *ACS Sensors* **4**, 2945–2951 (2019).

191. Di Bartolomeo, A. Graphene Schottky diodes: An experimental review of the rectifying graphene/semiconductor heterojunction. *Phys. Rep.* **606**, 1–58 (2016).

192. Young, S. J. & Lin, Z. D. Acetone gas sensors composed of carbon nanotubes with adsorbed Au nanoparticles on plastic substrate. *Microsyst. Technol.* **24**, 3973–3976 (2018).

193. Shafiee, S. A. *et al.* Recent advances on metal nitride materials as emerging electrochemical sensors: A mini review. *Electrochem. commun.* **120**, 106828 (2020).

194. Rasaki, S. A., Zhang, B., Anbalgam, K., Thomas, T. & Yang, M. Synthesis and application of nano-structured metal nitrides and carbides: A review. *Prog. Solid State Chem.* **50**, 1–15 (2018).

195. Chen, W.-F., Muckerman, J. T. & Fujita, E. Recent developments in transition metal carbides and nitrides as hydrogen evolution electrocatalysts. *Chem. Commun.* **49**, 8896 (2013).

196. Ham, D. & Lee, J. Transition Metal Carbides and Nitrides as Electrode Materials for Low Temperature Fuel Cells. *Energies* **2**, 873–899 (2009).

197. Niu, T. Old materials with new properties II: The metal carbides. *Nano Today* **18**, 12–14 (2018).

198. Deng, Y. *et al.* Molybdenum Carbide: Controlling the Geometric and Electronic Structure of Noble Metals for the Activation of O–H and C–H Bonds. *Acc. Chem. Res.* **52**, 3372–3383 (2019).

199. Ma, Y., Guan, G., Hao, X., Cao, J. & Abudula, A. Molybdenum carbide as alternative catalyst for hydrogen production – A review. *Renew. Sustain. Energy Rev.* **75**, 1101–1129 (2017).

200. Majhi, S. M., Mirzaei, A., Kim, H. W., Kim, S. S. & Kim, T. W. Recent advances in energy-saving chemiresistive gas sensors: A review. *Nano Energy* **79**, 105369 (2021).

201. Geng, D., Li, M., Bo, X. & Guo, L. Molybdenum nitride/nitrogen-doped multi-walled carbon nanotubes hybrid nanocomposites as novel electrochemical sensor for detection l-cysteine. *Sensors Actuators B Chem.* **237**, 581–590 (2016).

202. Cho, S.-Y., Kim, J. Y., Kwon, O., Kim, J. & Jung, H.-T. Molybdenum carbide chemical sensors with ultrahigh signal-to-noise ratios and ambient stability. *J. Mater. Chem. A* **6**,

23408–23416 (2018).

203. Hantanasirisakul, K. & Gogotsi, Y. Electronic and Optical Properties of 2D Transition Metal Carbides and Nitrides (MXenes). *Adv. Mater.* **30**, 1804779 (2018).

204. Giordano, C., Erpen, C., Yao, W. & Antonietti, M. Synthesis of Mo and W Carbide and Nitride Nanoparticles via a Simple "Urea Glass" Route. *Nano Lett.* **8**, 4659–4663 (2008).

205. Howalt, J. G. & Vegge, T. Electrochemical ammonia production on molybdenum nitride nanoclusters. *Phys. Chem. Chem. Phys.* **15**, 20957 (2013).

206. Ma, L., Ting, L. R. L., Molinari, V., Giordano, C. & Yeo, B. S. Efficient hydrogen evolution reaction catalyzed by molybdenum carbide and molybdenum nitride nanocatalysts synthesized via the urea glass route. *J. Mater. Chem. A* **3**, 8361–8368 (2015).

207. Guardia-Valenzuela, J. *et al.* Development and properties of high thermal conductivity molybdenum carbide - graphite composites. *Carbon N. Y.* **135**, 72–84 (2018).

208. Zang, X. *et al.* Laser-Induced Molybdenum Carbide-Graphene Composites for 3D Foldable Paper Electronics. *Adv. Mater.* **30**, 1800062 (2018).

209. Abou Hamdan, M. *et al.* Supported Molybdenum Carbide and Nitride Catalysts for Carbon Dioxide Hydrogenation. *Front. Chem.* **8**, (2020).

210. Liu, Y. *et al.* Coupling Mo 2 C with Nitrogen-Rich Nanocarbon Leads to Efficient Hydrogen-Evolution Electrocatalytic Sites. *Angew. Chemie Int. Ed.* **54**, 10752–10757 (2015).

211. Hafaiedh, I., Elleuch, W., Clement, P., Llobet, E. & Abdelghani, A. Multi-walled carbon nanotubes for volatile organic compound detection. *Sensors Actuators B Chem.* **182**, 344–350 (2013).

212. Lipatov, A. *et al.* Highly selective gas sensor arrays based on thermally reduced graphene oxide. *Nanoscale* **5**, 5426 (2013).

213. Kumar, R. & Ghosh, R. Selective determination of ammonia, ethanol and acetone by reduced graphene oxide based gas sensors at room temperature. *Sens. Bio-Sensing Res.* **28**, 100336 (2020).

214. Esquinazi, P. *et al.* On the low-field Hall coefficient of graphite. *AIP Adv.* **4**, 117121 (2014).

215. Tu, N. D. K., Lim, J. A. & Kim, H. A mechanistic study on the carrier properties of nitrogen-doped graphene derivatives using thermoelectric effect. *Carbon N. Y.* **117**, 447–453 (2017).

216. Delacroix, S., Wang, H., Heil, T. & Strauss, V. Laser-Induced Carbonization of Natural Organic Precursors for Flexible Electronics. *Adv. Electron. Mater.* **6**, 2000463 (2020).

217. Granier, B. *et al.* Carbide Synthesis from Graphite/molybdenum Powder Mixtures at Sub-Stoichiometric Ratios under Solar Radiation Heating to 1900°C. *Mater. Trans.* **49**, 2673–2678 (2008).

218. Oshikawa, K., Nagai, M. & Omi, S. Characterization of Molybdenum Carbides for Methane Reforming by TPR, XRD, and XPS. *J. Phys. Chem. B* **105**, 9124–9131 (2001).

219. Wan, C., Regmi, Y. N. & Leonard, B. M. Multiple Phases of Molybdenum Carbide as Electrocatalysts for the Hydrogen Evolution Reaction. *Angew. Chemie Int. Ed.* **53**, 6407–6410 (2014).

220. Song, C.-M., Cao, W.-C., Bu, C.-Y., He, K. & Zhang, G.-H. Preparation of ultrafine molybdenum carbide (Mo2C) powder by carbothermic reduction of molybdenum trioxide (MoO3). *J. Aust. Ceram. Soc.* **56**, 1333–1340 (2020).

221. Predel, B. C-Mo (Carbon-Molybdenum). in *B-Ba – C-Zr* 1–4 (Springer-Verlag). doi:10.1007/10040476_643.

222. Zhang, D., Liu, A., Chang, H. & Xia, B. Room-temperature high-performance acetone gas sensor based on hydrothermal synthesized SnO 2 -reduced graphene oxide hybrid composite. *RSC Adv.* **5**, 3016–3022 (2015).

223. Sun, P. *et al.* Hierarchical α-Fe2O3/SnO2 semiconductor composites: Hydrothermal synthesis and gas sensing properties. *Sensors Actuators B Chem.* **182**, 336–343 (2013).

224. Liu, F. *et al.* Acetone gas sensors based on graphene-ZnFe2O4 composite prepared by solvothermal method. *Sensors Actuators B Chem.* **188**, 469–474 (2013).

225. Moon, H. G. *et al.* On-Chip Chemiresistive Sensor Array for On-Road NO x Monitoring with Quantification. *Adv. Sci.* **7**, 2002014 (2020).

226. Hussain, T. *et al.* Sensing of volatile organic compounds on two-dimensional nitrogenated holey graphene, graphdiyne, and their heterostructure. *Carbon N. Y.* **163**, 213–223 (2020).

227. Shao, S. *et al.* Highly crystalline and ordered nanoporous SnO 2 thin films with enhanced acetone sensing property at room temperature. *J. Mater. Chem. C* **3**, 10819–10829 (2015).

228. Liu, H. *et al.* Novel acetone sensing performance of La1-Sr CoO3 nanoparticles at room temperature. *Sensors Actuators B Chem.* **246**, 164–168 (2017).

229. Liu, B. *et al.* Functionalized graphene-based chemiresistive electronic nose for discrimination of disease-related volatile organic compounds. *Biosens. Bioelectron. X* **1**, 100016 (2019).

230. Rodner, M. *et al.* Graphene Decorated with Iron Oxide Nanoparticles for Highly Sensitive Interaction with Volatile Organic Compounds. *Sensors* **19**, 918 (2019).

231. Yang, C.-M., Chen, T.-C., Yang, Y.-C., Meyyappan, M. & Lai, C.-S. Enhanced acetone sensing properties of monolayer graphene at room temperature by electrode spacing effect and UV illumination. *Sensors Actuators B Chem.* **253**, 77–84 (2017).

232. Buckley, D. J. *et al.* Frontiers of graphene and 2D material-based gas sensors for environmental monitoring. *2D Mater.* **7**, 032002 (2020).

233. Delacroix, S. *et al.* Using Carbon Laser-Patterning to Produce Flexible, Metal-Free Humidity Sensors. *ACS Appl. Electron. Mater.* in press (2020).

234. Hugosson, H. W. *et al.* Surface energies and work functions of the transition metal carbides. *Surf. Sci.* **557**, 243–254 (2004).

235. Politi, J. R. dos S., Viñes, F., Rodriguez, J. A. & Illas, F. Atomic and electronic structure of molybdenum carbide phases: bulk and low Miller-index surfaces. *Phys. Chem. Chem. Phys.* **15**, 12617 (2013).

236. Rouse, A. A., Bernhard, J. B., Sosa, E. D. & Golden, D. E. Field emission from molybdenum carbide. *Appl. Phys. Lett.* **76**, 2583–2585 (2000).

237. Su, W. S., Leung, T. C. & Chan, C. T. Work function of single-walled and multiwalled carbon nanotubes: First-principles study. *Phys. Rev. B* **76**, 235413 (2007).

238. Fabish, T. . & Hair, M. . The dependence of the work function of carbon black on surface acidity. *J. Colloid Interface Sci.* **62**, 16–23 (1977).

239. Ivey, H. F. Thermionic Electron Emission from Carbon. *Phys. Rev.* **76**, 567–567 (1949).

240. Singhal, A. V., Charaya, H. & Lahiri, I. Noble Metal Decorated Graphene-Based Gas

Sensors and Their Fabrication: A Review. *Crit. Rev. Solid State Mater. Sci.* **42**, 499–526 (2017).

241. Wehling, T. O., Katsnelson, M. I. & Lichtenstein, A. I. Adsorbates on graphene: Impurity states and electron scattering. *Chem. Phys. Lett.* **476**, 125–134 (2009).

242. Ye, R. *et al.* In Situ Formation of Metal Oxide Nanocrystals Embedded in Laser-Induced Graphene. *ACS Nano* **9**, 9244–9251 (2015).

243. Zhang, J., Ren, M., Li, Y. & Tour, J. M. In Situ Synthesis of Efficient Water Oxidation Catalysts in Laser-Induced Graphene. *ACS Energy Lett.* **3**, 677–683 (2018).

244. Ren, M., Zhang, J. & Tour, J. M. Laser-Induced Graphene Hybrid Catalysts for Rechargeable Zn-Air Batteries. *ACS Appl. Energy Mater.* **2**, 1460–1468 (2019).

245. Zhang, J. *et al.* Efficient Water-Splitting Electrodes Based on Laser-Induced Graphene. *ACS Appl. Mater. Interfaces* **9**, 26840–26847 (2017).

246. Ansari, Z. ., Ansari, S. ., Ko, T. & Oh, J.-H. Effect of MoO3 doping and grain size on SnO2-enhancement of sensitivity and selectivity for CO and H2 gas sensing. *Sensors Actuators B Chem.* **87**, 105–114 (2002).

247. Lu, F., Liu, Y., Dong, M. & Wang, X. Nanosized tin oxide as the novel material with simultaneous detection towards CO, H2 and CH4. *Sensors Actuators B Chem.* **66**, 225–227 (2000).

248. Xu, C., Tamaki, J., Miura, N. & Yamazoe, N. Grain size effects on gas sensitivity of porous SnO2-based elements. *Sensors Actuators B Chem.* **3**, 147–155 (1991).

249. Environmental Protection Agency. *Technical Overview of Volatile Organic Compounds*. *Retrieved from https://www.epa.gov/indoor-air-quality-iaq/technical-overview-volatile-organic-compounds#definition* (2017).

250. Szulczyński, B. & Gębicki, J. Currently Commercially Available Chemical Sensors Employed for Detection of Volatile Organic Compounds in Outdoor and Indoor Air. *Environments* **4**, 21 (2017).

251. Spinelle, L., Gerboles, M., Kok, G., Persijn, S. & Sauerwald, T. Review of Portable and Low-Cost Sensors for the Ambient Air Monitoring of Benzene and Other Volatile Organic Compounds. *Sensors* **17**, 1520 (2017).

252. Probert, C., Ahmed, I., Khalid, T., Smith, S. & Ratcliffe, N. Volatile Organic

Compounds as Diagnostic Biomarkers in Gastrointestinal and Liver Diseases. *J. Gastrointestin. Liver Dis.* **18**, 337–343 (2009).

253. Hayasaka, T. *et al.* An electronic nose using a single graphene FET and machine learning for water, methanol, and ethanol. *Microsystems Nanoeng.* **6**, 50 (2020).

254. Guo, L. *et al.* Portable Food-Freshness Prediction Platform Based on Colorimetric Barcode Combinatorics and Deep Convolutional Neural Networks. *Adv. Mater.* **32**, 2004805 (2020).

255. Yan, B. *et al.* Review on porous carbon materials engineered by ZnO templates: Design, synthesis and capacitance performance. *Mater. Des.* **201**, 109518 (2021).

256. Yan, R., Leus, K., Hofmann, J. P., Antonietti, M. & Oschatz, M. Porous nitrogen-doped carbon/carbon nanocomposite electrodes enable sodium ion capacitors with high capacity and rate capability. *Nano Energy* **67**, 104240 (2020).

257. Strubel, P. *et al.* ZnO Hard Templating for Synthesis of Hierarchical Porous Carbons with Tailored Porosity and High Performance in Lithium-Sulfur Battery. *Adv. Funct. Mater.* **25**, 287–297 (2015).

258. Kossmann, J. *et al.* Cu II /Cu I decorated N-doped carbonaceous electrocatalysts for the oxygen reduction reaction. *J. Mater. Chem. A* **10**, 6107–6114 (2022).

259. Strubel, P. *et al.* ZnO Hard Templating for Synthesis of Hierarchical Porous Carbons with Tailored Porosity and High Performance in Lithium-Sulfur Battery. *Adv. Funct. Mater.* **25**, 287–297 (2015).

260. Sadezky, A., Muckenhuber, H., Grothe, H., Niessner, R. & Pöschl, U. Raman microspectroscopy of soot and related carbonaceous materials: Spectral analysis and structural information. *Carbon N. Y.* **43**, 1731–1742 (2005).

261. Pawlyta, M., Rouzaud, J.-N. & Duber, S. Raman microspectroscopy characterization of carbon blacks: Spectral analysis and structural information. *Carbon N. Y.* **84**, 479–490 (2015).

262. Bandis, C., Scudiero, L., Langford, S. C. & Dickinson, J. T. Photoelectron emission studies of cleaved and excimer laser irradiated single-crystal surfaces of NaNO3 and NaNO2. *Surf. Sci.* **442**, 413–419 (1999).

263. Kazansky, L. P., Pronin, Y. E. & Arkhipushkin, I. A. XPS study of adsorption of 2-

mercaptobenzothiazole on a brass surface. *Corros. Sci.* **89**, 21–29 (2014).

264. Biesinger, M. C., Lau, L. W. M., Gerson, A. R. & Smart, R. S. C. Resolving surface chemical states in XPS analysis of first row transition metals, oxides and hydroxides: Sc, Ti, V, Cu and Zn. *Appl. Surf. Sci.* **257**, 887–898 (2010).

265. Wöll, C. The chemistry and physics of zinc oxide surfaces. *Prog. Surf. Sci.* **82**, 55–120 (2007).

266. Lee, M.-G., Lee, S.-W. & Lee, S.-H. Comparison of vapor adsorption characteristics of acetone and toluene based on polarity in activated carbon fixed-bed reactor. *Korean J. Chem. Eng.* **23**, 773–778 (2006).

267. Strauss, V. *et al.* Using carbon laser patterning to produce flexible, metal-free humidity sensors. *ACS Appl. Electron. Mater.* **2**, 4146–4154 (2020).

268. Kwon, S., Vidic, R. & Borguet, E. The effect of surface chemical functional groups on the adsorption and desorption of a polar molecule, acetone, from a model carbonaceous surface, graphite. *Surf. Sci.* **522**, 17–26 (2003).

269. Su, C. *et al.* Insight into specific surface area, microporosity and N, P co-doping of porous carbon materials in the acetone adsorption. *Mater. Chem. Phys.* **258**, 123930 (2021).

270. Chen, R. *et al.* Fundamental understanding of oxygen content in activated carbon on acetone adsorption desorption. *Appl. Surf. Sci.* **508**, 145211 (2020).

271. Tang, M., Huang, X., Peng, Y. & Lu, S. Hierarchical porous carbon as a highly efficient adsorbent for toluene and benzene. *Fuel* **270**, 117478 (2020).

272. Lu, S. *et al.* Synthesis of N-doped hierarchical porous carbon with excellent toluene adsorption properties and its activation mechanism. *Environ. Pollut.* **284**, 117113 (2021).

273. Biscoe, J. & Warren, B. E. An X-Ray Study of Carbon Black. *J. Appl. Phys.* **13**, 364–371 (1942).

274. Faber, K., Badaczewski, F., Ruland, W. & Smarsly, B. M. Investigation of the Microstructure of Disordered, Non-graphitic Carbons by an Advanced Analysis Method for Wide-Angle X-ray Scattering. *Zeitschrift für Anorg. und Allg. Chemie* **640**, 3107–3117 (2014).

275. Pfaff, T., Simmermacher, M. & Smarsly, B. M. CarbX : a program for the evaluation of

wide-angle X-ray scattering data of non-graphitic carbons. *J. Appl. Crystallogr.* **51**, 219–229 (2018).

276. Ruland, W. & Smarsly, B. X-ray scattering of non-graphitic carbon: an improved method of evaluation. *J. Appl. Crystallogr.* **35**, 624–633 (2002).

277. Naeem, S., Baheti, V., Wiener, J. & Marek, J. Removal of methylene blue from aqueous media using activated carbon web. *J. Text. Inst.* **108**, 803–811 (2017).

278. Rafatullah, M., Sulaiman, O., Hashim, R. & Ahmad, A. Adsorption of methylene blue on low-cost adsorbents: A review. *J. Hazard. Mater.* **177**, 70–80 (2010).

279. Hang, P. T. Methylene Blue Absorption by Clay Minerals. Determination of Surface Areas and Cation Exchange Capacities (Clay-Organic Studies XVIII). *Clays Clay Miner.* **18**, 203–212 (1970).

280. Li, Y., Täffner, T., Bischoff, M. & Niemeyer, B. Test Gas Generation from Pure Liquids: An Application-Oriented Overview of Methods in a Nutshell. *Int. J. Chem. Eng.* **2012**, 1–6 (2012).

281. Lucas, G., Burdet, P., Cantoni, M. & Hébert, C. Multivariate statistical analysis as a tool for the segmentation of 3D spectral data. *Micron* **52**–**53**, 49–56 (2013).

282. Ophus, C. Four-Dimensional Scanning Transmission Electron Microscopy (4D-STEM): From Scanning Nanodiffraction to Ptychography and Beyond. *Microsc. Microanal.* **25**, 563–582 (2019).

283. Savitzky, B. H. *et al.* py4DSTEM: A Software Package for Four-Dimensional Scanning Transmission Electron Microscopy Data Analysis. *Microsc. Microanal.* **27**, 712–743 (2021).

284. Pauw, L. J. van der. A Method of Measuring Specific Resistivity and Hall Effect of Discs of Arbitrary Shape. *Philips Res. Reports* **13**, 1–9 (1958).

285. Chu, P., Niki, S., Roach, J. W. & Wieder, H. H. Simple, inexpensive double ac Hall measurement system for routine semiconductor characterization. *Rev. Sci. Instrum.* **58**, 1764–1766 (1987).

286. Kasai, A., Abdulla, A., Watanabe, T. & Takenaga, M. Highly Sensitive Precise Double AC Hall Effect Apparatus for Wide Resistance Range. *Jpn. J. Appl. Phys.* **33**, 4137–4145 (1994).

287. Wang, H. *et al.* In Situ Synthesis of Molybdenum Carbide Nanoparticles Incorporated into Laser-Patterned Nitrogen-Doped Carbon for Room Temperature VOC Sensing. *Adv. Funct. Mater.* 2104061 (2021) doi:10.1002/adfm.202104061.

9. Appendix

9.1 List of abbreviations

at%	Atomic percentage
BET	Brunauer–Emmett–Teller method
CNFAs	Carbon network-forming agents
CNTs	Carbon nanotubes
EA	Elemental analysis
EDX	Energy dispersive X-ray spectroscopy
EELS	Electron energy loss spectroscopy
FTIR	Fourier-transform infrared spectroscopy
(HR)TEM	(High-resolution) transmission electron microscopy
HAADF-STEM	High-angular annular-dark field scanning electron microscopy
IUPAC	International Union of Pure and Applied Chemistry
LP-C	Laser-patterned carbon
LP-NC	Laser-patterned nitrogen-doped carbon
NC	Nitrogen-doped carbon
PCA	Principal component analysis
PET	Polyethylene terephthalate
SEM	Scanning electron microscopy
SSA	Specific surface area
TGA	Thermogravimetric analysis

µm	micrometer
VOCs	Volatile Organic Compounds
wt.%	weight percentage
XPS	X-ray photoelectron spectroscopy
XRD	X-ray diffraction

9.2 Experimental section

9.2.1 Chemicals

Chemicals	Chemical formula	Purity	supplier
Citric acid	$C_6H_8O_7$	99%	Sigma-Aldrich
Urea	CH_4N_2O	>99.3%	Alfa Aesar
Adenine	$C_5H_5N_5$	>99%	TCI Europe N.V.
D-glucose	$C_6H_{12}O_6$	anhydrous	Thermo Fisher Scientific
Sodium iodide	NaI	99.5%	Alfa Aesar
Cytosine	$C_4H_5N_3O$	99%	Merck
Ethylene glycol	$(HOCH_2)_2$	≥ 99.7%	AnalaR Normapur
Polyvinylpyrrolidone	$(C_6H_9NO)n$	average mol wt. 10,000	Sigma-Aldrich
Ammonium heptamolybdate tetrahydrate	$(NH_4)_6Mo_7O_{24}$	≥99%	Acros Organics
Zinc nitrate hexahydrate	$Zn(NO_3)_2 \cdot 6H_2O$	standard grade	Thermo Fisher Scientific
Acetone	C_3H_6O	≥99.8% HPLC grade	Thermo Fisher Scientific
Toluene	C_7H_8	≥99.8% HPLC grade	Thermo Fisher Scientific
Ethanol	C_2H_6O	≥99.8% HPLC grade	Thermo Fisher Scientific Thermo Fisher Scientific
Hexane	C_6H_{14}	≥99.8% HPLC grade	Thermo Fisher Scientific

9.2.2 Methods

Chapter 3

Preparation of the CNFAs and references

citric acid and urea were annealed at 300 °C in a chamber oven for 2 hours. After annealing, the black reaction product was dispersed in deionized H_2O and stirred at 95 °C for 24 hours. The dispersion was centrifuged to obtain a black precipitate and a brown supernatant. The supernatant was removed and the washing process was repeated four times. After the last washing step, the precipitate was dried to obtain CA/U(300).

Glucose(300) and cytosine(300) were prepared by loading 10 ginto an alumina crucible and heating to 300°C with a heating rate of 3.11 K min^{-1}. The hold-time at 300°C was 120 min. The pre-carbonized products were used as obtained. CA/U(950), glucose(950), and cytosine(950) were prepared by loading 1 g into an alumina crucible and heating to 950°C with a heating rate of 3.11 K min^{-1}. The hold-time at 950°C was 120 min. To obtain samples for elemental analysis, large areas (10 × 10 cm) of the CNFA-films were laser-carbonized on Si-wafers. Subsequently, the laser-carbonized films were removed and the powders were collected. The powders were thoroughly washed with 1 M NaOH by sequential sonication and centrifugation until the supernatant was clear, i.e. all unconverted precursors were washed out. The remaining black solid was washed with H_2O and MeOH to remove all NaOH and to obtain the pure laser-carbonized product.

Preparation of the primary films

Ethylene glycol was added to either CA/U(300), glucose(300), or cytosine(300) and stirred for 24 hours to obtain a 1 g L^{-1} dispersion. A drop of the ink was applied onto the substrate, and the ink was doctor-bladed with a wet thickness of ~150 µm. Ethylene glycol was then evaporated at 80°C on a precision hotplate (PZ2860-SR, Gestigkeit GmbH) to obtain the final films with thicknesses of ~35 µm.

Laser-carbonization

Laser-carbonization was conducted with a high-precision laser engraver setup (Speedy 100, Trotec) equipped with a 60 W CO_2 laser. Focusing was achieved with a 2.5-inch focus lens providing a focal depth of ~ 3 mm and a focus diameter of 170 µm. The center wavelength of the laser is 10.6 ± 0.03 µm. The scanning speed v, generically given in %, was converted into

$ms\ mm^{-1}$. The resulting energy input per distance (or fluence) in the cutting mode onto the film is given by

$$F = P \cdot v = P \cdot \frac{t}{d} \qquad (9.1)$$

where P is the effective power, t is the time, and d is the distance irradiated by the laser. The laser settings (speed, power, and pulse frequency) were adjusted to meet the requirements of the precursor film and the substrate. The effective output power of the laser was measured with a Solo 2 (Gentec Electro-Optics) power meter.

WAXS fitting

Here, we provide a brief description of our model.[273] (**Figure S 5**). A more detailed description can be found in previous studies.[274–276] In principle, the obtained intensity of the scattering (I_{Obs}) is given by the normalized intensity distribution in electron units per carbon atom ($I_{e.u.}$), an absorption factor (A), a polarization factor (P), and a normalization constant (k):

$$I_{Obs} = k \cdot A \cdot P \cdot I_{e.u.} \qquad (9.2)$$

$I_{e.u}$ contains the intensity of the coherent scattering from the crystallographic structure (I_{coh}) and the incoherent Compton scattering (I_{ncoh}):

$$I_{e.u} = I_{coh} + I_{ncoh} \qquad (9.3)$$

The coherent scattering is in turn, calculated by the interlayer scattering (I_{inter}), i.e., the interference of the stacking of the different graphene layers ((00l)-eflections), the intralayer scattering (I_{intra}), i.e., the interference within a single graphene layer ((*hk*)-reflections), and the atomic form factor of carbon (f_c):

$$I_{coh} = f_c^2\ (I_{inter} + I_{intra}) \qquad (9.4)$$

I_{inter} and I_{intra} are defined by the stack size (L_c), the average (a_3) and minimal ($a_{3\ min}$) layer distance, the stacking disorder (σ_3), the layer size (L_a), and the layer disorder (σ_1). Furthermore, the average number of layers per stack N can be calculated by:

$$N = L_c / a_3 \qquad (9.5)$$

In addition to these physically meaningful parameters, the concentration of foreign atoms like hydrogen (c_H), nitrogen (c_N), oxygen (c_O), and sulphur (c_S), as well as a possible preferred orientation q during the WAXS measurement and the homogeneity of the stacks η is considered. Due to the small atomic form factor of hydrogen compared to carbon and the resulting low scattering intensity and the assumption that nitrogen is only present within the sp_2 layer

structure and the complete absence of sulphur inside these samples, only c_O was considered in this study.

Chapter 4

Preparation of the CNFAs

Glu300 and Ade300-400 were prepared by loading 1 g of D-glucose or 2 g of adenine into an alumina crucible or a quartz glass boat with a lid and heating at different temperatures between 300 and 400 °C in a tube furnace with a heating rate of 3 $K \cdot min^{-1}$. A gentle stream of N_2 (0.1 L min^{-1}) was ensured during the reaction. The hold time was 2 hours. The reaction products were retained and ground in a ball mill (diameter of the ball: 1cm) for 1h with a speed of 600 rpm to obtain finely powdered products Glu300 or Ade300-380.

Preparation of the primary films

Polyvinylpyrrolidone (PVP) (Film-forming agent) was dissolved in EtGly to obtain a 0.2 g mL^{-1} solution (PVP/EtGly). Sodium iodide (0.4g mL^{-1}) was added and dissolved. The solution was added to the CNFA and gently stirred for 24 hours to obtain homogeneous inks. The samples are labeled according to: $CNFA1_{content}$(/$CNFA2_{content}$), e.g., Ade380 and Glu300 as CNFAs synthesized from adenine and glucose by pre-carbonization at 380 °C and 300 °C, respectively. All concentrations of the different samples with respect to the volume of the solvent are given in **Table 9. 1**. A drop of the ink was applied onto the substrate, and the ink was doctor bladed with a blade distance between 300 and 500 µm. Ethylene glycol was then evaporated at 80°C on a precision hotplate (PZ2860-SR, Gestigkeit GmbH) to obtain the final films with thicknesses between 30-100 µm. The thickness was determined with a digital micrometer or vertical scanning interferometry.

Table 9. 1. *The concentrations of components in the inks.*

Inks	**Ade300-400** $g \cdot mL^{-1}$	**Glu300** $g \cdot mL^{-1}$	**EtGly/PVP** µL
Ink_Ade300-Ade400	0.57	0	350
Ink_Glu300	0	0.47	430
	Ade380 $g \cdot mL^{-1}$	**Glu300** $g \cdot mL^{-1}$	**EtGly/PVP** µL
Ink_$Ade380_{10}$/$Glu300_{90}$	0.06	0.51	350
Ink_$Ade380_{20}$/$Glu300_{80}$	0.11	0.46	350
Ink_$Ade380_{35}$/$Glu300_{65}$	0.2	0.37	350
Ink_$Ade380_{50}$/$Glu300_{50}$	0.29	0.29	350
Ink_$Ade380_{65}$/$Glu300_{35}$	0.37	0.2	350
Ink_$Ade380_{80}$/$Glu300_{20}$	0.51	0.06	350
Ink_$Ade380_{90}$/$Glu300_{10}$	0.51	0.06	350

Laser-carbonization

Laser-carbonization was conducted with a high-precision laser engraver setup (Speedy 100, Trotec) equipped with a 60 W CO_2 laser. Focusing was achieved with a 2.5-inch focus lens providing a focal depth of ~3 mm and a focus diameter of d = 170 µm. The center wavelength of the laser is 10.6 ± 0.03 µm. The scanning speed v, generically given in %, was converted into cm·s^{-1}. The effective output power P in watts of the laser was measured with a Solo 2 (Gentec Electro-Optics) power meter. The resulting energy input per area (or fluence) F in J·cm^{-2} in the vector mode onto the film is given by Equation 9.1.

For the experiments, the laser settings were adjusted to meet the requirements of the films according to **Table 9. 2**. A standard sensor strip is made of five parallel lines of 5 mm in length distributed across a width of 0.5 mm. An open-top atmospheric chamber was designed to generate a continuous flow of a selected gas (O_2 or N_2) for the fabrication of LP-NC under controlled gas atmospheres (Figure S3). The laser-patterned (LP) samples are labeled according to $LP_{atmosphere}$_$CNFA1_{content}$(/$CNFA2_{content}$), e.g., LP_{O2}_$Ade380_{90}$/$Glu300_{10}$ for a laser-patterned film of a mixture of Ade380:Glu300 (90:10 wt%) as CNFAs under O_2 reaction atmosphere.

Table 9. 2. *Laser parameters used in the experiments to fit the coating thickness.*

Samples	Thickness µm	Power % (generic)	Power W	Speed % (generic)	Speed cm·s^{-1}	Fluence J·cm^{-2}
LP_Glu300	75	2.20	1.12	0.30	0.53	125
LP_Ade380	75	2.10	1.07	0.30	0.53	119
$LP_{O2/N2/air}$_$Ade380_{90}$/$Glu300_{10}$	45	1.90	0.97	0.30	0.53	108
	75	2.10	1.07	0.30	0.53	119
	100	2.20	1.12	0.30	0.53	125

CO_2 sensing

The sensor platforms were placed in a gas-proof glass flow cell (V_{cell} ≈ 0.1 L) and their ends were connected to two electrode bins. The electrical characterization was performed with an impedance unit at a frequency of 80 Hz and an alternating current (AC) of 0.05 mA for all measurements.

The total flow of gas mixtures was set to 1 L·min^{-1}. Concentrations of 0.5%, 1%, 5%, and 10% CO_2 with respect to the total flow were controlled by mass flow controllers (GF040, Brooks Instrument GmbH). Humidity was controlled by a humidity generator (HUMIgen-04, Dr. Wernecke Feuchtemesstechnik).

Langmuir's model was used to describe the interaction between the gas molecules and the sensor surface. At a given temperature, the fraction of occupied sites on the sensor surface is *θ.* The equilibrium constant of adsorption K is defined as the ratio between the rate constants of adsorption k_A and desorption k_D. The variation of θ is given by eq (9.6), where P_A is the partial pressure of the analyte in the gas phase:

$$\theta = \frac{K * P_A}{1 + K * P_A} \qquad (9.6)$$

When molecules are adsorbed on the surface of the LP-NC, the resistivity decreases. Then θ is given by:

$$\theta = \alpha * (R_0 - R_{eq}) \qquad (9.7)$$

where R_0 is the initial resistance, and R_{eq} is the resistance at equilibrium, α is the proportionality coefficient.

The heat of adsorption of CO_2 or H_2O was determined according to the van't Hoff equation (eq (*9.8*).

$$\frac{d(lnK)}{dT} = \frac{\Delta H_{ads}}{RT^2} \qquad (9.8)$$

Bending experiments

The experiments were performed with a homemade movable stage. The PET-supported sample strip was mounted between two electrodes (one movable) at a distance of 25 mm and bent in a positive (upwards) direction (Figure S20). To provide better electrical contact, both ends of the carbon strip were connected with silver paint. The curvature of the bending was determined by translating the shapes from photographs into x-y data using the freeware Engauge Digitizer. The curvature is defined as the inverse radius at the maximum point of bending.

Sample preparation for electron microscopy

Cross-sectional preparation of the sensors was conducted by ultramicrotomy utilizing a Leica EM UC7 microtome. Individual sensor strips were separated by doctor-blade cutting and embedded in epoxy resin (Araldite 502, Science Services, Germany) to facilitate the sectioning of the highly porous sensor heterostructures. Impregnation of the pores was supported by evacuation and subsequent pressurization of the uncured resin using a dedicated pressure vessel (mini clave steel, Büchi AG, Switzerland). Curing was carried out overnight at 60 °C. To create

a trapezoid-shaped block face and to remove potentially damaged sample regions from cutting, trimming with a diamond knife (DiATOME 45° trim knife) was performed. A DiATOME 45° ultrasonic diamond knife was employed to obtain cross-sectional TEM samples with minimal compression. The floating sections (deionized water) were transferred onto lacey carbon TEM grids (Plano AG) to provide sufficient support at reduced impact during EELS measurements. The resulting block face was used for complementary analysis by optical microscopy (OM) and environmental SEM.

Chapter 5

Preparation of the CNFA

The CNFA (CA/U (300)) was prepared according to the methods described in **Chapter 3** above.

Preparation of the precursor films

Polyvinylpyrrolidone (PVP) (Film-forming agent) was dissolved in ethylene glycol (EtGly) to obtain a 0.2 g mL^{-1} solution (PVP/EtGly). Ammonium heptamolybdate ($(NH_4)_6Mo_7O_{24}$) (0.1 g mL^{-1}) and/or sodium iodide (NaI) (0.1-0.4 g mL^{-1}) were added and carefully dissolved. CA/U(300) was then added and stirred for 24 hours to obtain a 0.8 g mL^{-1} ink. All concentrations are given with respect to the volume of the solvent. A drop of the ink was applied onto the substrate, and the ink was doctor-bladed with a wet-thickness between 155 and 305 µm. Ethylene glycol was then evaporated at 80°C on a precision hotplate (PZ2860-SR, Gestigkeit GmbH) to obtain the final films with thicknesses between 13-70 µm. The thickness was determined with a digital micrometer or cross-sectional SEM.

Laser-carbonization

Laser-carbonization was conducted with a high-precision laser engraver setup (Speedy 100, Trotec) equipped with a 60 W CO_2 laser. Focusing was achieved with a 2.5-inch focus lens providing a focal depth of ~3 mm and a focus diameter of 170 µm. The center wavelength of the laser is 10.6 ± 0.03 µm. The scanning speed v', generically given in%, was converted into s m^{-1}. The effective output power P of the laser was measured with a Solo 2 (Gentec Electro-Optics) power meter. The resulting energy input per distance (or fluence) F in $J \cdot m^{-1}$ in the vector mode onto the film is given by (Equation 9.1)

For the experiments, the laser settings were adjusted to meet the requirements of the films according to ***Table 9. 3***.

Table 9. 3. *Laser parameters used in the experiments to fit the film thickness.*

thickness µm	power % (generic)	power W	speed % (generic)	speed s m^{-1}	fluence J m^{-1}
13	1.9	0.97	0.6	98	94.5
19	2.0	1.02	0.6	98	99.5
28	2.1	1.07	0.6	98	104.5
56	2.5	1.27	0.6	98	124.4
70	2.7	1.37	0.6	98	134.3

Determination of the specific surface areas

The specific surface areas of LP-NC were determined by the methylene blue adsorption method.[277–279] LP-NC films in a size of 2 × 1 cm were printed on PET sheets, and their masses were determined with a micro-balance. The PET-supported films were then immersed into 6 mL of 9.5×10^{-5} M solutions of methylene blue in polypropylene vials and stirred for 24 hours. The solutions were centrifuged, and the amount of adsorbed MB was determined by measuring the absorbance of the supernatant with respect to a reference solution. An area of 1.35 nm^2 per molecule MB is assumed.

VOCs sensing

The sensor platforms were placed in a gas-proof glass flow cell ($V_{cell} \approx 0.1$ L), and their ends were connected to two electrode pins. The electrical characterization was performed with an impedance unit at a frequency of 1000 Hz and a current intensity of 0.05 mA for all measurements. The total flow of nitrogen was set to 1 $L \cdot min^{-1}$. 30-minute cycles between pure nitrogen and a flow containing different contents of acetone were performed. Either 1, 5, or 10% of the total flow was passed through a reservoir of the liquid VOCs with a temperature fixed at 30 °C. The final concentration of the analyte was approximated using the ideal gas law based on the vapor pressure of the VOC.[280]

Chapter 6

Preparation of the CNFA

citric acid and urea were mixed in equivalent weight proportions in a quartz crucible. The mixture was annealed at 300 °C in a tube furnace (RHTC 80/450/15, Nabertherm) for 2 hours with a heating rate of 3.11 K min^{-1}. After annealing, the reaction products were ground by ball milling (PM 100, Retsch) for 1 h at 600 rpm. The resulting black powder is named CA/U(300).

Preparation of the ZnO nanorods

3g $Zn(NO_3)_2$ and 0.8g NaOH were added into 500ml H_2O. The resulting white suspension was partially added to the microwave vessel. Then using microwave power, 200 W to reach the reaction temperature 150 ºC held for 5 min. The reaction product mixture was centrifuged to remove the soluble part. The precipitate was washed with ethanol and centrifuged. The washing process was repeated 2 times. The obtained white solid ZnO nanorods were dried overnight at 70 ºC in the oven.

Preparation of the primary films

Polyvinylpyrrolidone (PVP) (film-forming agent) was dissolved in ethylene glycol (EtGly) to obtain a 0.2 g mL^{-1} solution (PVP/EtGly). Solutions with eight different concentrations of zinc nitrate ($Zn(NO_3)_2$) ranging from 0 to 0.6 mg mL^{-1} were prepared, referred to as LP-C/Zn(**1-8**), where the number represents the amount of Zn in wt% (**Table 9. 4**). CA/U(300) was then added and stirred for 24 hours to obtain a viscous suspension with a concentration of 0.8 g·mL^{-1}. All concentrations are given with respect to the volume of the solvent. A drop of the ink was applied onto the substrate, and the ink was doctor bladed with a blade distance of 300 µm. Ethylene glycol was then evaporated at 80 °C on a precision hotplate (PZ2860-SR, Gestigkeit GmbH) overnight to obtain films with a thickness of 40 µm. The thickness was determined with a digital micrometer or cross-sectional SEM.

Table 9. 4. *Composition of the investigated samples.*

sample	CA/U(300)	$Zn(NO_3)_2 \cdot 6\ H_2O$	ZnO nanorods	effective m_{Zn}
	mg	mg	mg	wt%
LP-C/Zn(0)	200	0		0%
LP-C/Zn(1)	200	10		1%
LP-C/Zn(2)	200	20		2%
LP-C/Zn(4)	200	40		4%
LP-C/Zn(5)	200	60		5%
LP-C/Zn(6)	200	80		6%
LP-C/Zn(7)	200	100		7%
LP-C/Zn(8)	200	120		8%
LP-C/ZnO(2)	200		5	2%
LP-C/ZnO(7)	200		20	7%

Laser-carbonization

A high-precision laser engraver setup (Speedy 100, Trotec) equipped with a 60 W CO_2-laser ($\lambda = 10.6 \pm 0.03$ µm) was used for laser-carbonization. Focusing was achieved with a 2.5 inch focus lens providing a focal depth of ~ 3 mm and a focus diameter of 170 µm. The scanning speed v', generically given in percentage, was converted into $s \cdot m^{-1}$. The effective output power P of the laser was measured with a Solo 2 (Gentec Electro-Optics) power meter. The resulting energy input per distance (or fluence) F in J m^{-1} in the vector mode onto the film is given by Equation 9.1.

For the experiments, the laser settings were adjusted to meet the requirements of the films according to Error! Reference source not found.. Each laser pattern consists of five parallel laser lines with a length of 5 mm and a line separation of 0.1 mm to obtain a sensor film.

***Table 9. 5**. Laser parameters used in the experiments to fit the film thickness.*

thickness µm	**power** % (generic)	**power** W	**speed** % (generic)	**speed** s m^{-1}	**fluence** J m^{-1}
20	2.0	1.02	0.6	98	99.5

Determination of the specific surface areas

The methylene blue adsorption method was used.[277–279] LP-C films of size 2 × 4 cm^2 were printed on PET sheets. Pieces of ~0.5 × 1 cm with the laser-patterned films on top were balanced and then immersed into defined solutions of methylene blue (9.5×10^{-5} M) to disperse the LP-C film in the solution. To determine the mass of the film, the PET substrate was removed and weighted. The LP-C dispersion in the MB solution was stirred for 24 hours and then centrifuged. The amount of adsorbed MB was determined by measuring the absorbance of the supernatant with respect to a reference solution. An area of 1.35 nm^2 per molecule MB is assumed. As a reference, the same mass of activated carbon was used (1269 m^2 g^{-1}). The standard error was determined by the standard deviation of six values obtained from six measurements.

VOCs sensing

The sensor experiments were performed in a gas-flow cell ($V_{cell} \approx 0.1$ L). The ends of the sensor films were connected to two electrode pins and electrically characterized with an impedance unit (Solartron 1287 potentiostat in combination with a SI 1260 impedance unit) at a frequency of 1000 Hz and in AC conditions applying a current of 0.05 mA. The gas flow was controlled with a set of three mass-flow controllers (GF040 from Brooks instruments). The total gas flow was set to 1 $L \cdot min^{-1}$. Cycles of 30 minutes between pure nitrogen and the analytes (acetone,

toluene, ethanol and hexane) were performed. To this end, a defined volume of the total flow was passed through a reservoir of the respective liquid VOCs. The final concentration of the analyte was approximated using the ideal gas law based on the vapor pressure of the VOC.

9.2.3 Instrumental methods

Scanning electron microscopy (Chapter 3 and Chapter 5) was performed on a Zeiss LEO 1550-Gemini system (acceleration voltage: 3 to 10 kV). An Oxford Instruments X-MAX 80 mm^2 detector was used to collect the SEM-EDX data.

***Scanning electron microscopy (Chapter 4)*:** Top-view *scanning electron microscopy* with secondary electrons was performed on a Zeiss LEO 1550-Gemini field-emission microscope (acceleration voltage: 3-10 kV). Cross-sectional EDXS element mapping and related imaging with back-scattered electrons of the embedded sensors (microtomy block surface) were performed using an environmental FEI Quanta 250 FEG-SEM. The instrument is equipped with an Apollo XL SSD detector for energy-dispersive X-ray spectroscopy and a differential pumping system to allow operation at low-vacuum levels for minimal charging. EDXS element maps were obtained at 5 keV primary electron energy to obtain sufficient count rates at the best achievable lateral resolution under low-vacuum conditions (around 100 Pa).

***Scanning electron microscopy (Chapter 6)*:** Top-view *scanning electron microscopy* with secondary electrons was performed on a Zeiss LEO 1550-Gemini system (acceleration voltage: 3 to 10 kV). An Oxford Instruments X-MAX 80 mm^2 detector was used to collect the SEM-EDX data. Cross-sectional imaging with back-scattered electrons and EDXS element mapping of the epoxy-embedded samples (microtomy block surface) were performed using an environmental FEI Quanta 250 FEG-SEM. An Apollo XL SDD detector was used to obtain EDXS element maps at 5 keV primary electron energy as a compromise between count rate and lateral resolution. To reduce sample charging, the instrument was operated at an N_2 pressure of 70-90 Pa.

Transmission electron microscopy (Chapter 3) was performed using an EM 912 Omega from Zeiss operating at 120 kV. To prepare the TEM samples, the carbon material was dispersed in methanol by sonication for 10 min and applying 5 µL droplets of the dispersion were on a carbon-coated copper TEM grid and dried at room temperature.

Transmission electron microscopy (Chapter 4): For bright-field *transmission electron microscopy* (bright-field TEM, BFTEM), selected-area electron diffraction (SAED, selected area diameter 150 nm), and high-resolution TEM (HRTEM), a FEI TitanX 60-300 TEM

(NCEM/LBNL) (Schottky emitter, super twin objective lens, no aberration corrector, operated at 200 kV acceleration voltage) with Gatan 2k Ultrascan CCD camera was utilized. A gold particle sample was used to calibrate microscope magnification and camera length.

High-angle annular dark-field *Scanning TEM* (HAADF-STEM) in conjunction with electron energy-loss spectroscopy (EELS) was carried out using an FEI Talos F200X S/TEM (MNaF/Univ. Siegen) at 200 kV acceleration voltage. The microscope is equipped with an XFEG high-brightness gun and a Gatan Continuum ER spectrometer (with high-speed DualEELS, DigiScan, EDXS integration, and GMS 3.5x). The acceleration voltage of 200 kV was chosen as a compromise between the mean-free path for inelastic scattering (EELS) and electron-beam-induced damage, the latter being minimized by sub-pixel scanning during EELS mapping acquisition.

EELS mappings were acquired from representative areas of the microtomic sensor cross-sections, which exhibit excellent and homogeneous relative thicknesses of $t/\lambda \approx 0.35\text{-}0.5$ depending on the local sensor density (around 0.25 for the adjacent embedding epoxy due to the lower density). Dual EELS mappings (step size ~20 nm) with core loss spectra in the energy-loss range of 200-800 eV (dispersion 0.3 eV/channel, ratio convergence/acceptance angle around 2) were recorded to cover the essential ionization of C, N, and O at around 285 eV, 400 eV, and 532 eV, respectively. Energy calibration was employed utilizing the respective low-loss datasets.

EELS element distributions for C, N, and O were derived by quantification with theoretical cross-sections as implemented in the Gatan software. For background correction, a power law function for C, O but a 1st-order log-polynomial function for N were employed (pre-edge fit range for all elements: 50 eV, post-edge fit ranges: 50 eV (C) and 25 eV (N, O)). As hydrogen as well as Na, I are not accessible in the recorded spectra range. The presented atomic concentrations refer to $c_C + c_N + c_O = 100$ at%.

To unravel variations of the local bond states within the sensor cross-sections without *a priori* knowledge of the resultant reaction products, principal component analysis (PCA), as implemented in GMS 3.40 (with Varimax orthogonal matrix rotation)[281] was applied to the recorded EELS datasets. As a result, PCA components were obtained, which describe individual phases, meaning which include all three ionization edges rather than individual element-specific signals. The spatial distributions in the main manuscript depict the lateral weighting factors of those identified components/phases. Due to better statistics, however, the

phase-specific PCA components were separated into their C, N, and O contributions (independent background correction for each ionization edge), normalized with respect to the maximal intensity of the C K ionization edge, and presented throughout the manuscript. To verify the validity of those obtained spectral PCA distributions, 50 experimental spectra were selected from the respective mapping datasets, summed, normalized, and compared to the corresponding spectral PCA components (**Figure S 8**).

Experimental 4D-STEM datasets were acquired using the TEAM I instrument (NCEM/LBNL), a double aberration-corrected Thermo Fisher Titan fitted with a Gatan Continuum energy filter and K3 direct electron detector (operated in electron counting mode, 4× binning).[282] The energy-filtered diffraction patterns (15 eV slit width, central beam covered by 2.5 mrad beam stop) were acquired at an accelerating voltage of 300 kV in microprobe mode with a beam convergence semi-angle of 0.7 mrad (beam diameter approx. 2 nm, beam current 70 pA) and a covered spectrometer semi-angle of maximum 21 mrad. A shadow image of the sample (i.e., a strongly defocused image of the STEM probe) was recorded to align the rotation between the scan field and recorded diffraction patterns. The datasets were evaluated employing the py4DSTEM software package.[283] Details are provided in the supporting information. Fourier-transform infrared spectroscopy

Transmission electron microscopy (Chapter 5) was performed using a double Cs corrected JEOL JEM-ARM200F (S)TEM operated at 80kV, 10µA and equipped with a cold-field emission gun and a high-angle silicon drift Energy Dispersive X-ray (EDX) detector (solid angle up to 0.98 steradians with a detection area of 100 mm^2). *Annular Dark Field Scanning Transmission Electron Microscopy* (ADF-STEM) images were collected at a probe convergence semi-angle of 25mrad. The so-called "beam shower" procedure was performed with a defocused beam at a magnification of 8000 fold for 30 minutes; it was necessary for reducing hydrocarbon contamination during subsequent imaging at high magnification. To prepare the TEM samples, the carbon material was dispersed in methanol, sonicated for 10 min, drop cast on a Lacey carbon TEM grid, and dried at room temperature.

Transmission electron microscopy (Chapter 6) was performed using a Thermo Fisher FEI Talos F200X operated at 200 kV. Besides an XFEG high-brightness gun and a large-area Super-X EDXS detector, the instrument is equipped with a Gatan Continuum ER spectrometer for electron energy-loss spectroscopy. Bright-field imaging, selected-area electron diffraction, high-resolution TEM, and high-angle annular dark-field scanning TEM were utilized to analyze the structure and morphology of the LP-C microtomic cross-sections. Dual EELS

mappings with an energy range of the core-loss spectra of 200-800 eV (dispersion 0.3 eV/channel) for the upper region and 200-1800 eV (dispersion 0.75 eV/channel) for the lower region were acquired to include the ionization edges of C, N, O and Zn at around 285 eV, 400 eV, 532 eV and 1020 eV, respectively.

To visualize the distribution of graphitized carbon in the top layer as well as the N and Zn distributions of the bottom layer, principal component analysis (PCA) was employed to analyze the STEM-EELS data. PCA was used as implemented in the Gatan Microscopy Suite (GMS) version 3.4. (The details of the data evaluation are described in our previous study).

Raman spectroscopy*: Raman* spectra were obtained with a confocal Raman Microscope (alpha300, WITec, Germany) equipped with a piezo-scanner (P-500, Physik Instrumente, Karlsruhe, Germany). The laser, λ = 532 nm, was focused on the samples through a 50 fold objective. The laser power on the sample was set to 5.0 mW.

Fourier-transform infrared spectroscopy was performed using a Nicolet iS 5 FT-IR-spectrometer in conjunction with an iD5 ATR unit from ThermoFisher Scientific.

Extinction coefficients were determined by measuring a series of transmission infrared absorption spectra with known concentrations in the range between 1.6 and 7.8 g/L pressed into KBr pellets. The absorbance was plotted against the concentration, and the extinction coefficients were determined from the slope of the fitting curve.

Thermogravimetric analysis was performed using a Thermo Microbalance TG 209 F1 Libra (Netzsch, Selb, Germany). A platinum crucible was used for the measurement of 10 ± 1 mg of samples in a nitrogen flow of 20 mL min^{-1} and a purge flow of 20 mL min^{-1} at a heating rate of 10 K min^{-1}.

Elemental analysis was performed with a vario MICRO cube CHNOS elemental analyzer (Elementar Analysensysteme GmbH). The elements were detected with a thermal conductivity detector (TCD) for C, H, N and O and an infrared (IR) detector for sulfur.

X-ray diffraction was performed on a Bruker D8 Advance diffractometer in the Bragg-Brentano mode at the Cu Kα wavelength.

Impedance measurements were performed on a Solartron 1287 potentiostat in combination with a SI 1260 impedance unit. For frequency measurements, the current was kept constant at 0.1 mA, and for current sweeps, a frequency of 100 Hz was used.

Hall measurements (Chapter 4): the electrical conductivity σ of carbonized films was determined at room temperature by the van der Pauw method[284] in a Hall effect measurement system 8404 (Lake Shore Cryotronics, Inc.). The samples, all shaped in precise cloverleaf geometry with 10 mm diameter, were placed on a commercial 10 mm prober pin sample card of the 8404 Hall effect measurement system. Excitation currents from -5 to +5 mA have been used for the I-V measurements. All the I-V curves for all four different four-probe contact configurations show the expected linear behavior.

Both the DC and the Double AC Hall method[285,286] employing two MFLI lock-in amplifiers (Zurich Instruments AG) and a CS580 voltage-driven current source (Stanford Research Systems) have been applied in the same setup to determine the charge carrier concentration. Different sets of oscillating excitation current (I =2 mA to 6 mA with frequency f_I = 88 Hz) and magnetic field (0.08 T, 0.16 T and 0.23 T with frequency f_B = 0.8 Hz) have been used to measure the Hall voltage $V_H = V(f_I + f_B) + V(f_I - f_B)$, automated by a home made LabVIEW program. The linear relationship between V_H and $I \times B$ (**Equation 9.9**) is used to calculate the charge carrier density

$$p = \frac{1}{et}\frac{\partial(I \times B)}{\partial V_H} \qquad (9.9)$$

Where e is the elementary charge and t is the thickness of the sample. The charge carrier mobility μ was calculated by the formula $\mu = \frac{\sigma}{pe}$.

Hall measurements (Chapter 5) were carried out at room temperature in an Accent HL5500PC using a magnetic strength of 0.3T. The samples were fabricated in a cloverleaf geometry and the pins contacted the film via indium pads. After checking the ohmic response of the contacts the measurements for LP-NC(NaI40) were done with the current source set for AC operation under vacuum. The entire Hall measurement was cycled 5 times and the averaged value was sent to the result area. For LP-MoC_{1-x}(10)@NC and LP-MoC_{1-x}(10)@NC(NaI40), the measurements were done in the DC mode. Each measurement was repeated a minimum 4 times.

X-ray photoelectron spectroscopy (Chapter 4) was performed at the ISISS beamline of the synchrotron radiation facility BESSY II of Helmholtz-Zentrum Berlin, Germany. The used endstation consisted of a bending magnet (D41) and a plane grating monochromator (PGM) in the soft X-ray range 80-2000 eV with an 80-200 µm beam spot. The photoelectron analyzer is provided by SPECS GmbH (Phoibos 150) hemispherical analyzer. In order to minimize losses of photons and electrons, a 50 nm thick SiNx X-ray membrane close to the sample was used.

Each sample was fixed on the sapphire sample holder. XPS spectra were analyzed through CasaXPS and Igor Pro. The spectra were deconvoluted with a combined Gaussian and Lorentzian function after a Shirley + linear background subtraction.

X-ray photoelectron spectroscopy (Chapter 5) was performed with a CISSY station (UHV) with a SPECS XR 50 X-ray gun Mg Kα radiation (1254.6 eV) and combined lens analyzer module. The Shirley background deletion was used in photoemission spectra analysis.

X-ray photoelectron spectroscopy (Chapter 6) was acquired using a Kratos Axis SUPRA using monochromated Al kα (1486.69 eV) X-rays at 15 mA emission and 12 kV HT (180W) and a spot size/analysis area of 700 x 300 µm. The instrument was calibrated to gold metal Au 4f (83.95 eV) and dispersion was adjusted to give a BE of 932.6 eV for the Cu 2p3/2 line of metallic copper. Ag 3d5/2 line FWHM at 10 eV pass energy was 0.544 eV. The source resolution for monochromatic Al Kα X-rays is ~0.3 eV. The instrumental resolution was determined to be 0.29 eV at 10 eV pass energy using the Fermi edge of the valence band for metallic silver. Resolution with charge compensation system on <1.33 eV FWHM on PTFE. High-resolution spectra were obtained using a pass energy of 20 eV, step size of 0.1 eV and sweep time of 60s, resulting in a line width of 0.696 eV for Au 4f7/2. Survey spectra were obtained using a pass energy of 160 eV. Charge neutralization was achieved using an electron flood gun with filament current = 0.4 A, charge balance = 2 V, and filament bias = 4.2 V. Successful neutralization was adjudged by analyzing the C 1s region wherein a sharp peak with no lower BE structure was obtained. Spectra have been charge corrected to the main line of the carbon 1s spectrum (adventitious carbon) set to 284.8 eV. All data was recorded at a base pressure of below 9×10^{-9} Torr and a room temperature of 294 K. Data was analyzed using CasaXPS v2.3.19PR1.0. Peaks were fit with a Shirley background prior to component analysis.

9.3 Appendix figures

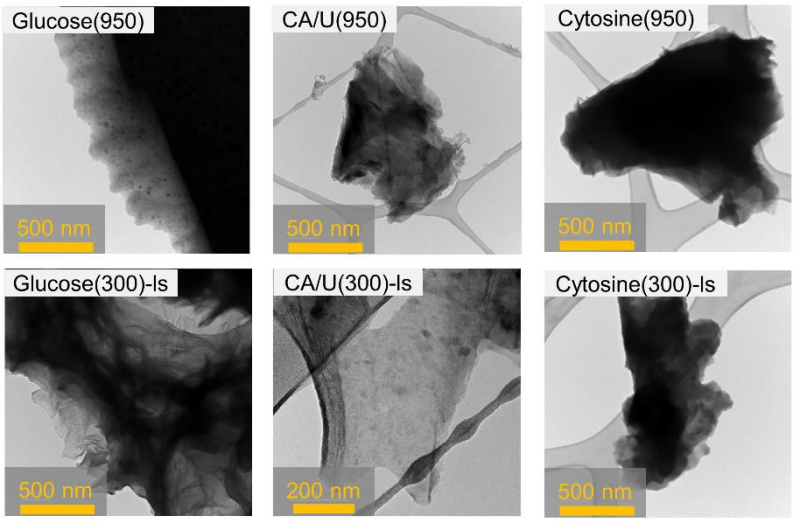

Figure S 1. High-resolution transmission electron micrographs of fragments of glucose(950), glucose(300)-ls, CA/U(950), CA/U(300)-ls, and cytosine(950), and cytosine(300)-ls. The insets show the electron diffraction pattern of the selected areas.

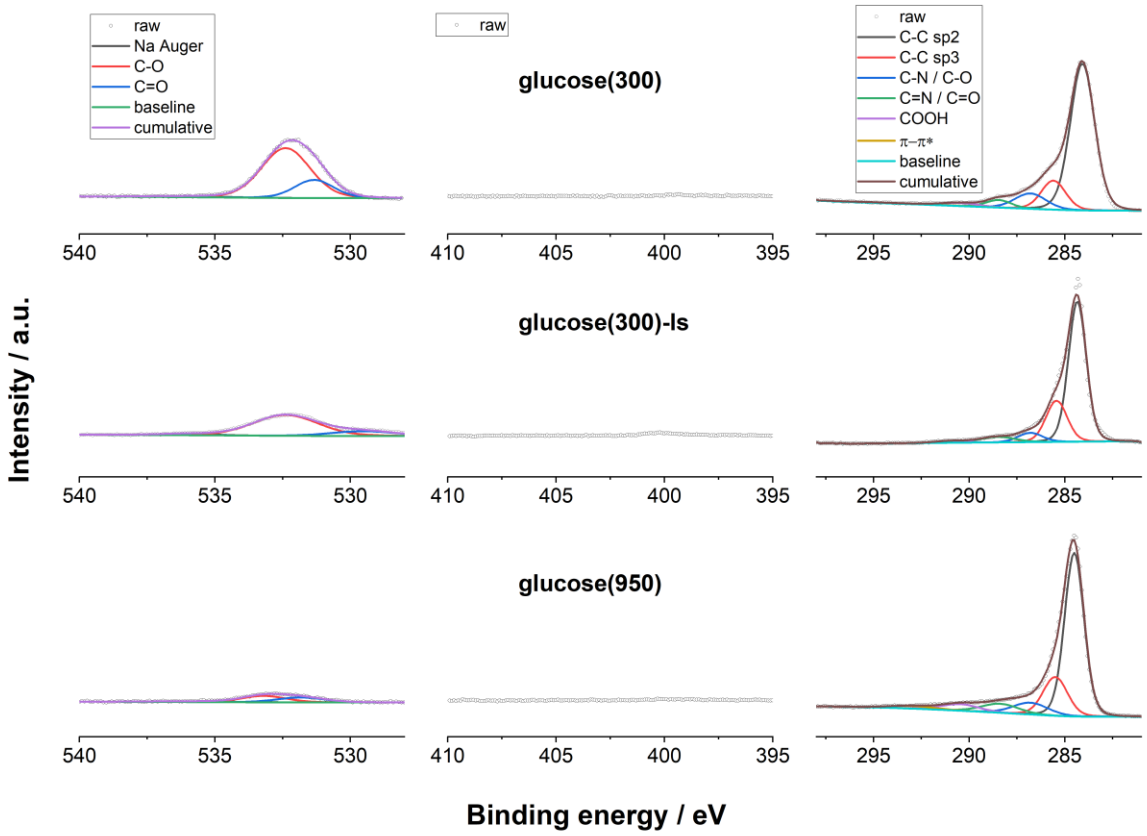

Figure S 2. X-ray photoelectron spectrographs of the O_{1s}, N_{1s}, and C_{1s} regions (from left to right) of glucose(300), glucose(300)-ls, and glucose(950) (top to bottom).

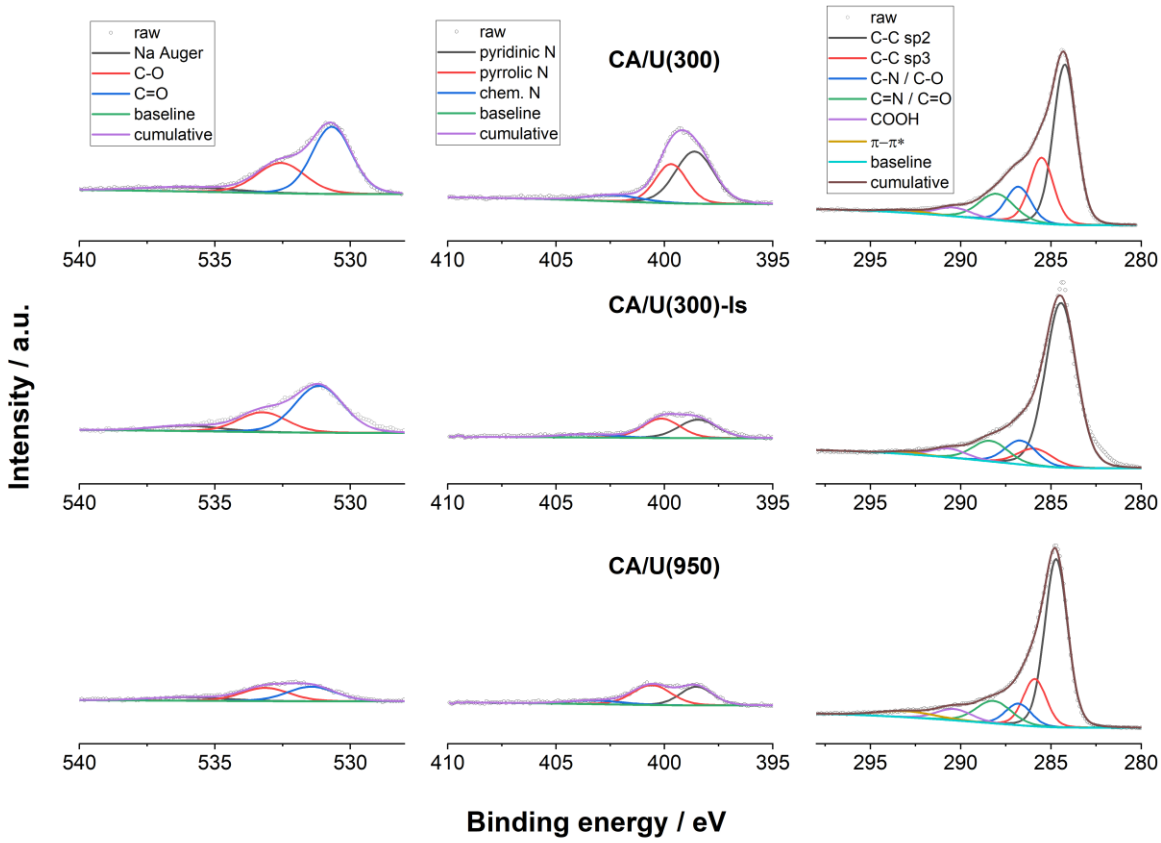

Figure S 3. X-ray photoelectron spectrographs of the O_{1s}, N_{1s}, and C_{1s} regions (from left to right) of CA/U(300), CA/U(300)-ls, and CA/U(950) (top to bottom).

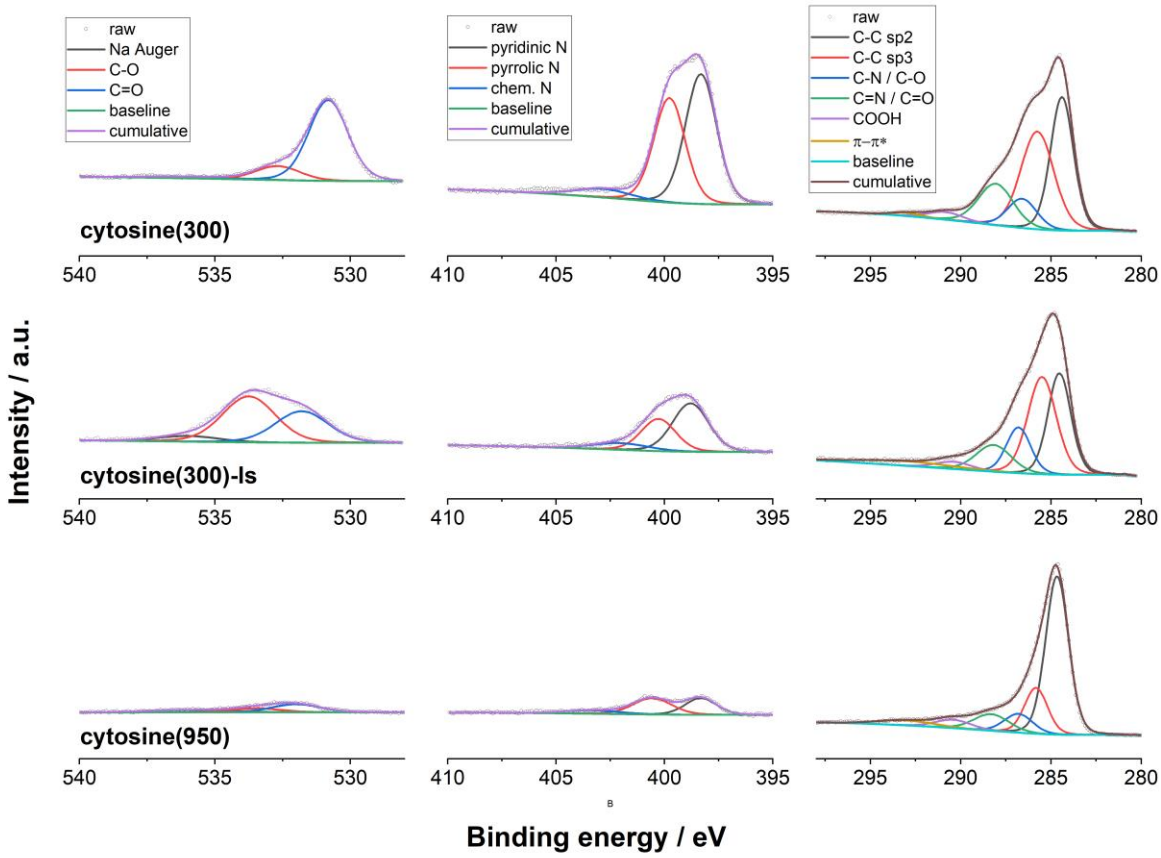

Figure S 4. X-ray photoelectron spectrographs of the O_{1s}, N_{1s}, and C_{1s} regions (from left to right) of cytosine(300), cytosine(300)-ls, and cytosine(950) (top to bottom).

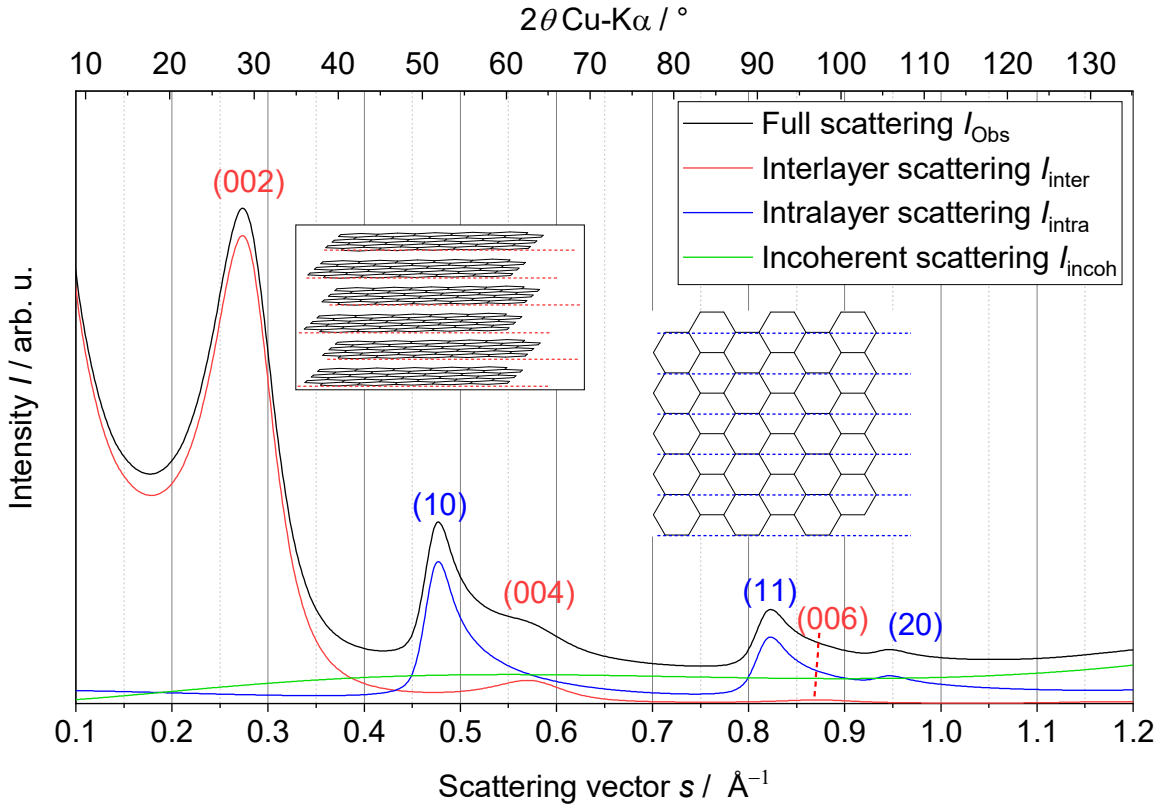

Figure S 5. Principle structure of non-graphitic carbons (NGCs) containing a turbostratic stacking arrangement of single graphene layers.

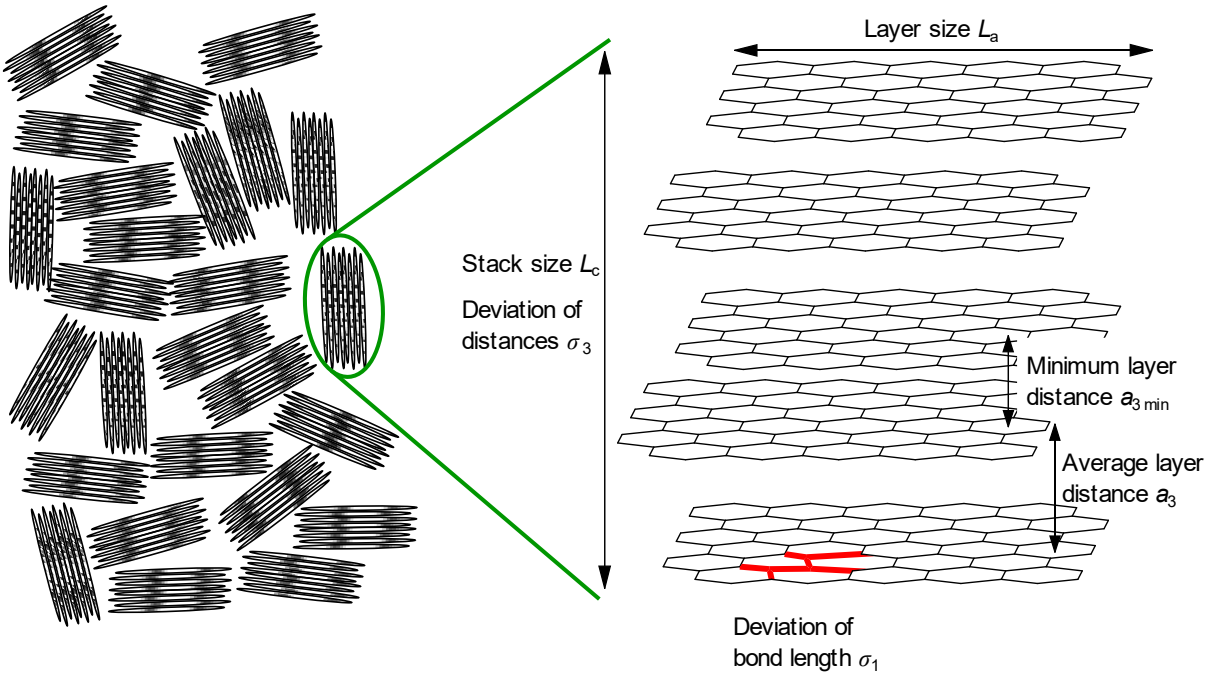

Figure S 6. Principle structure of non-graphitic carbons (NGCs) containing a turbostratic stacking arrangement of single graphene layers.

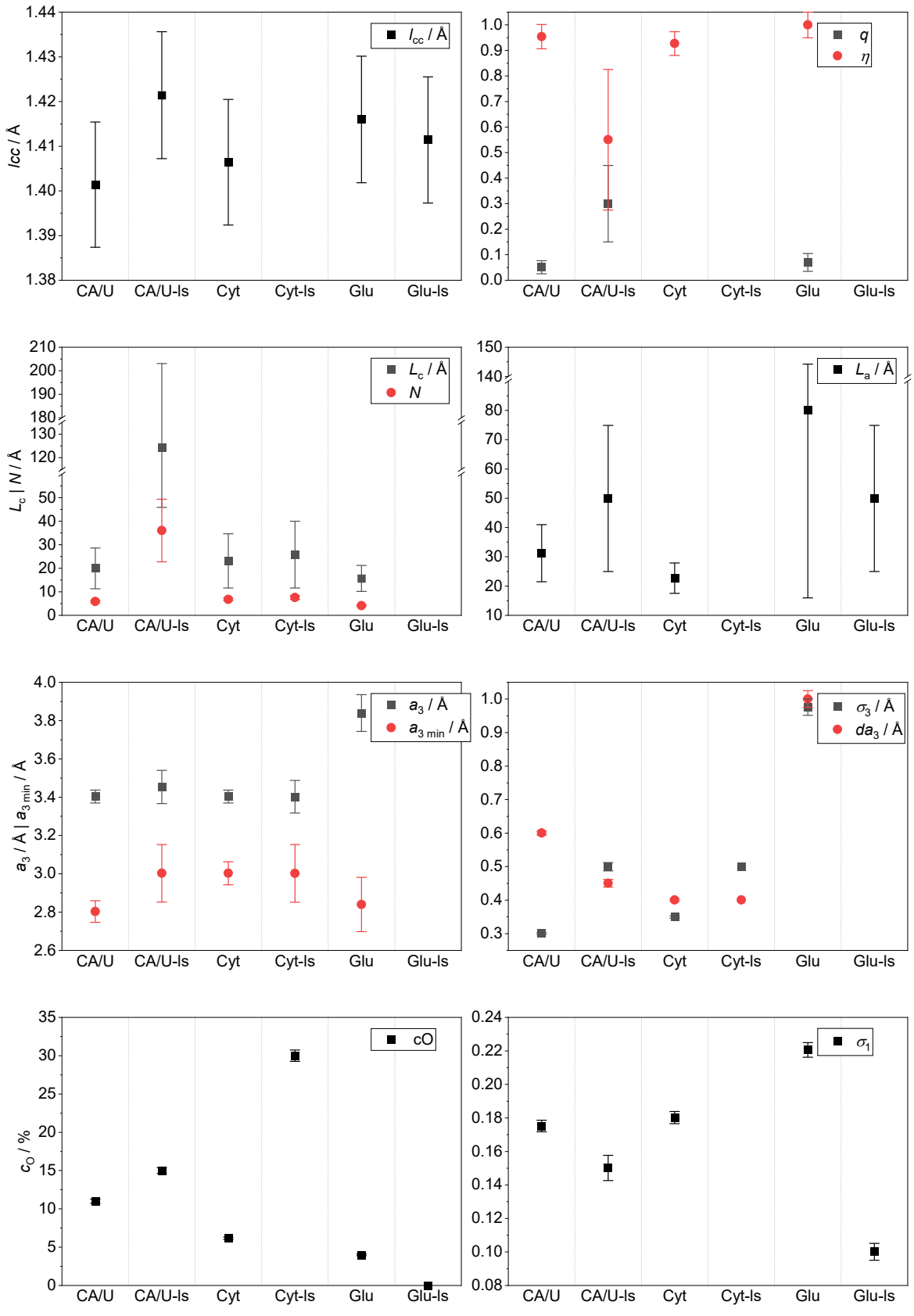

Figure S 7. Microstructure parameters of the resulting fits. Additional parameters are described in **Table S 1**.

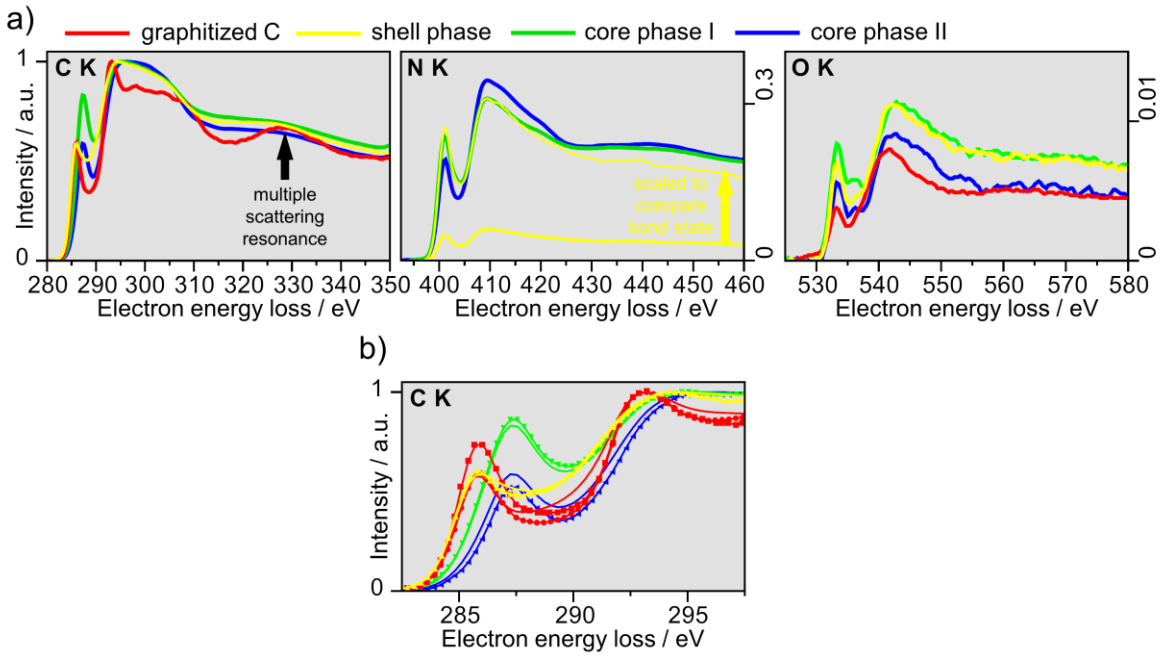

Figure S 8. **Supplementary data to EELS chemical-bond analyses:** a) PCA components of the C K, N K, and O K ionization edges (for each phase, the N, O edges are in scale with the respective C K edge): C K edge of graphitized carbon with pronounced MSR close to 330 eV (evolving in shell phase), B) validation of PCA components (continuous lines) by comparison to 50 summed and normalized experimental spectra from selected regions (marked by lines with symbols): two experimental curves are shown for the graphitized carbon, which are obtained from thin pore walls (squares) and an extended graphitized region (circles).

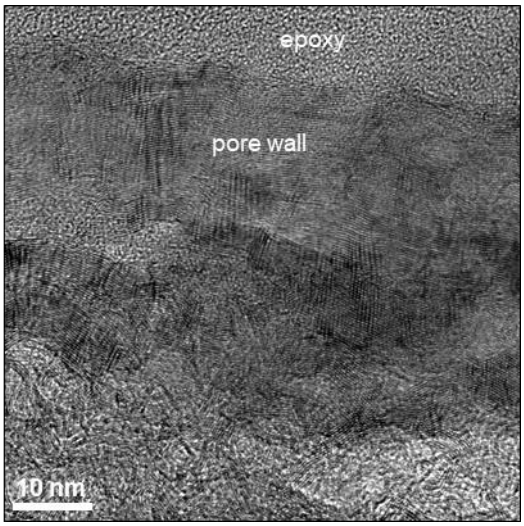

Figure S 9. Supplementary HRTEM image of the graphitized carbon phase of LP_{O2}-$Ade380_{90}/Glu300_{10}$ sensor.

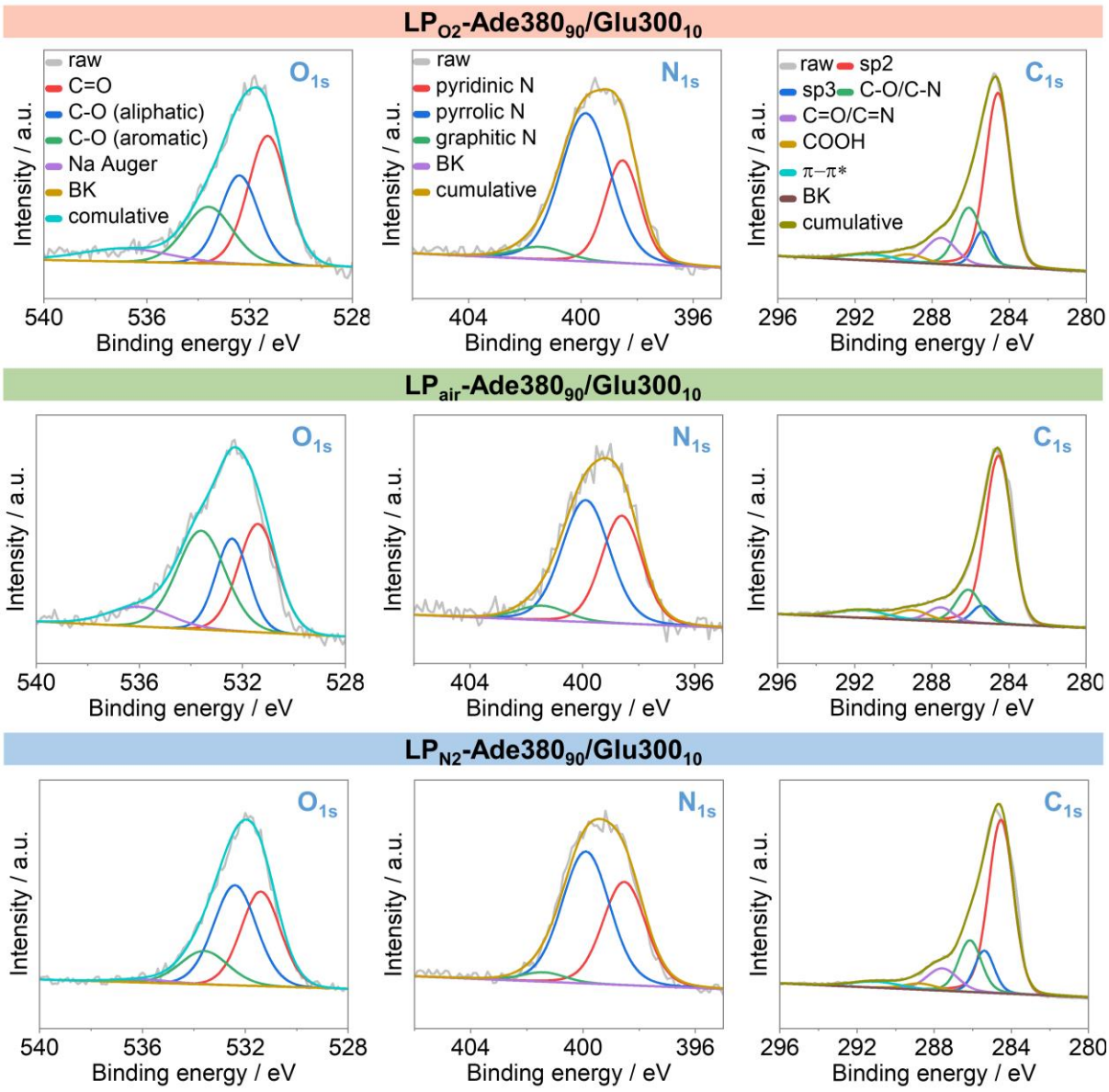

Figure S 10. X-ray photoelectron spectrographs of the O_{1s}, N_{1s}, and C_{1s} regions (from left to right) of LP$_{O2}$-Ade380$_{90}$/Glu300$_{10}$, LP$_{air}$-Ade380$_{90}$/Glu300$_{10}$ and LP$_{N2}$-Ade380$_{90}$/Glu300$_{10}$ (top to bottom).

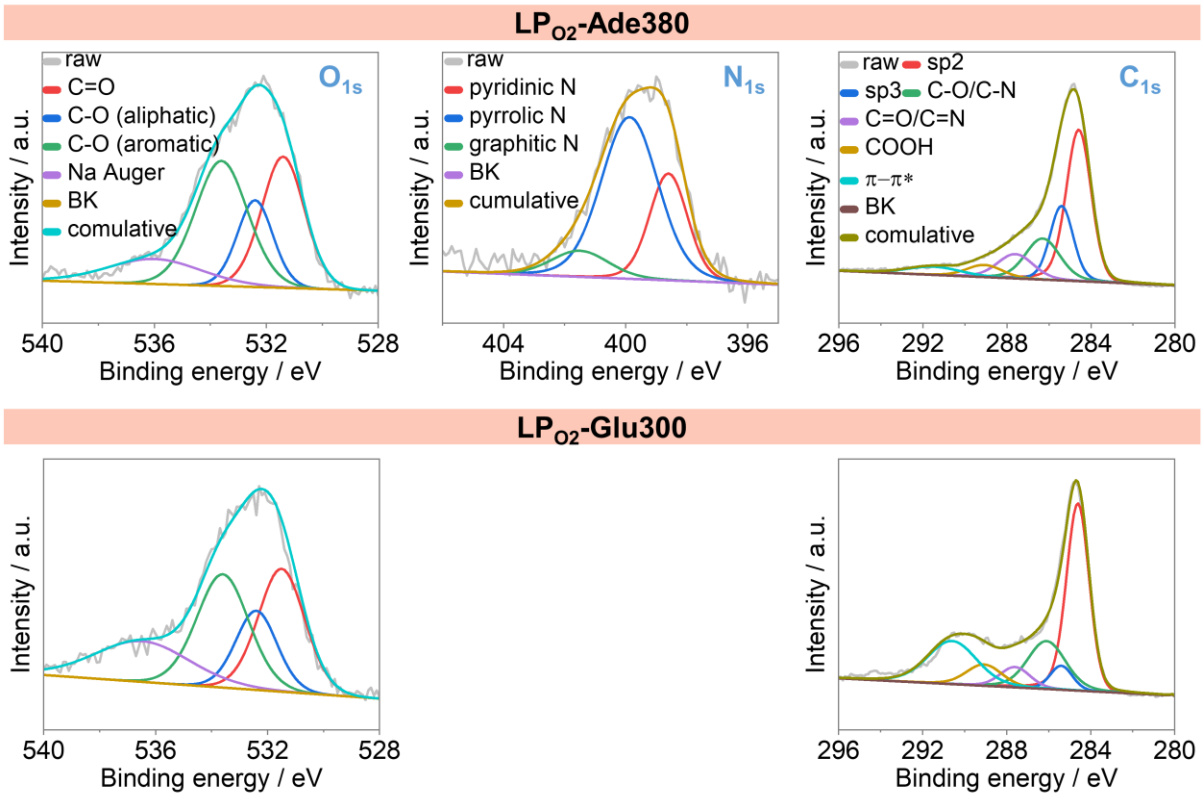

Figure S 11. X-ray photoelectron spectrographs of the O_{1s}, N_{1s}, and C_{1s} regions (from left to right) of LP_{O2}-Ade380 and LP_{O2}-Glu300 (top to bottom).

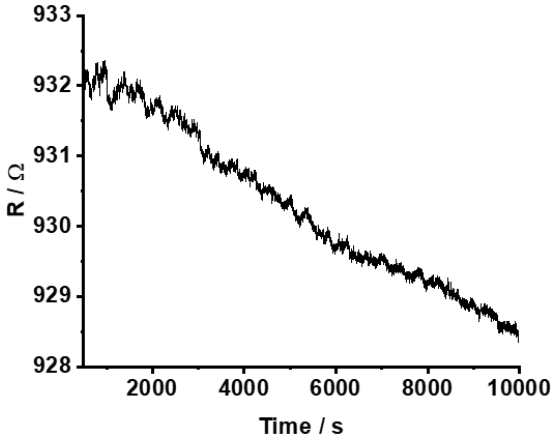

Figure S 12. Resistive response of the laser-patterning sensor film using an optimized cytosine based LP-NC towards 10% of CO_2.

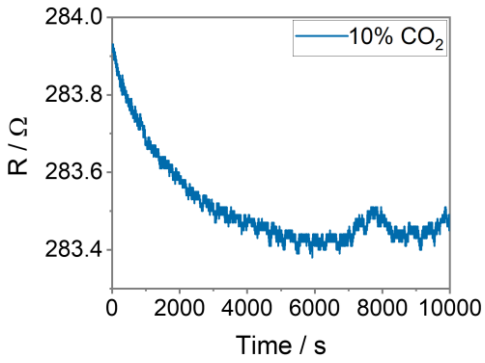

Figure S 13. Resistance response of laser-patterned polyimide (LP-PI) towards 10% CO_2 using N_2 as carrier gas.

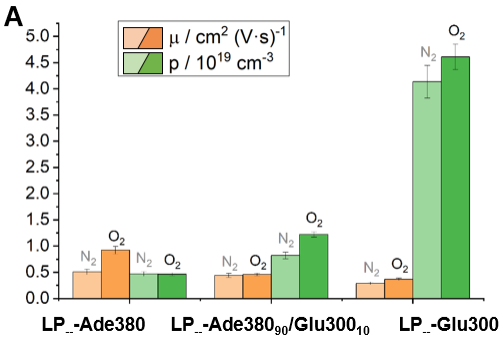

B

Sample	conductivity (σ) $S \cdot m^{-1}$	density (p) $\times 10^{-25}\ m^{-3}$	mobility (μ) $\times 10^{-5}\ m^2 \cdot (V \cdot s)^{-1}$
LP_{N2}-Ade380	38 ± 0.4	0.47 ± 0.043	5.1 ± 0.52
LP_{O2}-Ade380	68 ± 0.7	0.46 ± 0.031	9.2 ± 0.72
LP_{N2}-Glu300	192 ± 1.9	4.1 ± 0.31	2.9 ± 0.25
LP_{O2}-Glu300	270 ± 2.7	4.6 ± 0.24	3.7 ± 0.23
LP_{N2}-Ade380$_{90}$/Glu300$_{10}$	58 ± 0.6	0.82 ± 0.063	4.4 ± 0.38
LP_{O2}-Ade380$_{90}$/Glu300$_{10}$	89 ± 0.9	1.2 ± 0.051	4.6 ± 0.24

Figure S 14. a) Charge carrier mobilites (μ) and charge carrier densities (p) of all laser-carbonized films obtained by Hall measurements; b) Charge carrier properties of all laser-carbonized films obtained by Hall measurements.

Figure S13 presents the charge carrier mobilities (μ) (orange) and densities (p) (green) of LP-Ade380, LP-Glu300, and LP-Ade380$_{90}$/Glu300$_{10}$ produced in either N_2 or O_2 atmosphere. Obviously, LP-Glu300 exhibits generally high p with values up to 10 fold higher than in LP-Ade380. Throughout all tested samples, O_2 in the reaction atmosphere promotes an increase in both μ and p. Upon addition of Glu300 to Ade380, p is increased by a factor of ~2. In view of the band-structure and the influence of the charge density, for sensor applications, low p is favorable to achieve higher sensitivity.[287] However, the effect of Glu300 on the overall sensor performance is positive. We assume that the porogenic activity of Glu300 outweighs the detriment of the increased p.

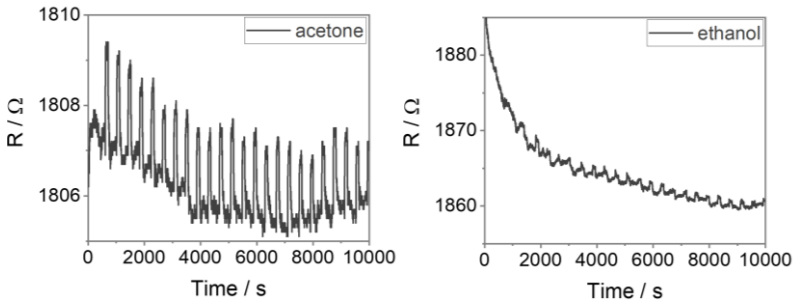

Figure S15. Resistance response of sensor films LP_{O2}-Ade380$_{90}$/Glu300$_{10}$ sensor towards 2.5% acetone (left) and 0.8% ethanol (right) using N_2 as carrier gas.

We performed some selectivity sensing experiments using volatile organic compounds (VOCs) acetone and ethanol as interference analytes. In **Figure S15**, the optimized sensor film LP_{O2}-$Ade380_{90}/Glu300_{10}$ shows a resistance response $\Delta R/R_0$ = 0.06% to 2.5 % acetone and almost no response to 0.8% ethanol.

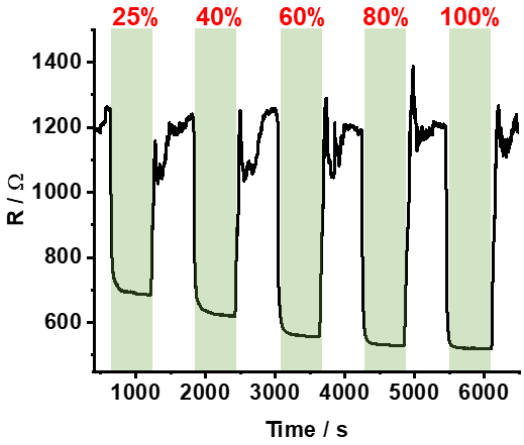

Figure S16. Resistance response of LP_{O2}_$Ade380_{90}/Glu300_{10}$ to different relative humidities in a 100% N_2 environment.

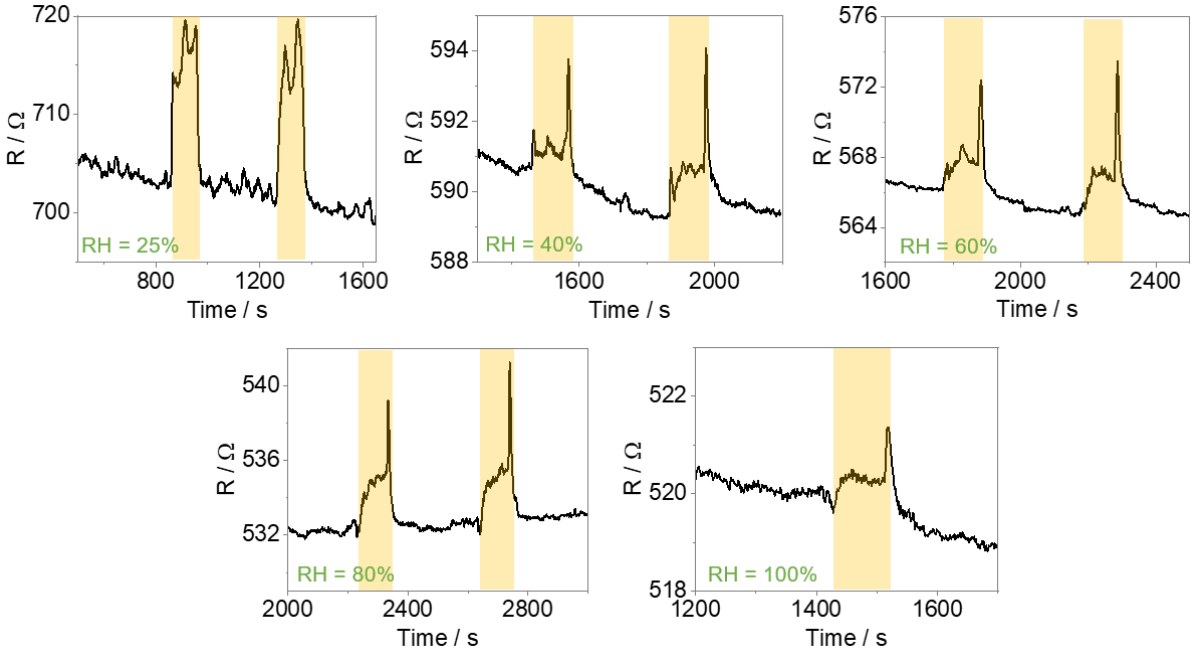

Figure S17. Resistance response of LP_{O2}_$Ade380_{90}/Glu300_{10}$ to 10% CO_2 (90%N_2) at different relative humidities. The sharp peak at the end of the cycles originates from a sudden pressure release from the valve.

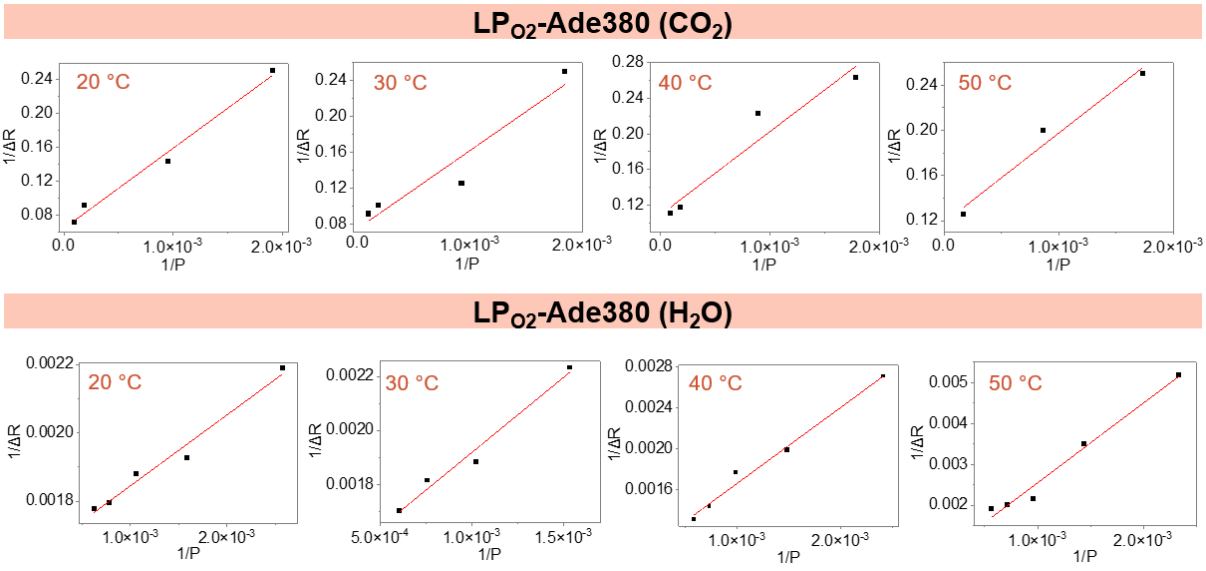

Figure S18. Plots of 1/ΔR as a function of 1/P at 20 ºC, 30 ºC, 40 ºC and 50 ºC for the determination of the equilibrium constants K of LP_{O2}_Ade380 to CO_2 (upper panel) or H_2O (lower panel).

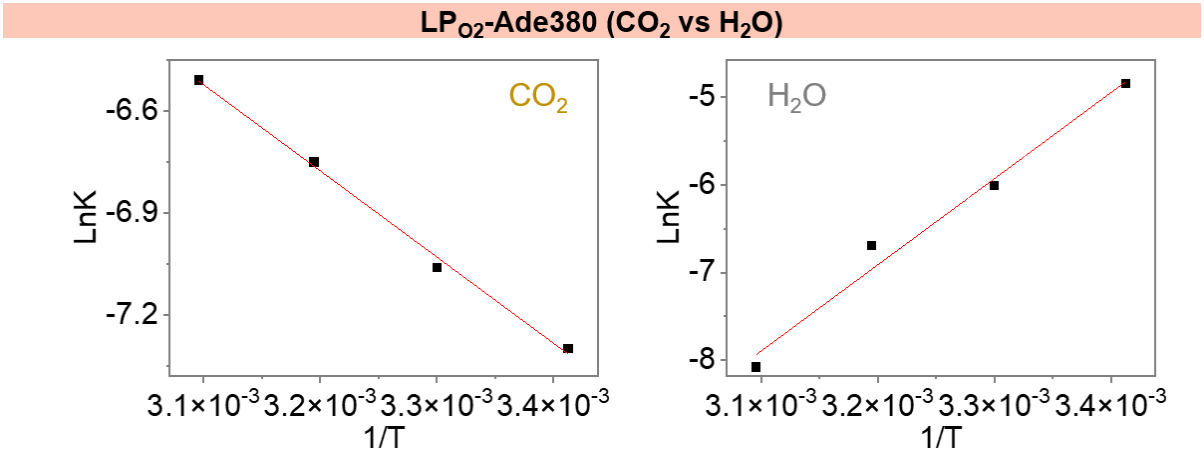

Figure S19. Plots of ln K as a function of 1/T for the determination of $\Delta_{ads}H$ of CO_2 and H_2O to LP_{O2}_Ade380.

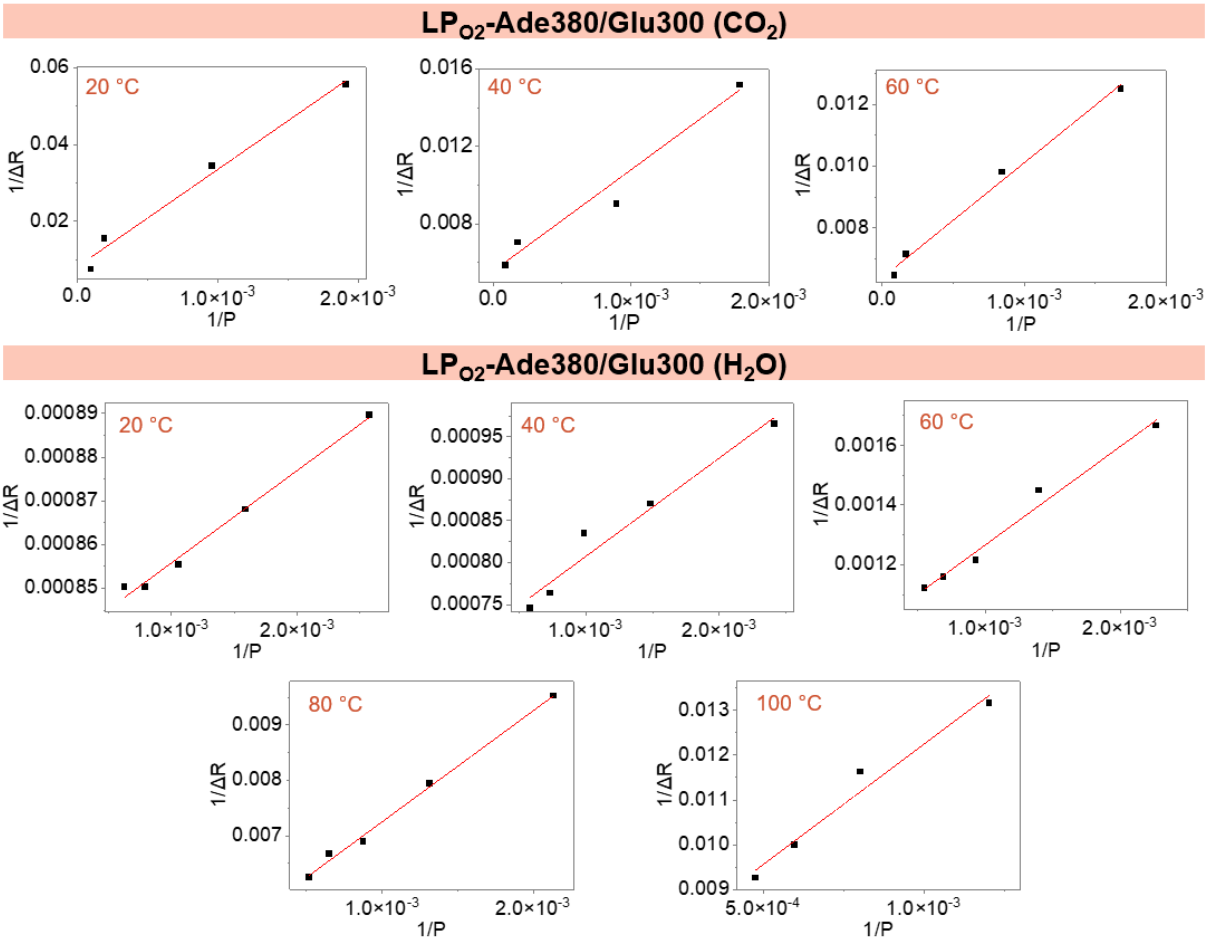

Figure S20. Plots of 1/ΔR as a function of 1/P at 20 ºC, 40 ºC and 60 ºC for the determination of the equilibrium constants K of LP_{O2}_$Ade380_{90}/Glu300_{10}$ to CO_2 (upper panel) and H_2O (lower panel).

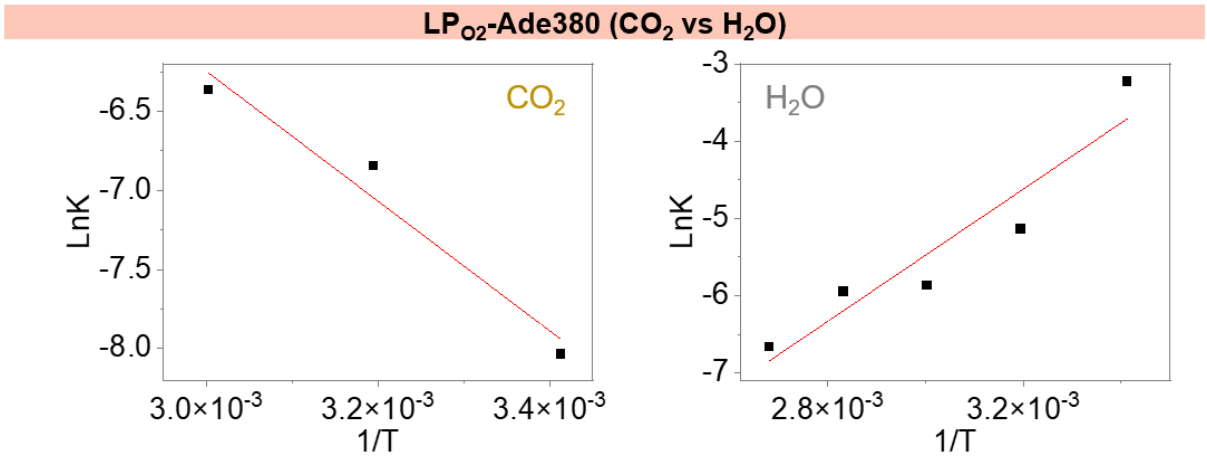

Figure S21. Plots of ln K as a function of 1/T for the determination of $\Delta_{ads}H$ of CO_2 and H_2O to LP_{O2}_$Ade380_{90}/Glu300_{10}$.

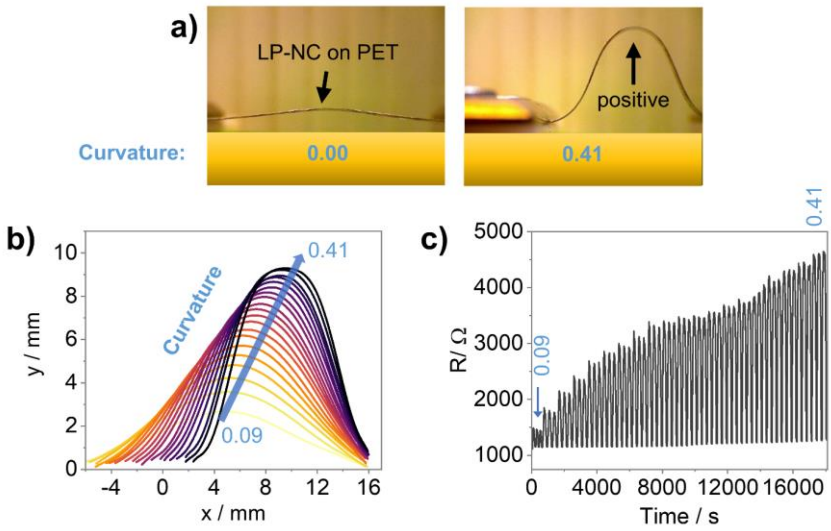

Figure S22. a) Photographs of the LP_{O2}-$Ade380_{90}/Glu300_{10}$ sensor strip on PET mounted between two electrodes (one movable). b) Curvature analysis of the LP-NC strip in dependence of the distance between the two electrodes in the movable stage; c) Change in resistance upon steadily increasing the curvature in the first run (training mode); d) Change in resistance upon steadily increasing the curvature in all subsequent runs (operation mode).

The curvature of the bending is dependent on the distance between the two electrodes and was determined in a range between a minimum value of 0.09 and a maximum value of 0.41 mm^{-1}.[187] The response changes gradually with the curvature. During the first (initial) bending sequence, the sensor strip was bent at a slow speed of only 10 µm s^{-1} starting at low curvatures of 0.09 mm^{-1} and slowly increasing to the maximum curvature of 0.4 mm^{-1} (three times for each curvature/amplitude). **Figure S22** shows the corresponding response of increasing R: small change at low curvatures, becomes larger at increasing curvatures. After the first run, the response remains stable in all subsequent runs and exhibit a quantitative response to any curvature.

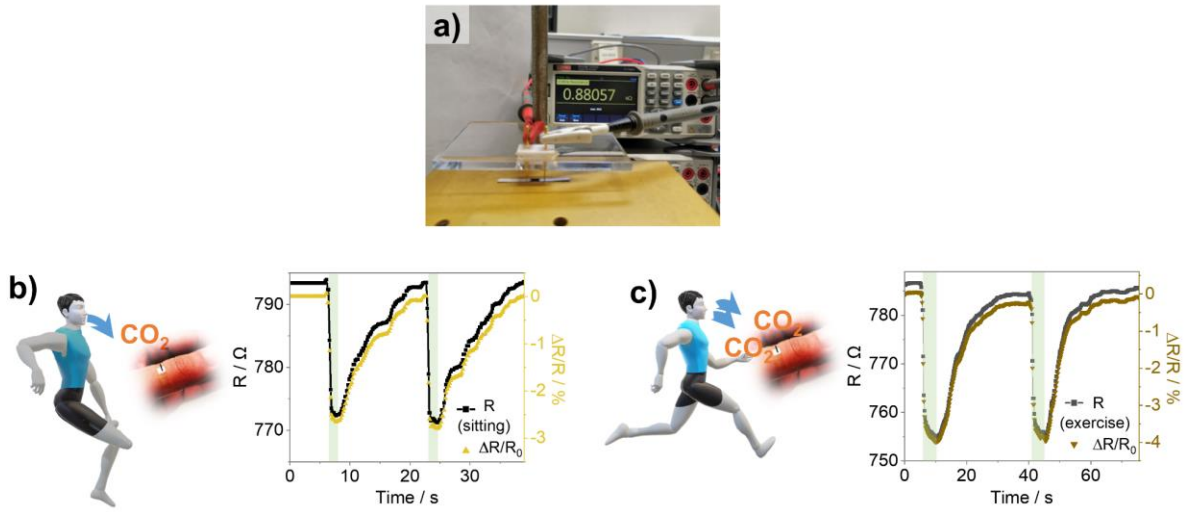

Figure S23. a) Photograph of breath monitoring test in an open environment; b) resistive and kinetic response of LP_{O2}-$Ade380_{90}/Glu300_{10}$ to exhaled breath of a human at rest; c) Resistive and kinetic response to exhaled breath of a human at exercise.

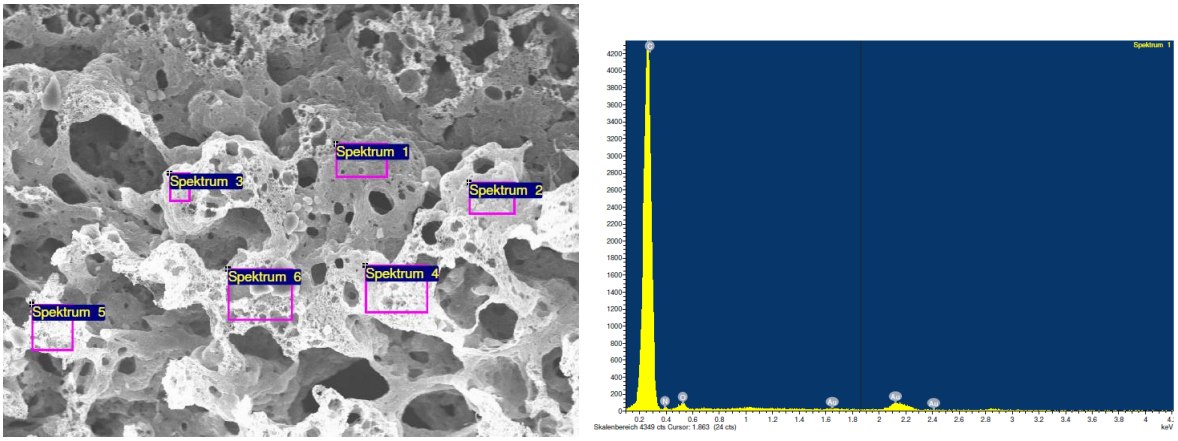

Figure S 24. Energy-dispersive X-ray analysis of LP-NC film produced with 40 wt% NaI. Au-impurities originate from the substrate. No sodium was detected (Kα of sodium has an energy of 1.041 keV).

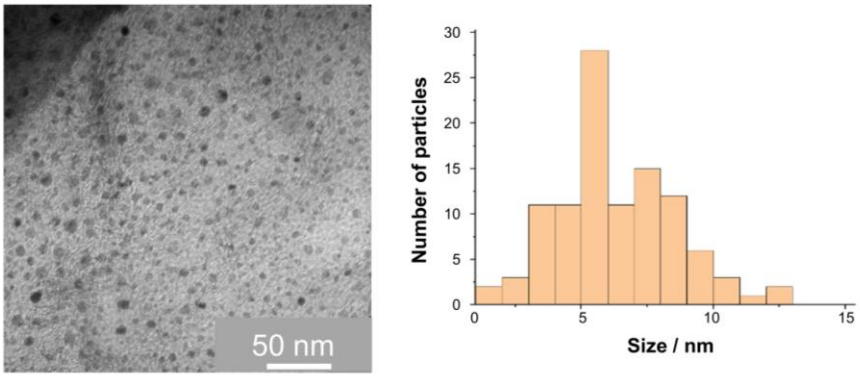

Figure S 25. Left: Transmission electron micrograph of LP-MoC_{1-x}@NC; right: Size distribution histogram of the diameters of the MoC_{1-x} nanoparticles (100 particles).

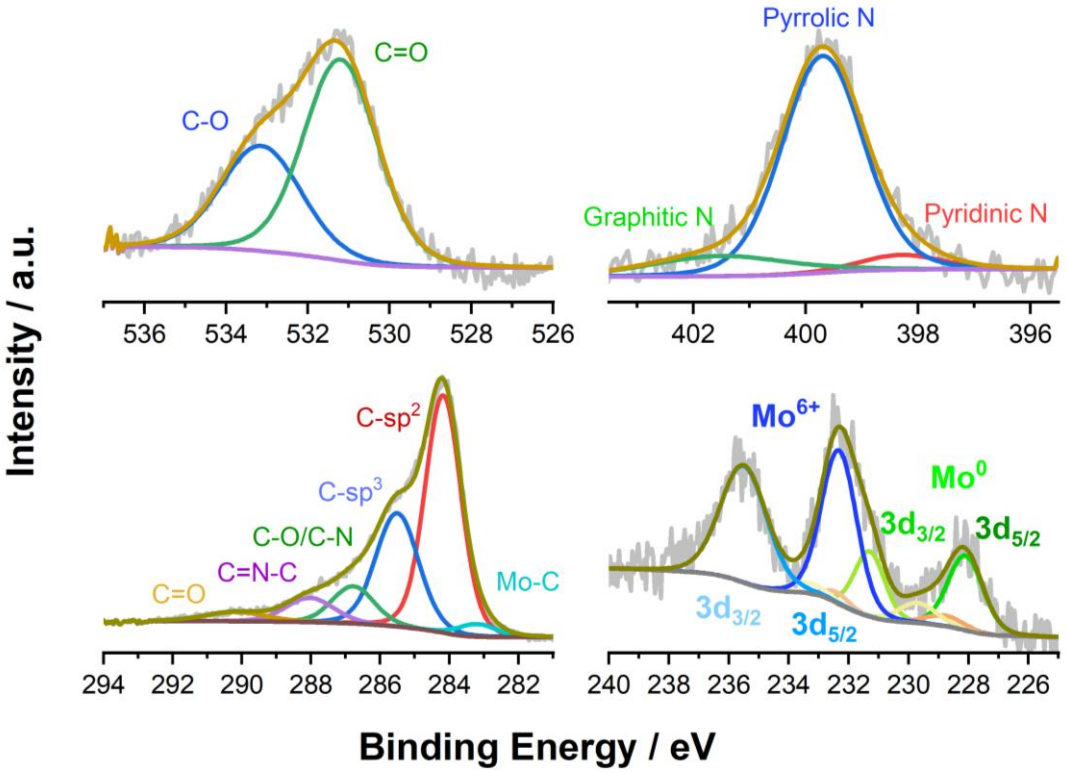

Figure S 26. X-ray photoelectron spectra of the O_{1s}, N_{1s}, C_{1s}, and Mo_{3d} regions (from top left to bottom right) of LP-MoC_{1-x}(10)@NC. The strong C-sp^3 and C-O/C-N signals are attributed to adventitious carbon.

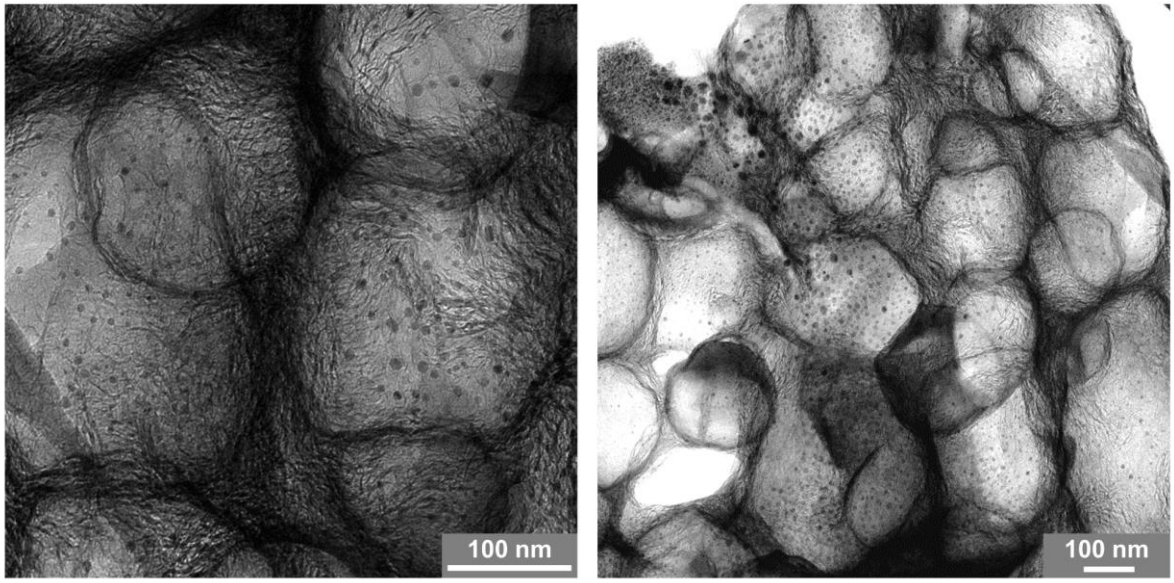

Figure S 27. TEM of LP-MoC_{1-x}(10)@NC(NaI40).

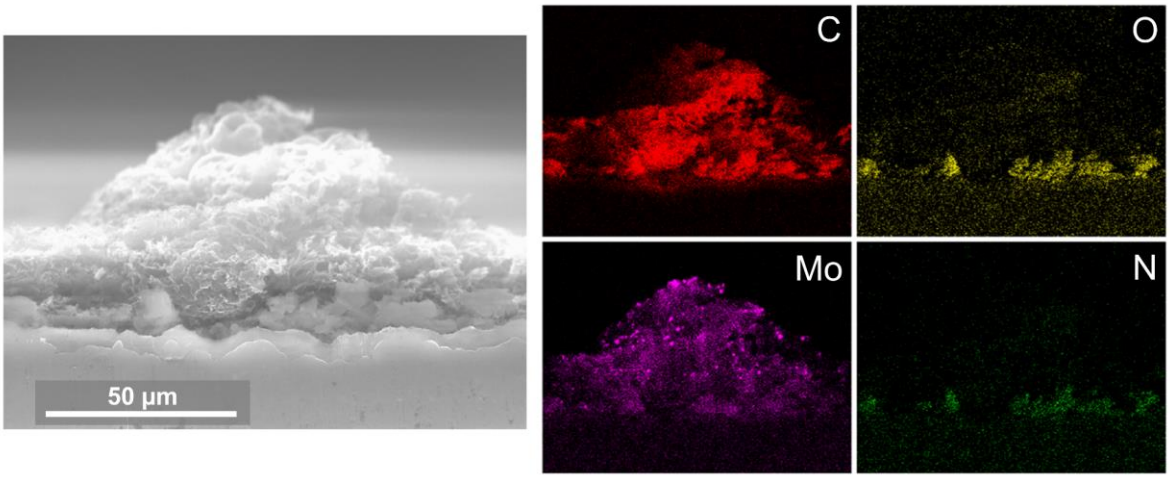

Figure S 28. Cross-sectional SEM and EDX analysis of LP-MoC_{1-x}@NC(NaI40) on an aluminium sheet.

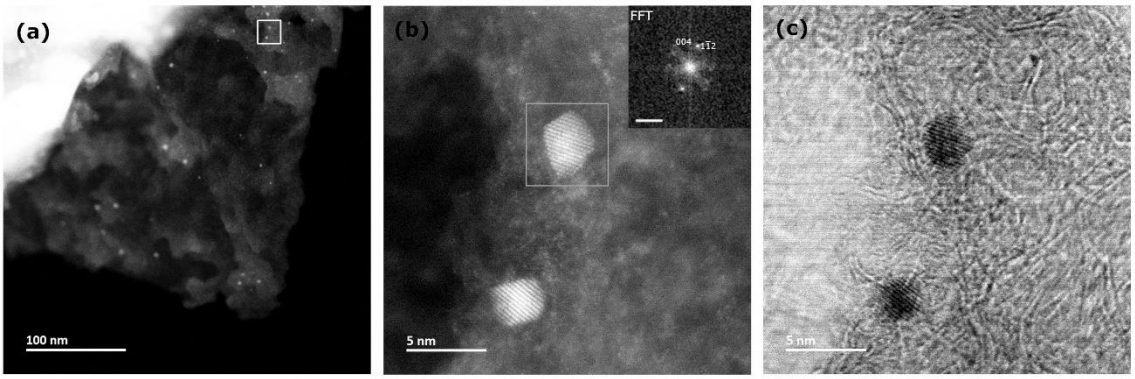

Figure S 29. a) ADF-STEM image of LP-MoC_{1-x}@NC(NaI40); b-c) ADF and BF STEM images of the region indicated by the grey square in (a). The inserted FFT from the selected particle in (b) consistent with tetragonal crystal structure from [110] zone axis.

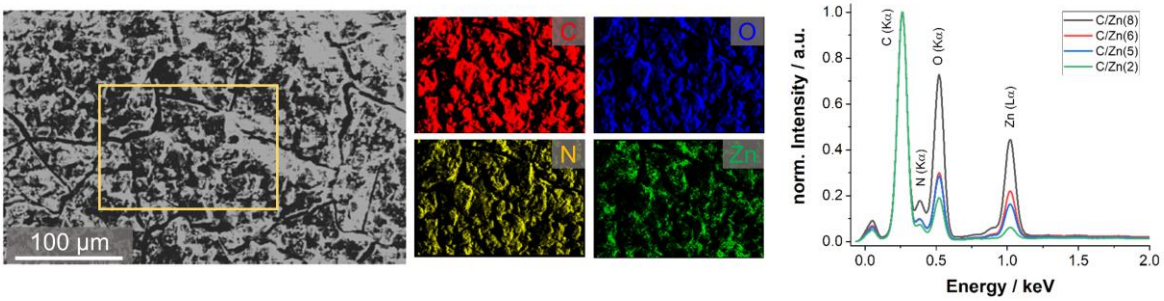

Figure S 30. Exemplary top-view EDX map of the precursor film C/Zn(8), EDX spectra of C/Zn(2), (5), (6), and (8).

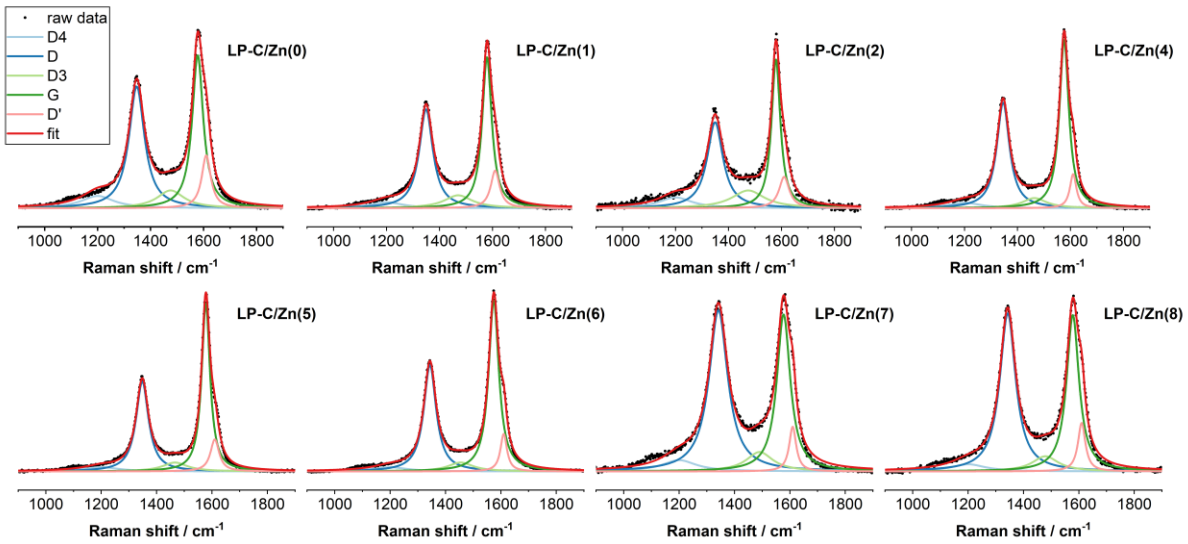

Figure S 31. Multi-peak fittings of the Raman modes in the region between 900 and 1900 cm^{-1}.

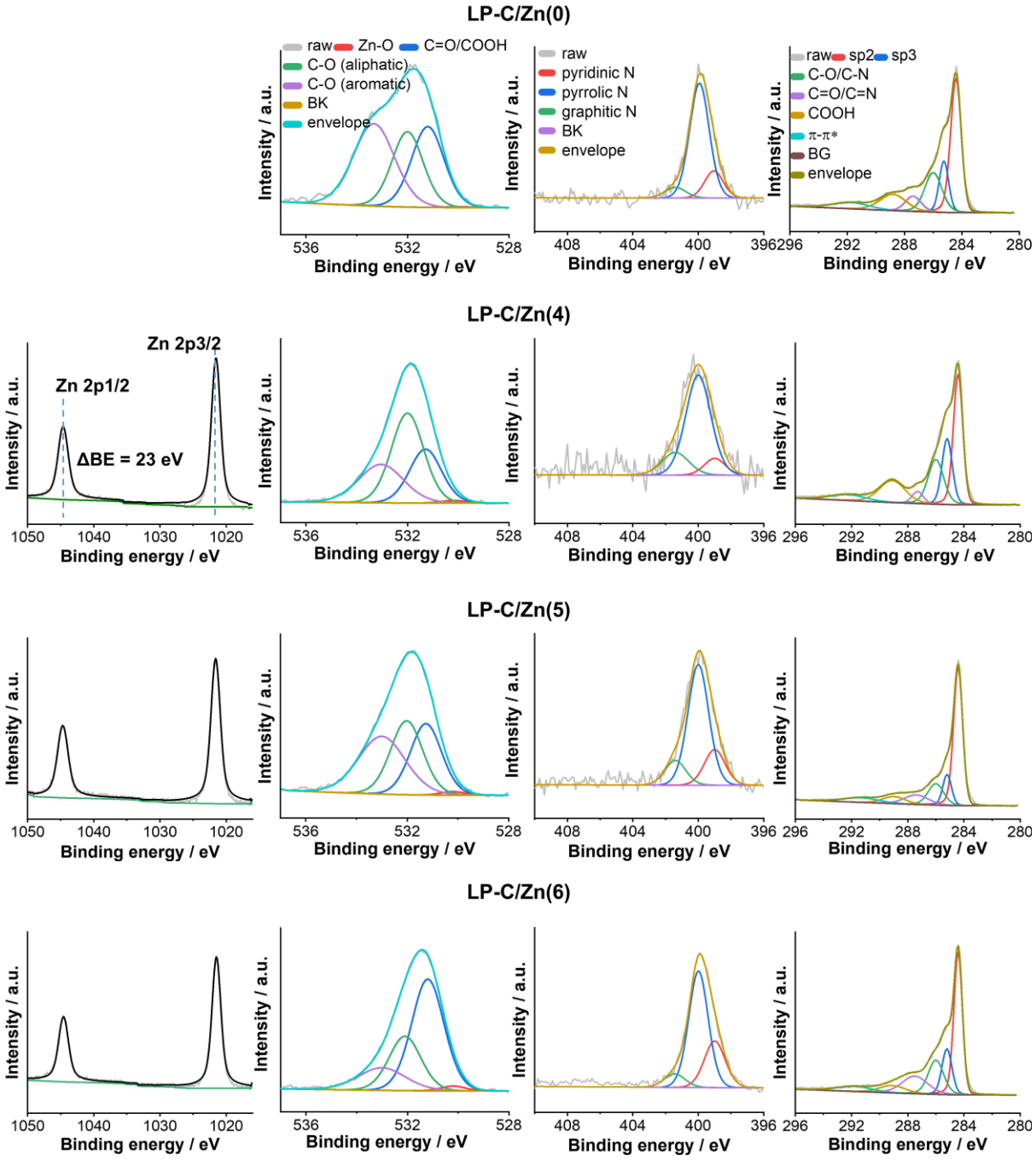

Figure S 32. X-ray photoelectron spectroscopic analysis of LP-C/Zn(0), (4), (5) and (6).

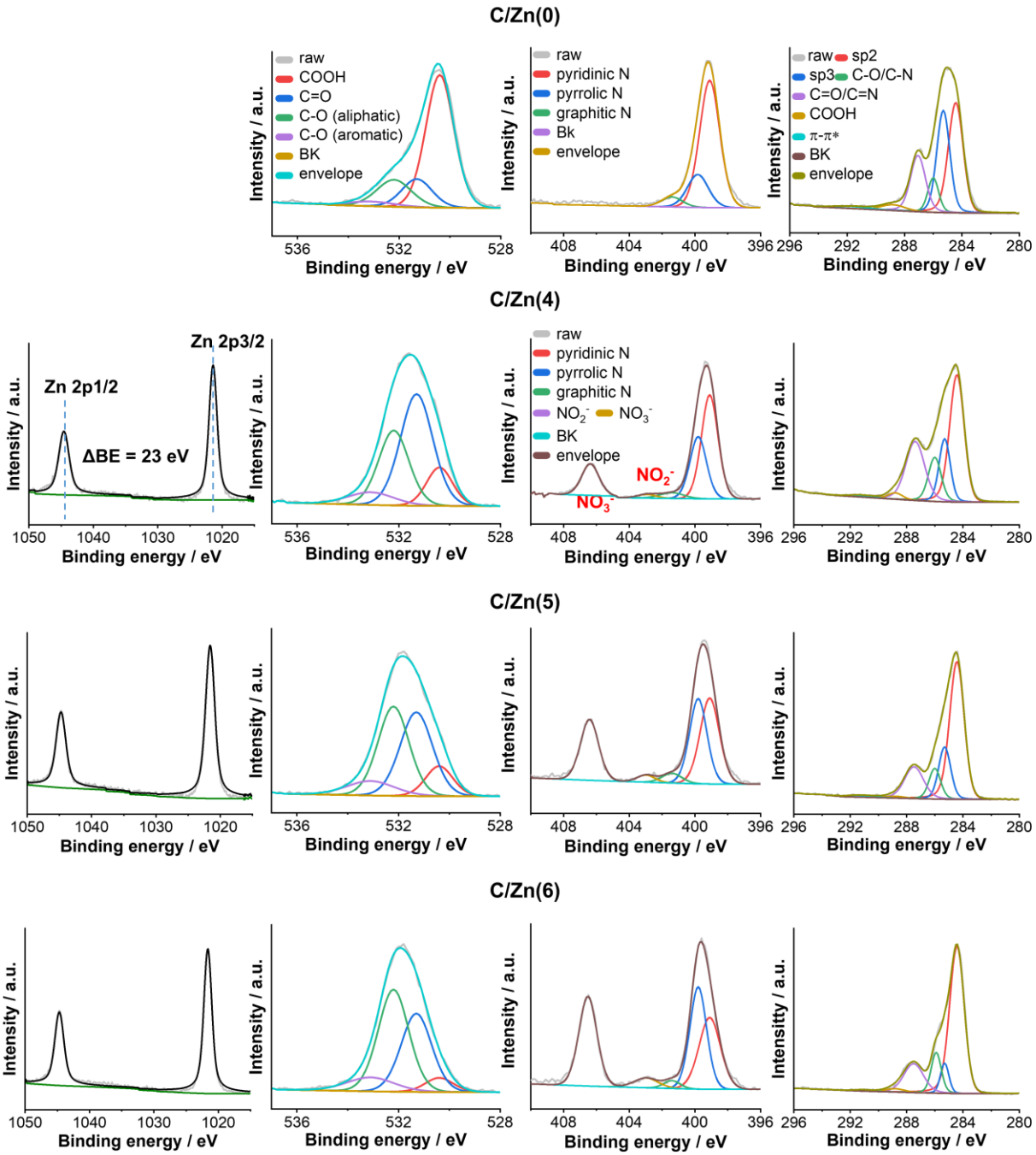

Figure S 33. X-ray photoelectron spectroscopic analysis of primary films C/Zn(0), (4), (5) and (6).

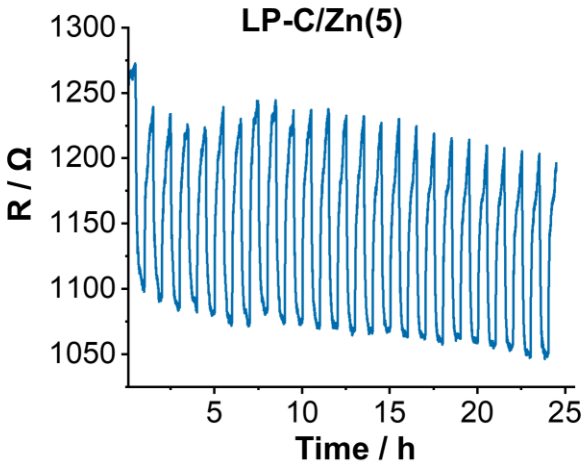

Figure S 34. Stability test over time of LP-C/Zn(5) film towards 2.5% acetone.

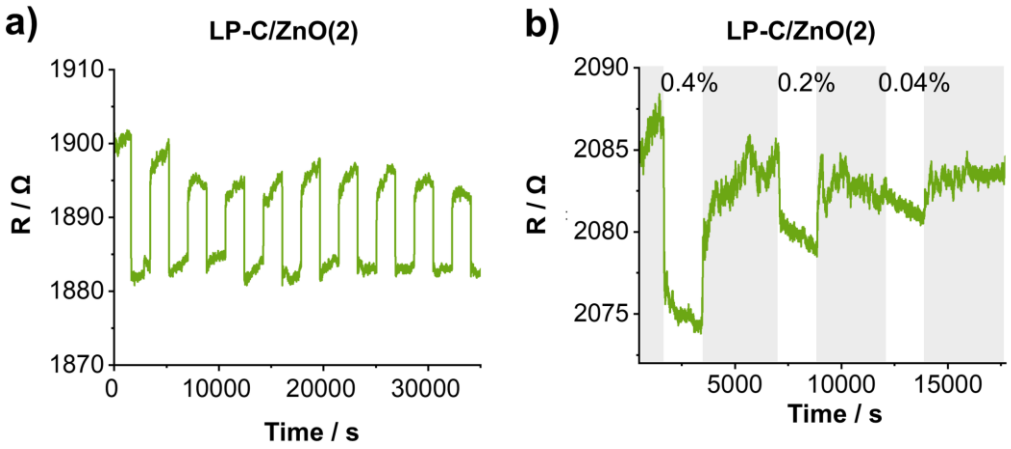

Figure S 35. a) Stability test over time of LP-C/ZnO(2) film. b) Resistive response of LP-C/ZnO(2) film towards 0.4%, 0.2 % and 0.04% toluene.

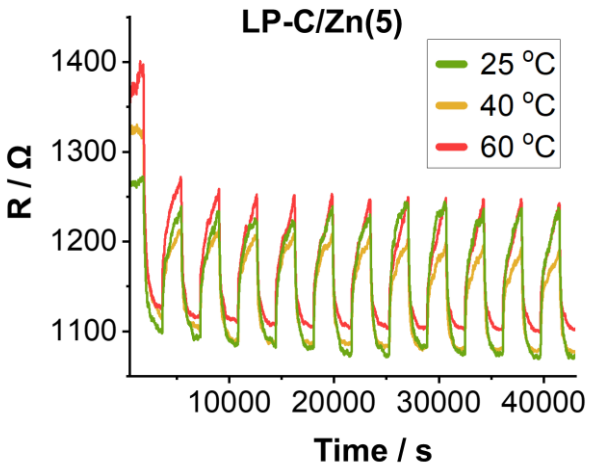

Figure S 36. Resistive response of LP-C/Zn(5) film towards 2.5% acetone at 25, 40 and 60 °C

9.4 Appendix Tables

Table S 1. Microstructure parameters of the resulting fit with assumed errors in brackets*.

	CA/U(950)	CA/U(300)-ls	cytosine(950)	cytosine(300)-ls	glucose(950)	glucose(300)-ls
a_3 / Å	3.40 (0.03)	3.45 (0.09)	3.40 (0.03)	3.40 (0.09)	3.84 (0.10)	- -
$a_{3\,min}$ / Å	2.80 (0.06)	3.00 (0.15)	3.00 (0.06)	3.00 (0.15)	2.84 (0.14)	- -
da_3 / Å	0.60 (0.01)	0.45 (0.01)	0.40 (< 0.01)	0.40 (< 0.01)	1.00 (0.03)	- -
σ_3 / Å	0.30 (< 0.01)	0.50 (0.01)	0.35 (< 0.01)	0.50 (< 0.01)	0.98 (0.02)	- -
L_c / Å	20.0 (8.7)	124.5 (78.6)	23.2 (11.5)	25.8 (14.2)	15.7 (5.5)	- -
N	5.9 (0.6)	36.1 (13.3)	6.8 (0.6)	7.6 (0.8)	4.1 (0.3)	- -
l_{cc} / Å	1.401 (0.014)	1.421 (0.014)	1.406 (0.014)	- -	1.416 (0.014)	1.411 (0.014)
σ_1	0.175 (0.004)	0.150 (0.008)	0.180 (0.004)	- -	0.221 (0.004)	0.100 (0.005)
L_a / Å	31.2 (9.7)	50.0 (10.0)	22.7 (1.0)	- -	80.1 (64.1)	50.0 (20.0)
q	0.05 (0.03)	0.30 (0.15)	- -	- -	0.07 (0.03)	- -
η	0.95 (0.05)	0.55 (0.28)	0.93 (0.05)	- -	1.00 (0.05)	- -
c_O / %	0.11 (0.003)	0.15 (0.004)	0.06 (0.002)	0.30 (0.008)	0.04 (0.001)	0.00 (0)

* Some parameters could not be calculated due to the absence of a stacking or sp^2 structure. da_3 describes the difference between the average layer distance to the minimal layer distance ($da_3 = a_3 – da_3$), N is the number of layers per stack, i.e., $N = L_c / a_3$, q is a parameter for the preferred orientation during the XRD measurements (q = 0 means no preferred orientation) and η is the homogeneity of the stacks (η = 1 means perfect homogeneity) and c_O describes the concentration of oxygen.

Table S 2. Composition of carbon of sensor obtained by deconvolution of the C1s and O1s peaks of the XPS spectra.

Sample	C_{1s} peaks (% of total peak area)						O_{1s} peaks (% of total peak area)		
	C-Sp^2	C-Sp^3	C-N/ C-O	C=N/ C=O	COOH	π- π*	C=O	C-O (aliph.)	C-O (arom.)
LP_{O2}-Ade_{90}/Glu_{10}	55.1	7.9	19.2	10.3	3.4	4.1	45.4	30.2	24.4
LP_{air}-Ade_{90}/Glu_{10}	66.1	5.2	12.4	5.5	5.0	5.8	35.4	25.1	39.5
LP_{N2}-Ade_{90}/Glu_{10}	56.8	11.1	16.0	9.4	2.7	4.0	38.7	44.6	16.7
LP_{O2}-Ade380	42.9	19.9	16.7	10.3	5.1	5.1	36.8	20.3	42.9
LP_{O2}-Glu300	41.4	5.2	18.2	6.2	7.7	21.3	38.5	21.9	39.5

Table S 3. Equilibrium constants K, parameter **α,** and heat of adsorption $\Delta_{ads}H$ of LP_{O2}_Ade380.

LP_{O2}_Ade380				
	CO_2		**H_2O**	
	K	**α**	**K**	**α**
20 ºC	6.76×10^{-4}	0.06	7.88×10^{-3}	1.64×10^{-3}
30 ºC	8.58×10^{-4}	0.07	2.45×10^{-3}	1.36×10^{-3}
40 ºC	1.17×10^{-3}	0.11	1.23×10^{-3}	9.19×10^{-4}
50 ºC	1.49×10^{-3}	0.12	3.08×10^{-4}	6.01×10^{-4}
$\Delta_{ads}H$	21.3 kJ·mol^{-1}		-81.7 kJ·mol^{-1}	

Table S4. Equilibrium constants K, parameter **α,** and heat of adsorption $\Delta_{ads}H$ of LP_{O2}_$Ade380_{90}/Glu300_{10}$.

LP_{O2}_$Ade380_{90}/Glu300_{10}$				
	CO_2		**H_2O**	
	K	**α**	**K**	**α**
20 ºC	6.23×10^{-4}	8.00×10^{-3}	4.00×10^{-2}	8.35×10^{-4}
40 ºC	1.07×10^{-4}	5.57×10^{-3}	5.86×10^{-3}	6.90×10^{-3}
60 ºC	1.72×10^{-3}	6.39×10^{-3}	2.83×10^{-3}	9.35×10^{-4}
80 ºC			2.62×10^{-3}	5.25×10^{-4}
100 ºC			1.28×10^{-4}	6.88×10^{-3}
$\Delta_{ads}H$	34.1 kJ·mol^{-1}		-35.6 kJ·mol^{-1}	

Table S 5. Comparative list of the specific surface areas of different N-doped carbons* obtained by BET sorption measurements and the MB adsorption method.**

	C/N ratio	BET surface area	MB surface area
activated carbon	∞	1672	1269
C8NZ	3.1	1834	497
C8LZ	5.7	1701	358
A8LK	2.1	389	71
LP-NC	5.2		238

** Bulk samples of the listed N-doped carbons were obtained from pyrolysis of nitrogen-rich precursors (internal compounds, not yet published).*
*** In contrast to the BET sorption method, the MB adsorption method is a liquid based method for the determination of the specific surface areas of small amounts of carbonaceous materials (< 1 mg) and allows only limited conclusions on absolute values, but good estimations on relative values. The accessibility of micropores is generally different in the gas and the liquid phase.*

Table S 6.*Comparative list of the electronic features obtained by Hall measurements.*

Sample	Mobility / $cm^2 \cdot (V \cdot s)^{-1}$	Charge carrier density / cm^{-3}	Hall coefficient / $cm^3 \cdot C^{-1}$
LP-NC	0.12	7.70×10^{19}	+0.099
LP-NC(NaI40)	0.23	3.68×10^{19}	+0.19
LP-MoC_{1-x}(10)@NC	1.42	1.96×10^{19}	+0.32
LP-MoC_{1-x}(10)@NC(NaI40)	4.35	2.34×10^{18}	+2.67

10. List of publications

1. H. Wang, G. Chen, V. Strauss, O. Savateev, G. Hai, L. Ding, H. Wang, M. Antonietti, Laser-induced nitrogen fixation, ***under revision*****, 2023**
2. H. Wang, P. Jiménez-Calvo, M. Hepp, M. A. Isaacs, C. Otieno Ogolla, I. Below-Lutz, B. Butz, V. Strauss, Laser-patterned porous carbon/ZnO nanostructure composites for selective room-temperature sensing of volatile organic compounds. ***ACS Appl. Nano Mater.*** **(2023)**
3. H. Wang, C. O. Ogolla, G. Panchal, M. Hepp, S. Delacroix, D. Cruz, D. Kojda, J. Ciston, C. Ophus, A. Knop-Gericke, K. Habicht, B. Butz, V. Strauss, Flexible CO_2 sensor architecture with selective nitrogen functionalities by one-step laser-induced conversion of versatile organic ink. ***Adv. Funct. Mater.*****,** 2207406 (2022)
4. H. Wang, M. Jerigova, J. Hou, N. V. Tarakina, S. Delacroix, N. López-Salas, V. Strauss, Modulating between $2e^-$ and $4e^-$ pathways in the oxygen reduction reaction with laser-synthesized iron oxide-grafted nitrogen-doped carbon. ***J. Mater. Chem. A.*** **10**, 24156–24166 (2022).
5. H. Wang, S. Delacroix, A. Zieleniewska, J. Hou, N. V. Tarakina, D. Cruz, I. Lauermann, A. J. Ferguson, J. L. Blackburn, V. Strauss, In situ synthesis of molybdenum carbide nanoparticles incorporated into laser-patterned nitrogen-doped carbon for room temperature VOC Sensing. ***Adv. Funct. Mater.*****,** 2104061 (2021)
6. H. Wang, S. Delacroix, O. Osswald, M. Anderson, T. Heil, E. Lepre, N. Lopez-Salas, R. B. Kaner, B. Smarsly, V. Strauss, Laser-carbonization: peering into the formation of micro-thermally produced (N-doped)carbons. ***Carbon*** **176**, 500–510 (2021).
7. M. Devi, H. Wang, S. Moon, S. Sharma, V. Strauss, Laser-carbonization-a powerful tool for micro-fabrication of patterned electronic carbons. ***Adv. Mater***., 2211054 (2023)
8. M. Hepp, H. Wang, K. Derr, S. Delacroix, S. Ronneberger, F. F. Loeffler, B. Butz, V. Strauss, Trained laser-patterned carbon as high-performance mechanical sensors. ***npj Flex. Electron***. **6**, 3 (2022).
9. S. Delacroix, H. Wang, T. Heil, V. Strauss, Laser-induced carbonization of natural organic precursors for flexible electronics. ***Adv. Electron. Mater***. **6**, 2000463 (2020).

10. V. Strauss, H. Wang, S. Delacroix, M. Ledendecker, P. Wessig, Carbon nanodots revised: the thermal citric acid/urea reaction. ***Chem. Sci.*** **11**, 8256–8266 (2020).

11. Declaration

Die vorliegende Dissertation entstand in dem Zeitraum zwischen Juni 2020 und Januar 2023 am Max-Planck-Institut für Kolloid- und Grenzflächenforschung unter Betreuung von Prof. Dr. Dr. h.c. Markus Antonietti.

Ich erkläre, dass ich die Dissertation selbständig und nur unter Verwendung der von mir gemäß § 7 Abs. 3 der Promotionsordnung der Mathematisch-Naturwissenschaftlichen Fakultät, veröffentlicht im Amtlichen Mitteilungsblatt der Humboldt-Universität zu Berlin Nr. 42/2018 am 11.07.2018 angegebenen Hilfsmittel angefertigt habe.

The present work was carried out during the period between June 2020 and September 2022 at the Max Planck Institute of Colloids and Interfaces under the supervision of Prof. Dr. Dr. h.c. Markus Antonietti.

I declare that I have completed the thesis independently using only the aids and tools specified. I have not applied for a doctor's degree in the doctoral subject elsewhere and do not hold a corresponding doctor's degree. I have taken due note of the Faculty of Mathematics and Natural Sciences PhD Regulations, published in the Official Gazette of Humboldt-Universität zu Berlin no. 42/2018 on 11/07/2018

Huize Wang

Erlangen, 17.06.2023